Development of an ^{90}Y calibration source and rejection of pileup backgrounds in the SNO+ experiment

Evelina Arushanova

Particle Physics Research Centre

School of Physics and Astronomy
Queen Mary University of London

Thesis submitted in partial fulfilment of the requirements of the

Degree of Doctor of Philosophy in the

Queen Mary University of London

· May 2018 ·

Statement of originality

I, Evelina Arushanova, confirm that the research included within this thesis is my own work or that where it has been carried out in collaboration with, or supported by others, that this is duly acknowledged below and my contribution indicated. Previously published material is also acknowledged below.

I attest that I have exercised reasonable care to ensure that the work is original, and does not to the best of my knowledge break any UK law, infringe any third party's copyright or other Intellectual Property Right, or contain any confidential material.

I accept that the College has the right to use plagiarism detection software to check the electronic version of the thesis.

I confirm that this thesis has not been previously submitted for the award of a degree by this or any other university.

The copyright of this thesis rests with the author and no quotation from it or information derived from it may be published without the prior written consent of the author.

Signature:

Date:

Details of collaboration and publications:

1. E. Arushanova, A. R. Back, *Probing neutrinoless double beta decay with SNO+*, NuPhys2014 conference proceedings (2015), arXiv:1505.00247;
2. S. Andringa et al. [SNO+ Collaboration], *Current Status and Future Prospects of the SNO+ Experiment*, Adv. High Energy Phys. **2016**, 6194250, arXiv:1508.05759;

3. E. Arushanova, J. Wilson, *SNO+ scintillator cocktail studies using an* ^{90}Y *source*, NuPhys2015 conference proceedings (2016), arXiv:1605.00134;

Abstract

SNO+ is a multi-purpose liquid scintillator detector with the main aim of investigating neutrinoless double beta decay ($0\nu2\beta$) of ^{130}Te. The sensitivity of such rare decay searches is limited by backgrounds, therefore it is crucial to reduce and constrain backgrounds in the energy region of interest (ROI).

This thesis presents the comprehensive study of particularly dangerous pileup backgrounds occurring in the scintillator with 0.3% of Tellurium-130 loading. The thesis determines which pileup backgrounds are the most problematic, estimates their event levels, describes their properties and methods to reject them from the ROI of $0\nu2\beta$. To show the vital importance of this analysis, the thesis demonstrates the improvement of the sensitivity to the ^{130}Te($0\nu2\beta$) half-life by 32%.

This thesis presents the Channel Software Status (CSS) framework which has been developed to check the performance of each photomultiplier tube (PMT). It is one component of a processing pipeline that is crucial to ensuring the SNO+ experiment takes quality data. The framework has been tested on the air-fill data and is ready for further tuning using the stable water data.

SNO+ has an extensive calibration program, including a proposed ^{90}Y β-emitting calibration source. This thesis outlines the benefits of using such a source to test the position and energy resolutions across the energy region spread up to 2.28 MeV. The thesis describes the design of the source and the manufacturing procedure. The performed tests demonstrated the promising potential for using ^{90}Y to study properties of scintillators.

Acknowledgements

Firstly, I would like to thank my supervisor, Jeanne Wilson, for her incredible support. She guided me with discussions and helped my better understanding of various aspects of SNO+.

I would like to express my gratitude to Simon Peeters for providing the Sussex radioactive laboratory to manufacture an ^{90}Y calibration source. Thank you to Josh Klein and the UPenn group for the hospitality and the assistance in taking the measurements with an ^{90}Y calibration source. Ian Coulter, Nuno Barros, Tanner Kaptanoglu, Eric Marzec and Andy Mastbaum, it was my pleasure to be a part of your group.

Many thanks must go to Phil Jones and Dr. Matt Mottram. They shared their experience and knowledge in SNO+ RAT and made sure that we, PhD students, enjoyed our time. A special thank you to my fabulous friend Stefanie Langrock with whom I shared the office and the coffee breaks. Thank you to Ashley Robert Back who was my companion to travel in the Canadian Rockies mountains. We were indeed hopeless wanderers. Thank you to Billy Liggins for taking good care of the CSS. I have to extend my thanks also to James Waterfield for being a good Sudburian neighbour, Rob Stainforth and John Walker for introducing the underground dining etiquette, and my afternoon helium leak checking team: Laura Segui and Jack Dunger.

I would like to extend my gratitude to all SNO+ collaborators and to everyone from the Queen Mary PPRC department. It was great working with you. I appreciate all of you a lot.

Finally, thank you to my parents and Phil for their love and understanding. Without you, I could not make it.

Contents

List of Figures

List of Tables

List of Abbreviations

$0\nu2\beta$	neutrinoless double beta decay
$2\nu2\beta$	two neutrino double beta decay
ADC	analog-to-digital converter
AMELLIE	attenuation module of ELLIE
AV	Acrylic Vessel
CC	charged current
CHS	channel hardware status
CL	confidence level
CMB	cosmic microwave background
CNO	carbon-nitrogen-oxygen
CSS	channel software status
CTC	capillary transport container
CWC	capillary washing container
DB	daughter board
ECA	electronic calibration
ELLIE	embedded LED Light Injection Entity
ES	elastic scattering
FEC	front end card
FV	fiducial volume
GM	Geiger-Müller tube
GT	global trigger
ID	inner diameter

IH	inverted hierarchy
LAB	linear alkylbenzene
LED	light-emitting diode
MC	Monte Carlo
MTC/A	analogue master trigger card
MTC/D	digital master trigger card
NC	neutral current
NH	normal hierarchy
OD	outer diameter
OWL	outward-looking PMT
PCA	PMT Calibration
p.d.f.	probability density function
PDG	particle data group
PGT	pulse global trigger
PMNS	Pontecorvo-Maki-Nakagawa-Sakata matrix
PMT	photomultiplier tube
PMTIC	PMT interface card
PPE	personal protective equipment
PPO	fluor 2,5 Diphenyloxazole
PSUP	PMT support structure
QHL	charge (Q) under high-gain (H) over long (L) integration time
QHS	charge (Q) under high-gain (H) over short (S) integration time
QLX	charge (Q) under low-gain (X) over long (L) integration time
RAT	reactor analysis tool
RPS	radiation protection supervisor
ROI	region of interest
SF	survival factor
SM	Standard Model

SMELLIE	scattering module of ELLIE
SNO	Sudbury Neutrino Observatory
SPE	single photoelectron
TAC	time to amplitude converter
TELLIE	timing module of ELLIE
UPW	ultra pure water

Chapter 1

Neutrinos

1.1 Neutrinos in the Standard Model

The neutrino is a fundamental particle in the Standard Model (SM). There are three types or flavours of neutrinos in the SM: an electron neutrino ν_e, a muon neutrino ν_μ and a tau neutrino ν_τ. They are neutral partners of the corresponding leptons and together with them they form the leptonic sector of the SM. A neutrino has a spin of 1/2 and interacts only via the weak interaction [1], [2]. As the cross-section for weak interaction processes is extremely small, neutrinos have incredible penetrating powers and become unique analysis tools.

On one hand, neutrinos from the core of the Sun and even from cores of distant stars can be detected, but on the other hand, as weakly interacting particles, neutrinos appear and participate in various nuclear processes, probing matter on very short scales as well. The ability to provide information about fundamental properties of matter from very distant objects along with the fact that a neutrino itself is one of the less studied particles in the SM, makes it an exciting and promising object of study.

In this chapter we briefly describe how basic properties of the neutrino particle have been established and also show that there are still a lot of open questions about them.

A neutrino was first predicted, or proposed, theoretically by W. Pauli in 1930 in a letter to participants of the meeting about open questions in radioactivity in

Tübingen [4]. Pauli proposed to introduce a new electromagnetically neutral spin-$\frac{1}{2}$ particle with a very low (if not zero) mass in order to save the energy conservation law in radioactive β-decays. The problem was that an observed energy spectrum of emitted electrons was continuously spread between zero and some maximum value, depending on the nucleus. These observations were incompatible with a two body decay model. Hence the only way to incorporate these observations with the energy conservation law was to postulate that β-decay is a three particle process. Soon after, in 1934, these ideas of Pauli were refined and a theory of β decay was developed by Fermi [5]. According to this theory, the neutrino had a tiny interaction cross section, as already predicted by Pauli. Therefore, it was assumed that neutrinos were almost impossible to detect. However, more then twenty years later, in 1956, the neutrino (electron anti-neutrino) was directly detected by Clyde Cowan and Frederick Reines [6]. They used an inverse β decay reaction, where an anti-neutrino was captured by a proton and produced a neutron and a positron

$$\bar{\nu}_e + p \to n + e^+ \tag{1.1.1}$$

The nuclear fission reactor at the Savannah River Plant in South Carolina was used as a source of anti-neutrinos. The detector consisted of two large tanks filled with water, which were sources of protons for the reaction (1.1.1). After neutron and positron production by the $\bar{\nu}$ and p interaction, the positron shortly met an electron and annihilated producing two photons, which were detectable. The neutron could then be captured by cadmium nuclei (from cadmium chloride, which was dissolved in the water). If the neutron produced in the inverse β decay reaction was captured by cadmium, then a gamma ray from the capture would have been detected within about 5 μs after the two photons from the electron-positron annihilation. The delay-coincidence signature was used as a signature of inverse β decay and helped to distinguish signal events from backgrounds. Cowan and Reines were able to collect data from about three neutrino events per hour in their detector over several months. The measured neutrino cross section for this reaction was $6.3 \times 10^{-44}\,\mathrm{cm}^2$, in good agreement with predicted values. The results were published in Science [6], and in 1995 Frederick Reines was awarded a Nobel Prize in Physics for his work on neutrino physics.

It is important to mention an earlier attempt to directly detect neutrinos from a nuclear reactor. In 1955 Ray Davis conducted an experiment near the Savannah River reactor trying to detect neutrinos using the reaction of neutrino capture [7]:

$$\nu_e + {}^{37}\mathrm{Cl} \rightarrow e^- + {}^{37}\mathrm{Ar} \tag{1.1.2}$$

There were several advantages of using this particular reaction. Firstly, an ordinary dry cleaning fluid was very rich in chlorine, therefore using it as a target of the detector significantly reduced costs of production for a large volume detector. Secondly, a product of the reaction, ^{37}Ar ($T_{1/2} = 35.04$ days) is chemically inert, hence providing a possibility to extract it from the detector and then count it. Davis invented a special technique for Argon extraction, which allowed him to accurately count the amount of ^{37}Ar nuclei [7,16]. During the experiment, when the reactor was operating, an increase in the amount of ^{37}Ar production wasn't observed. These results suggested that neutrinos produced in β decays inside the fission nuclear reactor were different from neutrinos produced in the electron capture reaction

$$p + e^- \rightarrow n + \nu_e \tag{1.1.3}$$

which was just an inverse reaction to (1.1.2), hence it had the same cross-section. In other words, Ray Davis's experiment of 1955 confirmed a proposed earlier suggestion that neutrinos (produced in (1.1.3)) were different from anti-neutrinos (produced during β-decays). Therefore, if an electron neutrino occurred in a final state of a reaction, it was always accompanied by a positron, and an electron anti-neutrino was always accompanied by an electron. This could be described by the introduction of a new conserved quantity, lepton number, equal to the number of leptons minus number of anti-leptons. The lepton number conservation law was introduced by Konopinski and Mahmoud in 1953 [8].

Shortly after the discovery of muons and pions in cosmic rays, it was observed that charged muons decayed into charged pions and a second neutral particle was produced in the process [9]. This particle was called the muon neutrino, ν_μ. However it was unclear whether it differed from an electron neutrino. This question was resolved by Lederman, Schwartz and Steinberger in 1962, when they performed an experiment at the Brookhaven National Laboratory [10]. They developed a method of obtaining a beam of muon neutrinos, using a very energetic beam of protons from an accelerator. These protons produced a beam of secondary π^+/π^- mesons after an interaction with a beryllium target. Then, during the 20 m flight, pions decayed into muons and muon neutrinos. All particles hit an iron protection wall and only neutrinos were able to penetrate through it. In such a way, after the iron wall, only the beam ν_μ and $\bar{\nu}_\mu$ are left, which then interacted with protons and neutrons in the detector. The results of the experiments showed that only muons were produced, hence the following reactions were not observed

$$\nu_\mu + n \nrightarrow e^- + p \tag{1.1.4}$$

$$\bar{\nu}_\mu + p \nrightarrow e^+ + n \tag{1.1.5}$$

This was a clear indication that $\nu_\mu \neq \nu_e$. The second generation of neutrinos was discovered, and Lederman, Schwartz and Steinberger received a Nobel Prize in Physics in 1988. The third generation of neutrinos, tau neutrinos, ν_τ, were discovered by the DONUT collaboration in 2000 [11].

1.2 Neutrino Physics Beyond the Standard Model

In this section we describe various properties of the neutrino, which cannot be explained by the Standard Model. As new properties were discovered in various experiments, it became clear that the correct description of a neutrino particle could be done only via an extension of the SM, hence it became a part of Beyond the Standard Model Physics.

1.2.1 Solar Neutrino Problem

By the 1960's, the Standard Solar Model [12] was developed into an accurate and quantitative theory, according to which most of the solar energy is produced in fusion nuclear reactions when light elements burn into heavier ones. According to the Standard Solar Model, the majority of solar energy is produced during so-called, pp-cycle reactions, see Figure 1.1, where Hydrogen burns into Helium through several intermediate states.

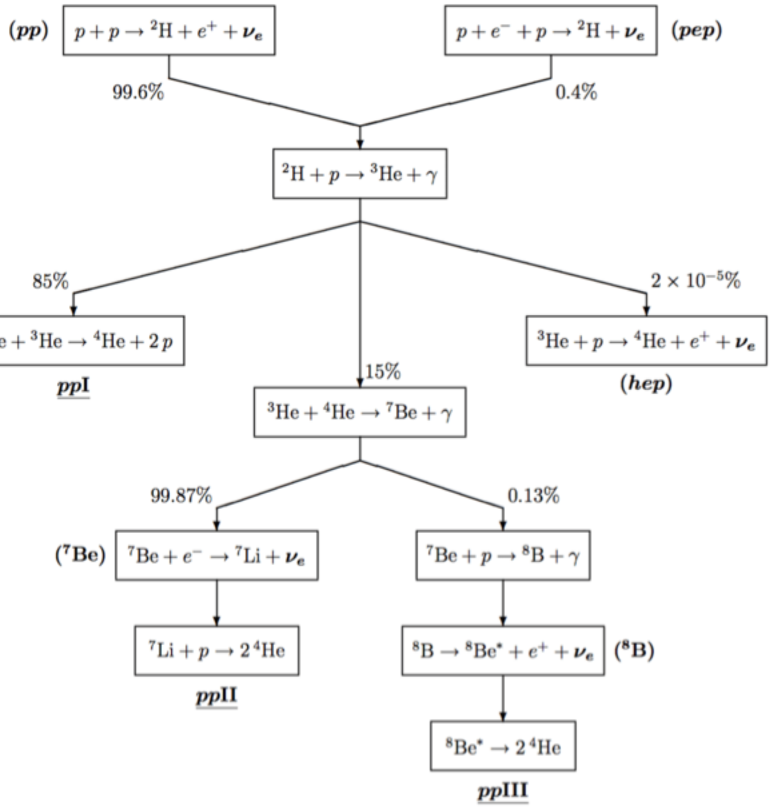

Figure 1.1: The pp-cycle of the Standard Solar Model. The plot was taken from [13].

The set of reactions in the pp-cycle can be represented as follows:

$$4p \to \cdots \to {}^4\mathrm{He} + 2e^+ + 2\nu_e + 2\gamma. \tag{1.2.6}$$

Apart from the pp-cycle, there is also the CNO-cycle represented in Figure 1.2.

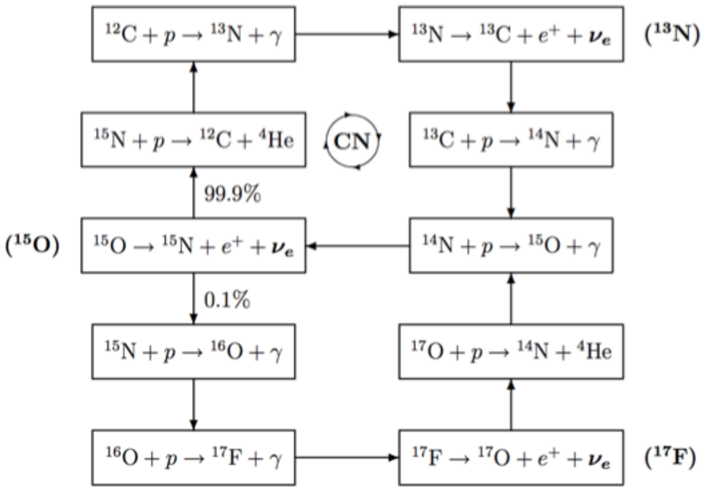

Figure 1.2: The CNO-cycle of the Standard Solar Model. The plot was taken from [13].

As a result of these reactions, in both pp and CNO cycles, only electron neutrinos are emitted. Since they are fusion reactions, only neutrinos are produced. The spectrum of the Standard Solar Model neutrinos is presented in Fugure 1.3.

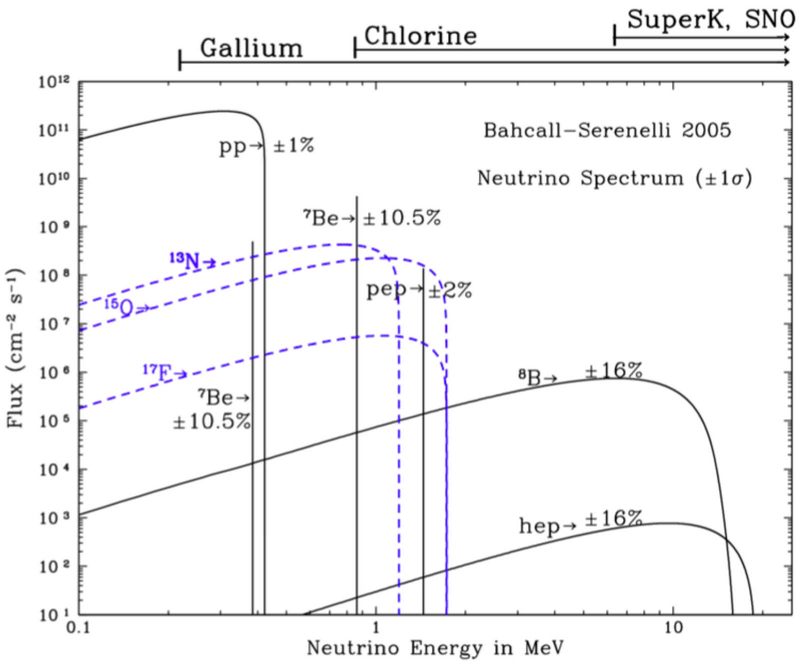

Figure 1.3: The spectrum of solar neutrinos according to the Standard Solar Model. The percentages show uncertainties. On top of the figure, the energy ranges of various experiments are present. As can be seen, the SNO experiment was sensible only to the high energy ^{8}B neutrinos. However, the new generation of the experiment, SNO+, will be able to probe solar neutrinos of lower energies, including CNO-neutrinos (blue lines in the figure) and pep-neutrinos. The plot was adapted from [14].

Knowing the total solar energy flux and using the Standard Solar Model, one can calculate a total neutrino flux from the Sun. This was done by John Bahcall and others in the 1960s [12, 14, 15] and after that Ray Davis proposed an experiment to detect solar neutrinos [16]. The idea was to use an upgraded version of the method Davis developed in 1955 for his experiment at Savannah River, which is described previously. The fact that the chosen method was sensitive only to electron neutrinos was not a problem, as only electron neutrinos were expected from the Sun.

The detector was situated in the Homestake mine in South Dakota and started to operate in 1968; it was run for almost 25 years [16]. The results of the experiment were consistent throughout all years. The measured value of the neutrino flux from the Sun was $2.56 \pm 0.16 \pm 0.16$ SNU[1], which is much smaller than 9.3 ± 1.3 SNU, the value calculated by Bahcall using the Standard Solar Model [16]. This apparent contradiction between theory and experiment was called the Solar Neutrino Problem.

There were solid evidences of correctness of the Standard Solar Model (SSM), such as the fact that SSM satisfies the well known structural equations of stellar evolution [15]. Also, obtained helioseismology observations confirmed that the interior temperatures of the Sun coincide with the predictions of the SSM [17]. All these factors have pushed an alternative solution of the Solar Neutrino Problem and the hypothesis of neutrino flavour oscillations was put forward.

1.2.2 Neutrino Oscillations

The idea of neutrino oscillations is somewhat analogous to the theory of quark mixing, where it is assumed that there is a difference between mass eigenstates of d, s and b and their flavour eigenstates d', s' and b'. Each one of the flavour eigenstates is a linear combination of mass eigenstates and due to the fact that each mass eigenstate is evolving in time with its own frequency, a particular flavour eigenstate can evolve to another one with time. A similar idea for oscillations in the neutrino sector of the SM was proposed by Pontecorvo in 1957 [18]. Initially, it was proposed for neutrino/anti-neutrino oscillations in the analogy with neutral kaon

---

[1] One Solar Neutrino Unit (SNU) equal to one interaction per 10^{36} target atoms per second

mixing, and later it was realised that oscillations were between different flavours, as in the quark sector.

Below, we describe a standard quantum mechanical framework and derive an expression for the probability of the flavour change.

The neutrino is a quantum mechanical particle, hence its wave functions should satisfy the Schroedinger equation. We use natural units and labels $\alpha = \{e, \mu, \tau\}$ to describe different neutrino flavours.

$$i\frac{\partial}{\partial t}\Big|\Psi(t)\Big\rangle_{\alpha} = \hat{H}\Big|\Psi(t)\Big\rangle_{\alpha} . \tag{1.2.7}$$

In terms of flavour wave functions $\mid \nu_e(t)\rangle$, $\mid \nu_\mu(t)\rangle$ and $\mid \nu_\tau(t)\rangle$, $\Big|\Psi\Big\rangle_{\alpha}$ can be written as a three-dimensional vector:

$$\Big|\Psi(t)\Big\rangle_{\alpha} = \begin{pmatrix} \mid \nu_e(t)\rangle \\ \mid \nu_\mu(t)\rangle \\ \mid \nu_\tau(t)\rangle \end{pmatrix} = \{\mid \nu_\alpha(t)\rangle\} \tag{1.2.8}$$

and the Hamiltonian $\hat{H}$ is a non-diagonal 3×3 matrix of operators. Since the $\hat{H}$ is not diagonal in the $\{\mid \nu_\alpha(t)\rangle\}$-basis this means that there is a mixing, or an interaction, between these wave-functions. However, after changing the basis

$$\mid \nu_\alpha(t)\rangle = U_{\alpha i}\mid \nu_i(t)\rangle \tag{1.2.9}$$

to the basis of mass eigenstates $\{\mid \nu_i(t)\rangle\}$, $i = 1, 2, 3$, and after the substitution of (1.2.9) into (1.2.7) we get

$$i\frac{\partial}{\partial t}\Big|\Psi(t)\Big\rangle_{i} = \hat{\tilde{H}}\Big|\Psi(t)\Big\rangle_{i} \tag{1.2.10}$$

where

$$\Big|\Psi(t)\Big\rangle_{i} = \begin{pmatrix} \mid \nu_1(t)\rangle \\ \mid \nu_2(t)\rangle \\ \mid \nu_3(t)\rangle \end{pmatrix} = \{\mid \nu_i(t)\rangle\} \tag{1.2.11}$$

and the Hamiltonian $\hat{\tilde{H}} = U^{+}\hat{H}U$ is diagonal:

$$\hat{\tilde{H}} = \begin{pmatrix} \hat{H}_1 & & \\ & \hat{H}_2 & \\ & & \hat{H}_3 \end{pmatrix} . \tag{1.2.12}$$

Additionally, since $|\ \nu_i(t)\rangle$ diagonalize the Hamiltonian, they are also energy eigenstates, and from (1.2.10) it immediately follows that

$$|\ \nu_i(t)\rangle = e^{-iE_it}|\ \nu_i(0)\rangle\ . \tag{1.2.13}$$

This induces time evolution of flavour states:

$$|\ \nu_\alpha(t)\rangle = \sum_i U_{\alpha i}|\ \nu_i(t)\rangle = \sum_i e^{-iE_it}U_{\alpha i}|\ \nu_i(0)\rangle\ . \tag{1.2.14}$$

The probability to find a neutrino in a flavour state β after a time t, if initially it has been in a state α, is

$$P_{\alpha\to\beta} = |\langle\nu_\beta(t)|\nu_\alpha(0)\rangle|^2\ . \tag{1.2.15}$$

One can expand this expression and obtain a general answer for the probability to oscillate in terms of elements of the matrix U and energies (masses) of neutrino mass eigenstates.

In order to demonstrate a qualitative dependence of the oscillation probability $P_{\alpha\to\beta}$ on various parameters, oscillations between two flavours only are considered. In this case, the matrix U is a unitary 2×2 matrix, hence it can be parametrized by a single angle θ:

$$U_{2\times 2} = \begin{pmatrix} \cos\theta & \sin\theta \\ -\sin\theta & \cos\theta \end{pmatrix} . \tag{1.2.16}$$

Then using $|\ \nu_e(0)\rangle = \sum_i U_{ei}|\ \nu_i(0)\rangle$, $i = 1,2$ and $|\ \nu_\mu(t)\rangle = \sum_i U_{\mu i}|\ \nu_i(t)\rangle = \sum_i e^{-iE_it}U_{\mu i}|\ \nu_i(0)\rangle$ the oscillation probability between electron and muon neutrinos is written as:

$$P_{e\to\mu} = |\langle\nu_\mu(t)|\nu_e(0)\rangle|^2 = \left|\sum_{i=1}^{2} e^{iE_it}U^*_{\mu i}U_{ei}\right|^2 \ . \tag{1.2.17}$$

Here $U^*_{\mu i}$ are complex conjugated elements of U. We assume that mass eigenstates are orthogonal to each other and properly normalised i.e. $\langle\nu_i(0)|\nu_j(0)\rangle = \delta_{ij}$. Using explicit values of elements of the matrix U (1.2.16), the expression (1.2.17) can be further simplified:

$$\begin{aligned} P_{e\to\mu} &= \left|-e^{iE_1t}\sin\theta\cos\theta + e^{iE_2t}\sin\theta\cos\theta\right|^2 \\ &= \sin^2\theta\cos^2\theta\left(e^{iE_2t}-e^{iE_1t}\right)\left(e^{-iE_2t}-e^{-iE_1t}\right) \\ &= \sin^2\theta\cos^2\theta\left[2-\left(e^{i(E_2-E_1)t}+e^{-i(E_2-E_1)t}\right)\right] \\ &= 2\sin^2\theta\cos^2\theta\left[1-\cos\left(\mathit{\Delta}E_{21}t\right)\right] \\ &= \sin^2 2\theta\sin^2\left(\tfrac{\mathit{\Delta}E_{21}}{2}t\right) \ . \end{aligned} \tag{1.2.18}$$

Neutrinos are relativistic particles, hence

$$E_i = \sqrt{p^2+m_i^2} \approx p + \frac{m_i^2}{2p} \ . \tag{1.2.19}$$

In this approximation we neglect variation of the momenta between the eigenstates. Furthermore, as neutrinos are ultra-relativistic particles, the substitutions $E = p$ and $t = L/c = L$ $(c = 1)$ in (1.2.18) can be made. The final result for the probability of oscillation between two neutrino flavours is:

$$P_{e\to\mu} = \sin^2 2\theta\sin^2\left(1.27\frac{\mathit{\Delta}m^2_{21}L}{E}\frac{[\mathrm{eV}^2][\mathrm{km}]}{[\mathrm{GeV}]}\right) \ . \tag{1.2.20}$$

It can be seen that the probability to oscillate depends on the distance a neutrino has travelled, L, with energy E, squared-mass difference $\mathit{\Delta}m^2_{21} = m_2^2 - m_1^2$ and a value of the mixing angle θ.

The parameters θ and $\mathit{\Delta}m^2_{21}$ have fixed values, while the parameters L and E can have different values, depending on the experiment. Hence, by performing measurements for various values (L, E) one can deduce values of $\mathit{\Delta}m^2_{21}$ and θ.

When all three flavours are involved in the oscillations, the matrix U becomes a

3×3 unitary matrix, which can be parametrized by three angles $(\theta_{12}, \theta_{13}, \theta_{23})$ and a CP-violating phase δ. This matrix is called the Pontecorvo-Maki-Nakagawa-Sakata (or PMNS) matrix [19]. Moreover, as there are now three masses, one can construct three squared-mass differences, $\mathit{\Delta} m^2_{21}$, $\mathit{\Delta} m^2_{31}$ and $\mathit{\Delta} m^2_{32}$. However, due to a relation

$$\mathit{\Delta} m^2_{21} - \mathit{\Delta} m^2_{31} + \mathit{\Delta} m^2_{32} = 0 \tag{1.2.21}$$

which holds due to definitions ($\mathit{\Delta} m^2_{ij} = m^2_i - m^2_j$), only two of the squared-mass differences will be independent.

1.3 Resolution of the Solar Neutrino Problem. The SNO Experiment.

From previous discussions, the neutrino flavour oscillations hypothesis was proposed as a possible solution of the Solar Neutrino Problem.

There are three types of reactions, which can be used to detect solar neutrinos. The first type,

$$\nu_e + n \to p + e^- \ , \tag{1.3.22}$$

is called the Charged Current (CC) interaction, as it is mediated by the charged W boson. It is sensitive only to electron neutrinos. The second type,

$$\nu_\alpha + n \to \nu_\alpha + n \ , \tag{1.3.23}$$

only occurs through neutral Z boson exchange, hence it is called the Neutral Current (NC) interaction. It is equally sensitive to all neutrino flavours. And the third type of reaction,

$$\nu_\alpha + e^- \to \nu_\alpha + e^- \ , \tag{1.3.24}$$

is called an Elastic Scattering (ES). It also corresponds to Z boson exchange, and therefore is sensitive to all flavours. However, for electron neutrinos ES can also be mediated by W bosons, hence the ES cross-section has a larger value for electron neutrinos. It is approximately 6 times larger for ν_e's than for ν_μ's or ν_τ's.

The ratio

$$R = \frac{N_{obs}}{N_{pred}} \tag{1.3.25}$$

between the amounts of observed and predicted (based on a solar model) neutrinos is introduced. If the solar model is correct, then for the NC reactions $R_{NC} = 1$, regardless the presence of the neutrino flavour oscillations. For CC and ES types of reactions, $R_{CC(ES)} = 1$ only if there are no flavour oscillations. In other words, $R_{CC(ES)} < 1$, along with $R_{NC} = 1$ observations, will experimentally prove the existence of neutrino flavour oscillations.

The first experiment that was built in order to explore all three types of solar neutrino reactions was SNO (Sudbury Neutrino Observatory), situated in a nickel mine in Sudbury, Canada [20].

A huge tank filled with heavy water was used as the detector. The presence of the Deuterium (^{2}H) in heavy water allowed the following realisation of all three types of reactions:

$$\begin{aligned} CC: &\quad \nu_e + {}^2H \to p + p + e^- \ , \\ NC: &\quad \nu_\alpha + {}^2H \to n + p + \nu_\alpha \ , \\ ES: &\quad \nu_\alpha + e^- \to \nu_\alpha + e^- \ . \end{aligned} \tag{1.3.26}$$

SNO results [22] confirmed Bahcall et al.'s Solar Model theory by measuring ^{8}B neutrinos fluxes, and showing that $\phi^{CC}(\nu_e) < \phi^{ES}(\nu_x)$ and $R_{CC} = 0.347 \pm 0.029$. Also they have shown an appearance of ν_μ or ν_τ in the solar neutrino flux by measuring

$$\frac{R_{CC}}{R_{ES}} \neq 1 \quad \text{and} \quad \frac{R_{CC}}{R_{NC}} \neq 1 \ . \tag{1.3.27}$$

Such ratios are much less sensitive to detector systematic uncertainties and depend only on the neutrino parameters.

For this work on solar neutrinos physics Arthur B. McDonald, leader of the SNO collaboration, together with Takaaki Kajita from the Super-Kamiokande Collaboration [21], received the Nobel Prize in Physics in 2015.

1.4 Limits on Values of Neutrinos Masses

Discovery of neutrino flavour oscillations experimentally proved that neutrinos are massive particles, specifically that at least one of the mass eigenstates has a non-zero mass eigenvalue. However, determining the actual values of neutrino masses is not trivial, since an oscillation probability depends on squared mass differences $\varDelta m^2_{ij}$, hence it is not possible to determine absolute values of the masses from neutrino oscillation experiments. Only partial information about the relative mass scale is available from such experiments.

In general, an oscillation probability $P_{\alpha\to\beta}$ will depend on a combination of all possible mass-square differences $\varDelta m^2_{ij}$. However, for certain physical phenomena and specific ranges of parameters L and E it is possible to single out a specific squared mass difference and neglect the rest.

Solar neutrino oscillations are mostly sensitive to $|\varDelta m^2_{21}| = |\varDelta m^2_{solar}|$. Moreover, in the case of solar neutrino oscillations, the presence of solar matter affects the probability of oscillations. The dense matter of the Sun contains e^- (but not μ^- or τ^-) producing additional interaction diagrams for ν_e over $\nu_{\mu,\tau}$. At high energies ($E_{\nu_e} > 5$ MeV) these interactions cause a resonance in conversion between mass states reducing the survival probability of ν_e and thus providing information on the sign of $\varDelta m_{12}$. In addition to that, some reactor experiments like KamLAND have also contributed to these measurements by studying reactor $\bar{\nu}_e$ disappearance [24]. Hence, combining solar neutrinos oscillation experimental data with reactor experimental data it was shown that $\varDelta m^2_{21} = (7.53 \pm 0.18) \times 10^{-5}$ eV^2 [25].

Initially the values of $\varDelta m^2_{32}$ were determined from atmospheric neutrino data. After that the most precise measurements of atmospheric parameters have been measured by long baseline accelerator experiments, like T2K and MINOS [26, 27]. However, in this case only an absolute value of this parameter could be determined. In other words, it is unknown whether the third neutrino mass eigenstate m_3 is heavier than m_2 (and m_1) or lighter. The former option corresponds to the, so-called, normal neutrino mass hierarchy (NH), and the later to the inverted neutrino mass hierarchy (IH). The current best measurement of $|\varDelta m^2_{32}|$ from atmospheric neutrino oscillations gives $|\varDelta m^2_{32}| = (2.44 \pm 0.06) \times 10^{-3}$ eV^2 for normal mass hierarchy, and

$|\mathit{\Delta} m^2_{32}| = (2.49 \pm 0.06) \times 10^{-3}$ eV^2 for inverted mass hierarchy [25].

Elements of the PMNS matrix, expressed through the angles $(\theta_{12}, \theta_{13}, \theta_{23})$, can also be determined in neutrino oscillation experiments. According to the PDG [25], collective analysis and global fits of data from various experiments give us the following values: $\sin^2(\theta_{12}) = 0.304 \pm 0.014$, $\sin^2(\theta_{23}) = 0.514 \pm^{0.055}_{0.056}$ (NH) and $\sin^2(\theta_{23}) = 0.511 \pm 0.055$ (IH), $\sin^2(\theta_{13}) = (2.19 \pm 0.12) \times 10^{-2}$.

Taking these data into account it is possible to draw a diagrammatic representation of the mixing for normal and inverted hierarchies, see Figure 1.4.

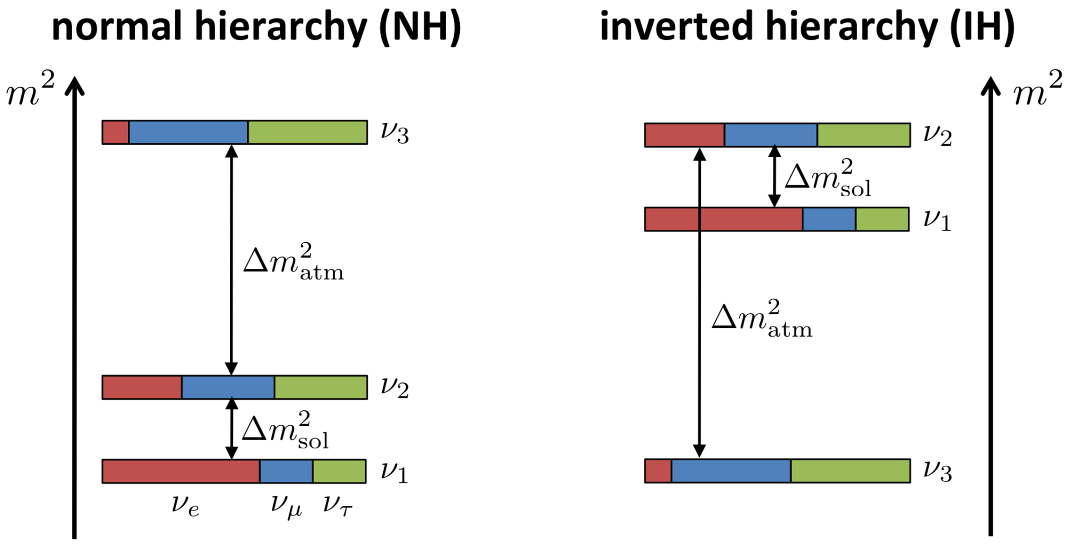

Figure 1.4: A diagrammatic representation of neutrino mixing for normal and inverted neutrino mass hierarchies. Note, that it is drawn not in scale, because $\mathit{\Delta} m^2_{atm} \approx 100 \times \mathit{\Delta} m^2_{solar}$. The plot was taken from [23].

It is not yet possible to determine the neutrino mass hierarchy from current neutrino oscillation experiments. The second generation of long-baseline experiments is aiming to measure the mass hierarchy [28]. Due to the longer baselines, they will be sensitive to the matter-induced effects and hence will be able to identify the sign of $\mathit{\Delta} m^2_{32}$. This will consequently help to determine the type of the neutrino mass hierarchy. However, even then the question about the absolute values of the masses will remain. In order to establish limits on the values of the masses of neutrinos several alternative approaches have been developed.

One possibility to determine the mass of the electron neutrino ν_e is a precise measurement of the endpoint of the energy spectrum of tritium beta-decays. A massive neutrino will reduce the phase space of the decay and will lead to a small change of the shape of the electron spectrum. Tritium is a usual choice due to its simple structure, which reduces uncertainties caused by nuclear effects and Coulomb interactions. Additionally, tritium has a low end point energy (Q-value) of 18.59 keV, simplifying the search for sub-eV deviations in the spectrum. However it is still a challenging task requiring very precise measurements and extremely high resolution. The current best limit on the electron neutrino mass obtained by this method is [25]:

$$m_{\nu_e} < 2.05 \text{ eV at } 95~\% \text{ CL} \tag{1.4.28}$$

where the electron neutrino mass is assumed to be equal to the following combination

$$m_{\nu_e}^2 = \sum_{i=1}^{3} |U_{ei}|^2 \, m_i^2 \; . \tag{1.4.29}$$

Limits on muon and tau neutrino masses could be established from an accurate investigation of the kinematics of various decays involving neutrinos in the final states. For the muon neutrino, the two body decay of the π meson is used:

$$\pi \to \mu\nu \; . \tag{1.4.30}$$

From a simple kinematic calculation for this decay in the pion rest frame it is easy to derive that the muon neutrino mass should be equal to

$$m_{\nu_\mu}^2 = m_\pi^2 + m_\mu^2 - 2m_\pi E_\mu = m_\pi^2 + m_\mu^2 - 2m_\pi \sqrt{\vec{p}_\mu^{\,2} + m_\mu^2} \; . \tag{1.4.31}$$

In principle, knowing precise values of the pion and muon masses and performing an accurate measurement of the muon momenta will give us the value of muon neutrino mass. However, due to uncertainties in the value of pion mass and systematic errors due to the high energy of the muons, the best limit, which was determined by this method, is not very restrictive [25]

$$m_{\nu_\mu} < 0.19 \text{ MeV at } 90 \text{ \% CL} \,. \tag{1.4.32}$$

For the tau neutrino it is possible to perform a similar analysis, however the result is even more vague due to the lack of statistics and an absence of convenient decays [25]

$$m_{\nu_\tau} < 18.2 \text{ MeV at } 95 \text{ \% CL} \,. \tag{1.4.33}$$

This result was obtained from kinematics of 2939 $\tau^- \to 2\pi^-\pi^+\nu_\tau$ and 52 $\tau^- \to 2\pi^-2\pi^+(\pi^0)\nu_\tau$ decays [30].

Finally, modern cosmological observations can be used to set a limit on the sum of neutrino masses. According to the Standard Cosmological Model, along with an ordinary Cosmic Microwave Background there is also a relic neutrino background, or cosmic neutrino background (CNB), with a smaller temperature. The CNB was produced by frequent weak interactions at large temperatures in the early Universe and then was decoupled at a smaller temperature. The value of this temperature was estimated with high level of uncertainty as it depends on the chosen cosmological model. Knowing the spectrum of neutrinos after decoupling and the decoupling temperature it is possible to calculate the energy density of CNB neutrinos and consequently their masses. Thus, advanced measurements of the structure of the CMB allows determination of a limit on the sum of all three neutrino masses $m_{\nu,tot}$ [31]. Unfortunately, this limit is very dependent on the selected cosmological model and very sensitive to the values of the various cosmological parameters. The Planck collaboration was able to to set the following limit [29]:

$$m_{\nu,tot} < 0.23 \text{ MeV} \,. \tag{1.4.34}$$

1.5 Nature of Neutrino Masses

Shortly after the discovery of the neutrino, its helicity (projection of a particle's spin to its momentum) was measured [32]. In this experiment a ^{152}Eu nucleus underwent electron capture at rest emitting a photon and an electron neutrino in two opposite directions with opposite spins. Having opposite momenta and spins, the photon and the neutrino had to have the same helicity. The helicity of photons was measured by studying their absorption in the fully magnetised iron. Photons can be absorbed by electrons of the target only if their spins are opposite. Therefore, by changing the direction of the magnetic field the helicities of photons were measured and were equal to -1 all the time. Hence, the helicity of the neutrino in the SM is -1. Moreover, since neutrinos are treated as massless in the SM, the negative or left-handed helicity is equivalent to a left-handed chiral state. Thus, all neutrinos are produced and propagated in the left-handed chiral state ν_L.

From the experimental evidence of neutrino oscillations it follows that the neutrino is a massive fermion. However, an attempt to add a Dirac mass term to neutrinos in the SM with a mass generated through the Higgs mechanism immediately encounters difficulty as we only observe left-handed neutrinos, but the mass terms for the Dirac fermions should include both left and right handed chiral states

$$\mathcal{L}_{Dirac} \propto c_\nu v \left(\bar{\nu}_R \nu_L + \bar{\nu}_L \nu_R\right) \ . \tag{1.5.35}$$

Here c_ν is a Yukawa coupling constant, v is the Higgs field vacuum expectation value and $\bar{\nu} = \nu^+ \gamma^0$ is the adjoint component of the Dirac fermion.

There is an alternative way to introduce the mass term for fermions, based on the assumption that left and right handed components of the fermion field are related to each other in such a way that the charged conjugated field becomes equal to the original field

$$\psi = \psi^C \ . \tag{1.5.36}$$

This possibility for fermions was proposed by Ettore Majorana in 1937 [33] and since then they are called Majorana particles. Their central property is that the Majorana particle is indistinguishable from its antiparticle, hence a Majorana particle should be neutral.

Neutrinos are the only neutral fermions in the SM, hence they potentially could be Majorana particles. Assuming the Majorana nature of neutrinos, it is possible to write the following expression for the neutrino mass term

$$\mathcal{L}_{Majorana} \propto \left(\bar{\nu}_L^C \nu_L + \bar{\nu}_L \nu_L^C\right) \ . \tag{1.5.37}$$

1.6 See-Saw mechanism

Unfortunately, the term (1.5.37) will be non-renormalizable in the Standard Model. One of the possibilities to resolve this issue is to assume that the SM is a low-energy limit of a more fundamental high-energy unified theory. In other words, the SM is an effective theory, and therefore could have non-renormalizable terms.

Another possibility is to assume that along with left-handed neutrinos there are sterile right-handed neutrinos, which do not couple to the weak interactions. The existence of sterile right-handed neutrinos will allow the writing of Dirac mass term (1.5.35) for neutrinos with the standard Yukawa coupling. However, in order to be in agreement with the current experimental bounds on neutrinos masses, the coupling of neutrinos to the Higgs field should be much smaller than the lepton-Higgs coupling. This issue together with the fact that there is no experimental evidence of the existence of sterile neutrinos makes this model look unnatural.

An alternative model of neutrino mass generation mechanism is to allow the possibility of combining Dirac and Majorana mass terms together with the assumption about sterile right-handed neutrinos. In this case, the general neutrino mass term in the Lagrangian can be written as a sum of three terms:

$$\mathcal{L}_{\nu-mass} = \mathcal{L}_{Dirac} + \mathcal{L}^{(L)}_{Majorana} + \mathcal{L}^{(R)}_{Majorana}, \tag{1.6.38}$$

where $\mathcal{L}^{(R)}_{Majorana}$ is the Majorana mass term for right-handed neutrinos, which, in contrast to left-handed neutrinos, is renormalizable in the SM. This general mass term for neutrinos can be rewritten in the following matrix form

$$\mathcal{L}_{\nu-mass} = \frac{1}{2}\left[\left(\bar{\nu}_L^C, \bar{\nu}_R\right)\begin{pmatrix} m_L & m_D \\ m_D & m_R \end{pmatrix}\begin{pmatrix} \nu_L \\ \nu_R^C \end{pmatrix}\right] + \text{h.c.} \tag{1.6.39}$$

The mass matrix in (1.6.39) can be diagonalized by a unitary transformation of neutrino fields and we will get the following mass eigenvalues

$$m_{1,2} = \frac{1}{2}\left[(m_L + m_R) \pm \sqrt{(m_L - m_R) + 4m_D^2}\right] . \qquad (1.6.40)$$

In order to avoid the non-renormalizability, we additionally assume that $m_L = 0$. We also assume that right-handed sterile neutrinos are very massive, $m_D \ll m_r = M$. Substituting this into (1.6.40), the mass eigenvalues become approximately equal to

$$m_1 = m_{heavy} = M, \qquad \text{and} \qquad m_2 = m_{light} = \frac{m_D^2}{M}. \qquad (1.6.41)$$

As can be seen from these expressions: the larger the value of m_{heavy} is – the smaller the value of m_{light}. Therefore, this mechanism of neutrino mass generation was named the see-saw mechanism. For example, for the values of $m_d \sim 1$ MeV and $M \sim 10^{15}$ eV we will get an meV-range value of the effective neutrino mass m_{light} for the field which is almost entirely made of ν_L.

1.6.1 (Neutrinoless) Double Beta Decay

If neutrinos are Majorana particles, then a neutrinoless double beta decay process is possible. As discussed above, some nuclei are unstable and can undergo a beta decay, emitting an electron and an electron anti-neutrino

$$(A, Z) \rightarrow (A, Z+1) + e^- + \bar{\nu}_e \; . \qquad (1.6.42)$$

This process is energetically allowed only when

$$m\,(A, Z) > m\,(A, Z+1) + m_e \; . \qquad (1.6.43)$$

When this condition is not satisfied, the beta decay is forbidden. However as M. Goeppert-Mayer proposed in 1935 [34] if (1.6.43) is not satisfied and at the same time the following inequality is satisfied

$$m\,(A,Z) > m\,(A,Z+2) + 2m_e \tag{1.6.44}$$

then a nucleus might undergo two simultaneous beta decays of two neutrons inside the nucleus, which will result in an increase of a charge Z of the nucleus by 2 and emission of four daughter particles, two electrons and two electron anti-neutrinos

$$(A,Z) \to (A,Z+2) + e^- + \bar{\nu}_e + e^- + \bar{\nu}_e \tag{1.6.45}$$

Such a process is called double beta decay, $2\nu 2\beta$. Its Feynman diagram is shown in Figure 1.5.

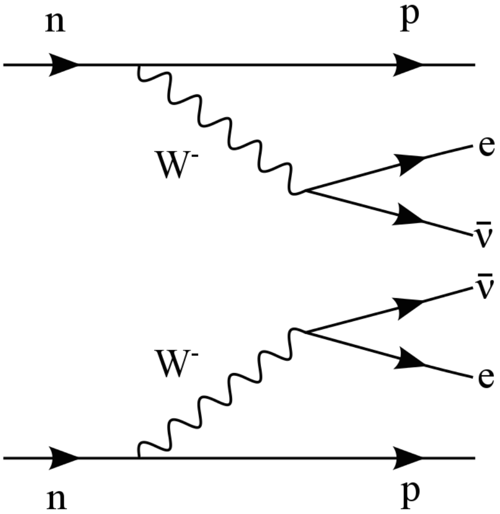

Figure 1.5: Feynman diagram of double β decay with two electrons and two electron anti-neutrinos in a final state. The plot was taken from [35].

There are more than thirty nuclei that can undergo double beta decay, but it has only been observed in 11 of these elements. Double beta decay is a second order weak process, hence the corresponding half-life should be very large (experimentally measured half-lives of the double beta decays of order 10^{21} years), making its measurement a hard task.

The Q value of the $2\nu 2\beta$ process, i.e. the total amount of released energy, is given by:

$$Q_{2\nu\beta\beta} = m\,(A,Z) - (m\,(A,Z+2) + 2m_e)\ . \tag{1.6.46}$$

As there are four particles emitted, an observable energy, which is carried by two electrons, could have any value between 0 and $Q_{2\nu 2\beta}$.

Combining the possible Majorana nature of neutrinos with the phenomenon of double beta decay has lead to the proposal of neutrinoless double beta decay [36,37], $0\nu 2\beta$, a double beta decay process with only electrons in a final state (without neutrino emission). If a neutrino is a Majorana particle, then an anti-neutrino emitted during first beta decay is just a right-handed state of a Majorana fermion field. Moreover, because neutrinos are massive particles, helicity is not a conserved quantity and therefore can change through a spin-flip. Hence, with a probability proportional to m_ν^2, the emitted anti-neutrino could became a neutrino and after that it could be absorbed by the W boson of the second beta decay, leaving only two electrons in a final state, see Figure 1.6

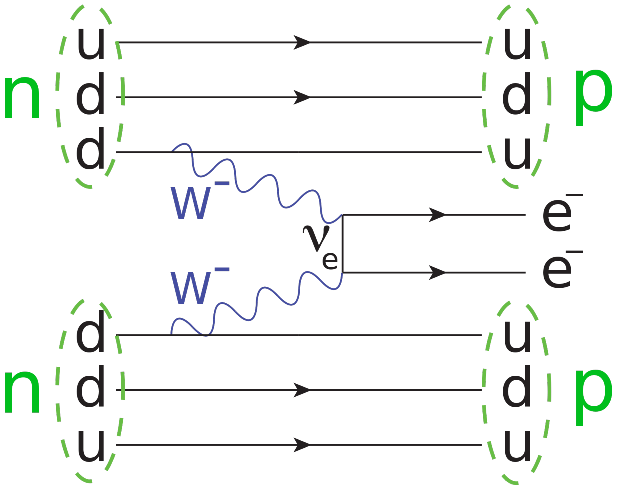

Figure 1.6: Feynman diagram of neutrinoless double β decay with only two electrons in the final state. The plot was taken from [38].

If neutrinos are indeed Majorana particles, then all nuclei suitable for double beta decay could also undergo a neutrinoless double beta decay, however as the spin-flip is necessary for the latter process it is heavily suppressed relative to the former one. The rate (inverse of the half-life $T_{1/2}$) of neutrinoless double beta decay is given by the following expression [13]:

$$\left(T_{1/2}^{0\nu\beta\beta}\right)^{-1} = G^{0\nu}(Q)\left|M^{0\nu}\right|^2 \frac{|m_{\beta\beta}|^2}{m_e^2} . \tag{1.6.47}$$

$G^{0\nu}(Q)$ is the phase space factor, which is dependent on the Q-value of the decay, or more generally, on the nucleus in consideration; $|M^{0\nu}|^2$ is the nuclear matrix element and it is calculated with a very high level of uncertainty and with a strong dependence of the chosen model, this is discussed in Section 1.7. This is the source of the biggest uncertainty in the calculation of the $T_{1/2}^{0\nu 2\beta}$.

The effective Majorana neutrino mass of the virtual electron neutrino $m_{\beta\beta}$ is equal to

$$m_{\beta\beta} = \sum_{i=1}^{3} U_{ei}^2 m_i. \tag{1.6.48}$$

Here U_{ei} plays the role of the probability of i-th mass eigenstate to interact with the W boson. This effective neutrino mass can be expressed in terms of the lightest neutrino mass state in each of the hierarchies m_{min} ($m_1 = m_{min}$ for normal hierarchy and $m_3 = m_{min}$ for inverted hierarchy) and solar and atmospheric squared mass differences:

$$\begin{aligned} m_{\beta\beta}^{IH} &\approx \left(U_{e1}^2 + U_{e2}^2\right)\sqrt{m_3^2 + \mathit{\Delta} m_{atm}^2} + U_{e3}^2 m_3 & (1.6.49) \\ m_{\beta\beta}^{NH} &\approx U_{e1}^2 m_1 + U_{e2}^2\sqrt{m_1^2 + \mathit{\Delta} m_{sol}^2} + U_{e3}^2\sqrt{m_1^2 + \mathit{\Delta} m_{atm}^2} & (1.6.50) \end{aligned}$$

here, $\mathit{\Delta} m_{sol}^2 << \mathit{\Delta} m_{atm}^2$ has been used several times for simplification. These expressions can be plotted, see Figure 1.7 for the $m_{\beta\beta}$ versus m_{min} plot.

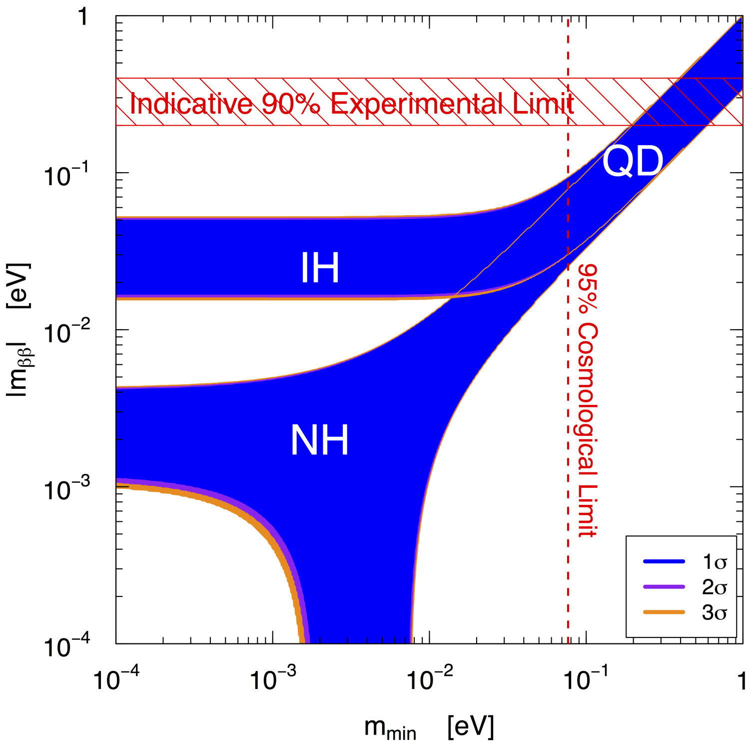

Figure 1.7: An effective Majorana neutrino mass as a function of lightest neutrino mass state m_{min} for both hierarchies (IS=IH, NS=NH) together with the limits on it from current $0\nu\beta\beta$ experiments and the cosmological limit on m_{min}. The plot was taken from [39].

From (1.6.47) it follows that an observation of neutrinoless double beta decay will not just prove the Majorana nature of neutrinos, but will also allow us to make a measurement of neutrino masses.

The mechanism of neutrinoless double beta decay with the annihilation of a light neutrino is not the only possible mechanism of how this decay can occur. There are other operators that can be added to the SM that will contribute to the transition of a nucleus $N(A, Z)$ to a nucleus $N(A, Z + 2)$ with two electrons [40]. For example, such a process is possible in a left-right symmetric extension of the SM, in some supersymmetric extensions of the SM, in theories with leptoquarks and in models with extra dimensions. However, it can be shown that regardless of the type of operators involved in $0\nu2\beta$ process, it contributes to the Majorana mass of neutrino [41, 42].

1.6.2 Experimental sensitivity of $0\nu2\beta$-decay experiments

The kinematics of the neutrinoless double beta decay is different from the kinematics of the ordinary double beta decay, since in the former case the sum of the energies of the two final state electrons is equal to the total energy release Q of the decay. The schematic illustration of the $0\nu2\beta$ signal on top of the $2\nu2\beta$ spectrum is shown in Figure 1.8.

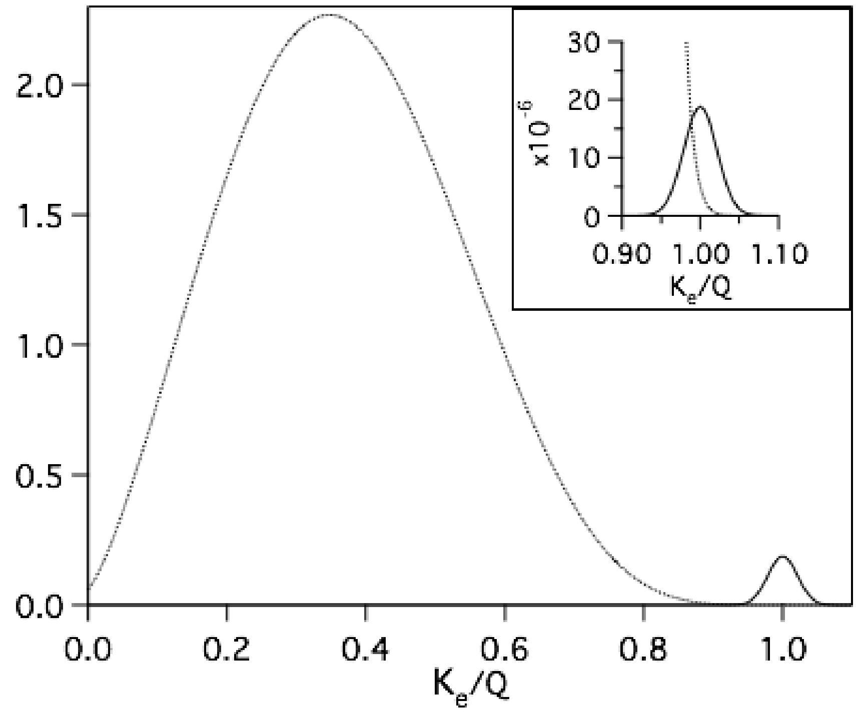

Figure 1.8: Schematic illustration of the spectra of two electron kinetic energies K_e, divided by the endpoint energy Q, normalized to 1 for $2\nu2\beta$ decay and to 10^{-2} (10^{-6} in the inset) for the $0\nu2\beta$ decay. All spectra are convolved with an energy resolution of 5%. The plot was taken from [43].

The rate of the $0\nu2\beta$ process is much smaller than the rate of the corresponding $2\nu2\beta$ process (due to an additional suppression factor proportional to $m_{\beta\beta}^2/m_e^2$) and in the idealised situation the spectrum of the $0\nu2\beta$ process is a delta-function at the endpoint energy Q. Therefore, it is important to minimise background contribution to this region and design the experiment with the best possible energy resolution. Other parameters that need to be optimised are the overall isotope mass M of a candidate element, exposure time t and a detector efficiency ε. In this section, we derive how the sensitivity to the effective neutrino mass $m_{\beta\beta}$ scales with the isotope mass M for two cases: when the background scales with the mass of the isotope and when the background is independent of the isotope.

Neutrinoless double beta decay is a radioactive decay, hence, it obeys the radioactive decay law:

$$N(t) = N_0 \, e^{\frac{-t \ln 2}{T_{1/2}}} , \tag{1.6.51}$$

where N_0 is the initial number of isotopes, $N(t)$ is the number of isotopes at observation time t and $T_{1/2}$ is the half-life of the process. Since $0\nu 2\beta$-decay is a second order weak process, its half-life will be much greater than any experimental observation time t. Therefore, (1.6.51) can be approximated by the following expression

$$N(t) = N_0 \left(1 - \frac{t \ln 2}{T_{1/2}}\right) . \tag{1.6.52}$$

Hence, the sensitivity to the half-life of neutrinoless double beta decay is

$$T_{1/2} = \frac{N_0 \varepsilon t \ln 2}{N_{0\nu\beta\beta}} = \frac{t \ln 2 M a \varepsilon}{N_{0\nu\beta\beta} W} , \tag{1.6.53}$$

where $N_{0\nu\beta\beta} = N_0 - N(t)$ is the number of neutrinoless double beta decay events, ε is the detector efficiency, and we have rewritten N_0 in terms of the active mass M of the isotope of study and its molecular weight W and isotopic abundance a.

The $0\nu 2\beta$ is a very rare process, therefore usually the major contribution to the signal energy region will be from the background events. Hence, by performing an optimisation procedure in the background limiting case we assume $N_{0\nu\beta\beta} \sim \sqrt{B}$, where B is the number of background events, and substituting this in (1.6.53) we get

$$T_{1/2} = \frac{t \ln 2 M a \varepsilon}{\sqrt{B} W} . \tag{1.6.54}$$

Backgrounds in the experiment can be divided into two groups with respect to the isotope of study: external and internal. External backgrounds are not introduced by the isotopes of study and hence they don't scale with it, and are proportional to the observational time and the energy resolution of the experiment:

$$B_{ext} \sim t \mathit{\Delta} E . \tag{1.6.55}$$

Substituting (1.6.55) into (1.6.54) we get

$$T_{1/2} \propto M\sqrt{\frac{t}{\Delta E}} \tag{1.6.56}$$

and by combining this expression with (1.6.47) we show that the sensitivity to the effective neutrino mass scales with the active mass M as

$$m_{\beta\beta} \propto M^{-\frac{1}{2}} \tag{1.6.57}$$

Internal backgrounds that are introduced by the isotope of study are proportional to its mass:

$$B_{int} \sim Mt\Delta E\ . \tag{1.6.58}$$

Therefore, in this case, the sensitivity to the effective neutrino mass scales as

$$m_{\beta\beta} \propto M^{-\frac{1}{4}}\ . \tag{1.6.59}$$

It is worth mentioning that such a notation does not correspond to the more generic one in SNO+ when the external backgrounds are the events that occur outside the detector volume and from the detector components, and the internal backgrounds are the ones occurring inside the detector.

1.7 Nuclear matrix element calculations

As we have mentioned above, the nuclear matrix element (NME) $M^{0\nu}$ is the greatest source of uncertainty in the neutinoless double beta decay calculations. Moreover, since the half-life of the process depends on the NME quadratically the uncertainty of a factor of three corresponds to almost an order of magnitude uncertainty in the observable quantities. Also, it is important to know precise values of the NMEs as it could help to choose an optimal candidate for the source of neutrinoless double beta decays in future experiments. In this section we briefly outline two major approaches to the calculation of the NME and discuss their limitations.

In order to calculate the NME one needs to specify the wave functions of the initial and final states and the proper transition operator, that will depend on the mechanism of the decay. It is very difficult to describe the wave functions of the initial and final states of the nucleus because it is a strongly interacting many-body quantum system and the corresponding Schrodinger equation cannot be solved exactly. Hence different sets of simplifying assumptions are used in order to find an approximate description of the initial and the final states.

The nuclear shell model (NSM) is based on the idea that only a subset of nucleons in the nucleus participate in this type of reaction, therefore the configuration space of the problem is restricted to the relatively small number of nucleons, whereas the rest are not included in the calculations [44]. Active nucleons are allowed to occupy a limited set of single-particle states around the Fermi surface and their interactions are described exactly by an effective Hamiltonian tuned in such a way that it will correctly reproduce the behaviour of the whole nucleus. In other words, the fact that the method involves an exact solution, usually via diagonalization of the Hamiltonian, allows only a small amount of nucleus to be treated accurately and the remaining nucleons have to be treated in an approximate way.

In another approach, called quasiparticle random phase approximation (QRPA), interacting pairs of nucleons are represented as boson quasiparticles. Therefore excited intermediate nuclear states are modelled as excitations of this system of quasiparticles [44]. In this model, larger number of nucleons can be included in the calculations, however, interactions between them are treated approximately.

Both these models are being upgraded and improved regularly and new variations with new ideas and better approximations often appear [44]. However, there are still a lot of uncertainties in the calculations of the NMEs for the neutrinoless double decay process and a lot of work needs to be done. For example, the value of $|M^{0\nu}|$ for ^{130}Te, which is planned to be used in the SNO+ experiment, varies between 2.12 in the interacting shell model [45] and 5.13 in energy density function approach to the NME calculation [46].

Due to the presence of uncertainties in the nuclear matrix element evaluation, it is important to study as many isotopes as possible in order to reduce the effect of this uncertainty in the evaluation of $m_{\beta\beta}$. The modern $0\nu2\beta$ experiments and their current results are presented in Section 1.7.1.

1.7.1 Review of current experiments

As of 2017, the only evidence of the measurement of neutrinoless double beta decay was made by part of Heidelberg-Moscow collaboration in 2006 [47]. However, this result was disputed since it was announced and recently the phase space was ruled out by the GERDA experiment [48]. In this experiment neutrinoless double beta decay in crystals of ^{76}Ge was studied. During the first phase of the experiment the lower limit on the $0\nu2\beta$ half-life $T_{1/2}^{0\nu2\beta} > 2.1 \cdot 10^{25}$ years (at 90% CL) was established [48] and the corresponding limit of the effective Majorana neutrino mass was $m_{\beta\beta} < 0.2 - 0.4$ eV (an uncertainty here is due to the dependence on the model for the nuclear matrix element evaluation). Currently, Phase II of the GERDA experiment with reduced background and increased mass of germanium crystals is running and preliminary results of the combined Phase I+II analysis have been presented recently [49], with $T_{1/2}^{0\nu2\beta} > 8 \cdot 10^{25}$ years (at 90% CL) and $m_{\beta\beta} < 0.12 - 0.26$ eV. Also, the very low background level of $1.0^{+0.6}_{-0.4} \cdot 10^{-3}$ cts/(keV kg yr) has been achieved. This means that the experiment is running in a background-free regime, hence its sensitivity grows linearly with exposure time t (see (1.6.53)) and it is expected to surpass 10^{26} yr within 2018 [50].

Neutrinoless double beta decay in ^{76}Ge is also studied by the MAJORANA collaboration and its Majorana Demonstrator experiment, which is currently running with first preliminary results of $T_{1/2}^{0\nu2\beta} > 1.9 \cdot 10^{25}$ years (at 90% CL) and $m_{\beta\beta} < 0.24 -$ 0.52 eV, which have recently been published [51]. The goal of this experiment is to demonstrate that the future 1-tonne experiment can achieve a very low background level, and as it was able to achieve a background level of $4.0^{+3.1}_{-2.5} \cdot 10^{-3}$ cts/(FWHM t yr), this strongly supports the development of a future large-scale ^{76}Ge experiment such as LEGEND [52].

The NEMO3 experiment placed several thin foils made of enriched isotopes into a tracking detector. Such construction allowed the study of various isotopes at the same time and the setting of limits for all of them. For example, for ^{150}Nd the obtained limit is $T_{1/2}^{0\nu2\beta} > 2.0 \cdot 10^{22}$ years (at 90% CL) [53], and for ^{100}Mo –

$T_{1/2}^{0\nu2\beta} > 1.1{\cdot}10^{24}$ years (at 90% CL) [54]. Other results of the NEMO3 experiment are presented in Table 1.1. The NEMO3 experiment operated until 2011 and since then it has been upgrading to the new generation of this experiment, called SuperNEMO, aiming to test half-life times of order 10^{26} years and neutrino masses of order 0.05 eV [55] with ^{82}Se.

The isotope ^{130}Te has been used by the CUORE collaboration in the CUORICINO and CUORE-0 experiments. The former one operated between 2003 and 2008 and set a limit of $T_{1/2}^{0\nu2\beta} > 2.8 \cdot 10^{24}$ years (at 90% CL) [56]; the latter one took data from spring 2013 till spring 2015 and the most recent results from CUORE-0 (combined with the results of CUORICINO) give a limit on the half-life of $T_{1/2}^{0\nu2\beta} > 4.0 \cdot 10^{24}$ years (at 90% CL) [57]. This limit can be interpreted in terms of the limit on the effective Majorana neutrino mass, $m_{\beta\beta} < 0.27 - 0.76$ eV. CUORE-0 is the smaller version of the larger CUORE experiment, which has started data taking in 2017 and the first results have recently been presented [58]: $T_{1/2}^{0\nu2\beta} > 1.3 \cdot 10^{25}$ years (at 90% CL) and $m_{\beta\beta} < 0.11 - 0.52$ eV.

The KamLAND-Zen experiment has used the ^{136}Xe isotope dissolved in a liquid scintillator as a source for $0\nu2\beta$ searches. This experiment has reached the end of its second phase of data collection, which operated between November 2013 and October 2015 and the combined results of the two phases are $T_{1/2}^{0\nu2\beta} > 1.07 \cdot 10^{26}$ years (at 90% CL) [59]. This corresponds to a limit on the effective mass of $m_{\beta\beta} < 0.061 - 0.165$ eV. The upgraded version of the experiment with 800 kg mass of the isotope is currently under development. It aims to probe neutrino masses of order 40 meV [60].

The same isotope, ^{136}Xe, is chosen by the EXO-200 collaboration, where 150 kg of liquid xenon is used as a source and a detection medium simultaneously. The results of phase I of the EXO-200 experiment are $T_{1/2}^{0\nu2\beta} > 1.1 \cdot 10^{25}$ years (at 90% CL) and $m_{\beta\beta} < 0.19 - 0.45$ eV [61]. Phase II of the experiment began in the end of January 2016 and the results of the first year of data taking are $T_{1/2}^{0\nu2\beta} > 1.8 \cdot 10^{25}$ years (at 90% CL) and $m_{\beta\beta} < 0.147 - 0.398$ eV [62]. Moreover, the nEXO project with a 5 tonne liquid xenon detector has been proposed [63].

Current $0\nu2\beta$ half-life limits for various isotopes are presented in Table 1.1.

Table 1.1: Collection of current lower limits on $0\nu2\beta$ decay half-lives for various isotopes together with corresponding limits on the effective Majorana neutrino mass

Isotope	$T_{1/2}^{0\nu2\beta}$ lower limit, years	$m_{\beta\beta}$, eV	Experiment
^{76}Ge	$8.0 \cdot 10^{25}$	0.12 - 0.26	GERDA
^{130}Te	$4.0 \cdot 10^{24}$	0.27 - 0.76	CUORE-0
^{130}Te	$1.3 \cdot 10^{25}$	0.11 - 0.52	CUORE
^{136}Xe	$1.07 \cdot 10^{26}$	0.061 - 0.165	KamLAND-Zen
^{136}Xe	$1.07 \cdot 10^{26}$	0.061 - 0.165	EXO-200
^{150}Nd	$2.0 \cdot 10^{22}$	1.6 - 5.3	NEMO3 [53]
^{48}Ca	$2.0 \cdot 10^{22}$	6 - 26	NEMO3 [64]
^{100}Mo	$1.1 \cdot 10^{24}$	0.3 - 0.9	NEMO3 [54]
^{82}Se	$3.6 \cdot 10^{23}$	–	NEMO3 [65]
^{96}Zr	$9.2 \cdot 10^{21}$	–	NEMO3 [65]

Predicted sensitivities to the $0\nu2\beta$ decay half-life and to the effective Majorana neutrino mass of current and future $0\nu2\beta$ experiments are presented in Table 1.2.

Table 1.2: Predicted median 3σ discovery sensitivities to the $0\nu2\beta$ decay half-life and to the effective Majorana neutrino mass of current and future experiments assuming 5 years of live time.

Experiment	Predicted sensitivity, $T_{1/2}^{0\nu2\beta}$, years	Predicted sensitivity, $m_{\beta\beta}$, meV
LEGEND 200 (^{76}Ge), [66, 67]	$8.4 \cdot 10^{26}$	40 - 73
LEGEND 1k (^{76}Ge), [66, 67]	$4.5 \cdot 10^{27}$	17 - 31
CUORE (^{130}Te), [68, 69]	$5.4 \cdot 10^{25}$	66 - 164
SNO+ Phase I (^{130}Te), [70, 71]	$1.1 \cdot 10^{26}$	46 - 115
SNO+ Phase II (^{130}Te), [72]	$4.8 \cdot 10^{26}$	22 - 54
KamLAND-Zen 800 (^{136}Xe), [73]	$1.6 \cdot 10^{26}$	47 - 108
nEXO (^{136}Xe), [74]	$4.1 \cdot 10^{27}$	9 - 22
SuperNEMO (^{82}Se), [75, 76]	$6.1 \cdot 10^{25}$	82-138

We have presented major discoveries from predictions to precise measurements in the expanding field of neutrino physics. At the moment one of the cutting edges is investigating $0\nu2\beta$ decays and therefore the fundamental nature of neutrinos. One of the experiments performing this study is SNO+ [77], described further in Chapter 2.

Chapter 2

The SNO+ experiment

In order to study neutrinoless double beta decay, SNO+ prepares the detector, whilst investigating other physics phenomena, making the experiment multipurpose. The data taking process will be divided into three phases: water phase, pure scintillator phase, and tellurium loaded phase.

After completing water filling in February 2017 the physics data taking started on May 4^{th}, 2017 and continued until the start of scintillator filling [80]. Scintillator fill was planned to start in July 2018 but unfortunately was shifted to early autumn [81]. During this process, the scintillator components were mixed and gradually poured into the AV replacing the water inside it. Tellurium will be loaded into the scintillator in spring 2019 [80] and ^{130}Te phase will last for about 5 years.

Physics goals set to each phase are discussed below.

2.1 Neutrinoless double β decay in SNO+

The main purpose of the SNO+ experiment is the search for neutrinoless double beta decay of ^{130}Te. This particular isotope of tellurium decays through $2\nu2\beta$ with the half-life of $T_{1/2}^{2\nu2\beta} = (7.0 \pm 0.9(\mathrm{stat}) \pm 1.1(\mathrm{syst})) \times 10^{20}$ years [78] and $Q_{2\beta} = 2527.518 \pm 0.013$ keV [79]. There are several advantages of using this isotope. First is its high natural abundance of 34.08%, allowing the loading of a large amount of the isotope without enrichment. Second, it has one of the longest $2\nu2\beta$ half-lives of all the $0\nu2\beta$ candidates, hence the rate of irreducible background events due to $2\nu2\beta$ decays will be lower. Tellurium will be dissolved in the liquid scintillator with the initial loading of 0.3% by mass, which is about 800 kg of the isotope[1]. At the moment we are investigating further loadings of up to 15%. Prior to performing any measurements, the detector components will be purified. Deployed water, scintillator, and tellurium will undergo several stages of purification [93]. Nevertheless, some impurities are expected to stay inside the detector. These isotopes will decay emitting α-, β- and γ- particles which will be registered by the detector. Such isotopes are discussed in detail in Chapter 4.

2.2 Other physics goals of SNO+

Prior to loading tellurium into the detector, SNO+ will first be filled with about 900 tonnes of ultra-pure water for a few months, allowing the comissioning and calibration of the detector, while searching for invisible nucleon decay. This is the process in which a nucleon decays to some undetectable final state, for example, $n \rightarrow 3\nu$. A candidate for studying this phenomenon is ^{16}O. If a neutron decays the isotope will become ^{15}O* which will deexcite emitting 6.18 MeV gamma in 44% of the time. In case a proton decays, the resultant isotope will be ^{15}N* which will deexcite emitting 6.32 MeV gamma in 41% of the time. In both cases, the resultant gammas are the target signals we are aiming to detect. [25, 82].

During the next phase, the pure scintillator phase, the water in the detector will be replaced by the liquid scintillator. It will be loaded straight onto the water to prevent exposure to air and potential radon contamination. The circulation process will mix the components making the scintillator homogeneous. The pure scintillation phase is planned to be short and mainly used for performing callibrations and testing the Monte Carlo models. This phase will allow the study of low-energy neutrino physics phenomena, such as low energy solar neutrinos, geoneutrinos, supernova neutrinos, and reactor antineutrinos.

In the context of solar neutrinos, the SNO+ experiment is aiming to make the first measurements of CNO neutrinos ($E_\nu \approx$ 0.7-1.7 MeV), which can help in under-

---

[1] Developments in the loading procedure have led to a new baseline loading of 0.5% by mass.

standing unresolved questions about solar metallicity [83]. Measurements of pep-neutrinos (E_ν = 1.44 MeV) will help to investigate the transition region between matter and vacuum oscillations, and probe for new physics [84].

SNO+ is in the vicinity of three nuclear reactors with baselines of 240 km and 350 km (other reactors within the North America continent with longer baselines will also contribute), hence study of reactor antineutrinos is an important part of the SNO+ experiment. These studies will allow the measurements of Δm^2_{12} with high precision [77]. The study of geoneutrinos, produced in Earth's crust and mantle, provides information on heat production mechanisms of the Earth [77].

It is also desirable that during both pure scintillator and tellurium loading phases, which will last about 6 years combined, SNO+ will be ready to detect neutrinos from galactic Supernova explosions.

2.3 The detector overview

The SNO+ detector is located in the underground laboratory SNOLAB with 2092 ± 6 m of rock overburden inside the Creighton mine near Sudbury, ON, Canada. Due its depth of 5890 ± 94 m.w.e[2], SNO+ has natural shielding that significantly reduces cosmic muon flux down to an average of 63 ± 0.2 muons a day through an 8.3 m radius circular fiducial area [77, 85].

The detector infrastructure is inherited from the previously operated SNO experiment [86]. Since the physics capabilities of the two experiments are different, serious upgrades have been made in the electronics system as well as the new detector components. The hold-down rope net was added, hold-up ropes were replaced, a new cover gas system was introduced and new calibration components. A schematic picture of the detector can be seen in Figure 2.1.

---

[2] The m.w.e. stands for the meter water equivalent. It is a measure to quantify the cosmic ray attenuation at a certain depth. Since in each case, the characteristics of the material of the overburden such as its density and shape are different a simple specification of the depth is not informative. Using the m.w.e. allows the consistent way of comparing cosmic ray levels at different underground locations. In the case of SNOLAB, the 94 m.w.e. is equivalent to the 94 m below water.

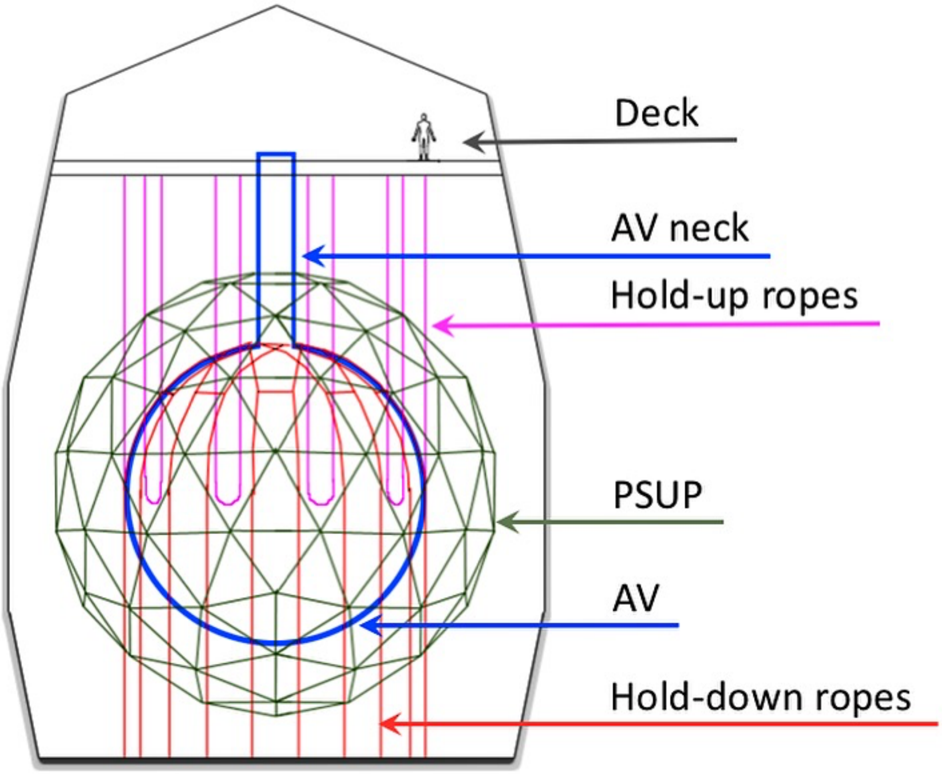

Figure 2.1: A schematic picture of SNO+ detector. This is a modified version of the figure from [77].

At every stage of running the detector, the material of study is contained within the Acrylic Vessel (AV) which is an acrylic sphere (diameter = 12 m) with an acrylic cylindrical neck (diameter = 1.5 m, height = 6.8 m) at the top. The AV neck extends to the deck level that allows the deployment of calibration sources, and allows personnel to access the AV.

One of the detector upgrades in SNO+ is a cover gas system designed to prevent radon from penetrating inside the detector. The system surrounds the deck and performs using 3 flexible 240 L bags filled with pure Nitrogen gas [87].

The AV is positioned inside a barrel-shaped cavity with diameter of 22 m and height of 34 m. In order to prevent contamination from the surrounding rock, the surface is covered with 8 mm of urylon that also provides a water tight seal. The cavity is filled with 7000 tonnes of ultra pure water (UPW) which realises another layer of shielding from radioactivity from the outside. The AV is held securely by a system of ropes, manufactured from high radiopurity Tensylon [88]. Ten 3/4” hold-up suspension ropes, reaching from the cavity ceiling through the deck, are attached to specially formed belly plate grooves at the equator of the AV. Twenty 1 1/4” hold-down ropes have been added, as in the final phase of the experiment the AV will be filled with liquid scintillator with density of 0.865 g cm^{-3} [89], which makes it buoyant in water. The ropes are arranged to form a net around the top part of the AV and anchored to the cavity floor with the purpose of preventing the AV from floating upwards.

Signals from the detector are obtained using 9300 8” Hamamatsu R1408 PMTs [77], some of which have been repaired in the transition to SNO+. PMTs are held by the geodesic spherical support structure (PSUP) made of stainless steel struts. Its diameter is 17.8 m. The PSUP is attached to the deck and walls by cables. Besides measuring signals from within the AV, outwards looking PMTs, OWLs, detect external signals, such as cosmogenic muons.

2.4 Scintillator

Liquid scintillator will be used in SNO+ to register physics events occurring in the detector. After absorbing energy, its molecules in response emit light which is detected by the PMTs and the electronics system. Luminescence or light emission arises only if molecules in the medium contain either one or two un-hybridized 2p valence electrons[3], also called π-electrons [91]. First, these molecules are excited into excited singlet states. Although direct excitement from the ground states into excited triplet states is forbidden by spin it can happen due to inter-system crossing from singlet to their equivalent triplet states. In case the molecules are already ionised they might undergo ion-electron recombination which leads to another possibility of indirect production of excited π-electron singlet and triplet states [91].

There are 3 types of luminescence: fluorescence, phosphorescence, and delayed fluorescence. Each process has a certain energy transition between molecule levels and scintillation emission time profile.

Fluorescence is a type of luminescence when π-electrons from the first excited

---

[3] These are 2p electrons that have not mixed with 2s electrons.

singlet state de-excite down to ground state. The lifetime τ of these states are in the order of 1 ns. The intensity of the fluorescence exponentially decays in time :

$$I = I_0\ exp(-t/\tau), \tag{2.4.1}$$

where I_0 and I are the initial fluorescence intensity and the fluorescence intensity at a time t correspondingly. Fluorescence is the main source of emitted light by the scintillator.

Phosphorescence is a type of luminescence when π-electrons from the excited triplet states decay down to the ground state. Similar to fluorescence, the phosphorescence intensity exponentially decays in time but the lifetime, in this case, is in the order of 10^{-4} s. Also, emitted light has longer wavelengths than in fluorescence.

Delayed fluorescence is a type of luminescence when de-excitation of π-electrons from excited triplet states happens in two stages. First, they de-excited to the excited singlet states through the inter-system crossing process and then down to the ground states as in case of the fluorescence. This causes delayed emission of light with wavelengths as in fluorescence, however, the intensity spectrum is not exponential. The lifetime of such a decay is in the order of 10^{-4} s.

In SNO+ ionising radiation is mainly caused by muons propagating through the scintillator and by radioactive decays which emit electrons, alpha- and gamma- particles. These are decaying isotopes of backgrounds and isotopes of study (^{130}Te $0\nu2\beta$). All physics events in SNO+ are discussed in detail in Chapter 4. Such particles can be of a broad energy range between 0.1–10 MeV. They deposit their energies in the scintillator whilst passing through it and hence define characteristics of luminescence and the scintillation emission time profile.

2.4.1 The SNO+ scintillator cocktail

The SNO+ scintillator cocktail which will be used during the Te-loaded scintillator phase consists of several components:

- **LAB**. The primary component of the scintillator cocktail is an organic compound LAB, which stands for linear alkyl-benzene [77]. It's chemical formula is $C_6H_5C_{12}H_{25}$ [90]. In response to deposited energy from events within the detector, LAB emits scintillation photons with wavelengths peaked at 300 nm, which coincides with the region of the highest absorption. As a result, produced light is re-absorbed. In order to avoid this problem, a wavelength shifter is added to LAB.

- **PPO** is a fluor 2,5 Diphenyloxazole. It receives excitations from LAB molecules and emits photons with wavelengths between 350-450 nm, i.e. in higher region, preventing re-absorption. PPO is added to LAB at a concentration of 2g/l of LAB; together this combination is referred to LABPPO. It is a primary scintillator used in SNO+. During the pure scintillator phase we perform calibrations to test the detector hardware and Monte-Carlo models of processes inside the scintillator, which will be adjusted accordingly. Moreover, we will be able to measure backgrounds and compare with expected levels. We will collect data to study low-energy solar neutrinos, reactor neutrinos and geo-neutrinos.

- **Secondary wavelength shifter** absorbs photons previously emitted by PPO and re-emits them at longer wavelengths, and thus reaches the region of highest quantum efficiency of the SNO+ PMTs. Moreover, it further reduces re-absorption. At the time of writing of this theses, two wavelength shifters have been under consideration: perylene and bisMSB. Perylene shifts light emission to 440-500 nm region, bisMSB to 380-450 nm. [77]. The analysis presented in Chapter 5 is performed for the scintillator cocktail with bisMSB.

- **Surfactant** In order to load tellurium into the detector, telluric acid $Te(OH)_6$ will be disolved in water and mixed with a surfactant before adding it to the scintillator cocktail [77]. The originally planned surfactant PRS has been found to have too high levels of cosmogenic ^{24}Na, therefore a diol option is now investigated.

All components will be purified and mixed inside the specially designed facility called “the scintillator plant”. It was built in SNOLAB next to the SNO+ Cavity. The preparation of the scintillator plant is described in Section 2.5.

2.4.2 Scintillator properties

In this section we discuss scintillator properties that affect the sensitivity of SNO+ to physics events.

Light yield

Scintillator light yield is the number of photons emitted per MeV of deposited energy. The amount of emitted scintillation light is quantified by the number of registered PMT hits. Thus, the light yield has the empirical unit of Hits MeV^{-1}.

Light yield is one of the most important parameters as it defines the sensitivity of SNO+ to physics events. If it is too low physics events might not cause enough PMT hits to trigger the detector. As a result, we will lose data. If the light yield, on the contrary, is too high it will excessively fire PMTs and constantly trigger the detector. We might lose data due to oversaturation of signals.

The light yield can be approximated with a linear function in the lower energy region. At higher energies, the linearity breaks due to the quenching effect, which will be discussed in Section 2.4.3.

The light yield of the scintillator cocktail, LABPPO + BisMSB + 0.3% ^{130}Te, used in the studies presented in this thesis is 200 Nhits/MeV around 2.5 MeV [77].

Scintillation time profile

Understanding the scintillation emission profile is important as it allows us to distinguish and reconstruct different particles passing through the scintillator.

Light, relativistic particles such as photons and electrons mainly undergo elastic collisions with molecular electrons of the scintillator and hence produce excited π-electron singlet states. The emitted light is via fluorescence. Heavy, non-relativistic particles such as α-particles mainly ionise molecules of the scintillator producing π-electron triplet states. In this case, light is emitted via the phosphorescence process. Consequently, these two types of particles have different timing in the scintillation profiles.

In order to study the scintillation timing profiles for β- and α-particles, SNO+ performed the tests in the laboratory at the University of Pennsylvania [92]. The measurements were performed for two scintillator cocktails: LABPPO+bisMSB and LAB+bisMSB+0.3% ^{130}Te. The obtained results are presented in Figure 2.2. It can be observed that the timing profiles of α-particles have larger tails. This is due to delayed fluorescence.

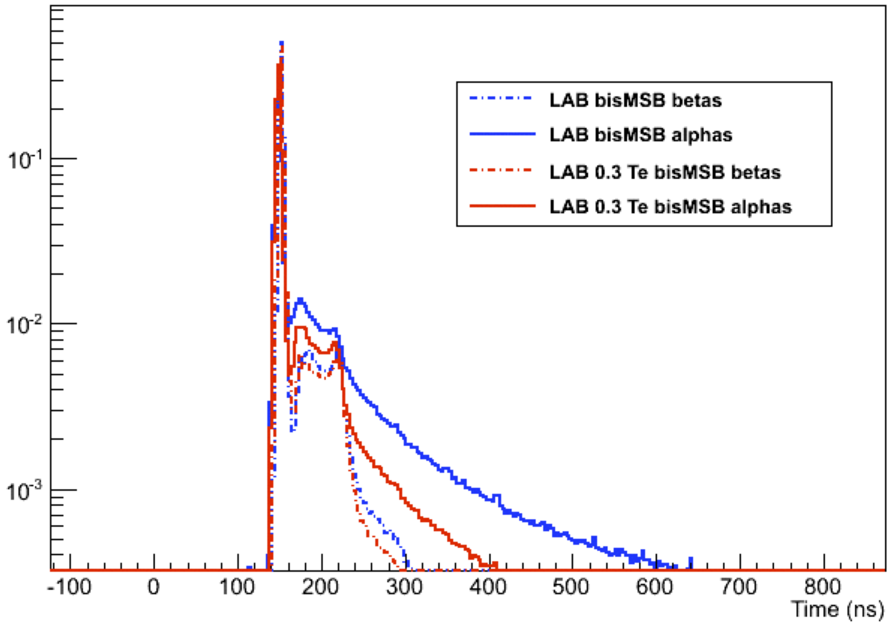

Figure 2.2: The scintillation time profiles for α- and β- particles passing through 2 scintillator cocktails: LABPPO+bisMSB and LAB+bisMSB+0.3% ^{130}Te. The plot was taken from [92].

2.4.3 Quenching

Highly energetic particles such as cosmogenic muons and α-particles when passing through the scintillator not only ionise its molecules but can also damage them temporarily or permanently. This process is called quenching. Molecules damaged permanently do not emit light and hence reduce the light yield of the scintillator. Molecules damaged temporarily recover via ion-recombination into triplet states which slows down light emission. Due to the quenching, the amount of light produced by the scintillator after interacting with highly energetic particles is reduced. Consequently, the reconstructed energy of such particles is lower.

For the scintillator cocktail, LABPPO + BisMSB + 0.3% ^{130}Te, the quenching factor estimated for α-particles is approximately 10 for energies between 5 MeV and

9 MeV [77]. This affects such α-decaying backgrounds as ^{210}Po, ^{212}Po and ^{214}Po.

2.5 Scintillator plant

Preparing scintillator cocktails requires purifying and mixing the composite elements. For this purpose SNO+ established an underground facility, the scintillator plant, that has replaced the old SNO D_2O facility. It is located in SNOLAB next to the SNO+ Cavity.

The scintillator plant stretches over two levels separated by a grated steel floor and a 2 m pit. It is contained inside an area of 15.3 m × 4.6 m; the ceiling height of the first level is 3 m and changes between 2 – 3 m on the second level, as it coincides with the cavity ceiling. The plant consists of 13 vessels, 17 kettles and 9 columns connected with 2 km of pipes [93]. The volume of these components vary between 0.5 – 4 m^3. The pit extension stores larger columns. The pictures of some parts of the plant can be observed in Figure 2.3.

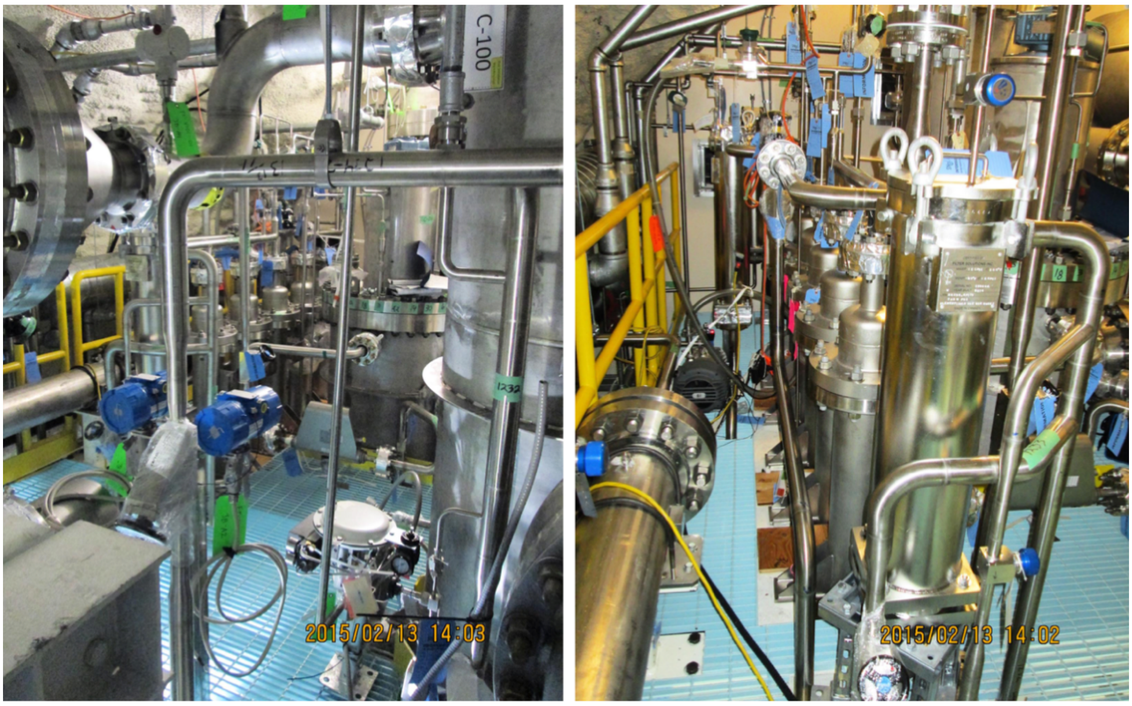

Figure 2.3: Pictures of some parts of the scintillator plant on the second level. The pictures were taken during leak checking before insulation was applied. The pictures are provided by Aleksandra Bialek.

Prior to exploitation, the plant was examined for leaks and any leaks found were fixed. This task was essential since allowing radon air to penetrate inside components of the plant and therefore mix with the scintillator in the future would significantly increase background levels in the AV. In order to achieve the target levels in LABPPO for ^{238}U (1.6×10^{-17} g/g) and ^{232}Th (6.8×10^{-18} g/g) the leak rate of each element should be less than 1×10^{-9} mBar L s^{-1} [94]. After manufacturing, the fabricator tested pneumatically and/or hydrostatically all vessels for fissures. Further checks for micro-leaks have been made in SNOLAB. The project started in 2013 and was successfully completed in 2015. The author spent four months leak checking between September - December 2013 and November - December 2014 in a team with other collaborators.

The method used in this project was a standard leak checking with Helium. The basic conception is the following: a vacuum is created inside a pipeline, then Helium is sprayed at suspected leak sites on the pipe, whilst measuring its traces inside the pipe. Detecting Helium will indicate that the connection is not seal tight. An overview of the leak checking procedure and performed steps are presented below.

During the first phase of Helium leak checking, isolated vessels and instrumentations were tested. The second phase was intended to study their connections.

The scintillator plant is designed in such a way that the pipeline is continuous, which makes it operate as a whole. Considering its overall volume, obtaining the leak rate of the entire plant at once was not feasible. Therefore, it was split into smaller sections or loops, which became plausible to study. The loops were isolated with either VCR blinds (plugs or caps), hand-valves or blinding flanges used as termination ports.

The elements that required testing were the following: connections, seals between vessels and their instrumentation, instrumentation (flowmeters, rotameters, thermowells), filters, valves, pumps. Moreover, although all welds that join the pipes were pressure tested, some of them were still randomly checked with Helium. In the beginning of the project all welds were checked.

Loop preparation. Some of the connections in the plant, such as VCR fittings and flanges, were not ready for the exploitation. Therefore, the responsibility of the

Helium leak checking teams was to prepare permanent connections. A VCR fitting consisted of internal nut, gland, S316 gasket[4] and a body with external nut (see Figure 2.4. With all components in place the VCR connections were tightened.

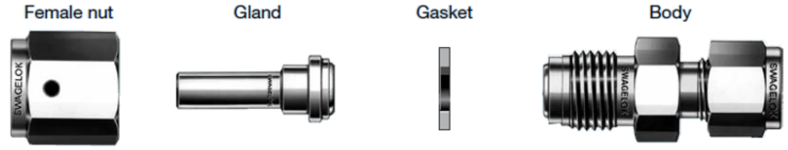

Figure 2.4: VCR connection. The schematic picture was taken from [96]

.

Initially temporary PTFE gaskets were positioned between metal plates in flanges. The teams replaced them with Helicoflex gaskets and ANSI-flex gaskets. Helicoflex gaskets were installed in grooves with metal-to-metal contacts and in flat flanges. The inner ring of the gasket was a metallic coil spring. Under pressure due to compression resistance of the spring, the casing deformed, which resulted in a highly tight seal. The ANSI-flex gasket was a combination of PTFE and EPDM rubber inner core. Either of those two gaskets required a delicate handling. If the connection was tightened inaccurately that would damage the gasket.

In order to perform the Helium leak checking, all the connections inside each loop were surrounded by aluminium tape to ensure impermeability.

Achieving vacuum. A studied loop was pumped down by either of Edwards nXDS 6i or XDS5 scroll vacuum pumps [97] (see Figure 2.5(left)) connected to a blind port. Deep vacuum was achieved by reducing the internal pressure from 1000 mBar down to 0.1 mBar [94]. Traces of dust or water which could be left inside the vessels, since they were hand cleaned with UPW before sealing, were evacuated with air as well. This procedure took several hours depending on the geometry of the loop, i.e. volume, pipeline length, tangles and kinks.

---

[4] There are only 4 sizes of gaskets used in the plant: 1/4”, 1/2”, 3/4”, 1”.

Figure 2.5: XDS5 scroll vacuum pump on the left [98] and Helium Leak Detector Leybold INFICON UL 200 [99].

In order to further increase the vacuum level to 10^{-3} mBar [94], a Mass Spectrometer Helium Leak Detector Leybold INFICON UL 200 [100] replaced the vacuum pump.

Leak checking. Once the loop was prepared, the Helium Leak detector was switched to work in “detector” mode. The helium-calibrated mass spectrometer inside it was able to identify and quantify the leak based on the amount of Helium present in pipeline. Connections were checked one at a time. In order to inspect a connection, Helium contained in a small vessel was sprayed inside a hole pierced in the aluminium tape of the connection. The hole was then closed again. If there was a leak, helium would penetrate inside the pipeline and while distributing inside it, would reach Helium detector. Depending on the distance between the connections, the waiting period could take up to an hour.

Fixing leak. If a leak was observed, a Helium leak checking team amended the connection. The most common cause was misaligned or damaged gaskets. For instance, tightening a Heliconflex gasket unevenly and therefore creating non-uniform pressure resulted in incorrect deformation of its spring. Moreover, dropping a gasket could lead to the same result. Once the gasket was replaced and carefully aligned the connection was resealed.

2.6 Electronics in SNO+

The trigger system is designed to read out collections of PMT hits that relate to physics events in the detector and is tuned to differentiate true events from the random noise rate due to PMT dark noise.

2.6.1 PMT system

There were 9662 PMTs in the ancestor SNO [101]. At a very early stage 14 PMTs were failing and were extracted from the PSUP before the data taking, and by the termination of the experiment 744 PMTs were identified as faulty [101]. The following SNO+ experiment aimed to repair and replace the failed PMTs. All such PMTs were pulled out for inspection and mending. The bottom part of the PSUP could be easily accessed from the cavity floor. In order to reach the sides a team was using a movable scaffold and Genie Lift, for the top part a tethered member of a team was lowered from the deck. Once the water fill has started, the PMTs were accessed by boat.

Only 10% of PMTs were found to have unfixable failure modes. The most common reason of PMT failure was broken circuit boards. Fortunately, spare boards were available to replace the damaged ones. After a base was resealed, a PMT was tested and returned back into the PSUP. In order to avoid the “blind” clusters, empty spots were strategically swapped with PMTs installed in the PSUP. By the time of writing this thesis there were 9484 PMTs in SNO+ in total [102]. In the data stream process they are divided into groups and operate as a system. The flow chart of the PMT system can be seen in Figure 2.6.

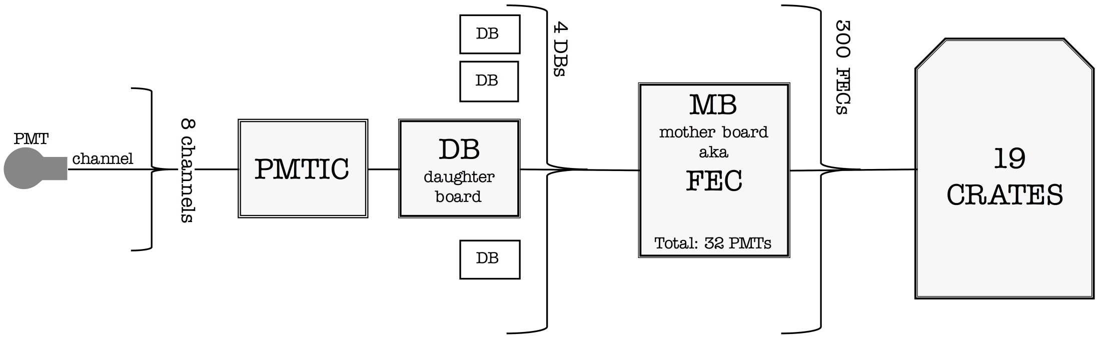

Figure 2.6: Block chart of the PMT system.

Each PMT is connected to a channel that makes it possible to transfer registered signals, raw charge and time, in the form of ADC (analog to digital converter) counts. Every 8 channels are connected to a PMTIC (PMT interface card) that is then connected to a DB (daughter board). Every 4 DBs are connected to a MB (mother board) also called a FEC (front end card). Thus, on each MB there are 32 channels and there are 300 MB in total. Those boards are physically housed in 19 crates located in the deck area of the SNO+ detector.

The functionality of the PMT system is closely related and determined by the trigger system, and therefore should be discussed together.

2.6.2 Managing time in the detector

The start time of the experiment was set to midnight on 1 January, 2010 (GMT). The time[5] passed since then is called “Universal Time” or “UT”.

There are three clocks in the detector with different precision: 10 MHz, 50 MHz and PMT times [105]. Each of them is used to describe its own timing characteristic.

The 10 MHz (100 ns) clock is used to calculate calendar time of an event. The 10 MHz clock start is set to the same starting time of UT. It will run for 28.5 years and therefore will be able to cover the lifetime of the SNO+ experiment. The 10 MHz clock performs accurately at time periods over an hour, but might wobble on shorter scale of a few seconds. The 50 MHz (20 ns) clock is used to measure the time between events. Some trigger pulses are issued to 50 MHz clock tick.

---

[5] The time is measured in days, plus seconds, plus nanoseconds

PMT time is the clock used to measure a PMT hit time with respect to the trigger system. It is discussed in Section 2.6.3.

2.6.3 Trigger system

When a PMT is hit, the electrical pulse is compared against the channel's discriminator threshold (currently set to $\frac{1}{4}$ of a photoelectron [103]). If it is above the discriminator threshold, a time to amplitude converter (TAC) starts ramping. If saved, it will be used to obtain the time when this PMT has been hit and consequently estimate the time when the event has happened. Furthermore, the charge detected on the PMT will be defined using electrical pulses, which start being accumulated from 10 ns before the signal crosses the threshold and continue for 390 ns after. Those values are [103]:

- QHL. Stands for charge (Q) calculated from pulse integrated under high gain (H) over long time (L). This value characterizes any charge obtained during the full time window of 400 ns capturing all pulses including the ones due to late light, such as reflection, scattering or slow scintillation. Thus, considering pulses recorded by all PMTs regardless of the time of Global Trigger (will be discussed in this section), it describes an entire event.

- QHS. Stands for charge (Q) calculated from pulse integrated under high gain (H) over a short time window of 60 ns. This value characterizes the size of the pulse that fires a channel.

- QLX. Stands for charge (Q) calculated from pulse integrated under low gain (X) over long time (L). Similarly to QHL this value characterizes charge obtained during the full time window of 400 ns except for gain reduced by a factor of 12.

If the PMT hit is saved, the TAC, QHS, QHL, QLX values will be stored in a form of ADC counts, which will be converted into physics parameters using Electronic Calibration (ECA) and PMT Calibration (PCA) (see Section 2.8). Those charge and time values are kept on each channel for 400 ns and reset after.

The decision on whether an event has occurred and should be stored will be executed by issuing a Global Trigger (GT). This decision follows from the pre-defined combinations of several trigger sums obtained along the trigger system path.

For each trigger type several trigger pulses[6] of uniformed height are generated for each PMT after a signal on it crosses the threshold. Those discrete pulses are: Nhit20 which is a square pulse of 20 ns wide and NHit100 of 100 ns wide. The trigger pulses of the same type are continuously summed up (see Figure 2.6 for the block chart):

> In each DB the pulses of the same type from 8 PMTs are summed up and passed to the MB.
>
> In each MB 4 pulse sums of each type are summed up and passed to the Crate Trigger Card (CTC).
>
> All intermediate sums of pulses in each CTC are summed up and passed to the Master Trigger Card/Analog (MTC/A+).
>
> MTC/A+ performs the final summation of sums of analog pulses from all CTCs, resulting in a single value for each trigger type. For NHit20 and NHit100 these values represent number of channels fired in previous 20 ns and 100 ns correspondingly. If any of the trigger sums is above a predefined threshold, MTC/A+ generates a corresponding signal and sends it to the Master Trigger Card/Digital.

The MTC/D receives signals and decides whether to generate a GT based on a pre-defined trigger mask. In the case of a real detector event those signals are sums of trigger pulses calculated by MTC/A+. Whenever a planned calibration of electronics takes place, trigger signals are fed into the MTC/D, bypassing the front end.

Before a GT is issued, the MTC/D generates a “raw” trigger pulse. Only after the raw trigger is synchronised to the 50 MHz clock, GT is generated or “latched”.

---

[6] All trigger pulses are described in [103].

Thus, a GT can occur only on 20 ns intervals. If the start of the raw pulse falls on the rising edge of the 50 MHz clock, the GT will be issued without a delay. The maximum time delay is 20 ns, due to complete asynchronisation of the two pulses.

The GT signal is sent back to the front end electronics to stop ramping of the TACs and integration of charge pulses; the obtained values in each channel are saved. If no GT reaches the front end within 400 ns from the PMT hit, then TAC and charge integrators are reset[7].

In addition to the GT, the MTC/D generates a "lockout" pulse [105]. This adds 50 ns to the 400 ns trigger window, expanding the time when another GT will not be generated up to 450 ns. Throughout this thesis we will refer to this time block as the event time window to avoid confusion with an actual trigger window.

PMT time

PMT time is the time of a PMT hit calculated (and recorded) with respect to when the GT has been latched.

When a pulse created at a PMT crosses the threshold, it takes 110 ns for trigger pulses to undergo all intermediate stages and reach the MTC/A+. It takes another 110 ns[8] to deliver the signal back to the front end. Therefore, the TAC has been ramping and the charges (QHS, QHL, QLX) have been integrating for 220 ns.

PMT hits

In this section we concentrate on PMT hits that occur in the 400 ns trigger window. The discussion will be supported by the timing diagram on Figure 2.7.

---

[7] This can happen if GT is either not issued or there appears break in the electronics.

[8] In the case that we consider the difference in time of generating a raw trigger and latching GT, the time that the GT reaches the front end will be 120±10 ns.

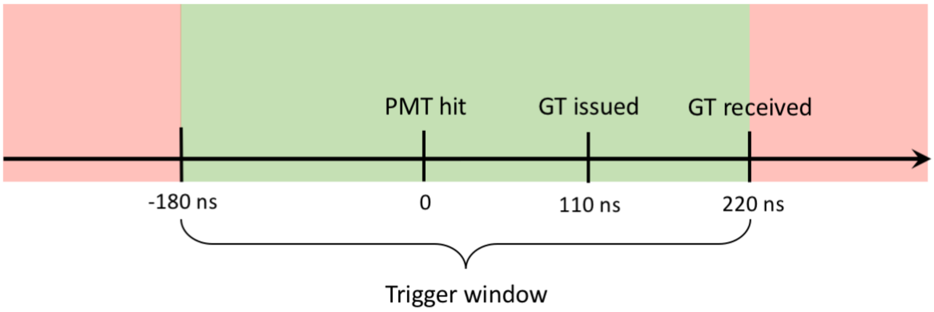

Figure 2.7: An event timing diagram.

All PMT hits that occur in the trigger window (green block on Figure 2.7) are included in a detector event. PMT hits that happened earlier (red block on Figure 2.7) will be reset before the GT reaches their front end electronics.

All PMT hits in a trigger window are assumed to be due to a single event in the detector, and will be reconstructed as such. However, as discussed earlier in Section 2.6.3, the GT will be issued given enough PMT hits, regardless of their origin.

2.7 Event reconstruction in SNO+

The goal of the event reconstruction in SNO+ is to propose position, time and deposited energy of a physics event. The software consists of several processors, "fitters", that are combined to provide the best estimates.

The position reconstruction uses a PMT hit pattern, i.e. coordinates of triggered PMTs and times at which they were hit, to determine the event vertex of the event that has caused them. As a default, all PMT hits occurring in the same trigger window are assumed to be due to one event and therefore are used to calculate its vertex. The SNO+ reconstruction is not designed to reconstruct multiple vertices in trigger window. That means that if more that one event has caused the PMT hits in the same trigger window they are still reconstructed as a single event. Such events are called "pileup events" and will be discussed in detail in Chapter 5. The average position resolution at 2.5 MeV is 15 cm at the centre of the detector [77].

The position reconstruction is performed by two fitters. The first fitter is the "quadFitter". It only roughly estimates the event vertex, as the speed of its performance is prioritised. The proposed coordinates will act as a starting point or a "seed" in the further and more accurate "PositionTimeLikelihood" fitter.

The energy reconstruction of an event is performed by the "EnergyRThetaFunction" fitter using the corresponding PMT hit pattern and the event vertex obtained earlier by the position reconstruction fitters. The energy resolution at 2.5 MeV is 270 keV (FWHM) [77].

2.7.1 QuadFitter

The quadFitter is inherited from the SNO experiment [104] and was integrated in SNO+ by I. Coulter [154]. The purpose of this fitter is to provide a quick estimate of the time and the position of the event. Since the speed of the execution of the fitter is prioritised, the lack of precision is accepted.

First, quadFitter considers vertices of hits (i.e. time of hit and position coordinates of PMTs) from 4 random PMTs and performs the backward derivation to define the possible event vertex (see Figure 2.8). The event vertex is (x_0, y_0, z_0, t_0) and the vertex of each of the 4 PMTs is (x_i, y_i, z_i, t_i), where i = 1,2,3,4.

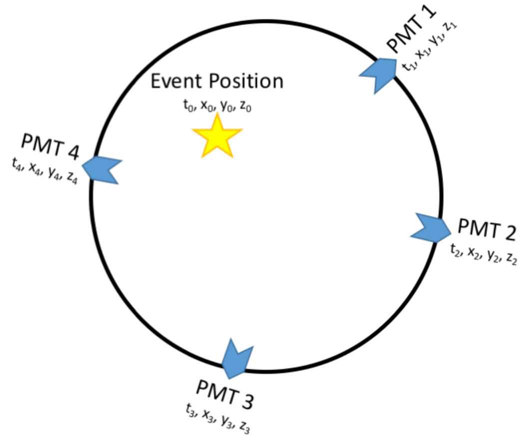

Figure 2.8: The geometry of an event in quadFitter.

The equation describing the geometry of the event is:

$$v^2(t_0 - t_i)^2 = (x_0 - x_i)^2 + (y_0 - y_i)^2 + (z_0 - z_i)^2, \tag{2.7.2}$$

where v is the effective velocity of light when passing through the matter. By solving these equations and rejecting unphysical values one of the event vertices is proposed. Those calculations are repeated for different random combinations of 4 PMTs and hence prepare “a cloud” of different event vertices. In [154] it was proposed to use 4000 event vertices as a compromise since adding more points to the cloud increases the time of estimation. The final event vertex at this stage is achieved by calculating medians of each coordinate.

One of the undertaken assumptions in quadFitter is that photons produced by an event in the AV are considered to travel towards PMTs on a straight line. In reality such photons traverse 3 media: scintillator inside the AV, acrylic itself and water inside the water shielding. As they pass through the boundaries of those materials, their light paths changes due to refraction, making it differ from straight lines. Introducing those corrections slows down the performance of quadFitter and therefore contradicts with the initial aim of the fitter [154].

2.7.2 PositionTimeLikelihood fitter

While quadFitter provides a quick estimate of an event vertex, the PositionTimeLikelihood fitter, developed in [151] and upgraded in [154], aims to achieve a more accurate result, using a maximum logarithmic likelihood estimation.

The goal of this method is to determine the event vertex, which is the parameter θ, given experimental observations of vertices of each fired PMT. We estimate the proposed model using the logarithmic likelihood function L:

$$\log L(\theta) = \sum_{i=1}^{n} \log P(x_i; \theta), \tag{2.7.3}$$

where i runs over the observed x_i values and $P(x_i; \theta)$ is the probability of observing x_i under the assumption of θ. The best fit is found by maximizing the logarithmic likelihood function L. In order to build the PDF we use time residuals as the parameter which quantifies the correspondence between the proposed event vertex and information obtained by a fired PMT.

Estimating time residuals. This parameter is defined as:

$$t_{res} = t_{PMT} - t_{path} - t_{event}, \tag{2.7.4}$$

where t_{res} is the time residuals, t_{PMT} is the time the PMT has been hit, t_{path} is the time that it takes a photon to reach the PMT and t_{event} is the time when the event has happened. The PMT hit pattern is known from the stored data, the event time is the parameter of study and the time of flight of the photon is calculated below.

Assuming that photons travel on a straight line, we consider the time of flight of photons in each medium separately:

$$t_{path} = \frac{s_{scint}}{v_{scint}} + \frac{s_{acrylic}}{v_{acrylic}} + \frac{s_{water}}{v_{water}}, \tag{2.7.5}$$

where v is the velocity of the photons and s is the distance travelled in each medium. Unfortunately, it is not possible to determine velocities from the obtained PMT hit data. Therefore, we use the representative values in each material [151, 154].

For the water and the acrylic, the velocity is chosen in such a way that the corresponding wavelength causes the most number of PMTs hits. The exact value is obtained by comparing the results from the simulations of photons with different wavelengths.

The same argument cannot be applied to photons travelling in the scintillator, due to absorption and further re-emission, which changes the initial wavelengths. Therefore, a different criterion is used – the wavelength has to provide the best reconstruction of the event vertex of a 2.5 MeV electron.

Building the PDF. As it is not plausible to prepare PDFs for each possible event type in advance, we build a generic PDF that shows the best performance for signal events, which in this case is neutrinoless double beta decay in Tellurium loaded scintillator. The PDFs are created by histogramming the t_{res} values for all hit PMTs from a simulation of 20000 2.5 MeV electrons evenly distributed inside the AV within a 5.5 m fiducial volume.

Reconstructing an event. For testing a proposed event vertex, θ, we calculate t_{res} for each fired PMT, substituting all the current values into Eq. 2.7.4. We then look for the corresponding probabilities, P, in the PDF and use them in Eq 2.7.3. The event vertex that provides the maximum of the logarithmic likelihood function L is found, using the Powell optimiser.

2.7.3 EnergyRThetaFunctional fitter

The EnergyRThetaFunctional fitter [155] reconstructs the deposited energy of the event using its earlier reconstructed position and the total number of PMT hits in this event. Like in the other fitters, this algorithm is guided by the performance for signal events, where the accuracy is desirable the most.

The basic idea of this method is the following. We first undertake an assumption, which we use to design the reconstruction method. We then build the approximation functions, using simulations of neutrinoless double beta decay. We apply this method to the energy reconstruction by substituting the relevant parameters of an event into the functions. These steps are detailed below.

The initial assumption of the fitter. The deposited energy of an event, its vertex and the number of caused PMT hits are the interconnected parameters. We consider that it is possible to represent those relations by building independent functions of energy $f(E)$ and position $f(w)$ and introducing an estimator H [156]:

$$H = f_1(E) \times f_2(w), \tag{2.7.6}$$

$$H = \sum_{i=1}^{S} P_i \times \log(1 - \frac{N_i}{P_i}), \tag{2.7.7}$$

where S is the amount of segments we divide the detector in, N_i is the number of triggered PMTs and P_i is the total number of PMTs in segment i.

Energy function $f_1(E)$. The boundary condition of the position function is in the center of the detector, where $f_2(w) = 1$. Therefore, in this case Eq. 2.7.6 reduces to:

$$H = f_1(E) \tag{2.7.8}$$

The simulation[9] of electrons with energies up to 6 MeV has shown that the energy dependence is linear and Eq. 2.7.8 can be rewritten as:

$$H = \alpha E \tag{2.7.9}$$

The value of α is determined from the simulations and stored for use in the algorithm.

Position function $f_2(w)$. Due to the approximate spherical symmetry of the detector, we will describe the position of the event w with radial distance from the centre of the detector r and polar angle θ measured from the z-axis. After defining the energy function, Eq. 2.7.6 turns into:

$$H = \alpha E \times f_2(r, \theta), \tag{2.7.10}$$

The parameters r and θ do not affect events the same way. While the change of angle dependence appears only in the neck area, where θ is small, the events with different radial coordinates cause different numbers of PMT hits. Therefore, we split the position function $f_2(r, \theta)$ into several functions of a single variable. In order to do so, we choose several[10] fixed values of $\theta = \theta_i$ and for each angle perform the simulations of $0\nu2\beta$ events with different r values and approximate them by the polynomial functions.

Energy reconstruction of an event. To conclude, the energy of an event is calculated as:

$$E = \frac{H(r, \theta)}{\alpha \times f_2(r, \theta)} \tag{2.7.11}$$

The position of an event (r_0, θ_0) is reconstructed earlier by the quadfitter and positiontime likelihood fitters. We are able to calculate the H value from Eq. 2.7.7, using the stored data of PMT hit pattern. Applying the position function $f_2(r, \theta)$ might not be straightforward, as the angle θ_0 is not necessarily equal to any of the fixed angles we discussed earlier. In that case, we calculate the values of the two functions of the nearest fixed angles and linearly interpolate between them to obtain

---

[9] The simulations were performed for 1000 electrons of energies between 1 MeV and 6 MeV with the step of 1 MeV. For each energy region the mean H was calculated.

[10] We fix 4 values of θ: 0°, 60°, 90°, 180°.

the value for the angle θ_0.

2.8 Calibration

The goal of the calibration is to understand and completely describe the detector. That is to confirm performances of the PMTs and the electronics system and introduce them into the simulations, investigate the scintillator properties and incorporate them into the reconstruction methods, confirm the reconstruction methods or adjust them if needed. These steps will prepare the experiment for physics analyses. The full scheme is described in [109]; the document is regularly updated. At the time of writing, the required precisions of measuring the parameters and performing the model tests have not yet been fully established.

There is a set of parameters used in the Monte Carlo simulations and in data reconstruction that we need to estimate. In order to do so, we develop the calibration sources and then apply them to study the corresponding parameters. The parameters are determined by tuning a Monte Carlo model to the reconstructed calibration data.

Another category of calibration procedures is the testing. After all the parameters are identified and input to RAT we run calibrations to test how accurately our models describe the data. In order to do so, we compare the Monte Carlo simulations and the data. From performing a number of tests we determine systematic uncertainties. If the discrepancy between the model and the data in any of the tests is not on the order of the acceptable precision, the model must be revisited. Some calibration sources will also be used for cross-calibration.

There are four types of calibrations: the electronics calibration (ECA) [106], the PMT calibration (PCA) [107], the optical calibration [108] and event-based calibrations with deployed sources.

ECA will measure various electronics parameters and input them into the database so that they could be applied to characterize the detector in each run. The calibration will be performed regularly starting from first runs during the water phase. PCA will measure the parameters related to PMTs and corresponding channels and introduce them to the database. For calibration, PCA will use data obtained by other calibration sources: TELLIE [111] and Laserball [112]. PCA will also run regularly and the time-frame for first working runs will be determined by the readiness of optical calibration sources.

The optical calibration is used to measure and test such properties of the medium as scattering and absorption. TELLIE and Laserball which both are optical sources are also used to test the detector geometry such as PMT positions, directions, and mapping. Since some of the functionalities of the two are similar, when one of the sources performs measurements the second is used to perform tests. The optical calibration will be performed during each phase of the experiment.

The main purpose of using the radioactive sources is to perform energy calibration of the detector across the range between 0.122 – 6.1 MeV. The sources are planned to be deployed in the water and in the pure scintillator phases, however, the complete plan for the Te-loaded scintillator phase hasn't yet been approved.

We describe each calibration source in more detail below.

2.8.1 The ECA calibration

All physics events in SNO+ are obtained using the electronic system. It controls the whole process of preparing events for analyses, starting from receiving signals occurring in the detector. Therefore, it is necessary to understand the behaviour of the electronics and quantify its impacts to stored PMT hits. Such a task is performed by the ECA calibration. With its help for each channel we define time constants, which will be used to convert TAC values from ADC counts into ns. It also prepares the charge values for the subsequent PCA calibration.

In Section 2.6.3 we briefly covered charge and time information recorded from a PMT hit. Below we provide more details necessary for further discussion of the ECA calibration.

Each channel is connected to a CMOS (complementary metal-oxide semiconductor) chip, which has 16 capacitors used as storage cells. They are cycled in turn to prevent losing information during a channel's dead-time. Once a PMT is hit, 2 TAC values and QHS, QHL, QLX values are temporarily stored in one of the channel's cells. To obtain and store resultant time and charge values CMOS chips will loop through all cells in the channel. Since cells might have different properties, the electronic calibration is performed for each of them separately.

Charge calibration. For each channel the ECA calibration identifies "pedestals" that are naturally present in all recorded QHS, QHL and QLX values. They are found as follows.

During ECA dedicated runs, the DAQ system selects 512 channels randomly distributed across the detector. It enables a pedestal trigger on each of them and disables all other triggers. In that way, a selected channel can only be fired due to a pedestal event. In such an event, the channel is not fired by a real PMT hit, but by a pulse sent by MTC/D. Once the discriminator receives a pedestal pulse, charge integrators are forced to integrate and the TAC to start ramping. After some time, which is called a PED-GT delay time, the GT is issued to stop the process. The PED-GT delay time is set to 150 ns. As the whole process is controlled by the electronics, and no real charges are present, the measured values represent zero charges or pedestals. In order to find pedestals, ECA generates 10 events for each cell of a channel. QHS, QHL, QLX charge offsets are then found as medians of the corresponding charge integration data.

The ECA calibration will be performed in 10 minute long pedestal runs on a weekly or a biweekly basis. As a result, the ECA will return charge pedestals for each cell on each channel. Those constants are then applied to the following physics runs – pedestal values are subtracted from raw charges recorded on relevant cells.

Time calibration. The ECA calibration in addition to defining pedestals, obtains timing constants or "slopes" to convert TAC values from ADC counts to nanoseconds. It also reverses time which is recorded as backward-going, i.e. a PMT hit happening earlier in time will correspond to a smaller value.

The procedure of performing the time-slope calibration is similar to the pedestal calibration, except that based on a predefined set of intervals the PED-delay is changed to sample the full TAC slope. As a default, the slope is programmed to be sampled by 50 points at 10 ns intervals. Thus, as a result, we obtain 50 points: times in nanoseconds between the start of the TAC ramp and the arrival of the

GT, and the resulting TAC values in ADC counts. These points are the time-slope calibration constants of a channel and are stored.

In order to convert time recorded in ADC counts into nanoseconds, ECA uses a linear interpolation between nearest time-slope points. After the time is written in nanoseconds, it is reversed by adding the time offset of -500 ns.

The ECA calibration performs an 80 minute long time-slope run, which follows pedestal runs.

ECA tests. Whilst defining constants for time and charge conversion, the ECA processor runs tests on each channel and writes results in corresponding bit masks. It checks the performance of MB and DB; number of events on each cell – if any cell has fewer than 10 events, the channel fails this test. Values of QHS, QHL, QLX, TAC and constants are tested against pre-defined tolerances.

Relying only on ECA tests might not be feasible to draw the conclusion about the channel. However, we use those results in combination with other tests. This is performed by the Channel Software Status (CSS) and discussed in Chapter 3.

Performing the calibration. The ECA calibration is performed in two stages: data collection and obtaining the constants. The SNO+ detector operator carries out pedestal and Time Slope runs to obtain the calibration data. Then the ECA processors are run over these raw data files to extract the constants and write them to the database after making tests of their validity.

2.8.2 The PCA calibration

While the ECA calibration studies the influence of the electronic system on channels, the PCA calibration concentrates on the PMTs' related properties. Thus, the goal of this next step in data conversion is to define hit times, relative to a global time (set to 01 Jan 2010 GMT) and provide constants describing charge spectra of each PMT. Those parameters are then introduced to the RAT (see Section 2.9) software for accurate modelling of the detector response.

Time calibration. The ECA calibration provides us with the time at which the electric pulse from a PMT crosses the channel's discriminator threshold. However, this time is not necessarily the time at which the PMT has been hit by a photon.

An additional time offset is composed of the contributions from electronics delay and delay due to the channel's discriminator.

Electronics delay consists of transit time inside PMT, cables that connect the PMT with parts of the electronic system and delay due to electronic components. Transit time is the time it takes an electron, emitted from the photo-cathode, to reach the anode. Transit times of PMTs are not identical, as the emitted electrons might have different energies and different trajectories from photo-cathodes to first dynodes[11]. Cable delay is the time it takes a signal from a PMT to reach the MTC/D, and consequently to issue GT, which stops ramping of the TAC. Therefore, such a delay depends on a path length, which varies between PMTs.

After the electric pulse from the PMT reaches the channel's discriminator threshold, it takes some time to fire it. The larger the pulse is, the faster it crosses the discriminator threshold. This is schematically demonstrated in Figure 2.9. The difference in time of pulses crossing the threshold ΔT in Figure 2.9 is called a "Time Walk".

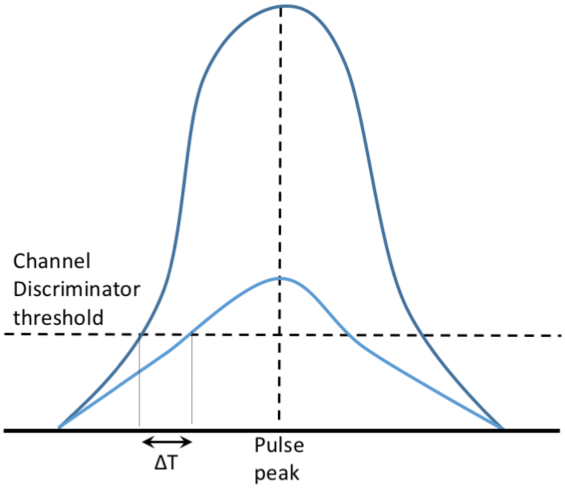

Figure 2.9: Schematic demonstration of time delay due to discriminator threshold.

When performing the PCA calibration of a channel the time delays are not distinguished but considered together as an overall time delay. However, due to the nature of the electronic delay, it introduces an individual global offset and the Time

---

[11] Transit times inside SNO PMTs were 30±1.5 ns, where the contribution from differences in energy of emitted electrons was 0.2 ns [107]

Walk effect can be observed in the low charge region by studying the correlation between the charge (QHS) and time, after the ECA calibration has been applied, see Figure 2.9.

Charge calibration. Applying the ECA calibration for each channel we obtain QHS, QHL, QLX charges above pedestals in ADC counts. Next, the PCA calibration determines constants that will convert them into units proportional to number of photo-electrons. The constants are defined from building charge spectra created by a single photo-electron (SPE)– in this case one photo-electron corresponds to numbers of ADC counts in charge spectra. This is called a “gain calibration”.

The number of ADC counts in a charge spectrum depends on properties of a PMT and the electronics. Since PMT gains are not identical, the number of counts in each SPE spectrum can vary. Moreover, a PMT gain changes over time due to aging effects. Charge integrators and ADC converters on each channel are also individual and can affect the number of counts.

At the time of writing, the charge corrections are not planned to be applied and the extracted constants will be used as input to RAT.

PCA runs. The PCA time and charge calibrations are performed using Laserball (see Section 2.8.4) and TELLIE (see Section 2.8.3) which produce SPE to determine constants.

During calibration runs, the laserball is placed in the center of the detector and produces isotropic light at low intensity. Thus, each PMT receives 10000 hits in total due to single photons. After a PMT is hit, the electronic system follows all steps described in Section 2.6.3 up to latching a GT. Since the GT is synchronised to the 50 MHz clock, it causes a time delay up to 20 ns, which results in an uncertainty in estimating the PMT hit time. In order to avoid this issue, in these runs, we enable the external asynchronous (EXTASYNC) which makes MTC/D immediately issue GT. When the laser box generates light and sends it through the fibres into the laserball, it also directs some fraction of the beam to a photo-diode. The signal from the photo-diode will be used as the input to EXTASYNC.

TELLIE stands for Timing Embedded LED/Laser Light Injection Entity. The LEDs (light emitting diodes) generate light which is transferred via optical fibres into the detector. There are 91 TELLIE fibres mounted on the PSUP throughout the detector. Since the system has already been installed before data taking, running it won't introduce additional contamination. Therefore, TELLIE will provide continuous PCA data. However, before using TELLIE for the first time it needs to be calibrated against the laserball in order to identify fibre-related offsets.

PCA tests. Whilst performing the calibration, PCA runs tests over channels. They check the validity of the identified constants, QHS and QHL charges, i.e. whether the values are too high or too low in comparison with the pre-defined values, and the check of continuities in the conversion of voltage to ADC counts. After PCA identifies a bad channel it flags each hit that has been taken with this channel at the time of the PCA data-taking.

PCA run plan. First, PCA data will be obtained from the laserball positioned in the centre of the AV. It will be used to verify the PCA data from the subsequent TELLIE run. After TELLIE is verified it will be possible to continuously run TELLIE and extract PCA constants. Whenever a detector medium changes, another benchmark laserball run has to be performed. Like in the ECA calibration, the PCA processors first collect data and then run over these raw data files. The determined constants will be stored in the database.

2.8.3 Optical calibration

In order to understand the detector response to events occurring in the detector we have to understand and characterize effects introduced by detector media (water, acrylic, scintillator, tellurium loaded scintillator), as they affect obtained signals. Produced light can undergo absorption, scattering, reflection and refraction, before reaching PMTs. The optical calibration studies the dependence of those phenomena on wavelengths of emitted photons and on their position inside the detector. As a result, the optical calibration provides parameters for SNO+ Monte-Carlo models of media. Additionally, optical calibration provides data for PCA to calculate PMT constants. Optical calibration is performed by the ELLIE system and laserball.

ELLIE

ELLIE stands for the embedded LED Light Injection Entity (ELLIE) [108]. It consists of three systems: the TELLIE module provides timing calibration [113], the SMELLIE module is responsible for studying the scattering properties of the detector media and the AMELLIE module [114] studies the attenuation of the scintillator. ELLIE provides continual calibration in order to monitor the changes in the detector. The components of the ELLIE system have already been installed in the detector and there will be no future deployment of additional supplements. Hence, ELLIE won't introduce the risk of contamination.

Each module contains a light source and transmission system to deliver and distribute produced light into the detector. Located in the deck area, the corresponding electronic system generates light for each module, see Figure 2.10. Light is directed into the detector via 120 optical fibres with low intrinsic radioactivity from the single point on the deck. The fibres terminate at the nodes located on the PSUP.

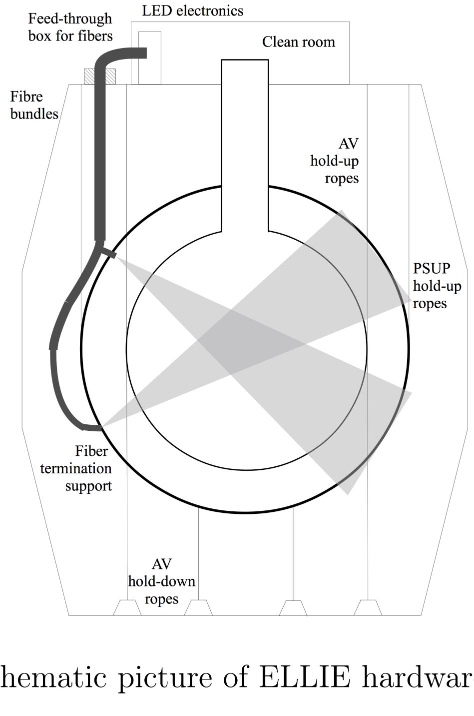

Figure 2.10: A schematic picture of ELLIE hardware in the detector.

The main goal of the TELLIE calibration is to obtain PCA constants [111], i.e. time offset and gain calibration of each PMT. The light is produced by LEDs (light emitting diodes) and is transferred into the detector via 92 wide aperture optical

PMMA (polymethyl methacrylate) fibres mounted on the PSUP, which allows the overlapping PMT coverage. TELLIE will also perform geometry tests such as the PMT positions, directions, and mapping and the AV position. These parameters will be measured with the laserball.

SMELLIE studies the wavelength dependence of optical scattering across the detector [115]. The system uses 4 pulsed diode lasers to emit light at wavelengths of 375 nm, 407 nm, 446 nm and 495 nm. They are chosen over LEDs due to higher light intensity and efficiency of beam collimation. The light is passed from lasers situated on the deck onto one of the 12 SMELLIE fibres. The fibres are mounted on the PSUP at 4 injection points in such a way that at each injection point 3 fibres are facing the center of the detector at 0°, 10°, and 20°. The fibres are connected to collimators in order to reduce the emission angle of photons. The full description of the SMELLIE hardware can be found in [110].

During the SMELLIE calibration, wavelength, beam direction and position of the light-source are known. Due to scattering, photons change directions and therefore might arrive at PMTs at later times. By studying positions and times of PMT hits we tune parameters of the Monte-Carlo model for media in the detector and hence improve the simulations and reconstruction algorithms.

AMELLIE studies the attenuation of the scintillator that might worsen the optical properties in case of strong contamination [114]. The system has 4 injection points on the PSUP with 2 differently orientated fibres with light from LEDs of different wavelengths, which allows studies of wavelength dependency. At the time of writing, the LED selection is still ongoing.

2.8.4 Laserball

The laserball [112] is used for the PCA calibration and the calibration of TELLIE. It will measure the absorption of the detector media and the absorbtion of acrylic. The laserball will also measure the PMT positions, directions and mapping, and the position of the AV.

Light for the laserball calibration is produced by a nitrogen laser located in the deck area and transmitted via a quartz optical fibre inside the umbilical into the center of the flask. The pulse rate can be set between 1– 45 Hz. Redirecting the light beam through cell cuvettes filled with different dyes allows us to study the following wavelengths: 337±0.1 nm, 369±10 nm, 385±8.0 nm, 420±8.0 nm, 505±14.0 nm, 620±10.0 nm. The flask consists of a quartz sphere with diameter of 109 mm and a neck with diameter of 19 mm sheathed by the stainless steel casing, which prevents reflected light from entering the detector media, see Figure 2.11. The sphere is filled with silicone gel and glass bubbles with the diameter of 50 μm.

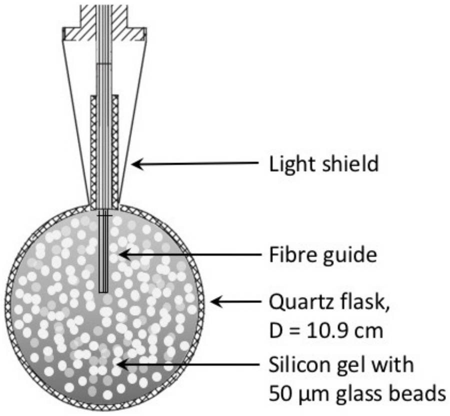

Figure 2.11: A schematic picture of laserball. The picture is inherited and modified from [116].

2.8.5 Deployed sources

SNO+ is developing the program of calibrating the detector with the radioactive sources deployed into the AV. The goal of this calibration is to measure and test energy scale, energy resolution, energy linearity and the position resolution. From the difference between the expected values of parameters and the obtained data, we will estimate the systematic uncertainties or correction factors. The isotopes planned to be deployed are listed in Table 2.1. The dominant mechanisms of the interactions of various particles with the scintillator are discussed in Section 2.4.2. The calibration plan for the Te-loaded scintillator phase hasn't been fully approved yet. The decision will be made with consideration of performance and achieved results during the pure scintillator phase.

The ^{16}N [117,118], ^{24}Na [119] and ^{60}Co [120] calibration sources are designed in such a way that their decays are tagged inside the containers. The tagged sources are used to test the energy and position resolution. The position reconstruction resolution and bias will be obtained from the difference between the true and the reconstructed position of the source. These values are estimated for a set of positions across the AV. Energy resolution will be found as a standard deviation σ of a fitted Gaussian function to the distribution of the differences between the true and the reconstructed energies.

The gamma-emitting calibration sources will be used to test the linearity of energy response of scintillator (the pure scintillator and the Te-loaded scintillator), as its energy response can be energy dependent. Ideal gamma-sources for that purpose would be isotopes with end-point energies across a wide energy range which emit single mono-energetic particles, as they behave like point sources. But such a set of sources either doesn't exist or is difficult to realise.

Using each developed gamma-calibration source, we will determine the light yield at the corresponding energy from the number of PMT hits. Having a set of points we will characterize it as a function of energy. This will quantify the energy non-linearity of the experiment during the liquid scintillator and, possibly, Te-loaded scintillator phases.

Table 2.1: A list of planned deployed sources in SNO+.

Source	Phase	Particle	Energy [MeV]
^{16}N, [117, 118]	water, pure scintillator	γ	6.1
^{24}Na, [119]	pure scintillator	γ	2.7, 1.3
^{57}Co,	pure scintillator	γ	0.122, 0.136
^{48}Sc, [121]	pure and Te-loaded scintillator	γ (sum)	3.3
^{60}Co, [120]	pure scintillator	γ	1.2, 1.4
AmBe, [122, 123]	water, pure scintillator	n, γ	2.2 (n), 4.4 (γ)

In order to test how accurately the energy reconstruction with the applied estimated correction factor can reproduce data, [165] proposed a beta-emitter ^{90}Y isotope as a potential new calibration source. Unlike gamma-spectra a β-spectrum is spread cross wider energy range. Since the signal of interest in SNO+ during the Te-loaded scintillator phase is $0\nu2\beta$, it is desirable to test the detector response of electron-like events.

An ^{90}Y isotope is an excellent candidate for this role for several reasons, one of which is being a pure beta-emitter, see Fig. 2.12 for the decay scheme.

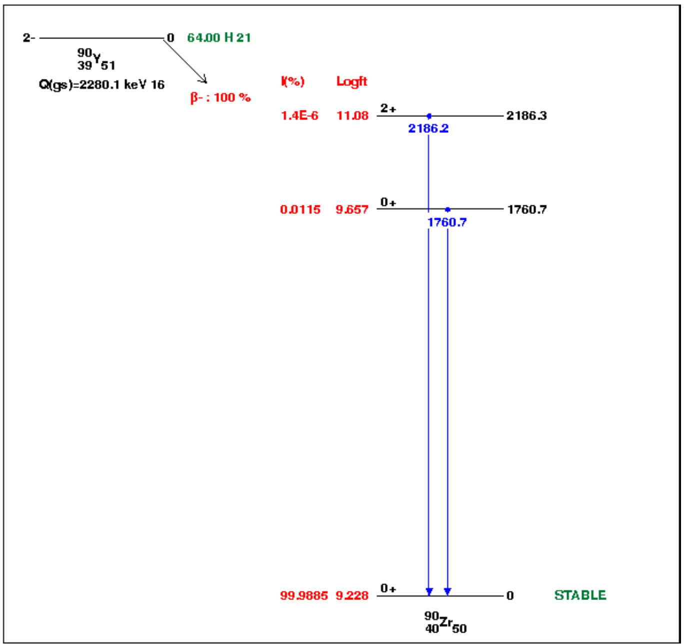

Figure 2.12: The decay scheme of ^{90}Y.

^{90}Y has the end-point energy of 2.28 MeV, which allows the coverage of a wide energy region that terminates near the strategic energy region of the ^{130}Te $0\nu2\beta$ decay. Another benefit of ^{90}Y from the safety perspective is its half-life of 64 hours. The decay time is too short to cause long-term contamination and yet enough to execute the calibration.

The physics motivation of using ^{90}Y as a calibration source, the manufacturing procedure, and the laboratory tests will be discussed in more details in Chapter 7.

2.9 SNO+ Monte-Carlo and software

SNO+ uses a private version of reactor analysis tools (RAT) to produce Monte-Carlo simulations of the detector [124]. The first version of RAT was developed by the Braidwood collaboration but several experiments, such as SNO+, MINI-

CLEAN and DEAP-3600 chose to use RAT and continued developing their own versions of the software. The RAT software is written in C++ with Geant4 [125] and GLG4Scint [126] libraries to describe physics processes in the detector. Data is stored in the ROOT [127] format.

There are several branches in RAT depending on their common properties. Two significant branches defining different types of simulations are the MC branch and the EV branch. While the MC branch represents true Monte-Carlo data, the EV branch incorporates the detector response to it, mimicking real data from the experiment, performing and testing reconstruction mechanisms in SNO+. The reconstruction algorithms (Fitters) first define the position and time of an event using PMT hit time residuals and then, based on this information, the event's energy. Since it is not possible to reach 100% efficiency in recording and reproducing all events, it is important to analyse signals reconstructed by RAT. Moreover, due to imperfection in reconstructing data, besides possibility of missing events, additional events might appear. Such events and methods to identify and reject them as described in Chapter 5.

The detector geometry is described in RAT using Geant4 libraries. RAT implements the full geometric model of the SNO+ detector, but some studies require implementation of additional objects. Modelling the calibration with a deployed source is one such task. Moreover, in order to test the calibration source ex-situ an additional setup is used that also requires computer modelling. In Chapter 7 we describe the proposed radioactive calibration source and present the HepRep [128] visualization of its design and the experimental setup we used.

A program in RAT that, as a part of event loop, analyses and / or updates an event's properties is called a processor. All primary properties of detector components are studied using processors. In Chapter 3 we discuss software developed to check the performance of PMTs that has been completed in the form of a RAT processor.

2.9.1 Echidna software

Joint groups from the University of Sussex and Queen Mary University of London, including the author of this thesis, developed the echidna software to perform a range of limit setting and fitting tasks [129, 130]. The software is written in python using NumPy [131] modules. The analyses presented in Chapter 5 and Chapter 7 were performed using echidna.

Chapter 3

Channel Software Status

The SNO+ PMT and electronic systems are responsible for obtaining the information from physics events occurring inside the detector (see Section 2.6) and therefore affect the recorded raw data. Hence it is important to regularly validate the data collecting process throughout the whole lifetime of the experiment. Some of the tests are either already being deployed or under development. The ECA and the following PCA perform the checks whilst running the calibrations. The Channel Hardware Status or CHS is tracing the channels with hardware failures. And finally, the Data Cleaning processors study certain misbehaviour of PMTs and channels, see Section 4.3.

In addition to this list, we are developing the software which will monitor the behaviour of the channels by combining the results from already fulfilled tests as well as introducing new checks. The performance of a channel also combines the performance of the PMT connected to it and the directly involved electronics, as it is not always possible to distinguish effects introduced by each of these systems individually. The software was historically named Channel Software Status or CSS.

CSS has two objectives. The first one is to identify misbehaving channels and to tag them. The second one is to quantify the misbehaviour of a channel and if possible to suggest the reason that caused it.

CSS is an evolving study. An initial approach of how to realize these goals was proposed by SNO [132] and carried on in [133]. The author of this thesis has designed the CSS framework. It includes retrieving the information from data needed for the check, extracting distributions for the checks, the design of the checks and their further application to data. Also, CSS was included in the data flow process and was tested as a part of the chain. The checks were implemented using the preliminary parameters, which will be tuned based on the real distributions from stable data.

At the time of writing the only data available was the air-fill commissioning data which wasn't of good quality since we haven't well prepared the detector and haven't tuned any of the electronics, for example, the channels thresholds. Since the channels performed sub-optimally, obtained CSS distributions couldn't be treated as expected distributions and hence using them for tuning the CSS checks was pointless.

We ran CSS on the commissioning data aiming to test the performance of the framework but not its output. The tests were successful and proved the readiness of the framework. After proper data is available we will determine CSS cut values.

3.1 CSS Logic

In CSS, we define criteria or checks to inspect certain properties of channels. Although every channel has unique characteristics, they have been tuned in such a way that their readouts from the same signal wouldn't vary significantly. We assume that a channel with a drastically different behaviour, an outlier, should be tagged. In order to do so, for every check, we identify the constraints or the limits for a channel to successfully pass a check.

Since the evaluated limits have to take into account properties of channels, they are estimated based on the channels' performances in a real SNO+ run. To apply a check to a channel the software tests each channel against the evaluated limits.

CSS analyses the channels on a run by run basis. That means that limits are defined using only the information from a single run, and the performance of channels is evaluated in each run separately using the data from this run and the limits. A run which is used to calculate the limits is carefully chosen and is called a Standard Run. It has to be stable and long-lasting so that the majority of PMTs will be hit and hence the majority of channels will checked. The Standard Run should be updated periodically, once the status of the detector undergoes changes such as changes in the electronic system and changes in the data taking phases. Since the Standard Run represents the latest status of the detector, the limits are relative only to runs that follow it and before a next Standard Run is chosen. A run which the checks are applied to is called a studied run; the checks can be also applied to the Standard Run.

The software uses statistical methods based on the average characteristics of a channel over many events. Few PMT hits in the Standard Run will provide imprecise or completely wrong check values. With a small number of PMT hits in the studied run, CSS might make wrong conclusions about channels. The minimum number of events will be estimated based on stable data.

3.2 Implemented checks

There are various checks implemented into CSS to study the channels behaviour. They are discussed below. Each check calculates a parameter, a Test Statistic, to test a certain property of a channel. In the Charge & Time check the Limits are calculated based on each individual channel's distributions. The High Occupancy, the Low Occupancy, the ECA and the PCA checks use the distributions of the corresponding Test Statistic across all channels.

CSS extracts parameters used to calculate Test Statistics, calculates the Test Statistics and builds the distributions. The exact method of estimation of the Limits will be developed once stable data from the detector will be available, as it requires studying the behaviour of channels over many runs.

In further studies described in [140], the high occupancy and the low occupancy checks are developed using water data. These two checks are being applied during the water phase and are planned to be applied in the scintillator phase as well [141].

3.2.1 Channel Hardware Status (CHS) Check

The information on whether channels were online or offline during a run is obtained through their Channel Hardware Status [142]. There are various reasons why a channel can be offline.

A channel should be connected to the data acquisition system to be able to send and receive signals. We will list several factors influencing this status, more details can be found in [143].

- **Electronics.** All electronic components such as PMTIC, DB and MB should be active for a PMT.
- **High voltage supply.** It should be provided for each crate and PMTIC.
- **Resistors.** Specific resistors can be removed to prevent damage that results in the offline status.

The CSS retrieves this information for every run. Channels that are offline in a Standard run are tagged by the ChanSWStatusProc processor and continue to be treated as such until a new Standard Run with updated Channel Hardware status is issued. Hence, in a studied run all offline channels retrieved from the CHS and all channels stated as offline in the Standard Run are combined. Thus, if in the studied run additional offline channels appear, they are simply added by ChanSWStatusCalib, see Figure 3.1.

In the opposite case, if there are fewer offline channels in the studied run than in the Standard Run, ChanSWStatusCalib keeps the offline channels from the Standard Run, see Figure 3.2. A channel can become online, if it has been repaired. In this case a new Standard Run has to confirm a new status of the channel, and until then it is still considered to be offline.

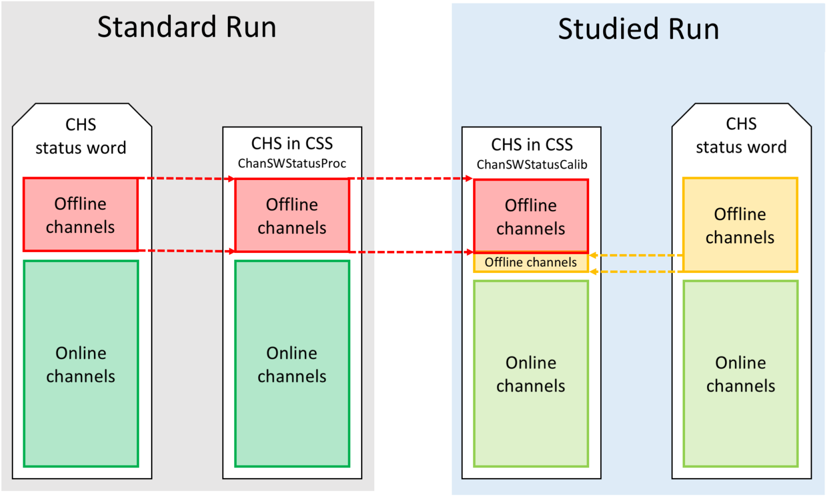

Figure 3.1: Scenario of assigning CHS status of a channel. Offline channels, indicated by the ChanSWStatusCalib processor, is a combination of offline channels in a Standard Run and in a studied run due to CSS.

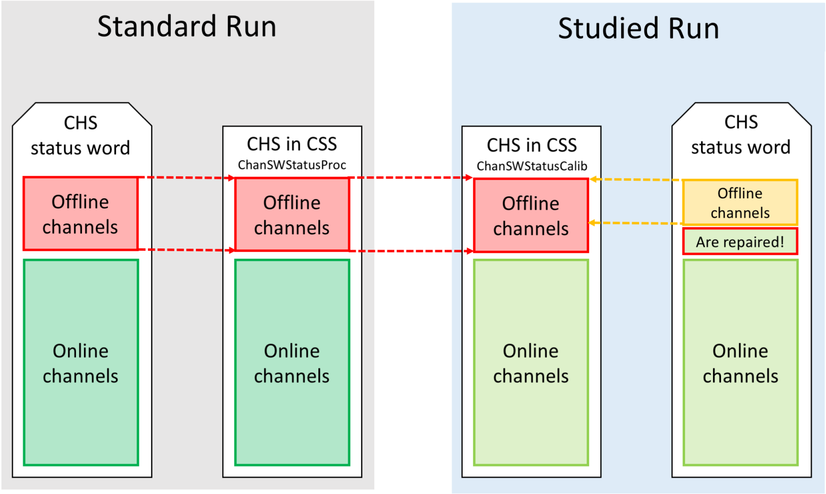

Figure 3.2: Scenario of assigning CHS status of a channel. The ChanSWStatusCalib passes the indication of offline channels from a Standard run to a studied run, even if some channels have been repaired.

The CHS check provides the lists of offline channels within the CSS. Those channels are ignored by both processors in estimating the Test Statistics. This is due to the fact that an offline channel might still produce signals, which could lead to wrong results in both calculations of check values and the application of them.

Moreover, an offline channel cannot pass any check, as it is considered broken. Therefore, all offline channels are tagged by ChanSWStatusCalib as failed in all checks by default.

3.2.2 ECA and PCA checks

The ECA and the PCA checks are included in CSS mainly to monitor that calibrations have been applied correctly. It is important, as only the calibrated hits are included in the analysis.

CSS uses the information about calibrated hits, provided by the ECA processor to study channels. Whilst performing the calibration the ECA holds several checks, and for every calibrated hit it saves a bit mask with statuses, indicating whether the hit has passed each check [106]. The CSS processors consider only the status of the overall performance of a hit in the ECA.

For each channel in a run, CSS counts the ratio between the number of failed ECA hits and the total number of hits. If a channel has a significant number of ECA failed hits, CSS tags it since such a behaviour might indicate either inaccurate calibration algorithms or a problem with the channel itself. If a significant number of channels regularly fails the check it will suggest that the ECA calibration algorithms require revision.

The PCA check in CSS proceeds identically to the ECA check, testing on the PCA status word. It also considers only the status of the overall PCA performance of a hit. A channel that has a significant number of PCA failed hits might indicate that the algorithms of charge (QHS, QHL, QLX) and time (TAC) calibrations should be adjusted or that there are some issues with this channel.

The numbers of ECA and PCA failed hits can only be obtained from data. Hence, the values that will be applied in these checks will be also estimated then.

3.2.3 High Occupancy Check

A channel that frequently fires when there are no photons due to a physics event is called “noisy”. Such a channel is dangerous as it might provoke issuing a GT by contributing with a faulty signal, which consequently leads to data loss. That is when channels are false triggered due to noise, they can't be triggered by any real event during the following 400 ns. The purpose of the High Occupancy check is to identify noisy channels. Such a study can't be made by analysing the data obtained from regular triggers, as the true photon distribution is not known. Instead, we use the data collected from the forced firing channels controlled by the DAQ which issues Pulse Global Trigger or PGT. In this mode, except for random coincidences with true PMT fires, we obtain hits with the absence of real physics events. Those hits are called the PGT hits. The High Occupancy check is performed over PGT hits, as their number is a measure of the noise. For this check the test statistic of a channel i is its PGT Occupancy:

$$O_{\text{high}}(i) = \frac{N_{\text{PGT\_hits}}(i)}{N_{\text{total}}}, \tag{3.2.1}$$

where $N_{\text{PGT\_hits}}(i)$ is the number of PGT hits of the i^{th} channel and N_{total} is a total number of all PGT hits in a run. The CSS defines a Limit as the maximum allowed PGT occupancy, when a channel is still considered as good. This value is obtained with respect to all channels in the Standard Run, therefore, $O_{\text{high}}(i)$ is histogrammed for all i. An example distribution can be observed in Figure 3.3.

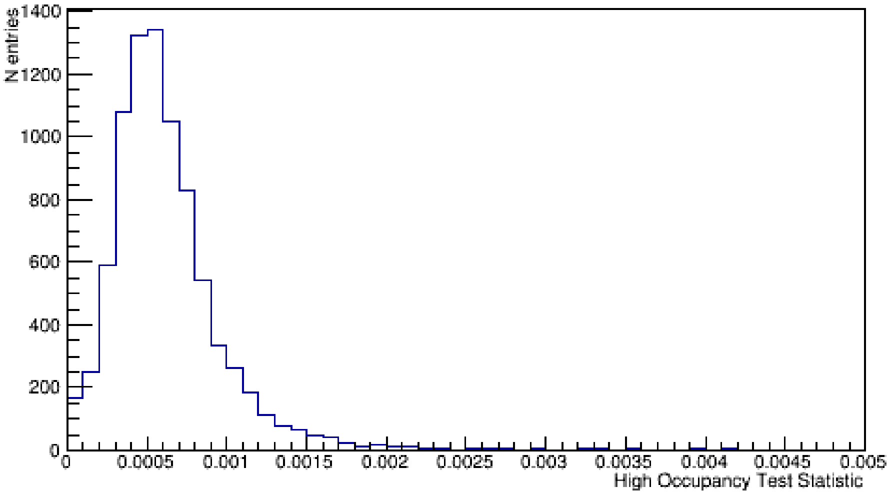

Figure 3.3: The distribution of the High Occupancy Test Statistic obtained from run 8500 while running the detector partially filled with water.

We will determine the method of estimating the limit $L^{high\_occ}_{\text{standard}}$ after studying the distributions built from many stable runs as we need to allow for tails but yet identify outliers.

To apply the check, the CSS evaluates $O_{\text{high}}(i)$ for every channel in a studied run and compares with the limit $L^{high\_occ}_{\text{standard}}$. A channel is considered noisy if its PGT occupancy is higher than the Limit:

$$O_{\text{high}}(i) > L^{high\_occ}_{\text{standard}}, \tag{3.2.2}$$

In this case it will be tagged as failed in the High Occupancy Check.

3.2.4 Low Occupancy Check

The Low Occupancy check aims to identify “slow” channels. Such a channel in contrary to a noisy channel collects abnormally few or no signals at all which might prevent issuing a GT and hence leads to data loss as well. A channel can be slow if its discriminator threshold is too high and only larger pulses are able to cross it. Any mechanical failure of the channel which can also lead to similar behaviour will be identified by CHS.

The check studies how well a channel behaves in a regular run. For this check, the run is divided into time blocks of 30 minutes[1]. For every time interval t, the Test Statistic of channel i is its occupancy that is calculated as:

$$O_{\text{low}}(i,t) = \frac{N_{\text{hits}}(i,t)}{N_{\text{total}}(t)}, \tag{3.2.3}$$

where $N_{\text{hits}}(i,t)$ is the number of hits on the i^{th} channel in time block t, and $N_{\text{total}}(t)$ is the total number of hits in the time block. In order to define a Limit, the $O_{\text{low}}(i,t)$ in the Standard Run for all i and t are histogrammed. An example distribution can be observed in Figure 3.4.

---

[1] Such a division was suggested by SNO [132] where the runs lasted for several hours. Depending on the average run length in SNO+ its division might be irrelevant.

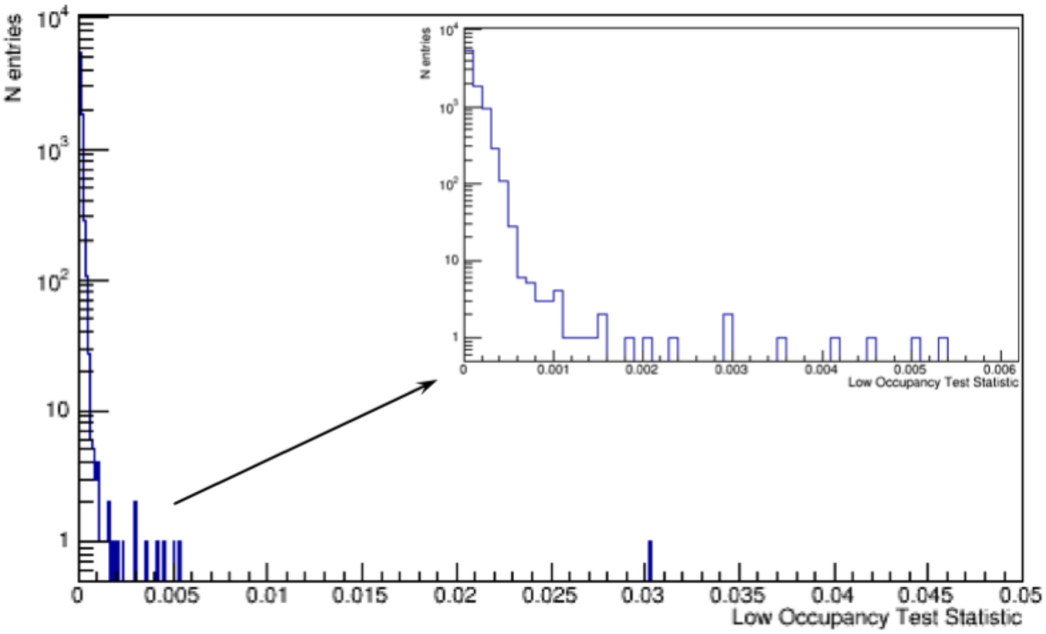

Figure 3.4: The distribution of the Low Occupancy Test Statistic obtained from run 8500 while running the detector partially filled with water. Inserted histogram is zoom in on x-axis.

An exact parameter required to estimate a Limit will be determined by studying a large data set. The Low Occupancy Limit is the minimum number of recorded hits for a channel in a run before the channel will be tagged as slow.

To apply this check, CSS evaluates $O_{\text{low}}(i,t)$ for each channel in a studied run in the same way. If $O_{\text{low}}(i,t)$ in any time block t of a studied channel is smaller than the Limit $L^{low\_occ}_{\text{standard}}$, this channel does not pass the Low Occupancy Check and will be tagged.

3.2.5 Charge & Time Checks

The purpose of implementing the Charge & Time checks is to confirm that channels were correctly PCA calibrated. Every hit has the following values:

- Obtained charge over short integration window of 60ns (QHS)
- Obtained charge over long integration window i.e. the full time window (QHL)
- Obtained charge over full time window, similar to QHL, but with the gain of a channel 12 times smaller (QLX)

- Time of hit (TAC)

Each value represents a unique characteristic of a PMT hit and is used as the Test Statistic of each corresponding check: QHL check, QHS check, QLX check and TAC check. All Charge & Time checks are performed in an identical way, therefore the described method should be generalized for all these checks. In order to calculate limits, Test Statistics of every PMT hit in a Standard Run are histogrammed. Example distributions of Test Statistics can be seen in Figure 3.5.

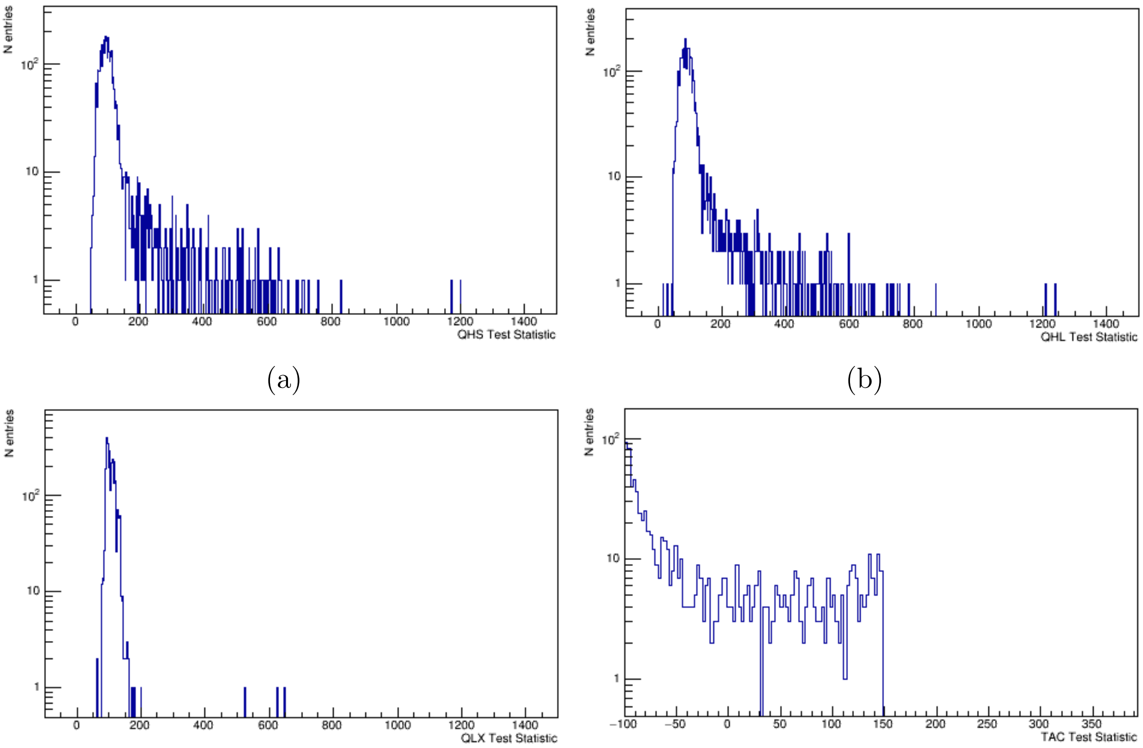

(a) (b)

(c) (d)

Figure 3.5: The Charge & Time distributions of 1st channel in run 8500.
Figure (a) QHS Test Statistic distribution
Figure (b) QHL Test Statistic distribution
Figure (c) QLX Test Statistic distribution
Figure (d) TAC Test Statistic distribution

Although the Test Statistic varies on a hit by hit basis, the distribution over a run should be similar. Hence, for each channel i a limit will be a pair of constraining values: a lower boundary $L\_low^{check}_{\text{standard}}(i)$ and an upper boundary $L\_high^{check}_{\text{standard}}(i)$.

When CSS applies the check to a channel i, it applies the corresponding limits $(L\_low^{check}_{\text{standard}}(i), L\_high^{check}_{\text{standard}}(i))$ to all hits collected by this channels. It counts the number of hits that lay outside the limit boundaries, and if there are more than the pre-defined number, the channel i will fail the check. Like the PCA check this might indicate miscalibration.

In order to choose suitable Limits or parameters to characterise the distributions, we need to study Charge and Time distributions obtained during many different runs. By monitoring and analysing large sets of stable data, we will be able to identify the properties of outliers.

3.3 CSS Structure

CSS is divided into two parts, and each is realized by a processor. Both processors use similar methods to evaluate the limits and to later apply them. A flow diagram of the CSS processors can be found in Figure 3.6. CSS works on a run by run basis, i.e. a run is an input for each Processor. Before running CSS, all channels have to be calibrated, i.e. the ECA and PCA calibrations have to be applied, since all checks require information posterior to the calibrations.

The first processor, ChanSWStatusProc, uses a Standard Run as an input. A Standard Run is defined by a user. It loads the information stored in the ECA, the PCA, and the CHS bitmasks, which are the results of the checks performed by the corresponding processors. It retrieves necessary parameters for other checks, calculates a Test Statistic for each check for each channel and defines the checks. ChanSWStatusProc calculates the Limits for each channel that has been hit at least once and stores results as a table. If a channel hasn't been hit the processor assigns the value 99999 to it. ChanSWStatusProc also stores the histograms that were used to estimate the limits.

In the second part of CSS the ChanSWStatusCalib processor tests each channel against the evaluated limits. It is applied to every regular SNO+ run. ChanSWStatusCalib uses a studied run and the limits as an input. Similarly to ChanSWStatusProc, it loads the ECA, the PCA, and the CHS status words and calculates Test Statistics. For each check, the processor assigns to every channel a status, whether it passes or fails a check. As a default, a channel is considered to pass a check, hence it passes the check if no limit was provided in the Standard Run. At the end of a run, a bit word of statuses is saved as a result of the ChanSWStatusCalib performance. The processor does not remove channels that fail checks from the data.

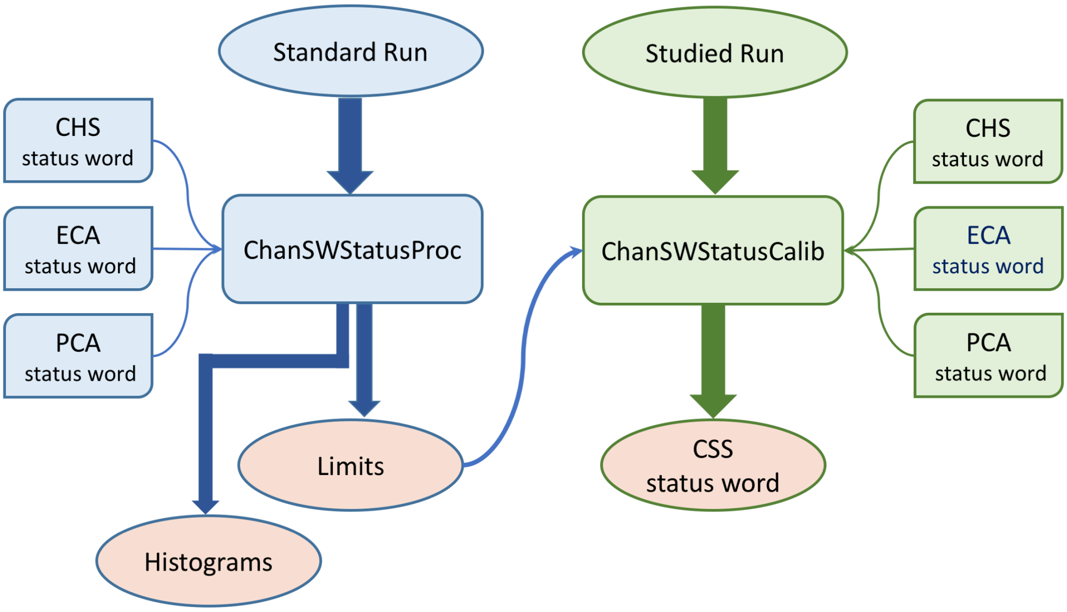

Figure 3.6: The flow diagram of the CSS processors. The ChanSWStatusProc processor identifies and outputs the limits of the checks. It also outputs the histograms used for the identification of the limits. The processor also uses the information obtained by other processors: CHS, ECA, and PCA. The ChanSWStatusCalib processor tests the channels using the limits provided by ChanSWStatusProc and the information obtained by CHS, ECA, and PCA. As a result, it outputs a bit mask with the results of the tests.

The CSS has a modular structure, which allows us to easily update the checks and add new ones.

We tested CSS on the data from December 2014 runs and confirmed that both processors ran as expected. This data was obtained when the AV was empty and there was less than 5 feet of water in the cavity. At this stage, the detector was not in a uniform, stable state and tuning of the channel thresholds and settings had not been performed. Consequently, since a high number of outliers was expected, validation of the checks and tuning cuts were not achievable.

The ChanSWStatusCalib processor was successfully implemented into the data flow process and ran off-line. It loaded the pre-defined test-limits and applied them to the runs.

Summary and Discussion

This chapter has described the implemented framework for CSS. The core functionality of the processors was tested on available runs, and performed as expected, but due to limited statistics and non-uniform detector could not be tuned for useful results.

Therefore, the next step for the CSS is to test both ChanSWStatusProc and ChanSWStatusCalib on the stable data and to confirm the methods of defining the limits and to define the method of how to apply them. Furthermore, the CSS can be applied to a set of runs which will provide the information about a channel's behaviour over the time.

Chapter 4

Backgrounds in the tellurium loaded scintillator

In SNO+ anything that triggers the detector resulting in an event that could be mistaken as signal is classed as a background and as the signal is different in each phase of the experiment, we must consider different background sources in each phase.

The focusing study of this thesis is performed in the Tellurium loaded scintillator and the signal is neutrinoless double beta decay. Its decay energy range is called the Region of Interest or the ROI. The reconstructed energy spectra of ^{130}Te $2\nu2\beta$ and ^{130}Te $0\nu2\beta$ can be seen in Figure 4.1.

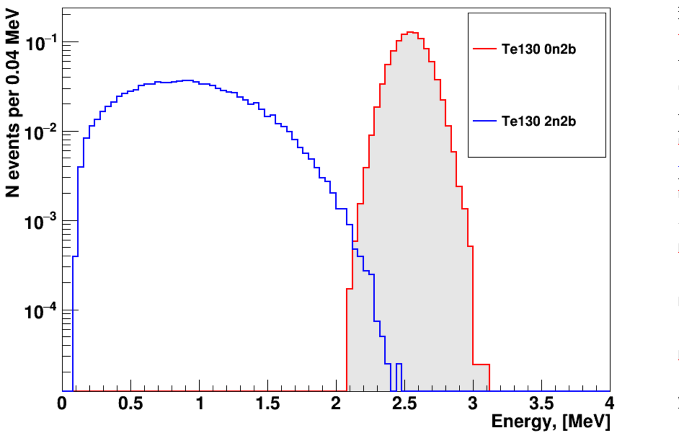

Figure 4.1: The normalised reconstructed energy spectra of ^{130}Te $2\nu2\beta$ and ^{130}Te $0\nu2\beta$.

Due to its steep slope below the $Q_{2\beta}$-value of 2.528 MeV the $2\nu2\beta$ energy spectrum overlaps with the signal and introduces significant number of background events. Therefore in order to considerably reduce unavoidable background from $2\nu2\beta$ decays, while retaining most of $0\nu2\beta$ decays the ROI is shifted from being symmetric around the $Q_{2\beta}$-value [77]. The ROI is defined in terms of standard deviation σ of the reconstructed energy spectrum of ^{130}Te $0\nu2\beta$:

$$[-0.5\sigma, +1.5\sigma] = [2.485, 2.733] \text{ MeV} . \tag{4.0.1}$$

An actual value of σ depends on the light yield of the scintillator cocktail. Since the scintillator cocktail is still under development the final energy ROI will be characterised and optimised once we have in-situ Te-loaded data. Further optimisation of the sigma range will also be performed. Such energy constraints made by introducing the ROI region significantly suppresses the number of background events.

Towards preparation to study $0\nu2\beta$-decay in Tellurium-130, SNO+ aims to understand backgrounds and to obtain and verify their levels. Various backgrounds occur in the detector depending on the origin of processes that caused them. Internal backgrounds are caused by impurities inside the scintillator volume, which includes the inner surface of the AV. External backgrounds are caused by impurities of the detector components surrounding the AV including its outer surface. Cosmogenically induced backgrounds are caused by events originating far away from the detector which create isotopes inside the scintillator.

In order to estimate the target levels of backgrounds we use the experience of the Borexino experiment [150] from working with the LAB and the CUORE experiment [145] which used the isotope of ^{130}Te as well, and interpolate it to the scale of the SNO+ detector. The external backgrounds[1] are assumed to still be at the levels previously measured in the SNO experiment for this analysis but will be measured during the water-phase. The ex-situ assays are used to understand and quantify the process of leaching of the AV. When data from the pure scintillator phase is available the actual levels of backgrounds will be characterised by fitting

---

[1] Excluding the hold-up ropes which were introduced only in the SNO+ experiment

the energy spectrum. The levels during the ^{130}Te-loaded scintillator phase will be characterised by fitting the energy spectrum outside the offset ROI of $0\nu2\beta$.

The major background in the ROI is expected to be irreducible solar ^{8}B, see Section 4.1. SNO+ aims to estimate the impact of other backgrounds to the ROI and to minimise it to reach the best physics capability. The general goal is to develop rejection techniques and to apply them in combination that will be able to reduce the total number of all backgrounds in the ROI to a negligible number compared to the level of solar ^{8}B in the ROI. Thus, the dominant background to ^{130}Te $0\nu2\beta$ will remain ^{8}B. In the analysis presented in Chapter 6, the ^{8}B number of counts in the ROI is 10.60 (see Table 6.1).

In future analyses, all background rejection methods will be applied and optimized in combination. In order to allow the development of rejection techniques for each class of background in parallel, the SNO+ collaboration has set a target that each analysis component must not reject greater than 1% of $0\nu2\beta$ signal events (this is called the signal sacrifice) [134, 135, 161]. The exceptions to this restriction are the energy range cuts and the fiducial volume cut which are the dominant effects on signal efficiency. The list of isotopes with non-negligible contributions to the ROI with the number of counts is presented in Appendix B.0.5. Further fine tuning of all the rejection cuts will be performed once we characterise the actual background levels.

There are various strategies used in SNO+ to reduce the background levels. The external backgrounds are strongly suppressed by water shielding between the cavity walls and the PSUP and between PSUP and the AV. Due to attenuation only highly energetic gammas are able to penetrate inside the scintillator volume. The purification of Tellurium and LAB will happen prior to filling the detector with the Tellurium loaded scintillator, reducing the amount of radioactive impurities. In addition, various software based techniques are used to reject particular event types and topologies. Using timing, position and energy information, designed classifications can be applied to identify, tag and reject background events.

In this chapter we discuss the backgrounds in the ^{130}Te-loaded scintillator phase, their target levels and rejection techniques developed at the time of writing of this thesis.

4.1 Solar Background

The SNO experiment studied the neutrino flux from the β-decay of ^{8}B produced in the Sun. Solar neutrinos have now become a direct background for studying $0\nu2\beta$-decay in tellurium in the SNO+ experiment. The ^{8}B-neutrinos interact with the scintillator via elastic scattering off electrons. The scintillation events caused by the scattered electrons make an irreducible flat continuum background. The expected number of events in the energy region between 0 – 15 MeV per year is 1264 and between 0 – 5 MeV is 847 [136]. According to the analytical estimations the number of ^{8}B events in the ROI in one year is 45.84 (see Section 5.1.3). The analytical energy spectra of ^{8}B can be observed in Figure 5.1 and the SNO+ RAT 5.0.3 Monte-Carlo simulations in Figure 6.1.

4.2 Cosmogenically Induced Backgrounds

These backgrounds are radioactive isotopes produced inside the scintillator from interactions between energetic cosmic neutrons, protons and muons with stable elements. The majority of those interactions occur while the scintillator components are on the surface. The resultant isotopes decay away and the remaining impurities are extracted in the purification plant [146].

Due to the depth of the underground facility, the muon rate is reduced to the average of three muons per hour through the SNO+ detector. An entering muon first passes through the water shielding and thus emits the Cherenkov light which is captured by outward-looking (OWL) PMTs. Later it crosses the AV and causes scintillation light detected by inward-looking normal PMTs. In order to start running a muon event reconstruction, we have to determine conditions which define a muon candidate. For the Tellurium phase, the conditions will likely include the predefined thresholds on the number of hits of OWL PMTs and normal PMTs. At the time of writing this thesis, such conditions haven't been developed yet. However, for the water phase, the threshold is set on 5 OWL PMT hits and 100 normal PMT hits [147].

When passing through the scintillator the muon ionises it which in response emits light and hence becomes background. Using the obtained PMT hit pattern the method designed in [149] reconstructs the muon event which will be then rejected. This is a developing study and its efficiency will be revised during the Tellurium phase. High energetic muons can also produce backgrounds, muon-induced backgrounds, due to spallation of elements in the scintillator. We list only the resultant isotopes with half-lives $>$ 1 second [149]: ^{16}N ($T_{1/2}$ = 7.13 seconds), ^{10}C ($T_{1/2}$ = 19.3 seconds), ^{11}Be ($T_{1/2}$ = 13.8 seconds) and ^{11}C ($T_{1/2}$ = 20 minutes). By vetoing the detector for a few minutes[2] after each muon event the created isotopes with short half-lives will decay away. The remaining ^{11}C isotope has an end point energy of 0.96 MeV which is lower than the ROI of ^{130} Te$0\nu2\beta$. Therefore, this background is concerning only if it piles up with other decays.

Carbon-14 (^{14}C) is a product of cosmogenic activation of ^{14}N, which occurred during the production of the LAB [149]. SNO+ as well as the Borexino experiment obtained the liquid scintillator from old oil fields, as oil was used as a raw product for LAB. The isotope has a half-life of 5730 years and β-decays to ^{14}N with a Q-value of 0.156 MeV. Based on the measurement performed in the Borexino experiment, the expected number of ^{14}C decays in SNO+ in one year is 6.9×10^{9}. ^{14}C acts as a background to low energy pp neutrinos and can contribute to the ROI in case it piles up with another event.

Moreover, while being on the surface, due to cosmogenic activation the following isotopes are produced by spallation reactions on tellurium [149]: ^{124}Sb ($T_{1/2}$ = 60.2 days, Q-value = 2.90 MeV), ^{22}Na ($T_{1/2}$ = 950.6 days, Q-value = 2.84 MeV), ^{60}Co ($T_{1/2}$ = 1925 days, Q-value = 2.82 MeV) and ^{88}Y ($T_{1/2}$ = 106.6 days, Q-value = 3.62 MeV). In order to prevent building-up of those backgrounds tellurium was delivered to the underground storage inside SNOLAB and will be kept there for a cool-down period of at least a year. The specially designed purification techniques will be

---

[2] The exact value will be determined in the Tellurium phase.

applied underground before mixing it into the scintillator cocktail.

4.3 Instrumental backgrounds

Instrumental backgrounds are produced by the electronic system and the PMTs by processes other than radioactive decays. These phenomena were discovered in SNO when the detector was first turned on. The number of PMT hits was two orders of magnitude greater than predictions. Since the majority of the same PMTs and parts of the electronics will operate in SNO+, instrumental backgrounds are expected to occur. Some of them are discussed below.

The most common type of the instrumental backgrounds is called a “flasher” event. When a PMT operates under high-voltage it can break down due to static discharge in the dynode and emit light. Such an event has 3 distinguishing characteristics. Firstly, a flashing PMT has a high charge. Secondly, since the charge of this PMT is high, channels connected to the same electronics crate will trigger due to crosstalk. Finally, the emitted photons cross the detector and trigger PMTs located on the opposite side, resulting in a certain PMT hit pattern. Those PMT hits will be later in time.

Another type of instrumental background is an electronic “pick-up”. This is the situation when an external action affects the electronics so that it forces channels to trigger. This can happen due to human activities near the electronics and the properties of the environment, such as temperature and humidity. In this case triggered channels will be located in different crates.

The instrumental backgrounds are planned to be removed in each phase of the experiment. This process is called “data cleaning”. It is still under development as this study requires data. Like other background rejections, data cleaning aims not to exceed 1% of the signal sacrifice. The rejection relies on distinctive properties of such events. For example, some instrumental backgrounds occur in groups, others like flashers can be identified by looking at PMT charges and event geometries. More information on data cleaning can be found in [144].

4.4 External backgrounds

Radioactive decays of isotopes originating in the surrounding materials that either cause events inside or mis-reconstruct inside the AV volume are called external backgrounds. They arise from radioactivity in the acrylic, water shielding between the AV and PSUP, the PMTs, and the ropes. Charged particles produced during radioactive decays are attenuated in the water before reaching the scintillator volume unlike gammas. Therefore, external backgrounds are the isotopes that emit high energy gammas. These are ^{40}K, ^{214}Bi in the Uranium chain and ^{208}Tl in the Thorium chain. The SNO+ target levels of the external backgrounds [144] are presented in Table 4.1.

Only a small frction of the decays in Table 4.1 result in energy deposits inside the scintillator, and, due to their nature, the number of events from external backgrounds decreases towards the center of the AV. Therefore, for 2β analysis, we constrain the effective AV radius to 3.5m [154], hence the new effective volume is 19.8% of the original volume of the AV.

Table 4.1: Target levels of the external backgrounds in one year.

Source	Target number of decays per year
Acrylic Vessel:	
^{214}Bi	4.15×10^{4}
^{208}Tl	2.48×10^{4}
Acrylic Vessel External Dust:	
^{214}Bi	7.75×10^{5}
^{208}Tl	4.6×10^{5}
Acrylic Vessel Internal Dust:	
^{214}Bi	4.15×10^{4}
^{208}Tl	2.48×10^{4}
Water Shielding:	
^{214}Bi	1.26×10^{8}
^{208}Tl	3.73×10^{6}
Hold-up Ropes:	
^{214}Bi	8.34×10^{5}
^{208}Tl	4.78×10^{5}
^{40}K	3.9×10^{7}
Hold-down Ropes:	
^{214}Bi	4.06×10^{6}
^{208}Tl	2.32×10^{6}
^{40}K	1.89×10^{8}
PMTs:	
^{214}Bi	3.7×10^{11}
^{208}Tl	4.4×10^{10}

4.5 Internal backgrounds

Internal backgrounds are radioactive decays of isotopes originating inside the scintillator volume. They are introduced by the impurities of the scintillator cocktail and the inner surface of the AV. The items deployed into the AV, such as calibration sources, can introduce additional contamination present on the containers.

4.5.1 Pileup backgrounds

When two or more events occur in the same time window, i.e. pile up, they are reconstructed in SNO+ as a single event. This new event is called a "pileup" event; its energy is equivalent to the sum of the individual energies. Some of the backgrounds which will be discussed in this section have low energy by themselves and thus do not contribute to the ROI directly. However, such decays can pile up with other events, and still cause an increase of background contribution to the ROI. Pileup backgrounds are discussed in detail in Chapter 5.

4.5.2 Tellurium 130 (^{130}Te)

SNO+ uses the isotope of tellurium 130 (^{130}Te) as a source of events of study – neutrinoless double beta decay. It has a half-life of 7.0×10^{20} years [53] and Q-value of 2527.518 ± 0.013 keV [53]. The natural abundance of ^{130}Te is 34.08%, which allows loading of the isotope without enrichment. At the time of writing in the first stage of the $0\nu2\beta$ phase the tellurium loading will be 0.3%. The estimated level in one year is 36,603,229 decays. In the future phases SNO+ considers increasing the ^{130}Te-loading which will also increase background levels.

^{130}Te is a source of $2\nu2\beta$ direct background. Inside the ROI of [2.485, 2.733] MeV the analytically estimated number of decays is 6.665, see Section 5.1.3. The analytical energy spectrum of ^{130}Te $2\nu2\beta$ can be observed in Figure 5.1 and the SNO+ RAT 5.0.3 Monte-Carlo simulations in Figure 6.1. Decays of ^{130}Te can also pile up with other decays which makes it possible for isotopes with lower energies to appear inside the ROI. Such pileup backgrounds are discussed in Chapter 5.

Tellurium is also a source of other naturally occurring isotopes from ^{238}U (see Section 4.5.3) and ^{232}Th chains (see Section 4.5.4), and ^{210}Po is which present due to chemical affinity between polonium and tellurium (see Section 4.5.6).

4.5.3 ^{238}U chain

Uranium-238 (^{238}U) is a naturally occurring isotope with a half-life of 4.47×10^9 years, which is present not only in the detector components, but also in the detector media. Through the purification we aim to reduce the level of impurity in the LAB-PPO scintillator to the one achieved by the Borexino experiment [150]. In the first year after 9 months of the water phase the target level is less than $1.6{\times}10^{-17}$ g/g or 4900 decays [149].

After introducing tellurium with a surfactant into the scintillator cocktail the new target level in the first year after 9 months of water phase and 6 months of pure scintillator phase is $2.5{\times}10^{-15}$ g/g or 755,258 decays/year [149]. The increase happens because ^{238}U isotopes are present in the tellurium acid and surfactant as well, but purification in this case is challenging.

The ^{238}U decay scheme can be observed in Figure 4.2. Secular equilibrium is assumed for all the daughter isotopes untill ^{210}Pb. And therefore, their levels (excluding the listed one) can be found by multiplication of the ^{238}U level by a corresponding branching ratio. ^{210}Pb has a half-life of 22.26 year, which is long enough to break the secular equilibrium with the top part of the chain. Additionally there are expected to be more ^{210}Po isotopes since removing them is challenging due to their ionic form[3]. These two breaks of the secular equilibrium were observed in the Borexino experiment. As a result the expected levels in the first year after 9 months of water phase are [149]: 790,274 decays of ^{210}Pb, 790,274 decays of ^{210}Bi and 1.66×10^7 decays of ^{210}Po. The total levels of ^{210}Pb, ^{210}Bi and ^{210}Po isotopes in the scintillator are discussed in Section 4.5.6 as there are additional sources of these backgrounds.

From its decay scheme in Figure 4.2 it can be observed that upon decaying, the daughter isotopes emit alpha, beta and gamma particles with different energies. The majority of them are not troublesome for studying ^{130}Te $0\nu2\beta$ due to their lower end-point energies. They only cause danger indirectly in case their decays pileup. However, ^{214}Bi is a direct background as it contributes to the ROI.

---

[3] There is also the possibility of the increase of ^{210}Po due to leaching of the pipes during filling in the scintillator in Borexino.

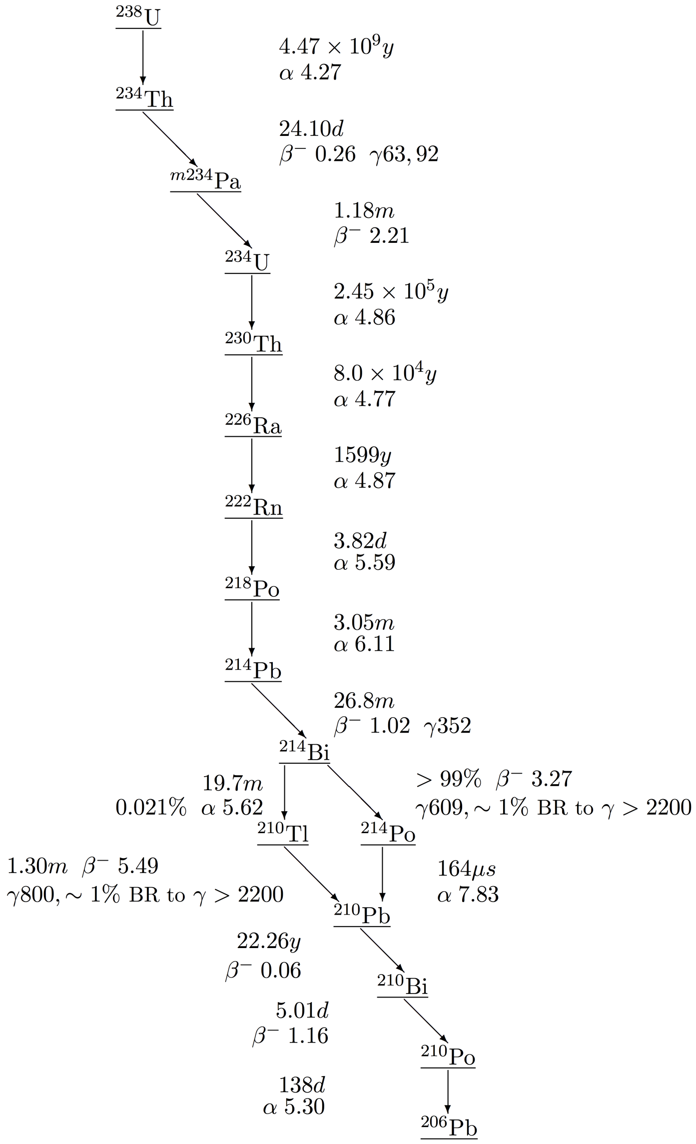

Figure 4.2: The decay chain of ^{238}U with half-lives, Q-values and decay branches. End-point energies of alpha and beta decays are in MeV, gamma rays in keV. This figure was taken from [169].

Bismuth 214 (^{214}Bi)

^{214}Bi has a half-life of 19.9 minutes and decays via two branches, see Figure 4.3. In 99.979% of cases ^{214}Bi β-decays to ^{214}Po. Shortly after the ^{214}Po, with a half life of 164.3 μs, decays emitting a 7.7 MeV α-particle. In order to reject ^{214}Bi from the ROI we consider the decays together and refer to them as ^{214}Bi-Po.

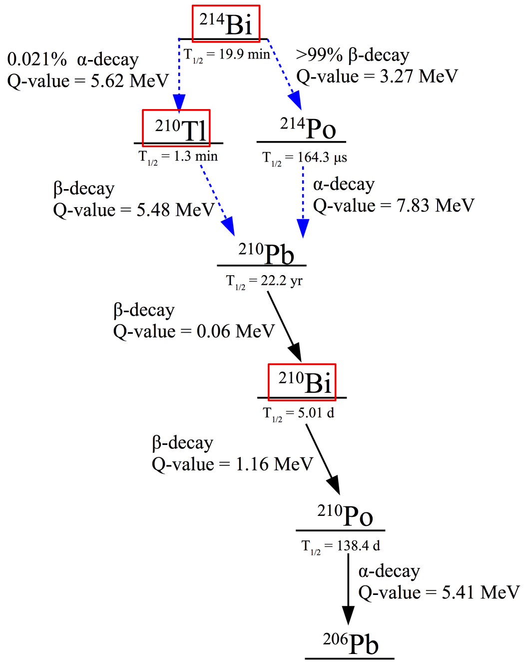

Figure 4.3: The decay chain of ^{214}Bi with Q-values, half-lives and decay modes. Isotopes of ^{214}Bi and ^{201}Tl are the direct backgrounds for $0\nu2\beta$. The decays involved in $\alpha-\beta$ and $\beta-\alpha$ delayed coincidences have blue arrows. This figure was taken from [77].

The possibility of having both the beta- and the alpha- decays in one trigger window is 0.17% [161]. We refer to such an event as an "in-window" ^{214}Bi-Po. Reconstructed as a single event, its energy may be inside the ROI region. In order to reject these events, we use the technique based on the differences in timing profiles of in-window ^{214}Bi-Po events and $0\nu2\beta$ events [134] optimising it to the target signal sacrifice of 1%. As a result, the background level is reduced by the factor of 49.2, and 0.29 ^{214}Bi-Po events per year are expected inside the ROI within the FV.

When ^{214}Bi-Po events happen in different trigger windows they are reconstructed as separate independent events. We will, on contrary, take the benefit of the relatively short time between the decays and will use ^{214}Po as a tag to determine this delayed coincidence.

Firstly, a ^{214}Po candidate is identified using the distribution of the number of PMT hits [161]:

$$51 \leq N_{hits} \leq 100 \tag{4.5.2}$$

Due to short half-life of ^{214}Po, the emitted alpha-particle is expected to be close to the decay position of ^{214}Bi and limited by the position resolution of reconstruction within the fiducial volume. Thus the spatial separation cut to reject random backgrounds is defined as [161]:

$$\left|\overline{R}_{^{214}Bi} - \overline{R}_{^{214}Po}\right| \leq 1.5\,\mathrm{m}, \tag{4.5.3}$$

where $R_{^{214}Bi}$ and $R_{^{214}Po}$ are the reconstructed positions of ^{214}Bi and ^{214}Po isotopes correspondingly. In order to increase the selection efficiency for this tag the time window in which we look for the coincidence is 16 half-lives of ^{214}Po [161]:

$$|T_{^{214}Bi} - T_{^{214}Po}| \leq 16 \cdot T_{1/2}, \tag{4.5.4}$$

where $T_{^{214}Bi}$ and $T_{^{214}Po}$ are the reconstructed decay times of ^{214}Bi and ^{214}Po isotopes correspondingly and $T_{1/2}$ is the half-life of ^{214}Po.

As a result 99.995% of ^{214}Bi events will be tagged, which reduces the contribution of ^{214}Bi to the ROI to less than 1 event per year. Using those parameters the signal sacrifice will be 1.96%[4]. The choice of parameters of position and timing selection defines the efficiency and signal sacrifice, see [161].

In 0.021% of occasions ^{214}Bi alpha-decays to ^{210}Tl. It has a half-life of 1.3 minutes and beta-decays to ^{210}Pb with a Q-value of 5.5 MeV. In order to tag and reject these events from the ROI an alpha-beta delayed coincidence, which is similar to previously described beta-alpha coincidence, can be applied. However, this decay branch is less worrying for the $0\nu2\beta$ studies due to the small branching fraction.

4.5.4 ^{232}Th chain

Thorium-232 (^{232}Th) is a naturally occurring isotope with a half-life of 1.4 × 10^{10} years. Like ^{238}U, it presents in various components of the detector including the media inside the AV and will be reduced by the purification system. The target

---

[4] At the time of writing this thesis this is the best optimisation of the out-window ^{214}Bi-Po tagging.

levels of the isotope in the LAB-PPO scintillator is 6.8×10^{-18} g/g or 700 decays and in tellurium loaded scintillator in the first year after 9 months of water phase and 6 months of pure scintillator phase is 2.8×10^{-16} g/g or 28099 decays [169].

The ^{232}Th decay scheme is shown in Figure 4.4. All daughter isotopes are expected to be in secular equilibrium with initial ^{232}Th. Except for ^{212}Bi and ^{208}Tl the isotopes in the chain have lower energies and can contribute to the ROI only if they pileup.

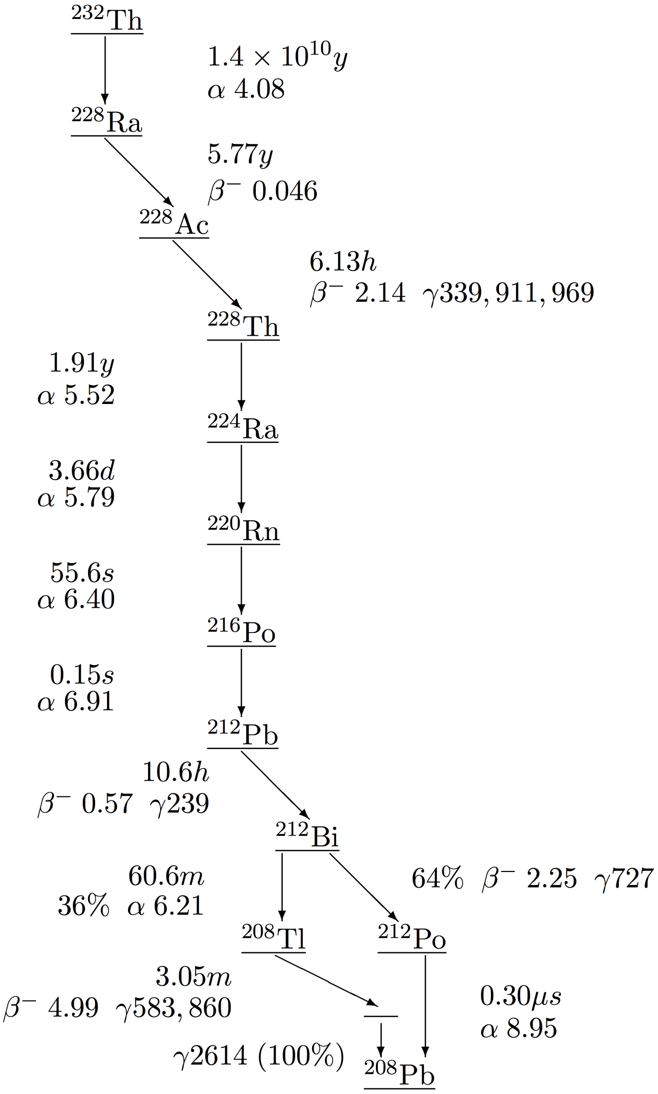

Figure 4.4: The decay chain of ^{232}Th with half-lives, Q-values and decay branches. End-point energies of alpha and beta decays are in MeV, gamma rays in keV. This figure was taken from [77].

Bismuth 212 (^{212}Bi)

^{212}Bi has a half-life of 60.6 minutes and decays via two branches, see Figure 4.5. In 64% of the cases it β-decays to ^{212}Po with a Q-value of 2.25 MeV. Then ^{212}Po, with a half life of 0.299 μs, α-decays with a Q-value of 8.95 MeV. This process is similar to ^{214}Bi-Po events and therefore we apply the same rejection methods [134, 161], i.e. we use a beta-alpha delayed coincidence to reduce this background.

The possibility of both the beta- and the alpha- decays occurring in one trigger window is 0.45%. Using the same technique, we achieve the rejection factor of 38.4 whilst 4.04 in-window ^{212}Bi-Po events per year are left inside the ROI and within the FV[5]. These values were obtained to keep the signal loss to be not more than 1%. Applying the rejection technique designed for out-window ^{214}Bi-Po to out-window ^{212}Bi-Po entirely rejects the latter from the ROI. This happens since both parameters, position and number of hits, satisfy Eq. 4.5.3 and Eq. 4.5.2.

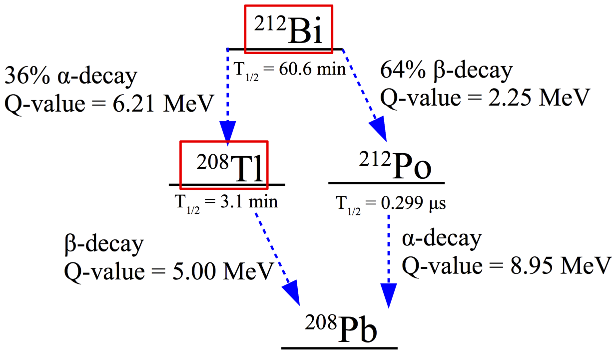

Figure 4.5: The decay chain of ^{212}Bi with Q-values, half-lives and decay modes. The direct backgrounds for $0\nu2\beta$ studies are ^{212}Bi and ^{208}Tl, others can contribute to the ROI only if pileup occurs. The decays involved in $\alpha - \beta$ and $\beta - \alpha$ delayed coincidences have blue arrows. This figure was taken from [77].

In the remaining 36% of the times ^{212}Bi alpha-decays to ^{208}Tl with a Q-value of 6.21 MeV. ^{208}Tl has a half-life of 3.1 minutes and beta-decays to ^{208}Pb with a Q-value of 5.0 MeV. These decays can cause problems for the neutrinoless double

---

[5] At the time of writing this thesis this is the best optimisation of the in-window ^{212}Bi-Po rejection.

beta decay study, as their energies can be inside the ROI region. In order to reject ^{208}Tl background an alpha-beta delayed coincidence tagging can be applied.

4.5.5 Leaching backgrounds

The AV has additional contamination from times it was exposed to mine air, which happened during the construction phase of SNO and during the transition to SNO+. Isotopes of the noble gas ^{222}Rn started to decay away, and due to recoil its daughters got implanted in the top few millimetres of the surface of the AV. All isotopes in the ^{222}Rn chain decay relatively fast till ^{210}Pb, see Figure 4.2. The half-life of ^{210}Pb is 22.26 years and therefore some of its fraction is still present on the inner surface of the AV and decays as follows:

$$^{210}\text{Pb} \xrightarrow{22.3\,\text{years}} {}^{210}\text{Bi} \xrightarrow{5\,\text{days}} {}^{210}\text{Po} \xrightarrow{138\,\text{days}} {}^{206}\text{Pb}.$$

If the lead and its daughters leach back out of the acrylic into the scintillator, this process will form additional “leaching” backgrounds. The majority of ^{210}Bi, ^{210}Po isotopes are expected to be located at the edge of the inner surface of the AV and are called the “AV” backgrounds. They can also be referred to as the external backgrounds. However, over time the diffusion processes moves some of them further into the scintillator. In the current model, those isotopes are considered uniformly distributed inside the scintillator and hence indistinguishable from the ones presented in the Uranium chain due to impurities of the medium. Consequently, the total levels of ^{210}Pb, ^{210}Bi and ^{210}Po inside the scintillator cocktail increase.

The levels of the leaching backgrounds were estimated using experiments performed in the table top experiment at SNOLAB [137–139]. The ^{210}Pb spiked acrylic sample was placed into the vessel filled with tellurium loaded scintillator for 30 days. The isotopes in the leached liquid were measured using a high purity Germanium detector. The experiment was held at a temperature of 12° C, which is the expected temperature of the scintillator in the AV.

The expected levels used in this thesis are presented in Table 4.2. These values will be re-estimated once data from the water phase is obtained and the current leaching model will be tested. The scintillation cocktail also affects the leaching rates.

Table 4.2: Expected levels of the leaching backgrounds in the first year of Te-loaded scintillator phase [149]. The values are presented for the backgrounds on the inner surface of the AV and the backgrounds which are distributed in the scintillator. The assumed leaching rates are at 12° C.

Source	Expected number of decays in the 1^{st} year
Inner surface of the AV	
AV^{210}Pb	2.14×10^{10}
AV^{210}Bi	2.14×10^{10}
AV^{210}Po	2.25×10^{10}
Liquid scintillator	
^{210}Pb	7.93×10^{9}
^{210}Bi	7.93×10^{9}
^{210}Po	7.4×10^{9}

All events located on the inner surface of the AV are modelled in SNO+ RAT in such a way that they originate exactly from its surface. To simplify notations throughout this thesis, those events are labelled with "AV", for example, AV^{210}Po.

4.5.6 Te-associated ^{210}Pb, ^{210}Bi and ^{210}Po backgrounds

There are three sources of ^{210}Po inside the scintillator. Earlier we discussed two of them: naturally occurring ^{238}U and leaching of the AV. The third source was observed in the CUORE experiment [145] – ^{210}Po is introduced with ^{130}Te due to chemical affinity between these two elements. Therefore, we estimate that there will be an additional 2.13×10^{9} events [149].

To summarize, the expected number of ^{210}Po decays in the first year is:

$$1.66 \times 10^7 + 7.4 \times 10^9 + 2.13 \times 10^9 = 9.54 \times 10^9. \tag{4.5.5}$$

There are two sources of ^{210}Pb and ^{210}Bi isotopes inside the scintillator: the

Uranium 238 chain and leaching of the AV. Hence, the total number of decays of each of those backgrounds in the first year is:

$$790274 + 7.93 \times 10^9 = 7.94 \times 10^9. \tag{4.5.6}$$

4.5.7 Internal ^{40}K, ^{39}Ar and ^{85}Kr Backgrounds

These backgrounds are lower energy and therefore predominantly affect solar analysis. ^{40}K is a naturally occurring isotope with a half-life of 1.248×10^9 years. The expected number of events in one year is 7860 [149]. It has two decay branches. In 89.28% of cases it β-decays to stable ^{40}Ca with a Q-value of 1.311 MeV. In the other 10.72% of cases ^{40}K decays to stable ^{40}Ar via electron capture, emitting a 1.460 MeV gamma. ^{40}K acts as a background for pep neutrinos. It can contribute to the $0\nu2\beta$ ROI only in the case that the potassium event piles up with another event.

^{39}Ar is a product of cosmogenic activation of ^{40}Ar. It has a half-life of 269 years and beta-decays to stable ^{39}K with a Q-value of 0.585 MeV. The expected number of events in one year is 79,243. ^{85}Kr is a product of nuclear fission. It is released into the atmosphere due to current nuclear fuel reprocessing, nuclear testing and accidents in nuclear power plants[6]. The isotope has a half-life of 10.739 years and beta-decays to ^{85}Rb, with Q-value of 0.687 MeV. The expected number of events in one year is 79,552 [149]. Since both isotopes get into the LAB through air, their amount can be minimised by reducing the contact time and by degassing the scintillator. Since both ^{39}Ar and ^{85}Kr are low-energy decays, they can become concerning for $0\nu2\beta$ studies only if they pile up with other events.

4.5.8 (α,n) Background

The majority of neutrons inside the scintillator is produced through interactions of energetic α-particles. Their main source is ^{210}Po, as its amount in the scintillator dominates over other α-emitters from the Uranium and Thorium chains. The most

---

[6] Three Mile Island accident(1979), The Chernobyl accident (1986), the Fukushima Daiichi accident (2011).

common reaction is an (α, n)-reaction in which an energetic α-particle is captured by ^{13}C:

$$\alpha + {}^{13}C \rightarrow^{16} O + n. \tag{4.5.7}$$

The produced energetic (up to 7.5 MeV) neutron continuously scatters from protons. The protons then recoil and emit the scintillator light which can be a background to $0\nu2\beta$ studies. Later, in 99% of the cases the neutron is captured by a hydrogen atom, with the emission of a 2.2 MeV gamma. Depending on the definition of the ROI these events can be also dangerous. Otherwise, the neutron is captured on a tellurium isotope with emission of a 0.6 MeV gamma. The expected number of ^{13}C(α,n) processes in the te-loaded scintillator phase in one year is 310 [149].

In order to reject these backgrounds, we use two indicators of this reaction: prompt and delayed signals. The prompt signal is a combination of the scintillation light emitted by the stopping α-particle, by the recoiling protons and the de-excitation gammas. The delayed signal is a 2.2 MeV gamma due to the neutron capture. Using the delayed coincidence technique we tag a gamma particle candidate and then identify a source of prompt light.

As a result, the prompt signal is rejected by a factor of 250 and the delayed signal by a factor of 10, leading to fewer than 0.02 events in the ROI in the FV [149].

4.6 Summary

This chapter has described the SNO+ background model for the ^{130}Te-loaded scintillator phase. We specified the backgrounds with their target levels and the overviews of the rejection techniques. For convenience, the levels of all discussed backgrounds are listed in Appendix A.

SNO+ aims to reduce background levels in the ROI of $0\nu2\beta$ so that their combined level would be negligible in comparison with ^{8}B. To achieve this goal the background rejection techniques will be first developed independently with respect to the agreement of the maximum signal sacrifice of 1%. Then all the designed rejection methods will be applied and optimised together.

The presented information is based on the assumptions considered at the time of writing of this thesis.

Chapter 5

Pileup studies

The majority of backgrounds discussed in Chapter 4 are events that consist of single decays occurring in different trigger windows. Another type of event in SNO+ is a pileup event. It is an event that consists of multiple physics events that happen within the specified time window, which in this study is 450 ns. In a pileup event, a GT is usually issued by PMT hits from a radioactive decay like in a single decay event. But in this case, other PMT hits that occurred in the same time window are added and considered in the reconstruction (see Section 5.2.1, Section 5.2.3). Those hits can be due to radioactive decays and tails or delayed signals from decays that happened in the previous time window. PMT hits caused by instrumental backgrounds in principle could pile up, but luckily they will be rejected by the data cleaning process, see Section 4.3.

In the analysis presented in this thesis, we study pile up only between internal backgrounds. These are various combinations between decays with emission of β-, α- and γ- particles.

As discussed in Chapter 4 there are $N = 34$ radioactive isotopes intrinsic to the scintillator volume. Hence, there are $x_2 = \frac{N!}{(N-2)!} = 1122$ combinations of two decays and $x_3 = \frac{N!}{(N-3)!} = 35,904$ of three decays. Although in reality there will be fewer pileup backgrounds than $x_2 + x_3 = 37,026$ some of them can still occur and cause problem for $0\nu2\beta$ studies. To be more exact, in this chapter, we will shorten the list and will show that the remaining 48 pileup backgrounds contribute 83 events to the ROI. Since the expected number of ^{8}B events in the ROI is 10.60 (see Table 6.1), the pileup backgrounds have to be reduced below that value with less than the 1% signal sacrifice [135].

The difficulty is that a pileup event does not necessarily inherit the properties of the isotopes that form it, in fact, it is more likely that it has different characteristics. Therefore, the techniques designed for the rejection of the single backgrounds described in Chapter 4 should not be expected to perform as effectively. The exceptions are the pileup events in which one of the isotopes dominates over the other and behave like single event backgrounds (will be discussed in detail in Section 5.3.3 and Section 5.3.4). The energy of a pileup event is reconstructed using all PMT hits occurring in the same time window and hence is the summed energy of all contributing physics events. Therefore, the end-point energy of a pileup event is higher than the end-point energy of either of the isotopes that pile up. This consequently leads to an increase of the background contributions to the ROI from piling up low energetic decays. Additionally, due to the energy resolution of 270 keV (see Section 2.7), all events including pileup events with slightly lower or slightly higher energies will be included in the ROI as well.

In this chapter we present a comprehensive study of pileup backgrounds, which combines the analytical approach and consideration of pileup events taking into account the full SNO+ detector response.

Firstly, in Section 5.1 we analytically describe a pileup event and calculate which pileup backgrounds are likely to have events in the ROI given the target levels of the background isotopes from Appendix A in the Tellurium loaded scintillator cocktail.

Secondly, in Section 5.2 we describe pileup events in the SNO+ experiment and identify the characteristics of such events and use their properties to develop techniques to reject as many pileup events from the ROI as possible. In order to do so we perform simulations of the pileup backgrounds, described in Section 5.2.2. As a result of this part we present the effect of application of these techniques.

Looking towards future phases of SNO+ with increased isotope loading, for those pileup events that were not rejected completely, we estimate at what maximal levels of isotopes they cause pileup events that contribute significantly to the ROI. These calculations will be discussed in detail in Section 5.4.

5.1 Analytical approach to pileup backgrounds

There are numerous ways that radioactive decays can pile up. While energies of some of those events are clearly outside the ROI and/or their levels are too low, others might have end point energies inside the ROI. In order to avoid performing the simulations of all possible pileup combinations, we analytically estimate the expected numbers of all such backgrounds and build their analytical spectra. This allows us to shorten the list of pileup backgrounds and concentrate on studying the ones that contribute to the ROI of $[2.485, 2.733]$ MeV.

The analytical estimations benefit in the time of performance and require less computation power. However, they don't take into account the detector response and therefore, in reality some events won't occur or will be mis-reconstructed. Hence, the calculations performed in this chapter provide upper limits on numbers of events.

5.1.1 Pileup event

The number of pileup events within the specified time window can be described analytically by Poisson statistics which changes depending on how many decays cause this pileup. In the case that the pileup is between the decay B_1 and B_2, with N_1 and N_2 the mean numbers of events in a given time window correspondingly, the number of pileup events N_{PU} in the same time window is:

$$N_{PU} = N_1 \cdot \frac{N_2 e^{-N_2}}{1!}. \tag{5.1.1}$$

The number of pileup events between the isotopes B_1, B_2 and B_3, with N_1, N_2 and N_3 number of events in the time window correspondingly, is calculated below for two cases. If $B_2 \neq B_3$, then the number of the pileup events is:

$$N_{PU} = N_1 \cdot \frac{N_2 e^{-N_2}}{1!} \cdot \frac{N_3 e^{-N_3}}{1!}. \tag{5.1.2}$$

If $B_2 = B_3$, the formula in this case is[1]:

$$N_{PU} = N_1 \cdot \frac{N_2^2 e^{-N_2}}{2!}. \tag{5.1.3}$$

It can be observed that Eq. (5.1.1 - 5.1.3) are not symmetrical with respect to N_1, N_2 and N_3. Hence, the order in which the isotopes decay in a pileup does matter as it affects the number of pileup events N_{PU}. Consequently, this also means that numbers of pileup events, formed of decays of the same isotopes but in different orders, will be different.

Additionally, the higher the original decay rates of the isotopes the more likely they are to pileup. Through these formulas one can estimate the level of any pileup background that is needed for the pileup study. An example of this estimation follows in Section 5.1.2.

For the analytical studies, the order of decays changes only the resultant number of pileup events. However, for the analysis performed using the detector simulations and the event reconstruction, we have to consider the physics characteristics of events. In such an analysis, a pileup between decays A and B and between B and A might not be reconstructed identically (this will be discussed in Section 5.2). Therefore, at this stage, we also consider that such events are of different types and don't sum them up.

5.1.2 Level of pileup background

For these calculations we assume that the events are uniformly distributed within the full detector volume and no additional effects, such as detector response, have been taken into account. We have chosen the pileup between ^{130}Te $2\nu2\beta$ and ^{210}Po-decay as an example. As explained in Section 2.6.3 the time window of a pileup event is chosen to be 450 ns which is 50 ns larger than the SNO+ trigger window. The target loading level at the time of this study was conducted is 0.3% by mass loading of Tellurium with natural abundance of 34.08% of ^{130}Te, and therefore the

---

[1] In order to describe the probability that exactly 2 events of type B$_2$ are following the event of type B$_1$ in a given time window we use the Poisson distribution with $k = 2$: $P_2(n) = \frac{n^2 \cdot e^{-n}}{2!}$.

total mass of Tellurium 130 in the scintillator is

$$m_{130Te} = 780\,\mathrm{t} \cdot 0.003 \cdot 0.3408 = 7.97472 \cdot 10^5\,\mathrm{g}. \tag{5.1.4}$$

The total number of ^{130}Te atoms is determined as ratio of this total mass and the mass of a single nucleus, which is equal to the mass number of Tellurium A_{130Te} multiplied by the mass of a single nucleon $m_n = 1.66 \cdot 10^{-24}$ g:

$$N_{130Te} = \frac{m_{130Te}}{A_{130Te} \cdot m_n} = \frac{7.97472 \cdot 10^5\,\mathrm{g}}{130 \cdot 1.66 \cdot 10^{-24}\,\mathrm{g}} = 3.695 \cdot 10^{27}. \tag{5.1.5}$$

Using a ^{130}Te half-life of $T_{1/2} = 7.0 \cdot 10^{20}$ years [78], the rate of $2\nu2\beta$ decays in the full scintillator volume $R_{2\nu2\beta}$ can be obtained as:

$$R_{2\nu2\beta} = \frac{\ln 2 \cdot N_{130Te}}{T_{1/2}} = 0.116\,\mathrm{Hz}. \tag{5.1.6}$$

So, the average number of $2\nu2\beta$-decays during the time window is

$$N_{2\nu2\beta} = R_{2\nu2\beta} \cdot 450\,\mathrm{ns} = 5.22 \cdot 10^{-8}\,\mathrm{events}. \tag{5.1.7}$$

It is estimated that there will be 9.54×10^9 decays of ^{210}Po in the scintillator volume in the first year of the double beta decay phase (see Appendix A). The number of events of ^{210}Po per second, or the rate, is:

$$R_{210Po} = \frac{9.54 \times 10^9}{3600 \cdot 24 \cdot 365} = 302.5\,\mathrm{Hz}. \tag{5.1.8}$$

Hence, the average number of ^{210}Po events during one time window is

$$N_{210Po} = R_{210Po} \cdot 450\,\mathrm{ns} = 1.36 \cdot 10^{-4}\,\mathrm{events}. \tag{5.1.9}$$

Knowing the rates of both isotopes, we can calculate the rate of the pileup between them. The number of pileup events within one time window is

$$N_{PU} = N_{2\nu2\beta} \cdot N_{210Po} \cdot e^{-N_{210Po}} = 7.10 \cdot 10^{-12}\,\mathrm{events}. \tag{5.1.10}$$

The corresponding rate of pileup events is

$$R_{PU} = \frac{N_{PU}}{450\,\mathrm{ns}} = 1.58 \cdot 10^{-5}\,\mathrm{Hz}. \tag{5.1.11}$$

This rate corresponds to 498 pileup events per year.

5.1.3 Snopy prediction

Similar calculations as in Section 5.1.2 can be performed for other pileup backgrounds. For that purpose we have developed a software package, called snopy. It analytically calculates the pileup levels for given levels of the isotopes and plots their analytical energy spectra. The main blocks of snopy software are “core” and “generators”. The “core” block is the set of classes that represent the core methods implemented in the software package, such as the description of a pileup event and the resolution. A pileup event is described in the same way as was stated in the formulae in Section 5.1.1 and in Section 5.1.2. Snopy calculates all pileup combinations caused by the chosen decays and keeps only those with total number of events above 1. The energy resolution has been applied to every event, via a library function for Gaussian Convolution from ROOT [127]. For this study a light yield Y of 200 Nhits/MeV was assumed [77]. This was then converted into energy resolution using Poisson statistics:

$$\sigma = \frac{\sqrt{Y \cdot E}}{Y} \tag{5.1.12}$$

where E is the energy in MeV and σ is the standard deviation of the Gaussian distribution. It is possible to add the signal efficiency factor and the fiducial volume restriction in snopy, but for this study the only detector effect we use is the energy resolution. The “generators” block includes the information about the listed backgrounds, such as the decay branches, the half-life and the end-point energies of every decay.

In snopy all events are programmed to be uniformly distributed within the detector, i.e. within the specified volume. The actual SNO+ detector response is not included. Hence the calculated levels of pileup events will provide upper limits or the worse case scenario.

Snopy was originally designed in [151] for setting the limit of neutrinoless double beta decay in Neodymium loaded scintillator and was updated in this work for pileup studies in the Tellurium loaded scintillator. The author of this thesis developed and verified the software, included all backgrounds inherent to the current scintillator cocktail and the energy resolution.

For this study we have included all isotopes present in the scintillator volume, such as naturally occurring impurities, cosmogenically induced backgrounds, backgrounds due to leaching and ^{8}B with their expected levels in the first year of the Tellurium loaded scintillator running, see Chapter 4 and Appendix A. One of the approximations is considering all the leaching backgrounds to be uniformly distributed within the detector, although some of them are located near the AV, see Section 4.5.5. We added “AV” to the names of those isotopes. The leaching backgrounds which became isotropically distributed keep their names.

The software calculates the total number of events of every possible pileup as well as the number of events in the ROI, which allows us to concentrate only on the pileup backgrounds that are worth detailed study. Only the pileup backgrounds that are calculated to contribute greater than 0.5 events[2] in the ROI per year continue to the next step of the analysis for the accurate pileup rejection study.

Using Snopy we have created the analytical energy spectra of single event backgrounds, see Figure 5.1 and listed the ones that contribute to the ROI in Table 5.1.

---

[2] Note, the fiducial volume limitation is not applied. The given number of events is considered for the full detector volume.

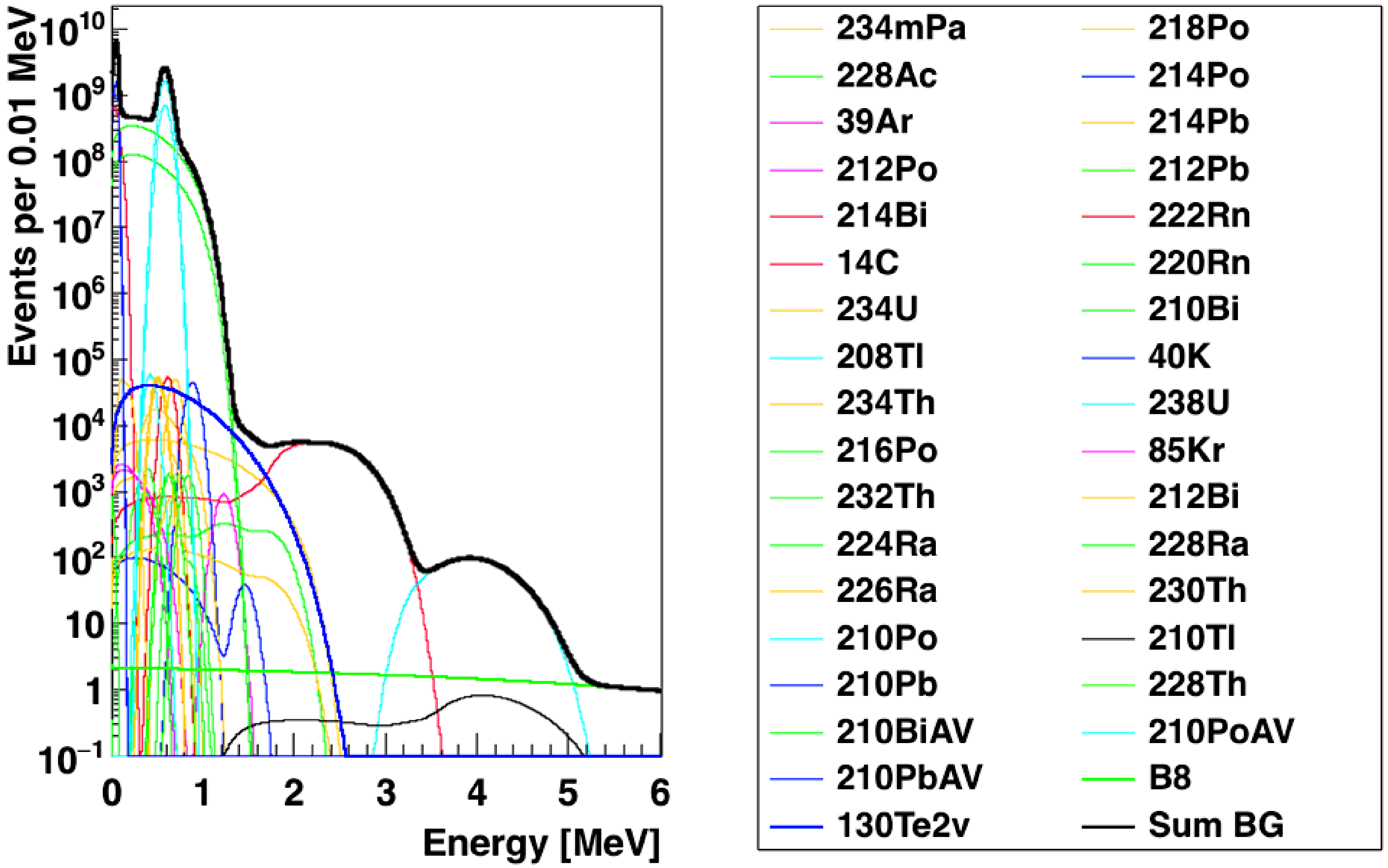

Figure 5.1: Analytical energy spectra of single background events during the first year of running the detector with the Tellurium loaded scintillator created by snopy software. The expected levels are given in Chapter 4 and Appendix A.

From Figure 5.1 it can be observed that based on the analytical estimations the majority of single internal backgrounds do not reach the ROI. However, four backgrounds have significant contributions; we list them in Table 5.1.

Table 5.1: Estimated number of single event backgrounds in the ROI during the first year of running the detector with the Tellurium loaded scintillator.

Background	Number of events in the ROI
^{214}Bi	108876.50
^{210}Tl	8.14
^{130}Te	2.92
^{8}B	45.82

Note, the obtained numbers are the analytical estimates for the full detector volume. The rejection techniques discussed in Chapter 4 are not applied within snopy as they require full event reconstruction.

Once the pileup backgrounds are included, a new energy spectrum plot becomes very busy and impossible to read as illustrated in Figure 5.2a and in Figure 5.2b. We list all pileup events that contribute to the ROI and present them in Table 5.2.

Throughout this thesis we adopt the convention of using the symbol "+" between the isotopes to indicate the pileup between them, i.e. the pileup between the decay A and the decay B will be written as A+B.

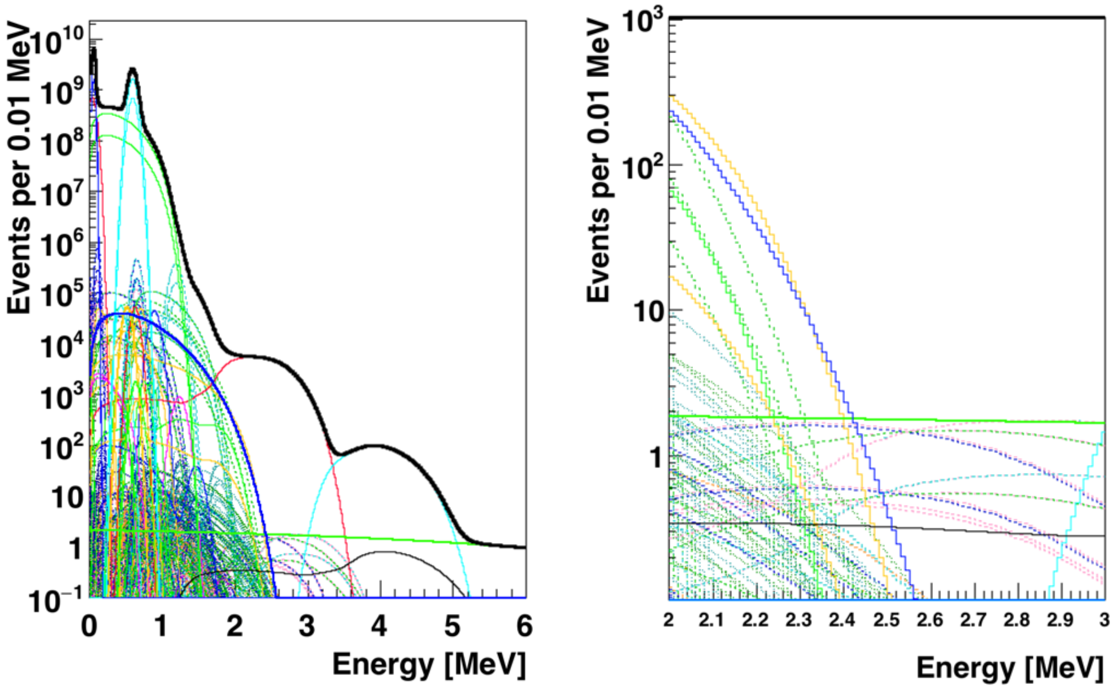

(a) (b)

Figure 5.2: Analytical energy spectra of all background events during the first year of running the detector with the Tellurium loaded scintillator created by snopy software. All pileup events are included as well as single background events in Figure (a); the closer look at the backgrounds around the ROI of [2.485, 2.733] MeV can be found in Figure (b). There are too many pileup events that contribute to the ROI and therefore the legend would not help in reading this plot. However, all pileup events that contribute to the ROI can be found in Table 5.2.

Table 5.2: Expected levels of pileup events during the first year of running the detector with the Tellurium loaded scintillator that contribute to the ROI of ^{130}Te $0\nu2\beta$ signal. We highlight the pileup combinations with the ^{214}Bi decay. We will show in Section 5.3.4 that regardless of their numbers of events in the ROI they can be rejected. The estimations have been performed with the snopy software.

Pileup	Total number of events in the first year	Number of events in ROI in the first year
^{130}Te$2\nu2\beta$ + AV^{210}Bi	1116.55	1.75
AV^{210}Bi + ^{130}Te$2\nu2\beta$	1116.54	1.75
^{130}Te$2\nu2\beta$ + ^{210}Bi	414.35	0.65
^{210}Bi+^{130}Te$2\nu2\beta$	414.27	0.65
^{130}Te$2\nu2\beta$ + AV^{210}Po	1173.92	2.23
AV^{210}Po + ^{130}Te$2\nu2\beta$	1174.34	2.23

Table 5.2: (continued)

Pileup	Total number of events in the first year	Number of events in ROI in the first year
^{130}Te2ν2β + ^{210}Po	497.84	0.94
^{210}Po + ^{130}Te2ν2β	497.92	0.94
^{214}Bi + ^{14}C	**61.57**	**10.77**
^{14}C + ^{214}Bi	**61.20**	**10.07**
^{214}Bi + ^{210}Bi	**76.38**	**14.24**
^{210}Bi + ^{214}Bi	**76.36**	**14.19**
^{214}Bi + ^{210}Po	**91.77**	**17.15**
^{210}Po + ^{214}Bi	**91.78**	**17.15**
^{214}Bi + ^{210}Pb	**76.28**	**13.33**
^{210}Pb + ^{214}Bi	**76.03**	**12.84**
^{214}Bi + AV^{210}Bi	**205.82**	**38.37**
AV^{210}Bi + ^{214}Bi	**205.82**	**38.25**
^{214}Bi + AV^{210}Po	**216.40**	**40.43**
AV^{210}Po + ^{214}Bi	**216.47**	**40.45**
^{214}Bi + AV^{210}Pb	**205.82**	**35.96**
AV^{210}Pb + ^{214}Bi	**205.18**	**34.66**
^{210}Bi+AV^{210}Bi+^{210}Bi	274.19	0.38
AV^{210}Bi+^{210}Bi+^{210}Bi	137.14	0.19
^{210}Bi+AV^{210}Bi+AV^{210}Bi	369.54	0.52
AV^{210}Bi+^{210}Bi+AV^{210}Bi	739.00	1.03
AV^{210}Bi+AV^{210}Bi+^{210}Bi	739.00	1.03
^{210}Bi+^{210}Bi+AV^{210}Bi	274.19	0.38
^{210}Bi+AV^{210}Bi+AV^{210}Po	776.83	0.88
^{210}Bi+AV^{210}Po+AV^{210}Bi	776.83	0.88
AV^{210}Bi+^{210}Bi+AV^{210}Po	776.98	0.88
AV^{210}Bi+AV^{210}Po+^{210}Bi	776.98	0.88
AV^{210}Bi+AV^{210}Bi+^{210}Po	887.90	1.01
^{210}Po+AV^{210}Bi+AV^{210}Bi	444.16	0.51

Table 5.2: (continued)

Pileup	Total number of events in the first year	Number of events in ROI in the first year
AV^{210}Bi+^{210}Po+AV^{210}Bi	887.90	1.01
^{210}Po+^{210}Bi+AV^{210}Bi	329.56	0.38
^{210}Bi+AV^{210}Bi+^{210}Po	329.44	0.37
AV^{210}Bi+^{210}Bi+^{210}Po	329.50	0.37
AV^{210}Bi+^{210}Po+^{210}Bi	329.50	0.37
^{210}Bi+^{210}Po+AV^{210}Bi	329.44	0.37
^{210}Po+AV^{210}Bi+^{210}Bi	329.56	0.38
^{210}Bi+AV^{210}Po+^{210}Bi	288.28	0.33
AV^{210}Po+^{210}Bi+^{210}Bi	144.24	0.16
^{210}Bi+^{210}Bi+AV^{210}Po	288.28	0.33
^{210}Bi+^{210}Bi+^{210}Po	122.25	0.14
AV^{210}Po+AV^{210}Bi+AV^{210}Po	2202.08	0.18
AV^{210}Po+AV^{210}Po+AV^{210}Bi	2202.08	0.18
AV^{210}Bi+AV^{210}Bi+AV^{210}Bi	996.00	1.39

From Table 5.2 it can be observed that there are pileup events created by the same set of isotopes but occurring in different orders. The properties of these combinations are not yet identified and therefore can not be fully treated as independent pileup events. Instead we sum up the estimated number of events in the ROI of all combinations of each pileup. Those pileup backgrounds that have more than 0.5 events in the ROI of all summed up combinations continue to the next step of study.

The pileup combinations highlighted in Table 5.2 include the ^{214}Bi decay. In Section 5.3.4 we will show that it is possible to apply the rejection techniques described in Section 4.5.3 to them.

In this step of the analysis, we have decreased the list of potentially troublesome pileup backgrounds down to 48.

5.2 Pileup in SNO+

The calculations discussed in Section 5.1 are not particularly tuned to the SNO+ detector, as among various properties only the backgrounds and partially the geometry of the AV are used. The results provided by snopy might be overestimated because some of the pileup decays wouldn't reconstruct.

In this part of the analysis, we perform simulations of pileup events, which take into account PMTs sensitivities, the SNO+ electronics, the SNO+ reconstruction model, optical properties of the media and the non-uniform distribution of AV leaching isotopes located near the surface of the AV. This allows us to study properties of pileup events and design methods to reject them.

5.2.1 Scenarios of pileup events

Depending on how a pileup event occurs in the detector, different rejection methods will be effective. There are several scenarios which we demonstrated on the event timing diagram in Figure 5.3. As was discussed in Section 2.6.3, when the PMT hits "I" cause the issue a GT at time 0 all PMT hits collected during the event timing window of 450 ns are recorded.

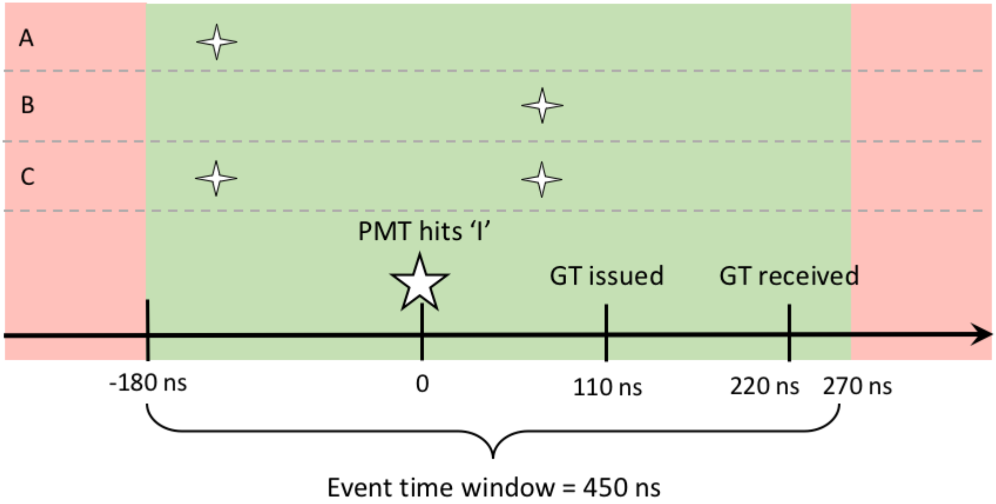

Figure 5.3: Pileup in event timing window. PMT hits "I" occurred at time 0 issue the GT. The event timing window includes 180 ns before "I" and 270 ns after. Cases A, B, C describe different scenarios of a pileup.

In Figure 5.3A we consider the case when PMT hits happen before the PMT hits "I" in the event window. Those hits can be due to occasional radioactive decays, and / or as tails of radioactive decays occurring in the previous timing window. Nevertheless, their resultant pulses are still not enough to issue GT.

Figure 5.3B describes the scenario when radioactive decays occur after the PMT hits "I". Herewith it might be weak and in principle unable to issue GT by itself, or it might create a lot of PMT hits and might even extend to the next timing window.

Figure 5.3C illustrates the combination of both previously described scenarios.

5.2.2 Simulation of a pileup event

The simulations of pileup events are performed with the Coincidence Generator [152] within the RAT 5.0.3 framework. It is designed to simulate two or more independent events occurring anywhere in the detector volume within the same specified time window of 450 ns. The author of this thesis adopted the existing framework and added the possibility of generating various radioactive decays and included the option of choosing the different order in which they can pile up. The latter is important as different orders of decays lead to different events with slightly different estimated levels, see Section 5.1.1. Additionally, the majority of pileup combinations were described.

In order to demonstrate the outputs of these simulations we are using pileup between ^{130}Te $2\nu2\beta$ and ^{210}Po-decay as an example, see Figure 5.4.

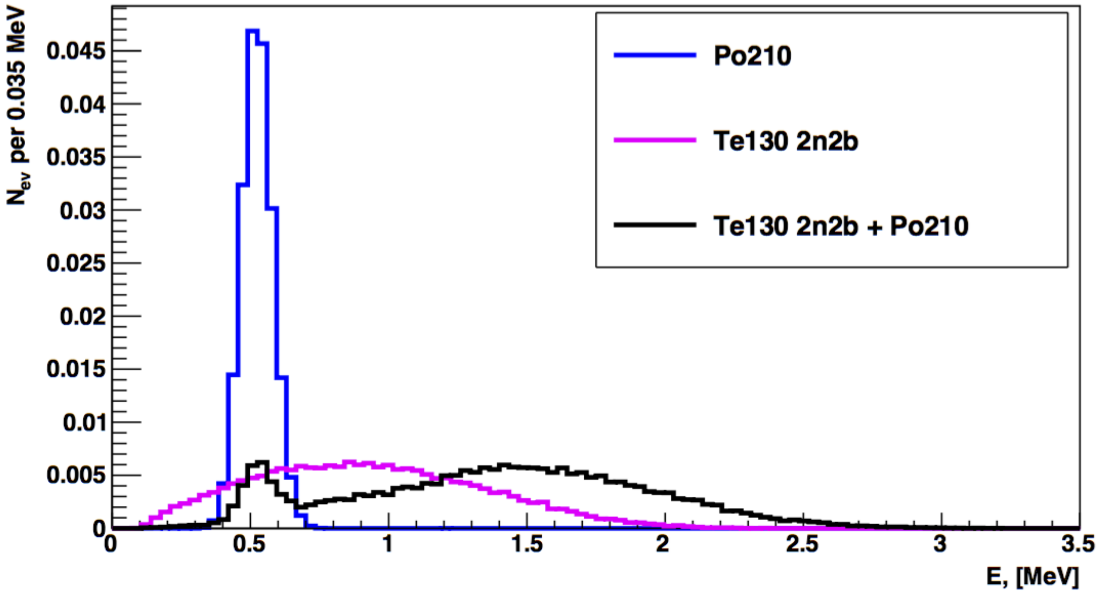

Figure 5.4: An example of a pileup event. The energy spectrum of pileup between ^{130}Te $2\nu2\beta$ and ^{210}Po-decay simulated using the coincidence generator in RAT 5.0.3 and the energy spectra of single decays of ^{130}Te $2\nu2\beta$ and ^{210}Po. It can be clearly seen that the end-point energy of the pileup events and the shape of the spectrum differs from that of ^{130}Te $2\nu2\beta$ and ^{210}Po-decay.

To study pileup backgrounds and perform the analysis we have performed simulations with $210 \cdot 10^3$ events of each pileup background that potentially contribute to the ROI, as presented in Table 5.2. This number was chosen as a balance between sufficient statistics and available computing resources for simulations, such as disk space and time it takes to obtain results. For example, it takes a minimum of 21 hours for the simulation of 10,000 pileup events between ^{130}Te and ^{210}Po to complete.

5.2.3 Reconstruction of a pileup event

In Section 2.7 we discussed the event reconstruction in SNO+. All the methods are elaborated for the case of a single decay event in a trigger window and are tuned for the optimum performance for ^{130}Te $0\nu2\beta$ events. Therefore despite the nature of a pileup event, it will be reconstructed as a single decay event. That is, the result of the calculations performed by the fitters is considered as a single event vertex.

Unlike a true single decay event, a pileup has a peculiar PMT hits pattern. Therefore, in the case of quadfitter, there will be more unphysical solutions of Eq. 2.7.2 and this results in the increase of failures during the reconstruction. For example, in 76% of cases the position reconstruction of a pileup between AV^{210}Bi and AV^{210}Bi fails to propose a vertex. Meanwhile, positions of only 4% of ^{130}Te $0\nu2\beta$-events can't be identified and these are mostly the decays happened in the AV neck and near the AV.

There can be different scenarios of pileup events. In the case when one of the decays causes significantly more PMT hits than the other participants in a pileup it pulls the reconstructed vertex towards itself. The topology of such events might be similar to a topology of a single decay event. Consequently, their reconstruction quality will be high. These pileup events are discussed in Section 5.3.3.

5.2.4 Techniques used to separate pileup events

A pileup event differs from an event with a single decay by its topology. In addition to uninformative values of reconstructed energy and position, there are other properties which can be used to discriminate events. Those specific properties can be described by algorithms, called classifiers, which return the results for the quantities of interest [153]. Based on the difference in distribution of classifier value between single events and pileup events, it is possible to design checks that reject the latter. This is the list of classifiers that are used for this study:

- Pre Trigger Hits
- Timing peaks
- Iso regions
- Mean Time
- Seeded Alpha

All of them will be discussed in detail below. Since the single event of interest is neutrinoless double beta decay, we compare its classifier distributions to the distributions from a pileup event. Indeed, the pileup events not only differ from the single events, they also differ from the pileup events formed by different combinations of decays. We have chosen the pileup between ^{130}Te $2\nu2\beta$ and ^{210}Po-decay to illustrate the distributions of classifier values.

Fiducial Volume

The volume of study is limited down to 3.5 m in order to reduce levels of external backgrounds, see Section 4.4. Such a strong cut also reduced uniformly distributed background contributions, and signal efficiency, by 80%. Since the fiducial volume (called as FV later on) restriction will be applied to all $0\nu2\beta$-analyses we apply this cut to pileup events as well. Throughout the pileup studies we analyse only the events inside the fiducial volume and therefore the distributions of all classifiers as well as their effect are presented inside it.

The Pre Trigger Hits Classifier

The Pre Trigger Hits classifier counts how many times PMTs were hit before the event trigger in the raw timing spectrum. While a single event is expected to have a few pre trigger hits due to PMT dark noise, a pileup might have several. Such a scenario is the scenario A discussed in Section 5.2.1. The Pre Trigger Classifier is an effective method in rejecting these type of events.

The situation in which the first physics event in a pileup appears to be the tail from a radioactive decay occurring in the previous time window cannot be easily simulated using the SNO+ software. Therefore, the pre-trigger PMT hits in simulated pileup events of the type A are caused by low energetic radioactive decays.

For example, although the end-point energy of ^{130}Te $2\nu2\beta$ decay is high, there are events below the SNO+ trigger threshold that are piling up with signal from ^{210}Po-decay. Such pileup events have an excess of pre-trigger hits. As another example, since the end-point energy of AV^{210}Bi-decay is relatively low and unlikely to trigger the detector, a pileup between AV^{210}Bi-decay, ^{210}Bi-decay and ^{210}Bi-decay has more pre trigger hits. Additionally, in the case that the first signal in a pileup occurs close to the AV it might cause a small number of PMT hits, due to optical effects. Both examples can be observed by looking at the tails of the distributions in Figure 5.5.

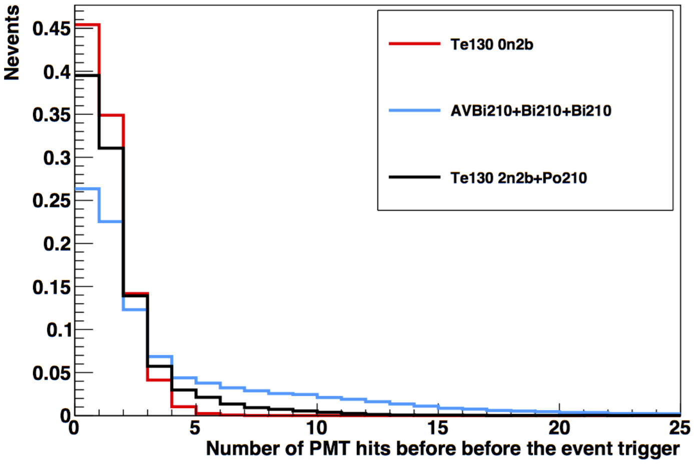

Figure 5.5: The distributions of the Pre Trigger Hits classifier of the pileup between ^{130}Te $2\nu2\beta$ and ^{210}Po-decay, the pileup between AV^{210}Bi-decay, ^{210}Bi-decay and ^{210}Bi-decay, and the ^{130}Te $0\nu2\beta$ signal.

The Timing Peaks Classifier

This classifier counts the number of distinct peaks in the raw timing spectrum. Pileup that consists of more than one signal in one time window, which have happened at different times and/or locations within the detector, will have more than one distinct peak. In Figure 5.6 we see that a single event has only one peak, while pileup events have up to four. Unfortunately, some pileup events have the timing peak characteristics of a single event, especially if one of the decays contributes only a small percentage of the PMT hits.

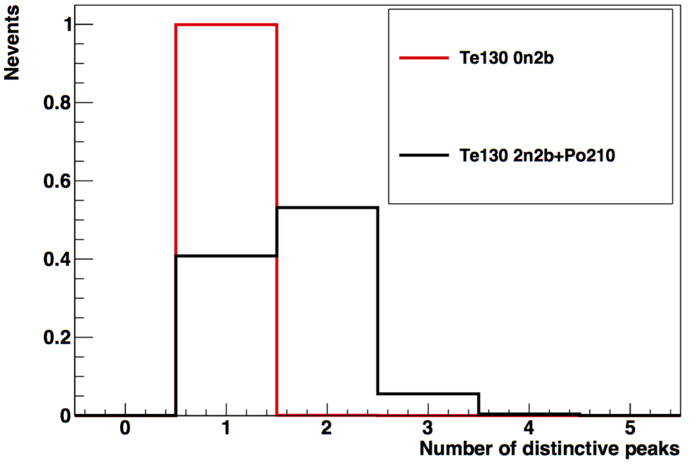

Figure 5.6: The distributions of the Timing Peaks classifier of the pileup between ^{130}Te $2\nu2\beta$ and ^{210}Po-decay and the ^{130}Te $0\nu2\beta$ signal.

The Mean Times Classifier

For every PMT hit in an event we can calculate the time residual t^i_{res} which can be used for differentiating single events from pileup events.

$$t^i_{res} = t^i_{trig} - t^i_{reco} - t^i_{flight} \tag{5.2.13}$$

Where t^i_{trig} is the recorded PMT hit time with calibration applied, t^i_{reco} is the reconstructed time of an event, t^i_{flight} the time of flight with the correction due to interactions with different materials. The mean time residual is then defined as:

$$\overline{t_{res}} = \sum_{i=1}^{N} \frac{t^i_{res}}{N} \tag{5.2.14}$$

Where N is the total number of PMT hits in the event. A single event is expected to be reconstructed close to its real decay time and position in the detector. Therefore, t^i_{reco}, t^i_{flight} and consequently t^i_{res} values are expected to be distributed around particular numbers. A pileup, since it is not a physical event, but the combination of several signals, is not expected to be reconstructed consistently. Hence, depending on various parameters, a pileup with the same combinations of the decays will have different values of t^i_{reco}. This can be seen in Figure 5.7.

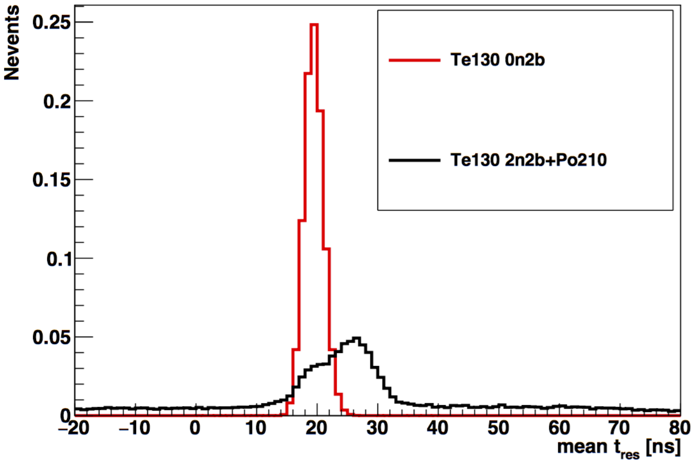

Figure 5.7: The distributions of the Mean Time classifier of the pileup between ^{130}Te $2\nu2\beta$ and ^{210}Po-decay and the ^{130}Te $0\nu2\beta$ signal.

It can be observed that the distribution of the classifier of a single event, ^{130}Te

$0\nu2\beta$, is symmetric, whereas a pileup between ^{130}Te $2\nu2\beta$ and ^{210}Po-decay has a broader, uneven and non symmetric distribution.

The Isotropy Classifier, The Latitudinal Isotropy Classifier

One of the characteristics of a single scintillation event is that the photons emitted from it should be distributed isotropically with respect to the point where the event has occurred. The Isotropy and the latitudinal Isotropy classifiers check the isotropy of the PMTs' spatial hit pattern.

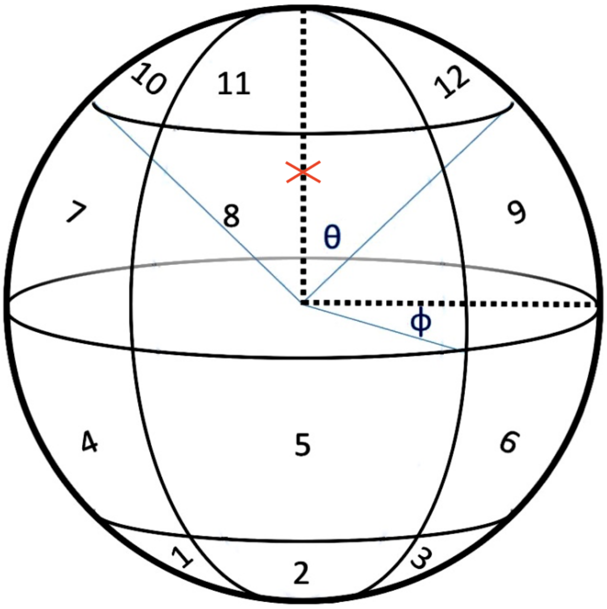

Figure 5.8: Schematic picture to show the division of the sphere into regions, used in the Isotropy and the Latitudinal Isotropy classifiers. The red cross represents an event and the vertical dotted line represents the "event axis". The sphere is first divided into four segments, which are shown via vertical black lines. A cone formed of blue lines is one of the four cones that are used to divide the already existing segments into four additional regions. There are 12 regions shown in this picture and 4 more are on the other side of sphere.

An efficient way to perform this check is to divide the PSUP sphere into 16 equal solid angle regions and compare the number of hits in each region as a measure of the isotropy of the event. The division is performed in both classifiers as follows:

a vector from the reconstructed event position to the detector centre defines the "event axis". Using this axis as a z-axis in a local coordinate system and introducing spherical coordinates with azimuthal angle ϕ and polar angle θ, the sphere is at first sliced into 4 equal segments by vertical sections at $\phi = 0, \frac{\pi}{2}, \pi, \frac{3\pi}{2}$ and then each segment is divided into 4 regions by cones of an equal $\cos\theta$, see Figure 5.8. Such regions have equal solid angles, hence the average number of hits from each region should be consistent with the $Nhit_{tot}/16$. In reality this number can vary, depending on properties of events. Therefore, the value of χ^2 calculated as:

$$\chi^2 = \sum_{i=1}^{16} (\frac{Nhit_{tot}}{16} - Nhit_i)^2 \tag{5.2.15}$$

where $Nhit_{tot}/16$ is the expected number of hits in any region, and $Nhit_i$ is the real number of hits in the i^{th} region, can be used as an effective criterion for the pileup rejection. In order to take into account the non-uniform distribution of PMTs along the PSUP sphere due to the presence of the AV neck the ϕ-segments are shrunk by an angle $\phi_{neck}/4$. The distributions of the Isotropy classifier can be found in Figure 5.9.

Some of the equal solid angle regions on the PSUP sphere are further from the event vertex than others and since the number of photons detected decreases with distance from the event vertex, the number of PMT hits from these regions will be significantly different even for good events occurring far from the center of the sphere. Because of this, such events will have bigger values of χ^2 and hence could be potentially cut by the Isotropy Classifier.

However, it is possible to divide all 16 regions into 4 groups of equal latitude, i.e. each group will contain 4 equal latitude regions. The distance between the event vertex and the regions from the same group is approximately the same by construction. Therefore, the additional Latitudinal Isotropy classifier is introduced to take advantage of this property. For every group it calculates the value of χ^2_{lat} and then averages these 4 results. The distributions of the Latitudinal Isotropy classifier can be found in Figure 5.10.

Uniformly distributed single events will have a bell-shape distribution for both classifiers. The closer the reconstructed event to the center of the AV, the smaller the value of χ^2. As soon as the reconstructed position of the event shifts, the value of χ^2 grows, whilst the number of events decreases towards the AV. This is clearly illustrated in Figure 5.9 and 5.10 with the ^{130}Te$0\nu2\beta$ as a single event. Meanwhile, a pileup event is caused by the combination of signals from different parts of the detector, and therefore, might have larger χ^2 values, consequently adding the tails to the distributions of the Isotropy Classifier and the Latitudinal Isotropy Classifier.

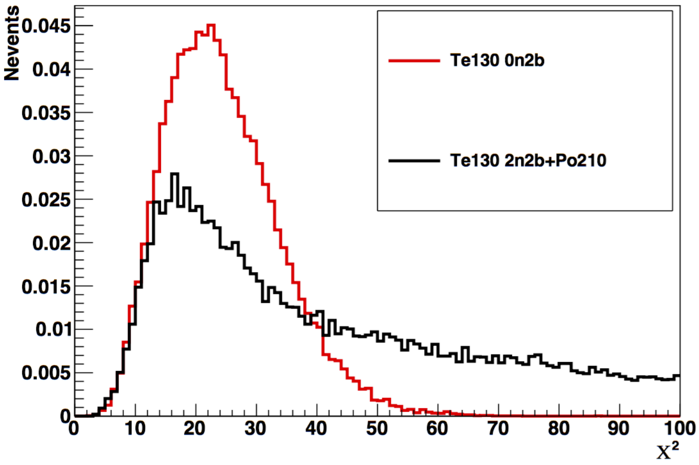

Figure 5.9: The distributions of the Isotropy classifier of the pileup between ^{130}Te$2\nu2\beta$ and ^{210}Po-decay and the ^{130}Te$0\nu2\beta$ signal.

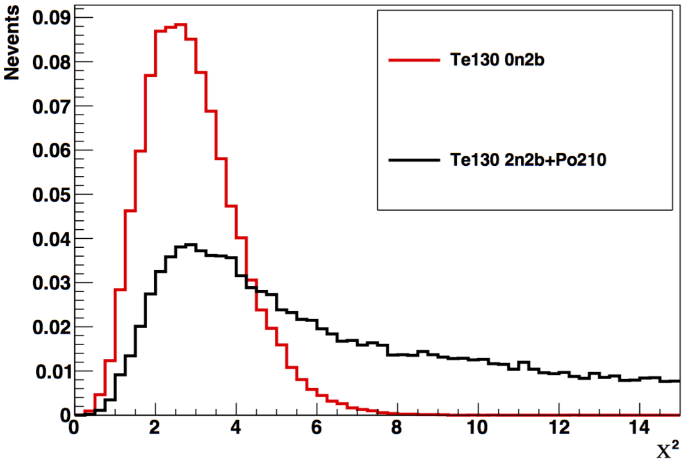

Figure 5.10: The distributions of the Latitudinal Isotropy classifier of the pileup between ^{130}Te$2\nu2\beta$ and ^{210}Po-decay and the ^{130}Te$0\nu2\beta$ signal.

The Seeded Alpha Classifier

This classifier was designed in [157], and it helps in separating the events with alpha particles and electrons. Based on the current target levels of the expected backgrounds from Appendix A, there will be several combinations of pileup events that include an alpha emitter ^{210}Po (see Section 4.5.6, Figure 4.2, Figure 4.4).

When passing through the detector volume, a charged particle excites the electrons of the scintillator material. Electrons excited to the singlet states have a shorter time constant than the electrons excited to the triplet states. Therefore, there is more "late" light contribution to the signal from the triplet state de-excitation. Since beta-events mostly cause singlet state excitations and alpha particles produce both singlet and triplet excited states, one can expect increased "late" light contributions from the alphas. This difference in timing profiles could be used to differentiate alpha and beta events.

This approach can be used for the separation between single electron-like events and pileup events, in which due to the presence of the secondary event later in the time window "late" light contribution increases. In order to take the advantage of this difference for every event the t^{i}_{res} is calculated, see Eq. 5.2.13. Then the ratio R between the number of PMT hits inside the "prompt" time region[3] and the total number of PMT hits is derived. The distribution of R values for pileup events are likely to be different from the distributions for single electron-like events. Therefore, despite the fact that the Seeded Alpha Classifier is not used for its original purpose, it still rejects significant amounts of pileup events. The distributions of the value R of the pileup between ^{130}Te $2\nu2\beta$ and ^{210}Po-decay and the ^{130}Te $0\nu2\beta$ can be found in Figure 5.11.

There are now other classifiers developed by other SNO+ collaborators that are showing better differentiation between alpha and beta events that could be investigated in future for pileup rejection [158, 159].

---

[3] The "prompt" time region is defined to be between 2 ns and 76 ns [134]

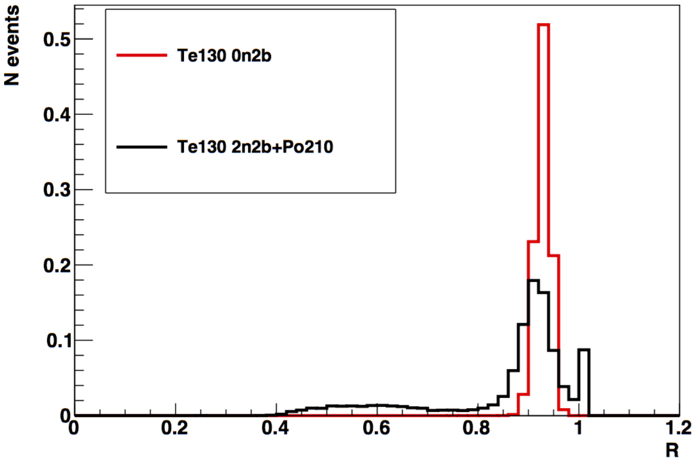

Figure 5.11: The distributions of the Seeded Alpha classifier of the pileup between ^{130}Te$2\nu2\beta$ and ^{210}Po-decay and the ^{130}Te $0\nu2\beta$ signal.

5.3 Pileup Rejection

The selection and rejection criteria of the backgrounds (see Chapter 4) are developed by different members of the collaboration independently and optimisations of these cuts proceed in parallel. The dominant criteria (i.e. those with most effect on signal efficiency) are the FV and energy cuts and their optimisation depends on the observed background levels, hence cannot be truly optimised until we measure the actual background levels in the first scintillator data. Therefore, each additional component of the analysis, such as pileup rejection, was given a target sacrifice of 1% [134, 135, 161], which is small with respect to the fiducial volume sacrifice and the pileup analysis was developed within this context.

In this study all the classifiers described in Section 5.2.4 are used to reject the pileup backgrounds from the ROI in the fiducial volume of 3.5m.

5.3.1 Cut Values

The pileup rejection cuts are relative and have to be changed depending on the particular study. For example, the analysis of solar signals will require a different approach, as the signals are in the low energy region which is overloaded by many pileup backgrounds. Moreover, the conditions of the detector, such as the scintillator cocktail, background levels and Tellurium loading affect the parameters of the applied criteria. Finally, since the performance of the classifiers is based on the SNO+ reconstruction algorithms, the pileup rejection study should be repeated for significant changes to reconstruction. The necessity of using all classifiers will be discussed in Section 5.3.5.

We took the same approach to pileup rejection as in Chapter 4[4], and we found the cut values of the classifiers that together reject not more than 1.02% of the signal [134, 135, 161] inside the FV. The cut values are presented in Table 5.3.

Table 5.3: Pileup rejection cuts. Events with classifier values that are satisfying the conditions stated in the table are rejected.

Classifier	Cut value
Fiducial Volume	> 3500 mm
Pre Trigger Hits	> 4
Timing Peaks	> 1
Mean Times	$14.5 <$ or > 24.0
Latitudinal Isotropy	> 6.9
Isotropy	> 57.0
Seeded Alpha	$0.87 <$ or > 0.98

The efficiency of these cuts in rejection of pileup events is presented in Section 5.3.2. The signal sacrifices of each cut, the cumulative signal sacrifices and the cumulative pileup rejection can be observed in Table 5.4. We have chosen the pile up between $^{130}\text{Te}2\nu2\beta$ and ^{210}Po as an example. The table is separated in two parts. In the first part, we demonstrate the effects of the strongest cuts, FV and ROI, which are applied to all events in the tellurium phase. In the second part, we show the performance of the cuts within the FV and ROI.

---

[4] The rejection techniques described in Sections 4.5.3, 4.5.4, 4.5.8 aim not to exceed the target signal sacrifice.

Table 5.4: Signal sacrifice and pileup rejection after applying pileup rejection cuts (see Table 5.3). In the first column, we name the classifiers. The numbers in the second column, are the signal sacrifices of each classifier applied independently. In the third column, we state the cumulative signal sacrifice after applying all classifiers above the current one. The pileup rejection classifiers are considered within the FV and inside the ROI region. In the fourth column, we give the cumulative rejection of the pileup background. ^{130}Te$2\nu2\beta$ + ^{210}Po is chosen as an example.

Classifier	Individual signal sacrifice [%]	Cumulative signal sacrifice [%]	Cumulative ^{130}Te$2\nu2\beta$ + ^{210}Po rejection [%]
Fiducial Volume	79.54	79.54	76.14
ROI	53.32	87.36	99.67
	inside FV&ROI	inside FV&ROI	inside FV&ROI
Pre Trigger Hits	0.31	0.31	2.45
Timing Peaks	0.04	0.35	48.47
Mean Times	0.28	0.60	86.35
Latitudinal Isotropy	0.49	0.91	95.55
Isotropy	0.42	0.98	95.86
Seeded Alpha	0.16	1.02	95.86

At the time of writing this thesis, the majority of the background rejection cuts are being developed and optimized individually with the maximum allowed signal sacrifice of 1%. Once the scintillator cocktail is finalized and the background model is approved, all the backgrounds will be considered together. The cuts will be identified in such a way that the best parameters will provide the highest $\frac{S}{\sqrt{B}}$ ratio, where S is the level of 0ν-events left after applying the cuts and B is the remaining level of backgrounds.

5.3.2 Pileup rejection

In order to prove the efficiency of the pileup rejection, we have applied the proposed checks listed in Table 5.3 to all pileup backgrounds that are expected to have events in the ROI. To do so, we have simulated these backgrounds using RAT 5.0.3 and have scaled the total number of events of each pileup to its expected number of events in the first year of running the detector filled with Tellurium, see Table 5.2. One should consider that snopy provides the estimation of the worst-case scenario.

The parameter that is used to evaluate the efficiency of the checks is called the survival factor, SF, and can be defined as:

$$SF = \frac{N_{after}}{N_{before}}, \tag{5.3.16}$$

where N_{after} - is the number of events after the pileup rejection cuts have been applied and N_{before} is the number of events after only the fiducial volume cut has been applied. The survival factor calculated for the total number of events will show the efficiency of the cuts in general, while calculated for the events in the ROI it will show how well the cuts can reject the pileup background particularly for the ^{130}Te $0\nu2\beta$ search. These parameters can be found in Table 5.5. It can be observed that some pileup backgrounds have non zero SF values.The ones with ^{214}Bi have also high numbers of events left in the ROI after cuts. Despite that, they are rejected with the different technique which will be discussed in detail in Section 5.3.4. As for the ^{130}Te$2\nu2\beta$ + ^{210}Bi, ^{210}Bi+^{130}Te$2\nu2\beta$, ^{130}Te$2\nu2\beta$ + AV^{210}Po, AV^{210}Po + ^{130}Te$2\nu2\beta$, ^{130}Te$2\nu2\beta$ + ^{210}Po, ^{210}Po + ^{130}Te$2\nu2\beta$ events, it is important that they are reduced in the ROI down to insignificant values. However, this still indicates that with higher event levels, these backgrounds might become problematic. Such possibilities are discussed in Section 5.4.

Additionally, for better illustration, we grouped the pileup events and made the energy spectra plots for each group which can be found in Figures 5.12 - 5.21. The division into groups is done solely for ease of visibility and is based on the similarity of components, i.e. number of decays in an event, different orders of contributing signals of the same pileup, number of events in spectra.

Table 5.5: Number of pileup events in one year of running Tellurium loaded detector survive the pileup rejection cuts. The table is divided into two parts. In the first part we present the information about the events from the full energy region, while in the second part only regarding the ROI. The numbers listed in the columns "FV" are the numbers of pileup events left after applying the fiducial volume cut only. The numbers in the column "cuts" are the events after all pileup rejection cuts have been applied. The survival factor (SF) parameters are the numbers of events left after all cuts have been applied over the total number of events.

Pileup	Total number of events			Events in the ROI		
	FV	cuts	SF, %	FV	cuts	SF, %
^{130}Te$2\nu2\beta$ + AV^{210}Bi	210.88	91.19	43.24	1.78	0.00	0.00
AV^{210}Bi + ^{130}Te$2\nu2\beta$	209.23	89.59	42.82	1.77	0.00	0.00
^{130}Te$2\nu2\beta$ + ^{210}Bi	86.86	19.47	22.42	0.88	0.04	4.55
^{210}Bi+^{130}Te$2\nu2\beta$	86.42	19.55	22.62	0.88	0.03	3.41
^{130}Te$2\nu2\beta$ + AV^{210}Po	219.08	97.79	44.64	5.07	0.01	0.20
AV^{210}Po + ^{130}Te$2\nu2\beta$	218.72	98.45	45.01	4.99	0.01	0.20
^{130}Te$2\nu2\beta$ + ^{210}Po	110.99	15.6	14.06	1.66	0.07	4.22
^{210}Po + ^{130}Te$2\nu2\beta$	111.38	15.71	14.10	1.71	0.07	4.09
^{214}Bi + ^{14}C	12.16	8.19	67.35	1.74	1.23	70.69
^{14}C + ^{214}Bi	11.85	7.92	66.84	1.61	1.13	70.19
^{214}Bi + ^{210}Bi	15.6	5.25	33.65	1.93	0.69	35.75
^{210}Bi + ^{214}Bi	15.51	5.13	33.08	1.91	0.70	36.65
^{214}Bi + ^{210}Po	19.14	3.75	19.59	2.22	0.38	17.12
^{210}Po + ^{214}Bi	19.14	3.74	19.54	2.22	0.38	17.12
^{214}Bi + ^{210}Pb	14.98	10.07	67.22	2.03	1.43	70.44
^{210}Pb + ^{214}Bi	14.78	9.86	66.71	2.06	1.44	69.90
^{214}Bi + AV^{210}Bi	38.48	21.69	56.37	4.97	3.02	60.76
AV^{210}Bi + ^{214}Bi	39.09	22.00	56.28	5.07	3.04	59.96
^{214}Bi + AV^{210}Po	40.93	22.63	55.29	5.05	3.18	62.97
AV^{210}Po + ^{214}Bi	41.37	22.68	54.82	5.03	3.18	63.22
^{214}Bi + AV^{210}Pb	40.20	31.48	78.30	5.58	4.61	82.62
AV^{210}Pb + ^{214}Bi	40.27	31.49	78.20	5.37	4.43	82.50
^{210}Bi+AV^{210}Bi+AV^{210}Bi	49.46	6.06	12.24	0.19	0.00	0.00

Table 5.5: (continued)

Pileup	Total number of events			Events in the ROI		
	FV	cuts	SF, %	FV	cuts	SF, %
AV^{210}Bi+^{210}Bi+AV^{210}Bi	98.85	12.55	12.70	0.37	0.00	0.00
AV^{210}Bi+AV^{210}Bi+^{210}Bi	99.41	12.16	12.23	0.39	0.00	0.00
^{210}Bi+AV^{210}Bi+^{210}Bi	51.12	4.35	8.51	0.17	0.00	0.00
AV^{210}Bi+^{210}Bi+^{210}Bi	25.94	2.21	8.52	0.07	0.00	0.00
^{210}Bi+^{210}Bi+AV^{210}Bi	51.66	4.46	8.63	0.17	0.00	0.00
^{210}Bi+AV^{210}Bi+AV^{210}Po	96.09	13.53	14.08	0.61	0.00	0.00
^{210}Bi+AV^{210}Po+AV^{210}Bi	96.32	13.61	14.12	0.66	0.00	0.00
AV^{210}Bi+^{210}Bi+AV^{210}Po	96.20	13.56	14.10	0.69	0.00	0.00
AV^{210}Bi+AV^{210}Po+^{210}Bi	96.54	13.97	14.47	0.77	0.00	0.00
AV^{210}Bi+AV^{210}Bi+^{210}Po	163.39	23.24	14.22	0.70	0.00	0.00
^{210}Po+AV^{210}Bi+AV^{210}Bi	81.60	11.62	14.24	0.31	0.00	0.00
AV^{210}Bi+^{210}Po+AV^{210}Bi	164.45	23.63	14.37	0.58	0.00	0.00
^{210}Po+^{210}Bi+AV^{210}Bi	69.22	5.51	7.96	0.28	0.00	0.00
^{210}Bi+AV^{210}Bi+^{210}Po	69.76	5.57	7.98	0.29	0.00	0.00
AV^{210}Bi+^{210}Bi+^{210}Po	69.37	5.54	7.99	0.28	0.00	0.00
AV^{210}Bi+^{210}Po+^{210}Bi	69.66	5.62	8.07	0.25	0.00	0.00
^{210}Bi+^{210}Po+AV^{210}Bi	69.44	5.64	8.12	0.30	0.00	0.00
^{210}Po+AV^{210}Bi+^{210}Bi	69.99	5.87	8.39	0.25	0.00	0.00
^{210}Bi+AV^{210}Po+^{210}Bi	49.75	4.88	9.81	0.25	0.00	0.00
AV^{210}Po+^{210}Bi+^{210}Bi	25.26	2.25	8.91	0.14	0.00	0.00
^{210}Bi+^{210}Bi+AV^{210}Po	50.29	5.19	10.32	0.28	0.00	0.00
^{210}Bi+^{210}Bi+^{210}Po	28.58	1.47	5.14	0.08	0.00	0.00
AV^{210}Po+AV^{210}Bi+AV^{210}Po	117.00	0.01	0.01	2.85	0.00	0.00
AV^{210}Po+AV^{210}Po+AV^{210}Bi	115.87	0.01	0.01	3.27	0.00	0.00
AV^{210}Bi+AV^{210}Bi+AV^{210}Bi	115.87	0.01	0.01	3.27	0.00	0.00

To summarize we have estimated that in the first year of the te-loaded scintillator data taking there will 83 pileup events in the ROI inside the fiducial volume of 3.5 meters. After applying the specifically designed rejection cuts, the number of events will be reduced down to 29.07. From Table 5.5 it can be seen that some double and all triple pileup backgrounds are completely rejected from the ROI. All pileup backgrounds with ^{214}Bi have events left in the ROI after cuts, but they will be rejected by other checks, as discussed in detail in Section 5.3.4. There are some double pileup events, such as ^{130}Te$2\nu2\beta$ + ^{210}Bi , ^{210}Bi + ^{130}Te$2\nu2\beta$, AV^{210}Bi + ^{130}Te$2\nu2\beta$, ^{130}Te$2\nu2\beta$ + ^{210}Po , ^{210}Po + ^{130}Te$2\nu2\beta$, ^{130}Te$2\nu2\beta$ + AV^{210}Po , AV^{210}Po + ^{130}Te$2\nu2\beta$, that still have fractions of events left in the ROI after cuts. This is not a problem with current background levels (see Appendix A), as they sum to less than 1 event per year, but with the increase of Tellurium loading the contribution from the pileup background could become significant. The pileup study for the higher loading of tellurium are discussed in Section 5.4.

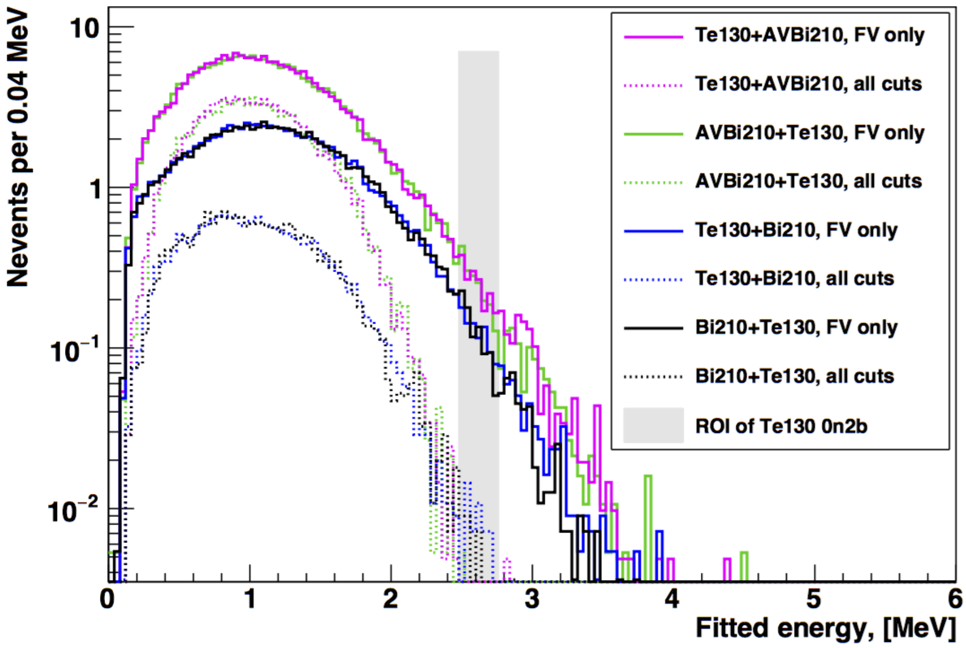

Figure 5.12: Energy spectra of pileup events from the first group before and after all cuts have been applied within the fiducial volume of 3.5 m.

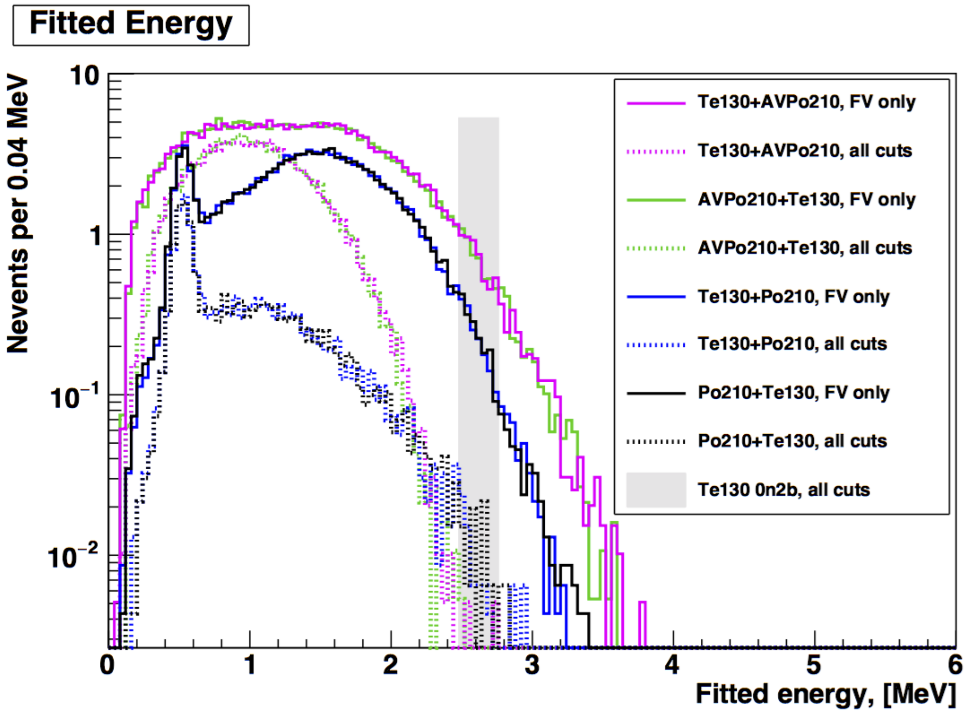

Figure 5.13: Energy spectra of pileup events from the second group before and after all cuts have been applied within the fiducial volume of 3.5 m.

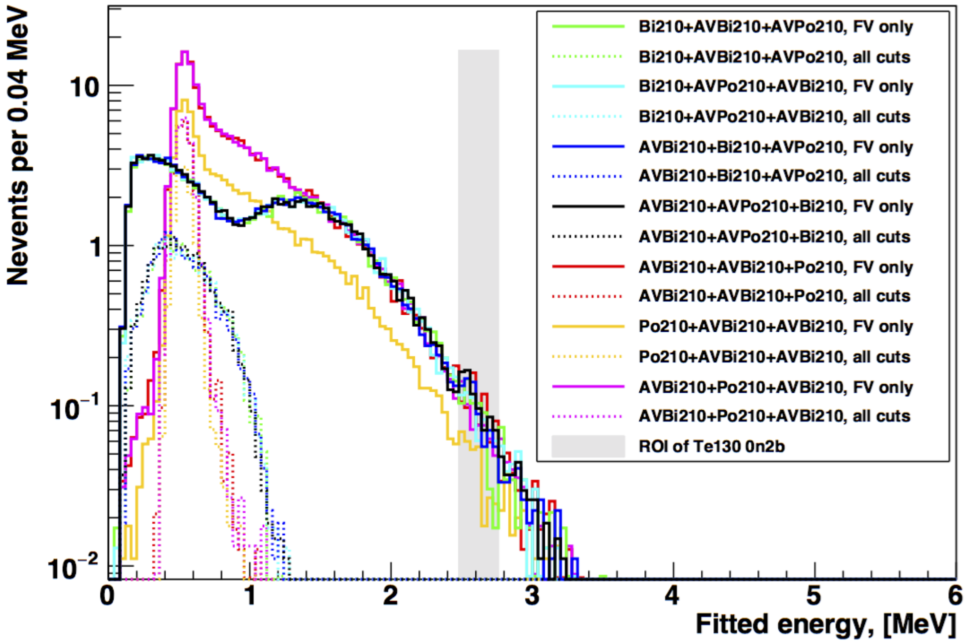

Figure 5.14: Energy spectra of pileup events from the third group before and after all cuts have been applied with the fiducial volume of 3.5 m.

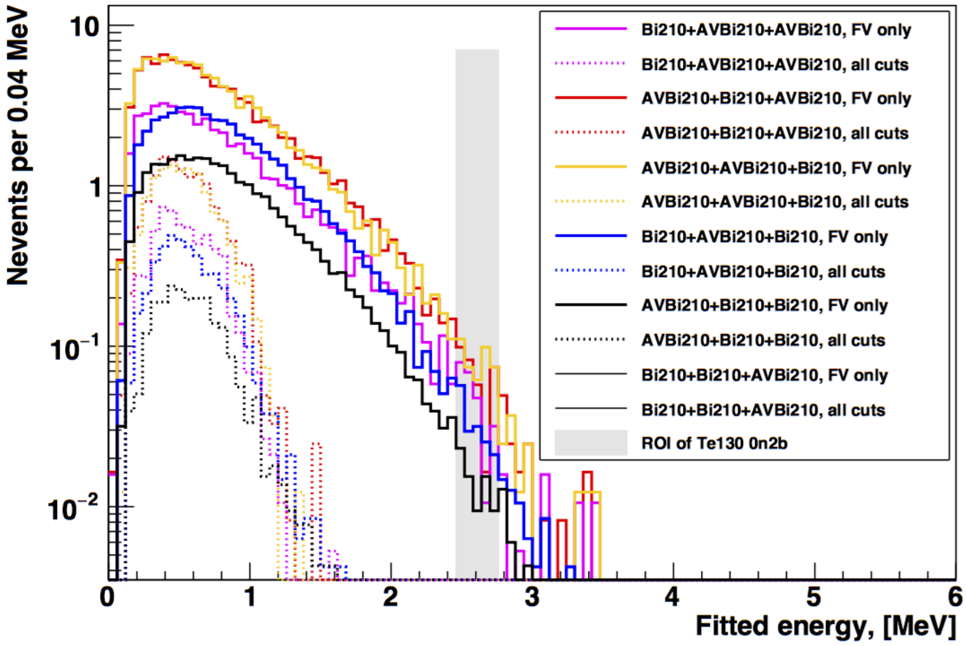

Figure 5.15: Energy spectra of pileup events from the fourth group before and after all cuts have been applied with the fiducial volume of 3.5 m.

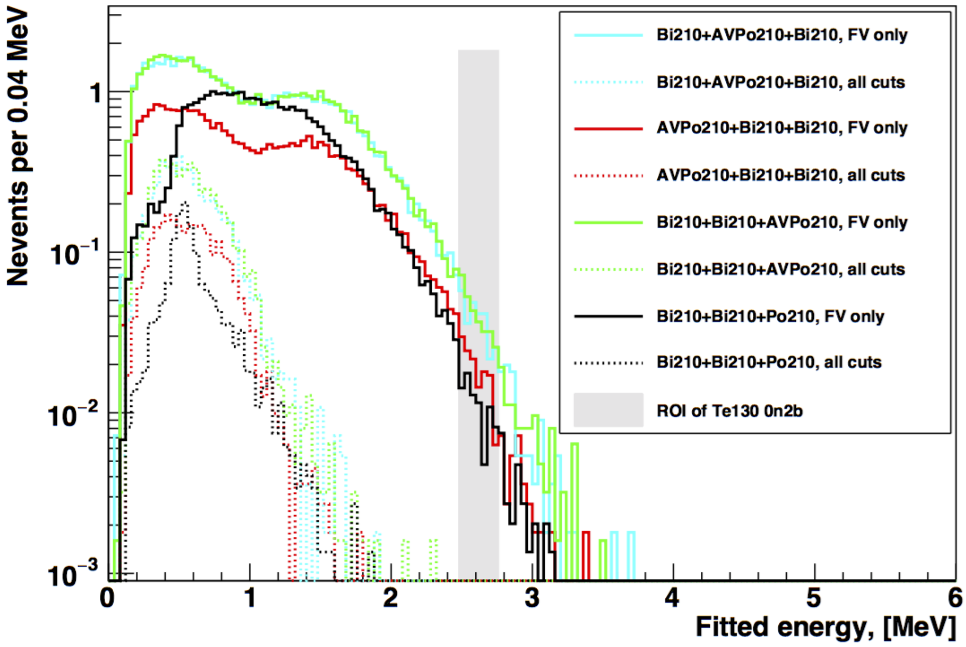

Figure 5.16: Energy spectra of pileup events from the fifth group before and after all cuts have been applied with the fiducial volume of 3.5 m.

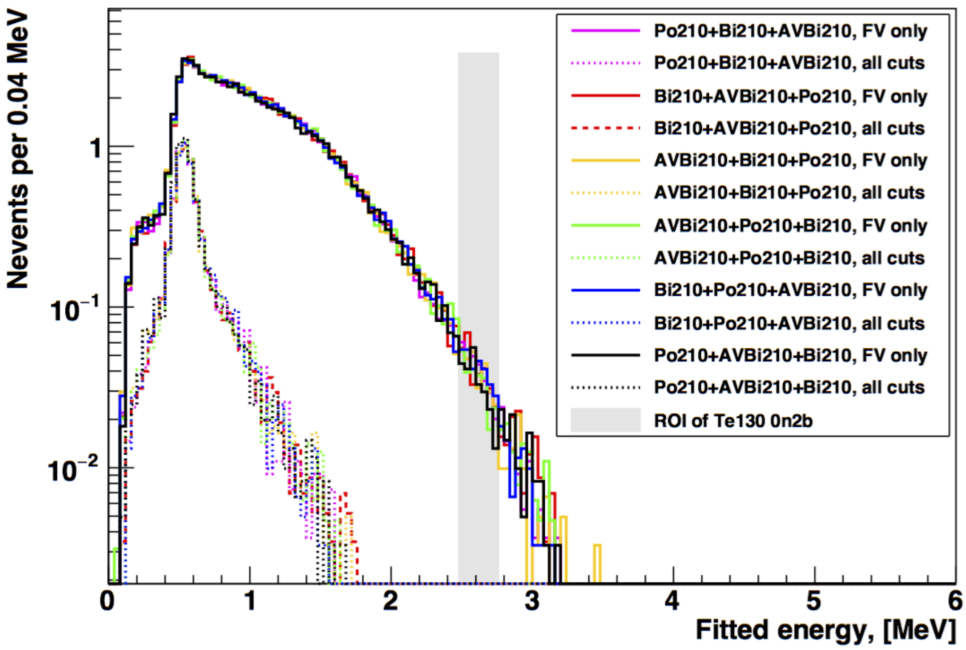

Figure 5.17: Energy spectra of pileup events from the sixth group before and after all cuts have been applied with the fiducial volume of 3.5 m.

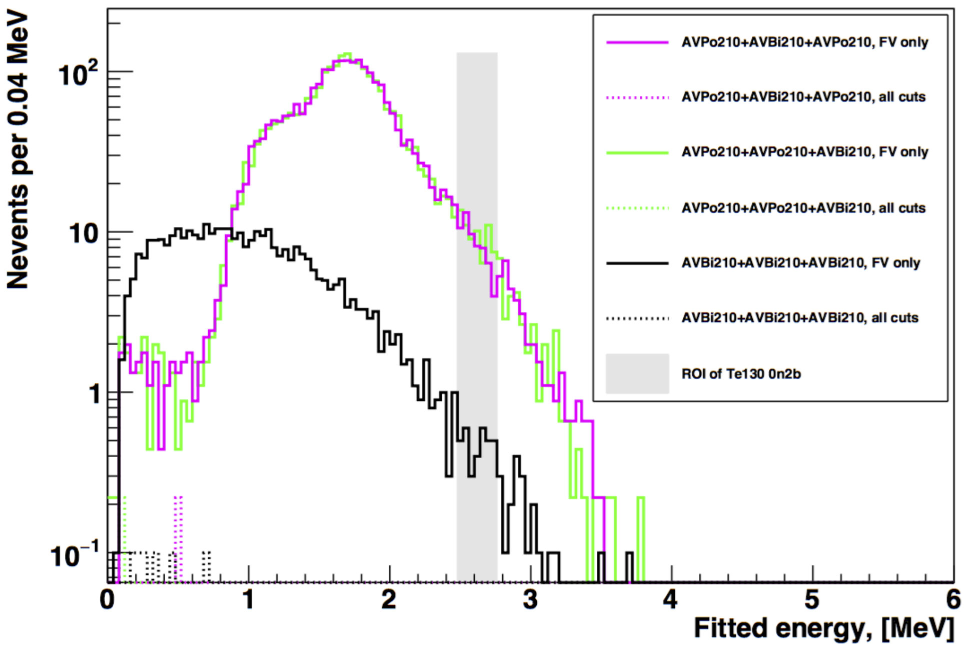

Figure 5.18: Energy spectra of pileup events from the seventh group before and after all cuts have been applied with the fiducial volume of 3.5 m.

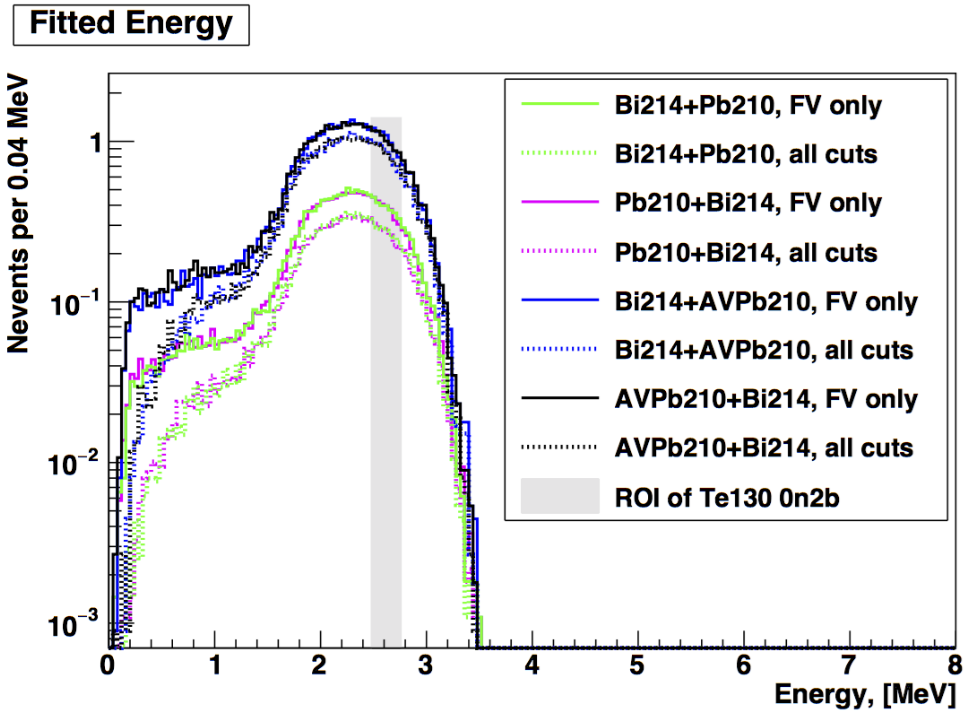

Figure 5.19: Energy spectra of pileup events from the tenth group before and after all cuts have been applied with the fiducial volume of 3.5 m.

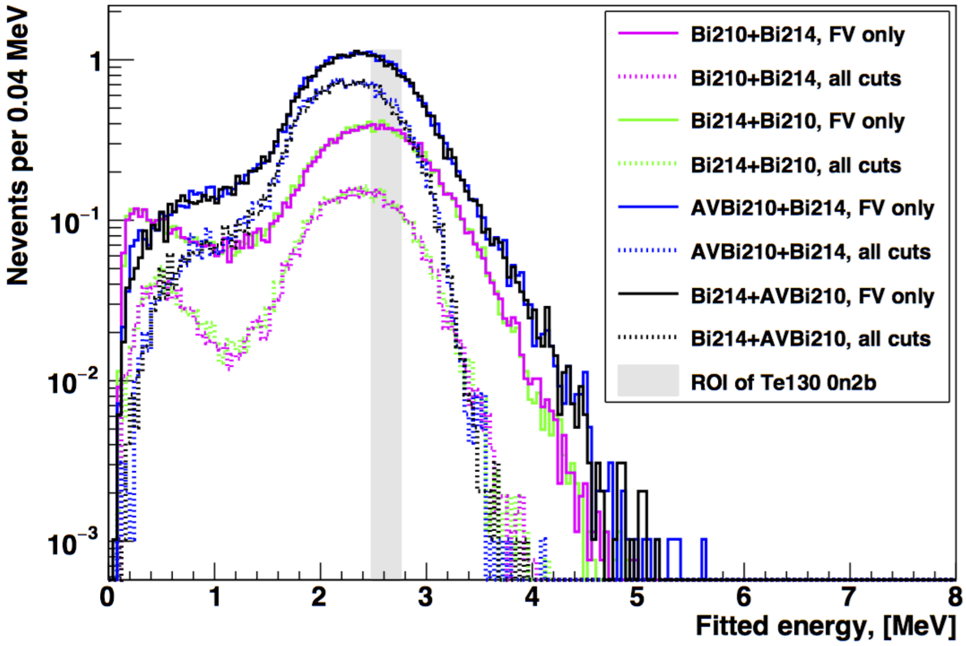

Figure 5.20: Energy spectra of pileup events from the eighth group before and after all cuts have been applied with the fiducial volume of 3.5 m.

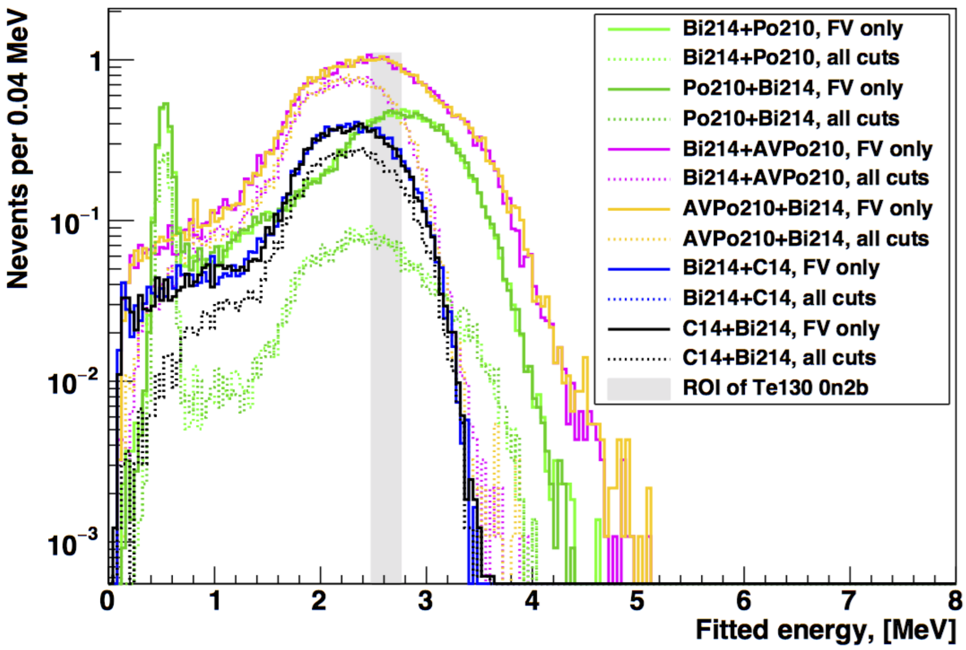

Figure 5.21: Energy spectra of pileup events from the ninth group before and after all cuts have been applied with the fiducial volume of 3.5 m.

5.3.3 Dominant isotope in a pileup event

There is a special type of a pileup event, when one of the signals that forms it dominates over the rest, i.e. contributes the majority of PMT hits. This could happen due to the combination of actual physical properties of decays and results of reconstruction algorithms of SNO+.

This behavior can be observed if isotopes decay in the same time window at vastly different energies. For example, in the pileup between ^{130}Te $2\nu2\beta$ and ^{210}Bi-decay there are events where ^{130}Te $2\nu2\beta$ decays at much higher energies than ^{210}Bi, consequently producing more PMT hits. Therefore, in those particular pileup events the signals from ^{130}Te $2\nu2\beta$ decay will be dominant in the high energy region. However, if the energy of ^{130}Te $2\nu2\beta$ decay is lower than the ^{210}Bi decay, the latter will be dominant. Since the region of interest for $0\nu2\beta$ is relatively high in energy, the dominant backgrounds from the pileup events there are those with higher end-point energies.

The type of particle emitted in the decay will strongly affect the number of observed PMT hits. Due to a large difference in quenching between electrons and alpha-particles, the light yield of alpha-emitters will be suppressed by approximately a factor of 10, see Section 2.4.3. Such events will not dominate in high energy regions.

Regardless of the energies of the signals in a pileup, the position in the detector where they decay may lead to the suppression of one signal over the others. Due to the geometry of the Acrylic Vessel events occuring around 5400 mm in radius experience total internal reflection of some proportion of the light, hence the same event will cause fewer PMT hits in that sector. There will be fewer PMT hits in the opposite part of the detector as well, since the photons travelling that far will experience more attenuation.

All reconstruction algorithms are based on PMT hits in an event. Therefore, if there are more PMT hits produced by one of the decays, the reconstructed position of this pileup event will be biased towards it. As a consequence, a pileup event with a clear dominant signal has the properties of that signal, i.e. behaves as a single event. Hence, such pileup events might not be rejected by the designed pileup rejection cuts. The worst isotope for this is ^{214}Bi due to the high endpoint of this decay. Luckily, other rejection algorithms can be applied to this decay as discussed in the next section.

5.3.4 Bi214 pileup

As can be seen in Table 5.5 there are a lot of pileup events with ^{214}Bi that are not rejected by the developed techniques. Although their total numbers of events are not high in general, they have a lot of events in the ROI, due to the high end-point energy of ^{214}Bi. We believe that events that contribute to the ROI after the rejection have dominant signals from the ^{214}Bi-decay and therefore look like single events and are not identified as pileup. Fortunately, there are methods to reject these events.

In the Uranium 238 chain a ^{214}Bi isotope with a half-life of 19.9 minutes β-decays into ^{214}Po. The ^{214}Po, with half-life of 164 μs, decays shortly after, emitting an α-particle. The possibility of having both decays in one trigger window is 0.17% [161], so the probability of these “in-window” BiPo events being involved in pileup is two orders magnitude lower than 0.17%. Thus, we do not assume that this scenario is likely to happen. When ^{214}Bi-Po events happen in different trigger windows they can be tagged, as the timing and position cuts allow rejection of both events. Due to the short half-life of ^{214}Po, the emitted alpha-particle is expected to be close to the decay position of ^{214}Bi and limited by the position resolution of reconstruction within the fiducial volume. Thus the position cut to reject random backgrounds is defined as [161]:

$$\left|\overline{R}_{^{214}Bi} - \overline{R}_{^{214}Po}\right| \leq 2\,\mathrm{m} \tag{5.3.17}$$

where $\overline{R}_{^{214}Bi}$ and $\overline{R}_{^{214}Po}$ are the reconstructed positions of ^{214}Bi and ^{214}Po isotopes correspondingly. The timing cut is chosen to be wider than the half-life of ^{214}Po to increase the selection efficiency [161]:

$$|T_{^{214}Bi} - T_{^{214}Po}| \leq 11 \cdot T_{1/2} \tag{5.3.18}$$

where $T_{^{214}Bi}$ and $T_{^{214}Po}$ are the reconstructed decay times of ^{214}Bi and ^{214}Po isotopes correspondingly and $T_{1/2}$ is the half-life of ^{214}Po.

In order to use this technique, it must be shown that the pileup events in the ROI with dominant signal from ^{214}Bi are reconstructed close enough to the real ^{214}Bi decay. Since the events in a pileup have happened within the time window of 450 ns, the maximum time difference between the real decay time of ^{214}Bi and the reconstructed time of this pileup event is 450 ns. This possible shift in reconstructed time does not lead to the violation of the time cut as it is an order of 3 magnitudes smaller. The position cut can be applied if the true decay vertex of dominant ^{214}Bi-decay in a pileup event is within 2 m from the reconstructed vertex of the pileup. This distance can be written as:

$$\varDelta R = \sqrt{(x_{reco} - x_{true})^2 + (y_{reco} - y_{true})^2 + (z_{reco} - z_{true})^2} \tag{5.3.19}$$

Where x_{reco}, y_{reco} and z_{reco} are the reconstructed x-, y- and z-coordinates of a pileup vertex correspondingly, x_{true}, y_{true}, z_{true} - are the true x, y, z coordinates of the ^{214}Bi decay. The $\varDelta$R distribution is illustrated for the example of the pileup between ^{214}Bi and ^{210}Po and can be found in Figure 5.22.

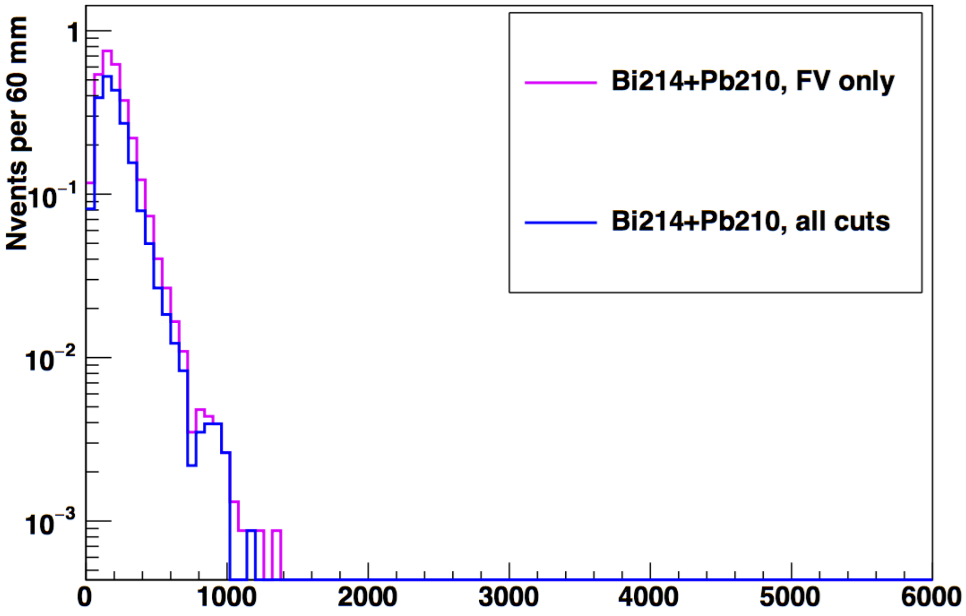

Figure 5.22: The distribution of the distance between the reconstructed vertex of the pileup between ^{214}Bi and ^{210}Po decays and the true vertex of ^{214}Bi-decay.

The majority of events are reconstructed within 2 m from the ^{214}Bi decay vertex;

the number of events that do not is insignificant, which can be seen in Table 5.6. This proves that the ^{214}Bi-Po rejection techniques can be applied to all current pileup events with ^{214}Bi. Since the rejection factor is 99.995% [161], the number of those pileup events is negligible in the ROI. Using the method, that will be described in Section 5.4, it is estimated that the levels of the isotopes have to be three orders higher than the current ones from Appendix A. Therefore, it is safe to assume that even future increase of Tellurium loading (and consequently backgrounds) will not change the high reduction factor of ^{214}Bi pileup events from the ROI.

Table 5.6: Number of events in the ROI after all cuts have been applied that have the distance between the reconstructed vertex of a pileup and the true vertex of ^{214}Bi-decay larger than 2 m. In case no events observed, limits derived from statistics available. In third column it can be found the fraction of such events in the total number of events in the ROI after cuts.

Pileup	Number of events in the ROI	Fraction, %
AV^{210}Bi + ^{214}Bi	0.00	0.03
^{214}Bi + AV^{210}Bi	0.00	0.03
AV^{210}Po + ^{214}Bi	0.00	0.00
^{214}Bi + AV^{210}Po	0.00	0.00
^{214}Bi + AV^{210}Pb	0.00	0.02
AV^{210}Pb + ^{214}Bi	0.00	0.02
^{214}Bi + ^{210}Po	0.00	0.00
^{210}Po + ^{214}Bi	0.00	0.40
^{210}Bi + ^{214}Bi	0.00	0.00
^{214}Bi + ^{210}Bi	0.00	0.09
^{214}Bi + ^{14}C	0.00	0.00
^{14}C + ^{214}Bi	0.00	0.00
^{214}Bi + ^{210}Pb	0.00	0.00
^{210}Pb + ^{214}Bi	0.00	0.02

5.3.5 The correlation between the classifiers

The presented classifiers are targeting different event properties, and used together, are expected to show effective rejection. Nevertheless, the correlation between the classifiers will show if some of them are not needed. The study is complicated due to the difference in properties of each pileup, such as the positions of the vertices, the number of decays that cause a pileup and the type of particles involved, which might strongly affect the characteristics. Thus all pileup backgrounds are separated into groups and a representative is chosen from each. Although it is hardly possible to make a precise statement about each classifier, the overall pattern can be followed and a general conclusion can be propagated.

In this study, we use two definitions of the term "correlation" and therefore address two different approaches.

In the first method, we study the performance of only two classifiers at once using the approach described in [162]. We introduce the parameter, a correlation index ρ, that indicates the correlation degree of the two chosen classifiers:

$$\rho = \frac{2 \times N^{FF}}{N^{TF} + N^{FT} + 2 \times N^{FF}}, \tag{5.3.20}$$

where N^{FF} is the number of pileup events that are not rejected by both classifiers, N^{TF} is the number of pileup events that are rejected by the first classifier but are missed by the second classifier and N^{FT} is the number of pileup events that are rejected by the second classifier but are missed by the first classifier. We consider only events inside the FV. A high value of ρ suggests that the correlation is strong.

Using this method we investigate correlations between 5 couples of the classifiers and apply them to 5 pileup representatives. We present the results in Table 5.23. In each case, the values are different but the trend can be followed.

The correlation indexes obtained for the ^{214}Bi + ^{210}Pb pileup are the highest (between 0.94 and 0.99). This can be explained by the similarity of these events and single ^{214}Bi events. As was demonstrated in Section 5.3.4, the pileup combinations with ^{214}Bi are not rejected well by the pileup rejection cuts which in this case means that N^{FT} and N^{TF} from Eq. 5.3.20 are small in comparison with N^{FF}.

1. 210Po + 130Te2v2β

	Timing Peaks	Mean Times	Lat Isotropy	Isotropy	Seeded Alpha
Timing Peaks	1	0.60	0.56	0.56	0.70
Mean Times	0.60	1	0.50	0.47	0.51
Lat Isotropy	0.56	0.50	1	0.87	0.56
Isotropy	0.56	0.47	0.87	1	0.59
Seeded Alpha	0.70	0.51	0.56	0.59	1

2. 130Te2v2β + AV210Bi

	Timing Peaks	Mean Times	Lat Isotropy	Isotropy	Seeded Alpha
Timing Peaks	1	0.85	0.86	0.86	0.85
Mean Times	0.85	1	0.82	0.81	0.83
Lat Isotropy	0.86	0.82	1	0.96	0.80
Isotropy	0.86	0.81	0.96	1	0.81
Seeded Alpha	0.85	0.83	0.80	0.81	1

3. 214Bi + 210Pb

	Timing Peaks	Mean Times	Lat Isotropy	Isotropy	Seeded Alpha
Timing Peaks	1	0.95	0.99	0.99	0.98
Mean Times	0.95	1	0.94	0.94	0.96
Lat Isotropy	0.99	0.94	1	0.99	0.98
Isotropy	0.99	0.94	0.99	1	0.98
Seeded Alpha	0.98	0.96	0.98	0.98	1

4. 210Po + 210Bi + AV210Bi

	Timing Peaks	Mean Times	Lat Isotropy	Isotropy	Seeded Alpha
Timing Peaks	1	0.51	0.55	0.54	0.59
Mean Times	0.51	1	0.42	0.40	0.47
Lat Isotropy	0.55	0.42	1	0.89	0.51
Isotropy	0.54	0.40	0.89	1	0.53
Seeded Alpha	0.59	0.47	0.51	0.53	1

5. 210Bi + AV210Po + AV210Bi

	Timing Peaks	Mean Times	Lat Isotropy	Isotropy	Seeded Alpha
Timing Peaks	1	0.66	0.62	0.61	0.70
Mean Times	0.66	1	0.60	0.59	0.66
Lat Isotropy	0.62	0.60	1	0.96	0.55
Isotropy	0.61	0.59	0.96	1	0.55
Seeded Alpha	0.70	0.66	0.55	0.55	1

Figure 5.23: The correlation indexes ρ (from Eq. 5.3.20) estimated for 5 combinations of the classifiers. For this study we use 5 pileup representatives which are specified above each table.

In the second method, we refer to the term "correlation" as the percentage of pileup events that can be rejected by either classifier. We describe this study below.

We first obtained the total number of events, N_{tot}, rejected by all classifiers within the fiducial volume. We then obtained the number of events, N_{clas}, that are rejected by each classifier separately. In order to get the relative power of each classifier, P_{clas}, the following ratio has been calculated:

$$P_{clas} = \frac{N_{clas}}{N_{tot}} \tag{5.3.21}$$

Comparing P_{clas} parameters will show which classifier rejects the most pileup events of a certain type. The correlation between all classifiers C_{all} will then be the ratio between the events that can be rejected by all classifiers at the same time $N_{\forall}$ and N_{tot}.

$$C_{all} = \frac{N_{\forall}}{N_{tot}} \tag{5.3.22}$$

All results for the chosen pileup events are presented in Table 5.7. We can see that even though most of the classifiers can identify many pileup events, the correlation C_{all} between them is not so high. This fact supports the statement that the techniques are targeting different properties of pileup events and therefore complement each other. At the same time it can be concluded that, since the sum over all classifiers of P_{clas} for any given pileup is much greater then 100%, some classifiers have to correlate between each other. While some characteristics are unique, others are similar, but calculated using slightly different approaches. Thus, considering only the classifiers that are sensitive to similar properties of events might show strong correlations between them. The correlation between two classifiers can be obtained similar to Eq. 5.3.22. In this case N_{tot} is the total number of events that are rejected by both classifiers, and $N_{\forall}$ is the number of events, that are rejected by either of the two.

Table 5.7: The correlation between the results provided by all classifiers. The numbers written in the column "correlation" are the fractions of events that can be rejected by any classifier. The values written in other columns are the ratios of number of events rejected by a classifier and the total number of events rejected by all classifiers together.

A pileup	Pre Trigger Hits , [%]	Timing Peaks, [%]	Mean Time, [%]	Isotropy, [%]	Lat Isotropy, [%]	Seeded Alpha, [%]	Correlation, [%]
AV^{210}Bi+^{210}Bi+AV^{210}Bi	27.47	60.34	71.68	58.31	60.82	44.20	4.16
^{210}Bi+^{210}Bi+AV^{210}Bi	30.64	68.20	83.33	44.15	51.20	53.34	4.06
^{210}Bi+AV^{210}Po+AV^{210}Bi	21.74	55.89	70.28	63.63	64.71	39.73	2.63
AV^{210}Po+^{210}Bi+^{210}Bi	25.26	63.61	82.01	49.8	53.99	49.34	2.60
AV^{210}Po+AV^{210}Po+AV^{210}Bi	4.75	60.18	66.53	99.83	99.19	27.48	1.05
^{210}Po+AV^{210}Bi+AV^{210}Bi	18.37	61.24	78.78	57.82	61.29	47.47	2.95
^{210}Po+^{210}Bi+AV^{210}Bi	21.32	69.85	86.84	51.61	58.4	55.01	3.51
^{214}Bi+AV^{210}Po	2.53	58.00	66.51	69.19	69.67	36.85	0.21
^{130}Te$2\nu2\beta$ + AV^{210}Bi	15.57	47.54	63.25	41.22	45.46	36.46	0.98
^{210}Bi + ^{130}Te$2\nu2\beta$	20.01	55.31	80.81	26.85	35.72	45.26	0.84
^{130}Te$2\nu2\beta$ + AV^{210}Po	8.18	49.85	65.21	62.06	63.32	33.23	0.62
^{210}Po + ^{130}Te$2\nu2\beta$	7.77	66.75	88.92	48.61	57.52	47.54	1.07

The Pre Trigger Hits Classifier and the Timing Peaks Classifier are both using the information from the raw timing spectrum, and provide us with the benefit of pre-reconstruction analysis. The Pre Trigger Hits classifier is able to identify a pileup in which the first physics events are below trigger threshold, such as low energy radioactive decays or PMT hits from a decay occurring in the previous time window. High correlation between this classifier and any other is not expected.

The Timing Peaks Classifier, on the contrary, might have a strong correlation with other classifiers, since it takes advantage of the pileup events that consist of equally high level signals that happen at different time or/and in different places in the detector. Such events are very likely to be traced by the Mean Time Classifier and by either the Isotropy or the Latitudinal Isotropy Classifiers. The correlation between the Timing Peaks Classifier and the Mean Time Classifier is high in general as can be seen in Table 5.8, since both are using the event timing information. The Mean Time Classifier rejects more pileup events as it is more accurate for events that are formed by the signals with different numbers of PMT hits. The same conclusion can be made from comparison of the performance of the Isotropy Classifier to some types of the pileup events, this can be confirmed by Table 5.9.

Table 5.8: The correlation between the results provided by the Mean Time and the Timing Peaks classifiers. The fractions written in the column "Mean Time" (or "Timing Peaks") are obtained as the ratio between the number of events rejected by the Mean Time classifier (or Timing Peaks classifier) and the total number of events rejected together by both classifiers. The fraction of events that can be identified by both classifiers are presented in the final column.

Pileup	Mean Time, [%]	Timing Peaks, [%]	either classifier, [%]
^{210}Po + ^{130}Te$2\nu2\beta$	96.74	72.62	69.35
^{130}Te$2\nu2\beta$ + AV^{210}Bi	90.55	68.06	58.61
^{214}Bi + ^{210}Pb	94.23	14.22	8.46
^{210}Po + ^{210}Bi + AV^{210}Bi	94.14	75.72	69.86
^{210}Bi + AV^{210}Po + AV^{210}Bi	87.55	69.62	57.18

Table 5.9: The correlation between the results provided by the Isotropy and the Timing Peaks classifiers. The fractions written in the column "Isotropy" (or "Timing Peaks") are obtained as the ratio between the number of events rejected by the Isotropy classifier (or Timing Peaks classifier) and the total number of events rejected together by both classifiers. The fraction of events that can be identified by both classifiers are presented in the final column.

Pileup	Isotropy, [%]	Timing Peaks, [%]	either classifier, [%]
^{210}Po + ^{130}Te$2\nu2\beta$	59.44	81.62	41.05
^{130}Te$2\nu2\beta$ + AV^{210}Bi	69.29	14.23	49.20
^{214}Bi + ^{210}Pb	14.60	79.91	0.66
^{210}Po + ^{210}Bi + AV^{210}Bi	63.23	85.59	48.82
^{210}Bi + AV^{210}Po + AV^{210}Bi	79.28	69.60	48.84

The Mean Times, the Isotropy, the Latitudinal Isotropy and the Seeded Alpha classifiers are post reconstruction techniques. Since both the Mean Time and the Seeded Alpha classifiers are based on the time residuals of the events, they should correlate, which can be supported by results in Table 5.10. The Mean Time Classifier rejects more events as it is more general.

Table 5.10: The correlation between the results provided by the Mean Time and the Seeded Alpha classifiers. The fractions written in the column "Mean Time" (or "Seeded Alpha") are obtained as the ratio between the number of events rejected by the Mean Time classifier (or Seeded Alpha classifier) and the total number of events rejected together by both classifiers. The fractions of events that can be identified by both classifiers are presented in the final column.

Pileup	Mean Time, [%]	Seeded Alpha, [%]	either classifier, [%]
^{210}Po + ^{130}Te$2\nu2\beta$	98.66	52.74	51.40
^{130}Te$2\nu2\beta$ + AV^{210}Bi	94.78	54.63	49.41
^{214}Bi + ^{210}Pb	94.38	32.70	27.08
^{210}Po + ^{210}Bi + AV^{210}Bi	96.87	61.37	58.24
^{210}Bi + AV^{210}Po + AV^{210}Bi	94.24	53.27	47.52

The Isotropy and the Latitudinal Isotropy Classifier are the only classifiers that are looking at the spatial difference. Since the Latitudinal Isotropy Classifier is a more accurate and efficient version of the Isotropy Classifier, they are naturally correlated, which can be seen in Table 5.11. In some cases, the parameter χ^2 of a pileup, calculated by the Isotropy Classifier, can be smaller than the χ^2 of a single event and therefore it will not be rejected. If in this case the signals that caused the pileup happened at different latitudes from the reconstructed vertex of the pileup, this event will be rejected by the Latitudinal Isotropy Classifier. However, if the signals have happened along the event vertex axis, the Latitudinal Isotropy Classifier might miss it too.

Table 5.11: The correlation between the results provided by the Isotropy and the Latitudinal Isotropy classifiers. The fractions written in the column "Isotropy" (or "Latitudinal Isotropy") are obtained as the ratio between the number of events rejected by the Isotropy classifier (or Latitudinal Isotropy classifier) and the total number of events rejected together by both classifiers. The fraction of events that can be identified by both classifiers are presented in the final column.

Pileup	Isotropy, [%]	Latitudinal Isotropy, [%]	either classifier, [%]
^{210}Po + ^{130}Te$2\nu2\beta$	79.83	94.47	74.28
^{130}Te$2\nu2\beta$ + AV^{210}Bi	87.35	96.34	83.69
^{214}Bi + ^{210}Pb	78.35	28.61	6.96
^{210}Po + ^{210}Bi + AV^{210}Bi	85.18	96.39	81.57
^{210}Bi + AV^{210}Po + AV^{210}Bi	95.91	97.53	93.44

There is another possible correlation between the Mean Time Classifier and the Isotropy Classifier. Both are looking at the anisotropy of PMT hits that is typical for a pileup event; the difference is that the first classifier checks the time distribution, while the latter checks the spatial distribution. The results of comparison are presented in Table 5.7 and Table 5.12, where it can be seen that the correlation between these two classifiers is high. The Mean Time Classifier identifies more pileup events in general as it is sensitive not only to the signals that have happened at different times within a pileup time window but also to the signals that are spatially separated. Indeed, the decays that have happened at distant positions are likely to reconstruct badly and, therefore, the distribution of the mean time residuals from this pileup will differ from the single event. Meanwhile, the Isotropy Classifier does not necessarily distinguish between a single event and a pileup event that was formed from the signals originated nearby, but at different times, as their spatial hit patterns will both look isotropic. Having said that, it is still possible that a pileup event will be reconstructed in such a way that the mean time residual will be within the allowed region, but rejected by the Isotropy classifier. This can be confirmed as the correlation between the Mean Time Classifier and the Isotropy Classifier is not absolute: the case when a pileup event has happened between three signals from the isotopes due to leaching of the Acrylic Vessel is an example.

Table 5.12: The correlation between the results provided by the Mean Time and the Isotropy classifiers. The fractions written in the column "Mean Time" (or "Isotropy") are obtained as the ratio between the number of events rejected by the Mean Time classifier (or Isotropy classifier) and the total number of events rejected together by both classifiers. The fraction of events that can be identified by both classifiers are presented in the final column.

Pileup	Mean Time, [%]	Isotropy, [%]	either classifier, [%]
^{210}Po + ^{130}Te$2\nu2\beta$	96.41	52.70	49.11
^{130}Te$2\nu2\beta$ + AV^{210}Bi	89.60	58.39	48.00
^{214}Bi + ^{210}Pb	97.83	2.51	0.34
^{210}Po + ^{210}Bi + AV^{210}Bi	94.89	56.39	51.28
^{210}Bi + AV^{210}Po + AV^{210}Bi	81.96	74.21	56.17

In this section in order to confirm the necessity of using all applied classifiers we have compared efficiencies between the ones that are either sensitive to similar properties or using similar approaches. These classifiers could have been potentially correlated, while the other coincidences are not expected to be high in general. As shown in Table 5.7 the triple pileup events have only about 4% of events that can be rejected by all classifiers at the same time. Other types of pileup events show even smaller correlations. This result by itself proves that regardless of analogy between some classifiers, they provide highly effective results applied together.

5.4 Maximum possible levels of backgrounds

The pileup events between ^{130}Te $2\nu2\beta$, ^{210}Po-decay and ^{210}Bi-decay in various combinations have non zero survival factor in the ROI. At the moment the levels of irreducible pileup backgrounds are low, but the planned increase of the Tellurium loading and therefore the background levels of ^{210}Bi and ^{210}Po will lead to an increase of the number of the pileup events. Therefore, we have estimated the maximum levels of the isotopes for different Tellurium loadings, beyond which it will not be possible to reject their pileup events from the ROI. The estimations are performed using "pumax" software, designed for this study. The study is based on several assumptions and hence the results should be treated as the worst case scenario. All introduced uncertainties are due to limits of simulated statistics.

Despite knowing the Tellurium loadings and keeping them fixed in the study, the future levels of the other isotopes are not clear, as they depend on various factors, such as the time that Tellurium was underground in SNOLAB, purification factors, the leaching levels, etc. These factors might be independent from each other, and hence it is difficult to predict their effect now. For these reasons a rough estimation of the maximum levels in the worst case scenario is made.

As has been done in Section 5.1.3 we use the snopy software to find additional pileup events that might appear with higher Tellurium loadings whilst keeping the levels of other isotopes the same as before (see Appendix A). With the increase of Tellurium loading numbers of events of already mentioned pileup combinations increase, new combinations of triple pileup backgrounds with ^{130}Te appear and finally a pileup between ^{130}Te and ^{130}Te starts contributing to the ROI. Therefore, we estimate maximal possible levels of isotopes in new pileup events as well. Hence, we perform simulations of those backgrounds and apply the similar pileup rejection cuts to them.

The estimation of the maximal possible levels of the isotopes is based on the simulated events and on the fact that the energy and the properties of a pileup stay the same, with the only difference being in amplitudes, determined by the levels of the isotopes that form it. Different combinations of the numbers of events of these isotopes affect neither its shape nor its properties.

As before, a pileup can be considered to contribute to the ROI if it has more than 0.5 events per year in the ROI after the cuts have been applied. Although the order in which the isotopes pileup matters, allowing every pileup combination to have 0.5 events in the ROI will lead to overestimation of the maximum possible levels. For this reason we limit all orders of isotopes in a pileup together by 0.5 events in the ROI. That means that every pileup now is limited by another number; the number of combinations of a pileup. All cases of pileup backgrounds are described below. For every case we calculate the maximum allowed number of pileup events in the ROI, $N_{ROI,cuts}$, after the cuts have been applied.

1. If $B1 \neq B2$, then the pileup events $B1+B2$ and $B2+B1$ can have $N_{ROI,cuts} = 0.5/2 = 0.25$ events separately.
2. If $B1 = B2$, then a pileup between them can have $N_{ROI,cuts} = 0.5$ events.
3. If $B1 = B2 = B3$, then $N_{ROI,cuts} = 0.5$ events.
4. If any two of three isotopes piling up are the same and the third one is different, then $N_{ROI,cuts} = 0.5/3 = 0.17$ events.
5. If all three isotopes piling up are different, then $N_{ROI,cuts} = 0.5/6 = 0.08$ events.

As we scale the amplitude of a background, and hence its pileup, only the amplitude of the pileup energy spectrum changes, not the shape. So we can use a constant factor f_{ROI} to scale from the number of pileup events in the ROI to the total number.

$$f_{ROI} = \frac{Number\ of\ events\ in\ the\ ROI}{Total\ number\ of\ events}. \tag{5.4.23}$$

This parameter can be obtained from any simulated data and hence it accuracy is limited only by simulated statistics. Using the maximum number of events in the ROI after all cuts have been applied which depends on a pileup, $N_{ROI,cuts}$, it is possible to calculate the maximum total number of pileup events $N_{tot,cuts}$:

$$N_{tot,cuts} = \frac{N_{ROI,cuts}}{f_{ROI}}. \tag{5.4.24}$$

Another factor that remains the same regardless of the level of a pileup is the survival factor SF, that was calculated earlier in Eq. 5.3.16. Again, it can be calculated for any simulated data.

Using the total maximum number of events after the cuts have been applied $N_{tot,cuts}$ and the survival factor, SF, the total maximum number of events before cuts have been applied, N_{tot} can be obtained as:

$$N_{tot} = \frac{N_{tot,cuts}}{SF}. \tag{5.4.25}$$

Knowing the maximal level of a pileup, it is possible to calculate the maximal levels of the contributing isotopes. Although the amounts of $^{130}\mathrm{Te}2\nu2\beta$, $^{210}\mathrm{Po}$ and $^{210}\mathrm{Bi}$ in the detector are connected, it is not possible to take into account all scenarios, therefore maximal levels of the isotopes have been estimated separately. In order to do so, the maximal level of each currently studied isotope is considered as an unknown parameter x and the levels of the isotopes left in the pileup are taken from Appendix A. Then for every pileup we can calculate (following from Sec. 5.1.1) the maximum level for each isotope separately, for example:

$$x \cdot \frac{N_2 e^{-N_2}}{1!} = N_{tot} \tag{5.4.26}$$

$$N_1 \cdot \frac{x e^{-x}}{1!} = N_{tot} \tag{5.4.27}$$

Where N_1 and N_2 are the levels from Appendix A. Solving the equations Eq. 5.4.26 and Eq. 5.4.27 for x leads to the maximum levels of the first and the second isotopes.

As was mentioned earlier, $^{130}\mathrm{Te}$ loadings of 0.3%, 0.5%, 3%, 5%, 15% are fixed for every study and the levels of the other isotopes are set to be the unknown parameter x. Although we performed the calculations for all Tellurium loadings, we only list the results for 0.3% and 15% loadings in Table 5.13. These two cases represent two important conditions. Maximal allowed background levels in the first Tellurium loading phase shows that the pileup rejection technique is applicable even if initial background levels turn out to be worse. The final Tellurium loading is chosen as it might have the most restrictions of background levels.

Table 5.13: Maximum possible levels that the piling up isotopes can have before their pileup with Tellurium start contributing more than 0.5 events to the ROI. A required change is expressed by a factor, i.e. by what parameter a current level has to be multiplied. That means that if a factor is below 1, the level has to be decreased. The factors were estimated for 0.3% and 15% of Tellurium loadings which are indicated in the second and the third columns correspondingly.

Pileup	Factors for 0.3% loading	Factors for 15% loading
$^{130}\mathrm{Te}2\nu2\beta$ + $^{210}\mathrm{Bi}$	6.14	0.12
$^{210}\mathrm{Bi}$+$^{130}\mathrm{Te}2\nu2\beta$	7.78	0.16
$^{130}\mathrm{Te}2\nu2\beta$ + $\mathrm{AV}^{210}\mathrm{Po}$	18.57	0.37
$^{130}\mathrm{Te}2\nu2\beta$ + $^{210}\mathrm{Po}$	3.60	0.07
$^{210}\mathrm{Po}$+$^{130}\mathrm{Te}2\nu2\beta$	3.47	0.07

From Table 5.13 it follows that the maximum background levels of $^{210}\mathrm{Bi}$ and $^{210}\mathrm{Po}$ can be higher before they significantly contribute to the ROI for 0.3% Tellurium loading.

Based on estimations made by snopy software among several triple pileup events with $^{130}\mathrm{Te}2\nu2\beta$ at 15% loading there are only few backgrounds that might contribute to the ROI. All combinations of the following isotopes piling up have more than 0.3 events in the ROI:

- $\mathrm{AV}^{210}\mathrm{Po}$, $\mathrm{AV}^{210}\mathrm{Bi}$ and $^{130}\mathrm{Te}2\nu2\beta$
- $\mathrm{AV}^{210}\mathrm{Po}$, $\mathrm{AV}^{210}\mathrm{Po}$ and $^{130}\mathrm{Te}2\nu2\beta$
- $^{210}\mathrm{Po}$, $\mathrm{AV}^{210}\mathrm{Po}$ and $^{130}\mathrm{Te}2\nu2\beta$

We have performed the simulations of those events. Applying the same pileup rejection techniques, the efficiency of rejection of the background events in the ROI proved to be high. Survival factors differ from 0.03% to 0.27% resulting in keeping only $8.91 \cdot 10^{-4}$ events in the ROI at maximum. Moreover, from the calculations obtained by pumax software, it follows that in order for those pileup events to contribute 0.5 events to the ROI, the levels of the isotope has to be more than two orders higher than the current levels (see Appendix A). Fortunately, the SF of a pileup between ^{130}Te$2\nu2\beta$ and ^{130}Te$2\nu2\beta$ is 0.73% and the number of events is 0.04 in the ROI. Hence, more dangerous are the pileup backgrounds listed in Table 5.13. In order to be be able to reject them from the ROI using the current techniques, the levels of the isotope have to be significantly reduced.

One of the sources of inaccuracy of this study is the expectation that all orderings of the isotopes contribute similarly and thereby could be limited by the same number. In reality, there are pileups where some orders of the isotopes contribute much less events to the ROI than others, therefore their maximum level can be slightly higher. However, since the goal was to consider the worst-case scenario, this assumption is conservative.

Another assumption is that in the higher Te-loadings the target maximum signal sacrifice will stay as 1%. In the case that the acceptable signal sacrifice increases, the cut values might become more effective in pileup rejection.

5.5 Summary

This chapter has described the comprehensive study of pileup backgrounds in SNO+. We have demonstrated the potential danger of pileup backgrounds to $0\nu2\beta$ studies and estimated their levels in the first year of Te-loaded scintillator phase in the ROI both analytically and using the Monte-Carlo simulations. Using the classifiers available at the time of writing we reduced the number of pileup events in the FV in the ROI from 83 down to 0.32 with 1.02% signal sacrifice.

In order to estimate levels of pileup backgrounds and to determine the ones that potentially leak into the ROI we used the analytical definition of a pileup event. We developed snopy software which took isotopes with their levels as an input and calculated the levels of all possible pile up combinations. In this study, we included all internal backgrounds and considered them being uniformly distributed. Consequently, the obtained levels were the upper limits. The software was used to perform quick estimates of pileup backgrounds relevant to future higher tellurium loadings phases. Due to its universality snopy could also be applicable in other liquid scintillator experiments.

Prior to performing the simulations of pileup backgrounds, we added such a possibility into SNO+ RAT software, i.e. we described the process of piling up of various radioactive decays in different orders. Due to the presence of other types of backgrounds, such as externals and instrumentals, the next step will be to consider them to pile up as well.

The classifiers which proved to be effective in separation and reduction of pileup backgrounds used differences in topologies between them and signal events. Those methods should be reconsidered after the scintillator cocktail will be affirmed and each time after the SNO+ reconstruction undergoes changes.

Similar approaches were taken to reject other types of backgrounds, see Chapter 4. Hence the combination of all the methods might improve the effectiveness of each background rejection. Once all the backgrounds are considered together the use of classifiers should be re-optimised.

Chapter 6

Limit setting in SNO+

The SNO+ background model in the tellurium loaded scintillator phase is described in Chapter 4. We perform the Monte-Carlo simulations of the backgrounds and design the rejection cuts; we estimate the number of surviving events left after applying the cuts. After the experimental data is obtained it will proceed through various filters starting from the low-level data quality selection to the previously developed background rejection cuts. The remaining events are counted. Then using the statistical techniques we evaluate the significance of the signal observation on top of the expected backgrounds. If the discrepancy between the observed data and the expected backgrounds is such that only a large background fluctuation (5σ or more) can explain it, the experiment can state an observation of the phenomenon of study. In other cases, an upper limit on the rate of the signal at 90 % confidence level (CL) is reported as the result of the experiment. The confidence level can be interpreted as the statement that there is a 90 % probability that the actual value of the signal rate is within the reported interval. This procedure is known as limit setting.

The performance of the limit setting heavily relies on the accuracy of the background model. Unless exactly all the parameters are proved to be carefully described, which is unlikely, we additionally introduce nuisance parameters. Usually, these parameters characterise the uncertainties in background levels and detector related systematic uncertainties.

In Chapter 5 we showed the excess of the pileup backgrounds, added them to the background model and presented the methods to reduce their levels in the ROI. In this chapter, to demonstrate the importance the pileup rejection analysis we set the limits of the $0\nu2\beta$ half-lives (and therefore effective neutrino masses) at 90% CL in the absence of signal before and after the cuts have been applied, and compare them.

6.1 Limit setting procedure

We set the limit by exclusion of the background model with additional signal contribution at certain significance level. The full statistical derivation of the limit setting procedure can be found in Appendix B. Here we present the general idea of the method and the final expression, which used to set the limit.

The statistical technique we use to set the limit is based on the likelihood ratio between the alternative (signal plus background) hypothesis and the null (background only) hypothesis:

$$\Lambda = \frac{L\left(\mathbf{n}|\mathbf{b}+\mathbf{s}\right)}{L\left(\mathbf{n}|\mathbf{b}\right)}, \tag{6.1.1}$$

where $\mathbf{n}$ is data, $\mathbf{b}$ is background and $\mathbf{b}+\mathbf{s}$ is background with signal contribution.

From this ratio we derive an expression for the Poisson likelihood test statistic χ^2 (see B for the detailed derivation), which is convenient to use with binned data. The test statistic can be used to quantify how good the model $\boldsymbol{\nu}$ describes the data $\mathbf{n}$ and is given by the following expression

$$\chi^2 = 2\sum_{i=1}^{N}\left[\nu_i - n_i + n_i \log\left(\frac{n_i}{\nu_i}\right)\right]. \tag{6.1.2}$$

Here i runs over the bins of the histograms and ν_i, n_i are bin contents of the corresponding histograms.

The lower the value of χ^2, the better the model describes the data. This quantity follows a chi-square distribution and can be used for goodness-of-fit testing and for the limit setting [163].

There are two cases of how the model can be fitted to the data. The first one, called a fixed background fit, corresponds to the situation when the parameters of the background model, such as background levels, energy resolution and detector efficiency are fixed and the only changing parameter is the amount of the signal contribution in the model. In the second case, called a fit with the floating parameters, the parameters of the model are not fixed and an additional optimization procedure is performed during the fitting.

In this thesis, we perform the fixed background fit in order to demonstrate the effectiveness of the pileup backgrounds rejection techniques, developed by the author. During the limit setting only the signal contribution to the background model is changing, so in this case, the χ^2 test statistic will depend only on the amount of the signal that has been added to the model. Each time varying the signal contribution, we calculate the difference

$$\varDelta\chi^2 = \chi^2 - \chi_0^2, \tag{6.1.3}$$

where χ^2 is the value of the test statistic for the current signal contribution and χ_0^2 is for the zero signal case. The upper limit on the signal (and the lower limit on the half-life) with 90 % CL is found when $\varDelta\chi^2 = 2.71$ [164].

6.2 A fixed background fit in SNO+

We performed the limit setting using the echidna software. Since there was no available data, we used the RAT 5.0.3 Monte Carlo simulations of the "fake data". The limits are obtained for 0.3% ^{130}Te loading after the first year of data taking. The signal and the background events are considered within the fiducial volume of 3.5 m.

In order to demonstrate the necessity of the pileup rejection and how it changes the limit on $0\nu2\beta$ half-life, we include pileup backgrounds and compare the two cases, with and without applying the specifically designed cuts (see Section 5.3.1). For their levels, we use the values from Table 5.5. We do not include the pileup backgrounds with ^{214}Bi to avoid double counting as we have proven that these behave like single ^{214}Bi events. Therefore, they are already rejected by the corresponding cuts and their residual events are included as internal backgrounds.

In both cases, we include ^{8}B, external and internal backgrounds. We use their levels (see Appendix A) left after applying all rejection cuts available at the time of writing this thesis except for the ones designed for pileup events. For this study, the levels are fixed.

In the limit setting procedure we used the following assumptions:

- isotopic abundance of ^{130}Te is 34.08%,
- atomic weight is 129.906224, [170]
- atomic weight of natural tellurium is 127.603, [170]
- phase space factor $G^{0\nu} = 3.69 \cdot 10^{-14}$, [171]
- nuclear matrix element $M^{0\nu} = 4.03$. [172]

By using the values of these parameters and the expression for the half-life of neutrinoless double beta decay.

$$\left(T_{1/2}^{0\nu\beta\beta}\right)^{-1} = G^{0\nu}(Q)\left|M^{0\nu}\right|^2 \frac{\left|m_{\beta\beta}\right|^2}{m_e^2}, \tag{6.2.4}$$

we can transform the lower limit on $T_{1/2}^{0\nu\beta\beta}$ into the corresponding upper limit on the effective neutrino mass $m_{\beta\beta}$.

In the first case, the obtained limit of $0\nu2\beta$ half-life, when major single-decay backgrounds and the pileup backgrounds before rejection are included is $T_{1/2}^{0\nu\beta\beta} > 1.951 \times 10^{25}$ years and the corresponding limit on the effective mass is $m_{\beta\beta} < 0.1494$ eV. The limiting number at 90% CL of $0\nu2\beta$ events in the ROI is 11.17. Counts of all background events in the ROI are listed in Appendix B.0.5, the total counts of single-decay background events in the ROI is 20.81 and the pileup backgrounds is 33.16. We also listed the counts of major internal backgrounds in Table 6.1. It can be noticed that the main type of backgrounds in the ROI is formed of pileup events. The spectral plot can be observed in Figure 6.1.

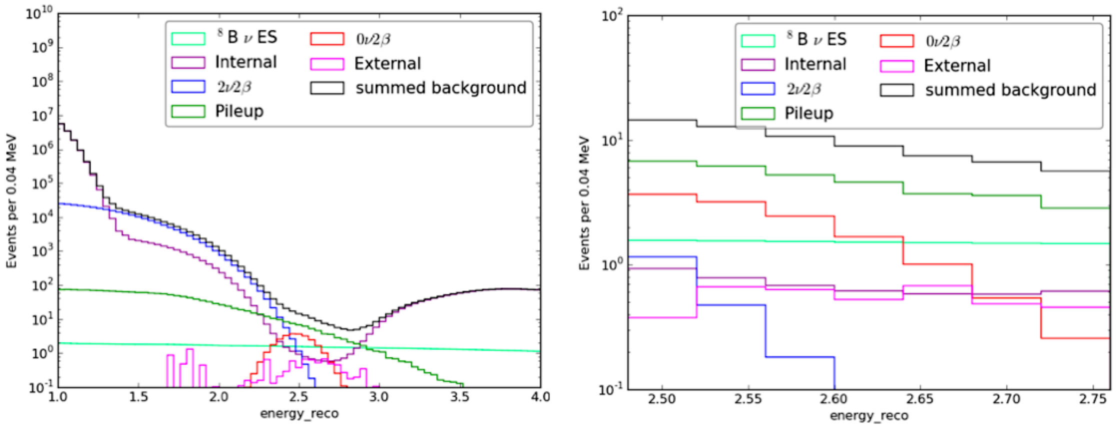

Figure 6.1: Spectral plot within the FV, produced by echidna software. All background events during the first year of running the detector with the 0.3 % Tellurium loading are scaled to levels from Appendix A and from Table 5.5. The Figure on the left shows the full energy region and the Figure on the right is a closer look at the ROI of ^{130}Te 0ν2β. The numbers of counts in the ROI are listed in Appendix B.0.5

Table 6.1: Counts of events in the ROI in the first year of running the Tellurium loaded detector. Here we sum up all pileup events except for the combinations with ^{214}Bi-decays.

Events	Counts in the ROI
^{130}Te 0ν2β	11.17
^{130}Te 2ν2β	1.90
^{8}B	10.60
^{212}Bi-Po	1.95
^{214}Bi-Po	0.27
Σ of pileup	33.16

In the second case, when we have applied the pileup rejection to the pileup events it has reduced their number down to 0.23 events in the ROI. The limit of 0ν2β half-life becomes $T_{1/2}^{0\nu\beta\beta} > 2.586 \times 10^{25}$ years and the corresponding limit on the effective mass is $m_{\beta\beta} < 0.1298$ eV. The limiting number at 90% CL of 0ν2β events in the ROI is 7.50.

6.3 Summary

We have shown in this chapter that without the rejection, the pileup background dominates greatly over all other background events in the ROI. We testified the developed rejection techniques described in Chapter 5 by improving the limit on $T_{1/2}^{0\nu\beta\beta}$ by 32.55 %.

In this study, we have undertaken the assumption that all rejection techniques are only applied to the backgrounds they are designed for. However, they can still be effective in reducing other types of events. Therefore, in further studies, all cuts will be revisited and optimised to show even better results.

Chapter 7

Development of an Yttrium-90 calibration source.

An ^{90}Y isotope is a pure beta-emitter with an end-point energy of 2.28 MeV with a half-life of 64 hours. For its decay scheme see Figure 7.1.

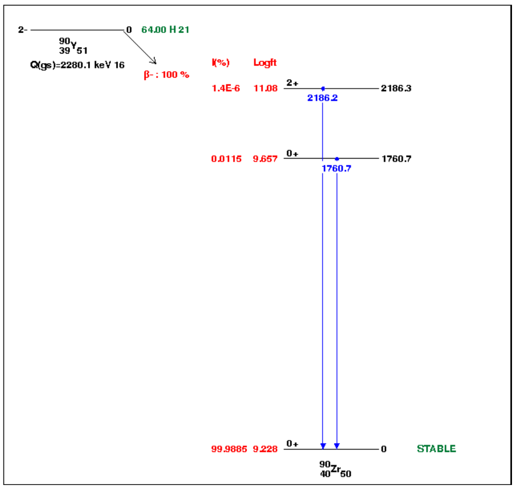

Figure 7.1: The decay scheme of ^{90}Y.

It was suggested to develop an ^{90}Y calibration source to test the position and the energy reconstruction in the Te-loaded scintillator [165]. The isotope has three clear advantages which make it a strong candidate:

1. Unlike other calibration gamma-sources described in Section 2.8.5, ^{90}Y will allow us to test the reconstruction of beta-particles, which is desirable since the signal of interest ^{130}Te $0\nu2\beta$ and some of the major backgrounds such as ^{130}Te $2\nu2\beta$, ^{210}Bi and ^{214}Bi are beta-events.

2. Due to its end-point energy, ^{90}Y will test the reconstruction across a wide energy region including the area near the energy ROI of [2.485, 2.733] MeV, see Figure 7.2.

3. The half-life of the isotope is relatively short, which allows us to obtain the sufficient statistics within a small exposure time. Particularly, after two weeks from the production of the 2 μL source, there will be 8.3×10^6 decays in 10 minutes[1]. At the same time, if the source leaks into the scintillator it will be possible to wait until it completely decays away[2]. In our case, in 95 days from the production, there will remain less than 1 decay per day.

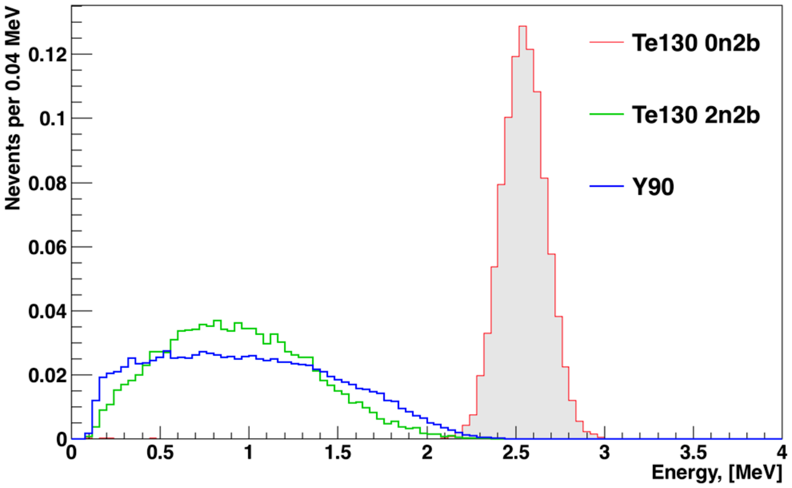

Figure 7.2: Energy spectra of ^{130}Te $2\nu2\beta$, ^{130}Te $0\nu2\beta$ and ^{90}Y.

Using ^{90}Y as a calibration source is an innovative idea. It is being developed for potential use in the Te-loaded phase after the $0\nu2\beta$-measurements are completed and if the results require additional supportive tests. The potential time-line of the deployment depends on the status and reliability of the source, i.e. the container must be proved to be safe. If deployed, the data from ^{90}Y with well-known characteristics will be an ultimate test of the output.

---

[1] The value is estimated with consideration of the activity of the full 1.4 mL sample of 370×10^6 Bq, see Section 7.4.1.

[2] It is be possible to deploy a source into the detector only if the construction is reliable and safe. We estimate the hypothetical worst case scenario when the entire 2μL source penetrates in the scintillator while the container stays unbroken.

7.1 Physics Motivation.

^{90}Y is planned to be amongst the last calibration sources deployed during the Te-loaded scintillator phase. In fact, it could only be deployed after all physics runs are finished to avoid the risk of contamination. By that time, the electronic and the PMT systems will be calibrated and the optical calibration and the calibrations using the gamma-emitting sources will already have taken place. Unlike the other calibrations where we tune certain parameters, we will use ^{90}Y to test the overall data reconstruction. The analysis will establish the systematic uncertainties which will be useful to understand measured properties of ^{130}Te $0\nu2\beta$ events.

There are several tests which are targeting different characteristics and based on their results the corresponding actions will be suggested. These are verifications of the light yield used in the simulations, the position reconstruction algorithms and its dependence on the position, and the energy reconstruction algorithms. All will be discussed further in this section.

7.1.1 Verification of models in RAT.

One of the first tests will be the comparison between the expected number of PMT hits and the number observed in the real data. This check will be able to verify such parameters of SNO+ simulations as light yield and the PMT responses. In this case, the outcome wouldn't be affected by the reconstruction model.

In order to demonstrate how the numbers of PMT hits from events depend on the light yield of the media, we simulated 100,000 events of the ^{90}Y point source placed in the centre of the AV for three different light yields of the scintillator cocktails, see Figure 7.3. We considered the light yields of 180 Nhits/MeV, 200 Nhits/MeV, and 220 Nhits/MeV.

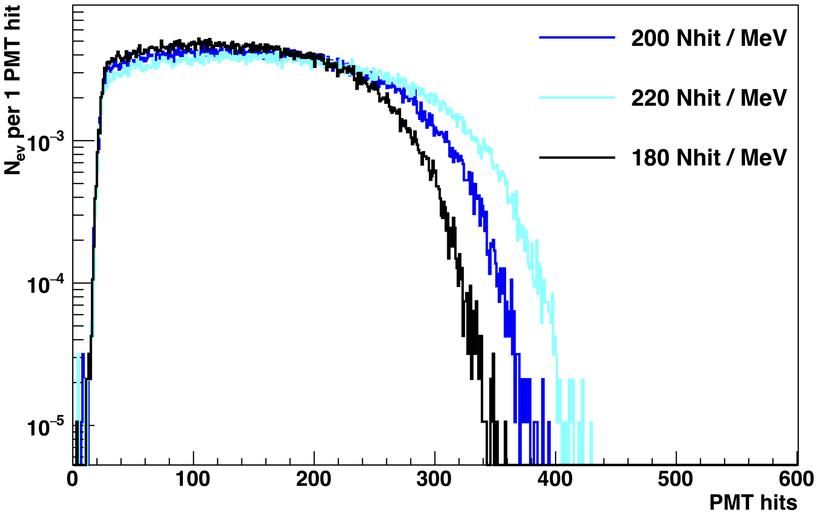

Figure 7.3: The comparison of the Nhits distributions of the ^{90}Y point source in three scintillator cocktails with different light yields.

7.1.2 Verification of position reconstruction algorithms.

The SNO+ position reconstruction will be tested using gammas from the laserball and gamma-emitting radioactive sources. However, the signal of interest and some of the major backgrounds emit betas, which interact with the scintillator differently. Therefore, repeating the calibration using ^{90}Y will allow us to describe the systematic uncertainty in position reconstruction across the energy region.

For the chosen source position, we compare the vertex reconstructed from the Monte Carlo simulations with the vertex obtained from the data. If the two are within the already established systematic uncertainties this will confirm that our expectations are in agreement with the data. If the difference is significant it will be considered as a systematic uncertainty. To make the estimations, we simulate ^{90}Y events emitted by the calibration source placed at a certain position inside the AV and reconstruct their event vertices. For each event, we then calculated the differences between the reconstructed and the true source positions in the three coordinates x, y and z and compile the corresponding histograms. We fit a Gaussian profile to each of these histograms and get the RMS deviation in each direction, σ_x,

σ_y and σ_z. The total resolution is calculated as:

$$\sigma = \sqrt{\sigma_x^2 + \sigma_y^2 + \sigma_z^2}. \tag{7.1.1}$$

The total reconstruction bias is calculated using the mean values μ_x, μ_y, μ_z of the Gaussian fits:

$$\mu = \sqrt{\mu_x^2 + \mu_y^2 + \mu_z^2}. \tag{7.1.2}$$

Since at the time of writing no data was available we estimated the resolution using the fake data and the true MC positions. We simulated 100,000 events of a point ^{90}Y source positioned in the center of the AV. We follow the procedure which has been described above and fit Gaussian profiles in each direction, see Figure 7.4. The total resolution and bias are σ_{tot} = 267.36±0.47 mm, μ_{tot} = 2.42±0.51 mm.

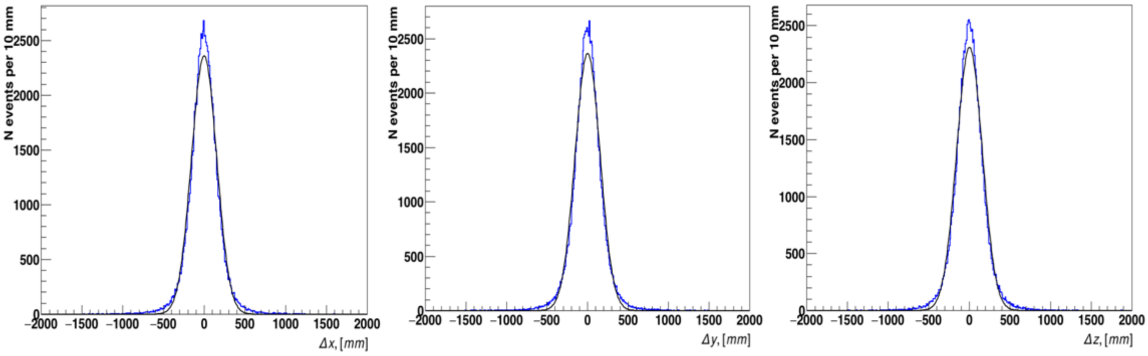

Figure 7.4: Directional resolution in position reconstruction: x-axis on left, y-axis in center, z-axis on right.

Position dependence of position reconstruction.

SNO+ reconstruction will be tuned in such a way that the events occurring within the FV of the detector will have the same position resolution and bias across this volume. In order to test this, the calibration sources will be positioned at the center of the detector and in various off-center positions. The ^{90}Y source will also be used in the same way.

7.1.3 Verification of energy reconstruction algorithms.

The calibration gamma sources described in Section 2.8.5 will be used to study the dependence of the energy resolution on the energy deposition. Each source, will provide us with the resolution in the corresponding regions. The fitted to those points function will determine a correction factor, which will be applied to the predicted reconstructed energy of an event.

Since ^{90}Y is a beta-emitter and has an end-point energy of 2.28 MeV it will be able to check the reconstruction smeared with the correction function across a wider energy region. We will simulate the source at a desired position inside the AV and compare the reconstructed energy spectra of simulation and real data. If the two do not coincide within the systematic and statistical uncertainties, we will quantify the difference.

7.2 ^{90}Y Strategy.

In order to develop the calibration source, we identified its geometry performing the Monte Carlo simulation using RAT 5.0.3 with respect to the possibility of implementation, i.e. availability of components, and the possibility of technical realization.

We investigated the feasibility of making the source and through testing and practice developed a procedure which could be repeated. During the production, a number of risks was identified making deployment of the source into the detector challenging.

The capillary was noticed to be very fragile and hence there were high chances of breaking it whilst placing inside the AV. A more reliable container will inevitably prevent betas from escaping. Placing the capillary inside a flask filled with scintillator will make the calibration source inaccurate, as the scintillator is not necessarily identical to the one inside the detector. Other concepts of double encapsulation of ^{90}Y are not effective because the source will stop being a point source.

Due to its delicate nature, the source must be manufactured in a laboratory closely located to the experimental setup, otherwise, it might be damaged during transportation. Such a condition is not always achievable. There are no available radioactive laboratories near SNOLAB and it is prohibited to work with the radioactive materials elsewhere. The availability of a laboratory is defined by the possibility of using the facilities and the permission to work with radioactive materials in the country where the laboratory resides.

Hence, the priority of this study shifted towards developing the source for an external test setup. The source was tested in two laboratories, the radioactive laboratory of the University of Sussex and the laboratory in the University of Pennsylvania. The test in the first setup primarily verified the possibility of observing ^{90}Y decaying over time. In the second setup, we periodically placed ^{90}Y in three scintillator cocktails to compare the distributions of PMT charges and to quantify relative performances in different media.

7.3 ^{90}Y calibration source design.

The calibration source consists of an ^{90}Y isotope suspended in liquid and a container to securely deploy it into the detector. The choice of the geometry of the calibration source is mainly driven by the possibility of the implementation. Hence whilst following the general requirements we perform the simulations to support the choice rather than to make it.

One of the requirements for the container is simplicity. There should be no easily detachable components or sharp edges. Such a geometry can be accurately modelled and manufactured, and the physics of the process inside it will be straightforward. During the manipulations inside the AV, such as lowering, lifting and changing the position, the robust container must not fall apart or lose components. Another requirement for the container is to cause a minimum energy loss to escaping electrons due to attenuation inside the source.

We have chosen to use a cylindrical-shaped container with an ^{90}Y source positioned inside it as an accessible solution, which also satisfies the requirements. A basic design of the calibration source, containing the source in a thin capillary, can be observed in Figure 7.5. Once the source is placed in a satisfactory position, the ends of the capillary will be sealed to avoid contamination.

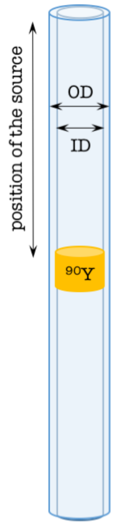

Figure 7.5: The basic design of ^{90}Y calibration source. A height, an inner and an outer diameter of the container can be chosen, as well as the size of ^{90}Y droplet and its position along the container.

The most suitable tube-shaped container identified is a hollow round micro capillary, manufactured by CMS Scientific [166] mostly for scientific and clinical applications, see Figure 7.6. The shortest length of available capillaries is 10 cm, while the diameter can vary from 0.08 mm to 2.4 cm. For example, the thickness of a capillary of small outer diameter can be 0.01 mm, while for larger outer diameters thicknesses of the walls vary between 0.1 - 0.2 mm.

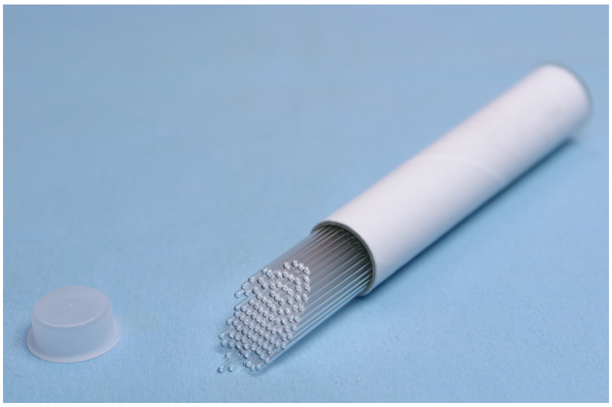

Figure 7.6: Micro capillaries used as a container for the ^{90}Y-source.

We have chosen to use the shortest available capillary to decrease chances of breaking it because pushing the source along the capillary is a delicate procedure. Besides, since we aim to use a small amount of ^{90}Y, there is no need for the remaining parts to be larger. In principle, it is possible to shorten a capillary by melting off or splitting off a piece from one of the sides. Such a procedure is difficult in execution and even if succeeds, it will reduce the solid angle of the remaining end, which will complicate the following sealing. Moreover, the source has to be away from both ends not to be affected by the heat when we seal them.

The requirement for the source is limiting its size. A droplet of ^{90}Y must be small enough to be approximated by a point source, however its dimensions are defined by manufacturing possibilities.

7.3.1 Material of capillary.

The micro capillaries can be made either of borosilicate glass or of fused quartz[3]. Since the edges must be sealed by melting, the material with a lower melting point is easier to work with and hence more preferable. The melting point of fused quartz is 1665 °C [166] and it is valued for withstanding high temperatures, while borosilicate glass can start softening at 820 °C [168]. Although it is possible to melt fused quartz with the flame from a blowtorch (T = 2200 °C), it will require more time and will increase the chances of movement and evaporation of the acid in which ^{90}Y has been mixed. Therefore, for the sake of simplicity in the manufacturing, we have chosen to use glass capillaries. Due to the minor advantage of quartz, it was decided to investigate this option to improve results obtained with glass capillaries.

To investigate how the choice of the material would affect the results of the calibrations we have compared the two cases when a droplet of ^{90}Y-source is positioned inside the glass capillary and inside the quartz capillary. The reconstructed energy spectra can be observed in Figure 7.7a.

---

[3] This information is based on the available supplier CMS Scientific [166].

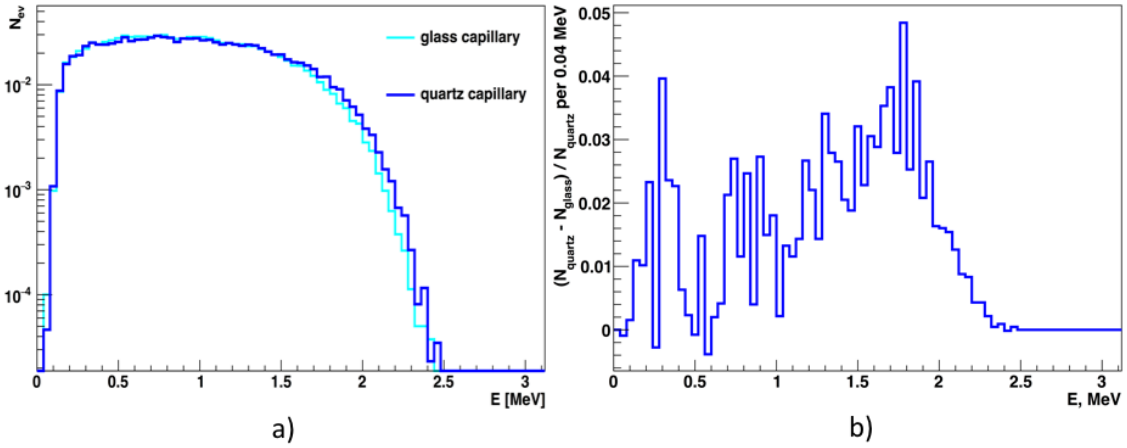

Figure 7.7: Comparison of materials of micro capillaries. The simulations were performed for 100,000 events using RAT 5.0.3. An ^{90}Y-droplet of 2 μL is positioned in the centre of the capillary, which itself is in the centre of the detector.
(a): The reconstructed energy spectra for glass and for quartz capillaries.
(b): The difference between the number of reconstructed events from quartz and from glass capillaries, see Eq. 7.3.3.

Unfortunately, the electrons emitted from the ^{90}Y-source attenuate more in the walls of the glass capillary. The level of the reconstructed events from the glass capillary is 79.7% against 86.2% from the quartz capillary. To demonstrate the difference, we histogram the ratio d:

$$d = \frac{N_q - N_g}{N_q}, \tag{7.3.3}$$

where N_q is the number of reconstructed events from the quartz capillary and N_g from the glass capillary. The resultant histogram can be observed in Figure 7.7b. The total difference between the two materials across the whole energy region is 7.5%. However, we will be able to compensate such a difference with a longer exposure time.

7.3.2 Diameter of capillary.

The minimal inner diameter (ID) of the capillary with respect to possibilities in production is 1.0 mm. In order to insert the source into a capillary with a smaller ID, a needle-like tip would be required, which is prohibited due to safety regulations.

Therefore, the smallest capillary possible to use is of [1.0 mm; 1.2 mm][4]. The only other available larger-sized capillary is of [2.0 mm; 2.4 mm], which has not only the larger inner diameter but also the larger thickness of the walls. Hence, the escaping electrons will attenuate in the source itself and in the glass volume more than in the case of the capillary of [1.0 mm; 1.2 mm], see Figure 7.8. The strongest effect of attenuation can be observed in the tails of the energy spectra. The level of the reconstructed event in the case of the capillary with the larger diameter is 66.7%.

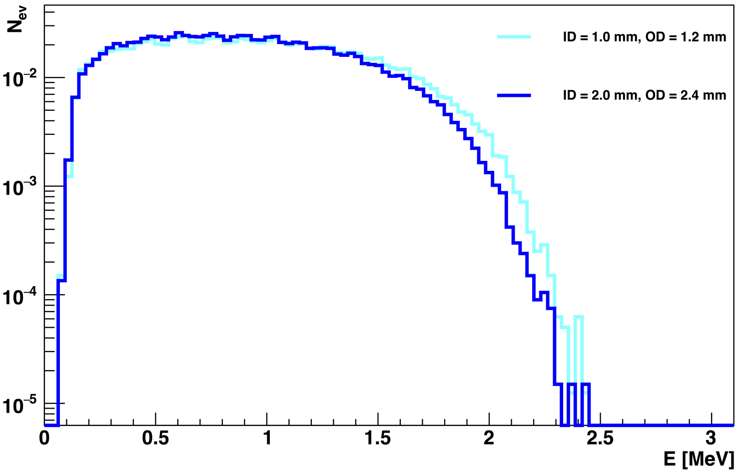

Figure 7.8: Comparison of diameters of micro capillaries. The difference between the energy spectra in the cases of [1.0 mm; 1.2 mm] and [2.0 mm, 2.4 mm] diameters is shown. The simulations were performed for 100,000 events using RAT 5.0.3. An ^{90}Y-droplet of 2 μL is positioned in the centre of the capillary, which itself is in the centre of the detector.

In addition to worsening the physics capabilities of the calibration source, the larger diameter of the capillary makes it more difficult for sealing. The larger the air gap is, the more time and manipulations are required. Thus, we have chosen to use capillaries with an inner diameter of 1.0 mm and an outer diameter of 1.2 mm.

7.3.3 Height of ^{90}Y in capillary.

The amount of ^{90}Y, and therefore the height of the droplet, can't be large, as it stops being approximated by a point, which is especially noticeable in the table-top

---

[4] Throughout this chapter, we will use the following notation of diameters of a capillary: [ID, OD].

experiment. At the same time injecting a small amount of the source might be problematic due to surface tension. Based on practical reasons we decided to inject 2 μL of the source, which is 2.5 mm height inside the capillary with ID of 1.0 mm.

7.3.4 Position of ^{90}Y along capillary.

The final check performed was an investigation of sensitivity to the position of the ^{90}Y source along the capillary. Although neither attenuation of emitted electrons nor decrease in reconstruction level are noticed depending on the source position the droplet is planned to be placed approximately in the middle or slightly shifted towards the bottom end of the capillary. This is done to avoid attenuation of electrons in the plastic holder attached to the capillary, see Figure 7.12. At the same time, the source shouldn't stay near the end of the capillary, as it might be affected by the flame from the blowtorch.

To conclude, the calibration source will be a glass micro capillary (ID = 1.0 mm, OD = 1.2 mm), with ^{90}Y placed near the centre. Simulations have shown that these practical dimensions give acceptably low beta attenuation and the tolerance in exact source position is not too limiting.

7.4 ^{90}Y calibration source production.

After defining the parameters, we prepared the procedure of manufacturing the calibration source, taking into account safety of personnel and ease in production. Plastic elements required for the production and secure usage of the source were designed and machined in Queen Mary University of London. The production of the calibration source took place in the University of Sussex radiation laboratory (see Figure 7.9). Prior to working in the laboratory all personnel obtained necessary training and received the licence to work with radioactive materials.

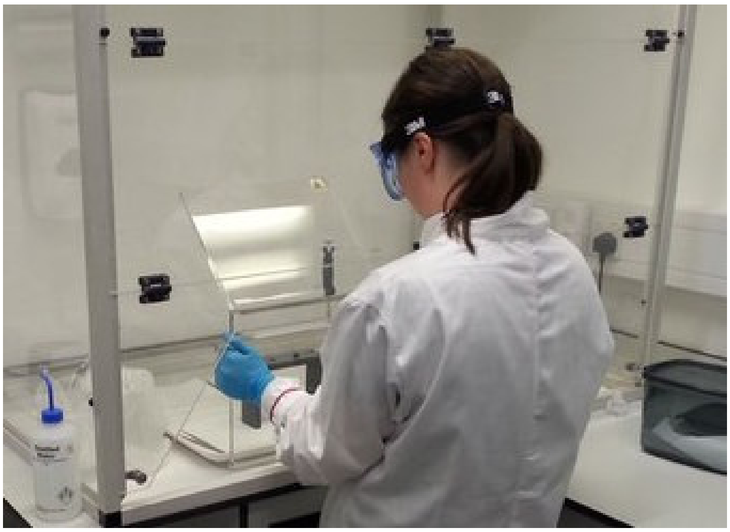

Figure 7.9: Radioactive laboratory in the University of Sussex. The author of this thesis is preparing the calibration source.

7.4.1 ^{90}Y source.

^{90}Y is a daughter isotope of ^{90}Sr (for decay scheme see Figure 7.10), which is a fission product of ^{235}U. Due to important applications of ^{90}Y, such as treatment of various cancers, the medical industry has developed a process of separating this isotope with a high purity[5].

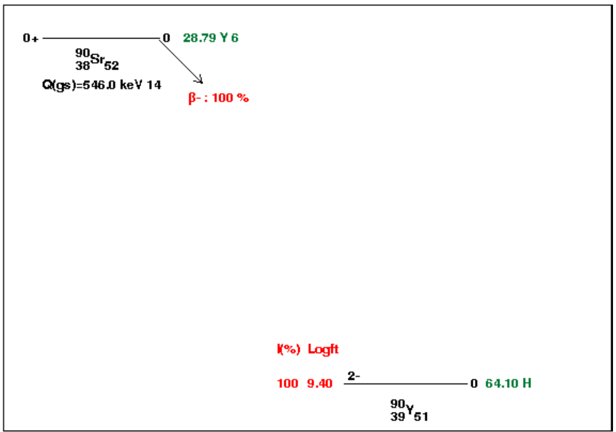

Figure 7.10: The decay scheme of ^{90}Sr.

We used ^{90}Y obtained and supplied by Perkinelmer Inc. [167]. The quality of the ^{90}Y source is very important, as all possible impurities can affect the analysis, if they will have long half-lives. We manufactured the calibration sources twice,

---

[5] This process is patented and the exact details are not publicly available.

using different ^{90}Y samples. The samples had the same full volume of 1.4 mL, but different activities of the isotope. Each sample was delivered in a NENSure vial, see Figure 7.11.

Figure 7.11: A vial for an ^{90}Y source. In the picture the vial is filled with water for training purpose. A vial with radioactive source is never taken outside of the container.

We manufactured the calibration source to test it in the University of Sussex using ^{90}Y from the first sample. As assured by the supplier, the activity of ^{90}Y in the whole sample at the time of calibration on 26/03/2013 at 18:00 CET was:

$$A_Y = 10 \text{ mCi} = 370 \cdot 10^6 \text{ Bq}. \tag{7.4.4}$$

Activity of ^{90}Sr in the whole sample was:

$$A_{Sr} = 8 \cdot 10^{-9} \text{ Ci} = 296 \text{ Bq}. \tag{7.4.5}$$

We used ^{90}Y from the second sample to perform the calibration source to take measurement in the University of Pennsylvania. As assured by the supplier, activity of ^{90}Y in the whole sample at the time of calibration on 12/02/2015 at 18:00 CET was:

$$A_Y = 12 \text{ mCi} = 444 \cdot 10^6 \text{ Bq}. \tag{7.4.6}$$

Activity of ^{90}Sr in the whole sample was:

$$A_{Sr} = 12 \cdot 10^{-9} \text{ Ci} = 444 \text{ Bq}. \tag{7.4.7}$$

7.4.2 Source capillary preparation procedure.

All manipulations with radioactive sources are performed inside the fume cabinet, which is turned on once the procedure starts. Only trained and authorized personnel are allowed to be in the laboratory. In this section we describe the key points of manufacturing the ^{90}Y calibration source, the full approved step-by-step procedure can be found in Appendix C.

Prior to manufacturing of an actual calibration source, we have tested meticulously each step of the procedure using water and ink. Performing a large amount of tests allowed us to evidence different outcomes of each step.

1. Described in Section 7.3 the capillary by itself is not practical to use due to several reasons. Holding it without extra shielding from radiation is dangerous (and will not be approved). Moreover, such capillary is difficult to handle during any part of manufacturing process. Therefore, we have designed a "stopper", a plastic cylinder, 1 cm in diameter 1 cm high, to be glued in place 2-3 cm from the end of the capillary at least 24 hours in advance to allow the glue to dry out (see Figure 7.12). Capillaries should be only held by the stopper once it is in place.

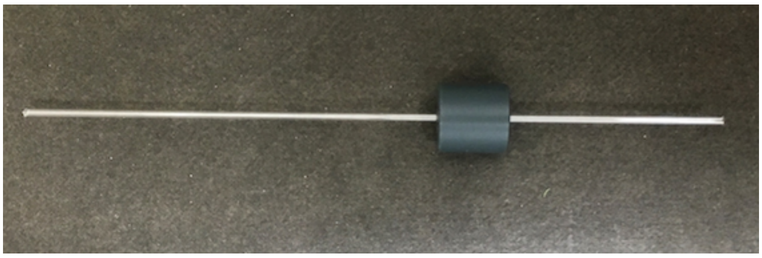

Figure 7.12: The capillary with the glued stopper.

2. Injecting ^{90}Y into the fragile capillary while holding it by hand introduces high risks of accidental breakage and direct contact with the source. To prevent that, we have designed a plastic stand (see Figure 7.13), where the capillary is placed supported by the stopper.

Figure 7.13: A plastic stand to support the capillary at the time of injection of an ^{90}Y droplet. A plastic holder is positioned to illustrate where a capillary is placed during the procedure.

The stand is placed behind a perspex radiation shield in the fume cabinet standing in the drip tray, which is lined with the Benchkote absorbent lab paper (see Figure 7.14). This precaution stops radioactive contamination especially in a situation where the capillary breaks.

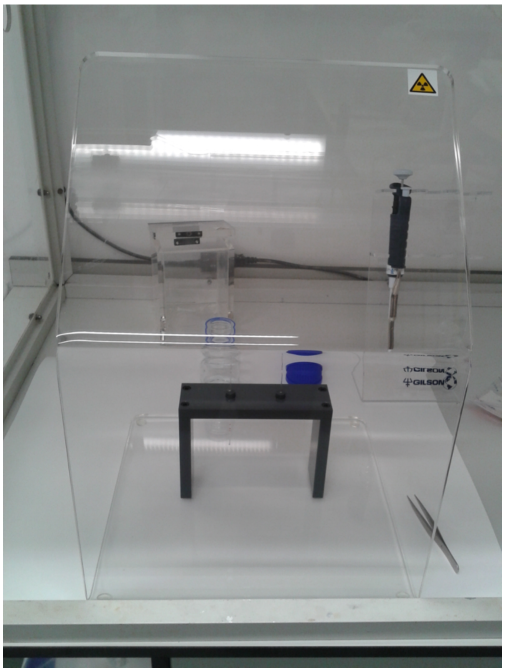

Figure 7.14: A section of the fume cabinet with perspex radiation shield.

3. The source is injected using a Gilson pipette (see Figure 7.15) with dial set to 2 μL. Each time a new plastic tip is attached by tweezers to prevent contami-

nation and to allow us to easily remove the used tip.

Figure 7.15: A Gilson pipette to inject the ^{90}Y source.

The source must be transferred to the capillary in one movement. The accuracy in this procedure is very important to avoid accidental breakage, as the diameter of a plastic end of the pipette is only slightly smaller than the inner diameter of the capillary, see Figure 7.16.

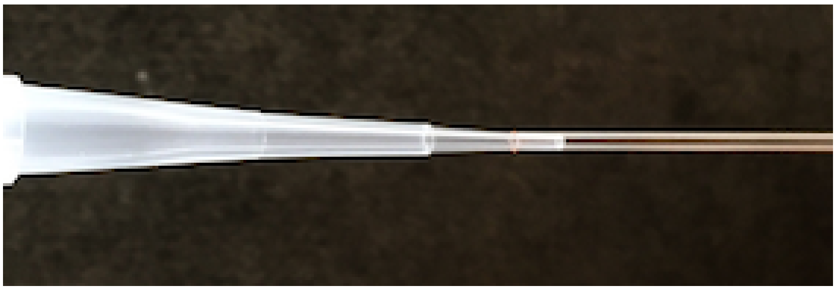

Figure 7.16: The capillary and the tip of the pipette.

After ^{90}Y is placed in the capillary, it must be moved to a desirable position, which is halfway between the bottom of the capillary and the stopper. This can be done by air injections. Therefore, a new tip must be attached to the pipette and the dial set to 5 μL. It was noticed that inaccurate air pipetting could split the ^{90}Y into small droplets and hence the source was not considered as a point source. Although accidental breakage of the capillary might happen at every stage of the manufacturing procedure, pushing the source and air are the most dangerous processes.

4. Once the source is in place, the edges of the pipette must be sealed using a blow torch. We empirically estimated that directing the central point of the

flame at the top of the capillary for 10-20 seconds provides the best seals. There are three methods to identify if the seal is acceptable. The easiest check is performed straight away by visual inspection of the melted ends with a magnifying glass. This will show if the seal has not been finished, i.e. the top part of the capillary is still open. Another problem is noticed to appear, if the blow torch is placed too close to the capillary. In this case a glass bubble will be created at the edge of the capillary. This seal will both make the capillary too fragile and too big for future usage.

5. If the seals look acceptable under the magnification, they are tested with techniques specifically developed for this study. For the next round of tests we designed the capillary washing container (CWC), see Figure 7.17, aiming to check the seals by tracing the movement of the source and possible external contamination.

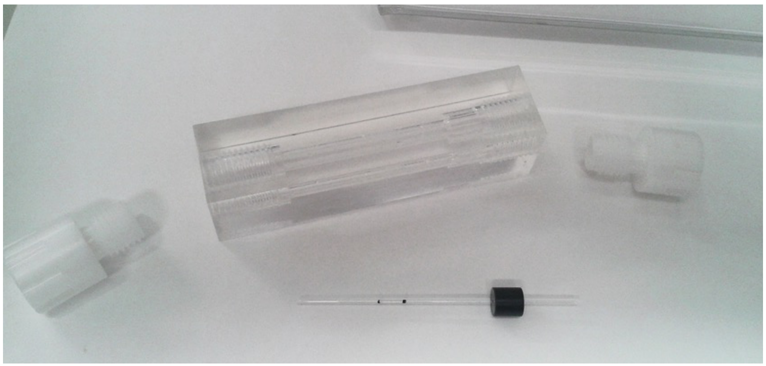

Figure 7.17: A capillary washing container (CWC).

We tag the exact location of the source in the capillary, by marking against a piece of paper and then using tweezers, transfer it to the CWC, which is then filled to about 60% capacity with ultra pure water. We gently shake the CWC for about a minute that allows the water circulation, while the capillary is securely held. Afterwards, when the capillary is removed, the position of the droplet is compared against the original. It was observed that such a change in a location is possible only if a seal is noticeably bad. The collected water is checked for radiation by the Geiger counter in case of transfer of radiation from the capillary outside.

Finally, in order to check the seals we perform pressure tests. A good seal must keep the pressure inside the capillary, and therefore prevents movement of the droplet. We place the capillary in the hand-pump vacuum chamber, Figure 7.18 and pump air out (at least 40 pumps)[6]. If the droplet either moves or splits into smaller droplets under vacuum, this will indicated a poor seal and has to be repeated.

Figure 7.18: A vacuum canister air pump used to test the sealing of a capillary.

Unfortunately, pressure tolerance of the capillary requires a thorough study before the source could be approved for deployment in SNO+. Using laboratory chamber with deep vacuum (10^{-4} mBar) showed that the seal might even break during the test and contaminate the setup.

6. If the source passes all these test, it can now be transferred directly into the dark box experimental setup for measurements or into the capillary transport container (CTC), see Figure 7.19. This perspex container is designed in a way that the capillary is tightly held inside by the stopper and at the same time allows us to remove the capillary with tweezers.

---

[6] This product is supplied for food storage and therefore, vacuum specification was not avaliable. However, test on both good and bad capillary samples showed the validity of this test.

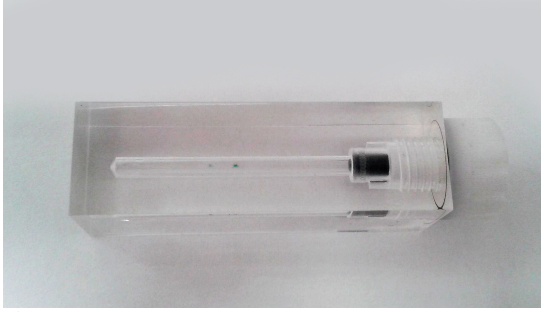

Figure 7.19: A transportation container for the capillary (CTC).

We manufactured several sources to perform tests in the University of Sussex and shipped two capillaries placed inside CTCs to the University of Pennsylvania.

7.5 Tests in the University of Sussex.

The first measurements of the calibration source were taken in the radioactive laboratory of the University of Sussex, aiming to prove the possibility of observing the source. For this study we designed an experimental setup described below.

7.5.1 Experimental setup.

All components of the experimental setup except for a Tektronix MSO2024 oscilloscope were positioned inside a custom made dark box (1 x 1.5 x 1.5 m) which was inherited from Oxford University. The core of the box is a metal construction, holding acrylic plates. Since there was an output for wires in one of the walls, penetrating light was reflected by bare parts of wires and the metal base. We covered the base and partially the wires with felt. The box was constructed in a way that its parts could be detached. Performing tests with LED light showed light leaks in areas of connections and openings for wires. Therefore, the box was covered with black felt. The components inside the back box are described below.

- A disk shaped vessel (with diameter D = 6 cm) filled with LAB PPO (see Figure 7.20a). The vessel was designed to be large enough to accommodate the capillary and attenuate the betas completely but not so large to worry about any appreciable cosmic ray background. The capillary was placed inside the vessel supported by the stopper. The end with ^{90}Y was immersed in the scintillator. In order to increase the light collection efficiency we added the mirror mall to one of the walls of the original vessel (see Figure 7.20b). To decrease the saturation of oxygen in the scintillator, we bubbled it with nitrogen gas for several minutes.

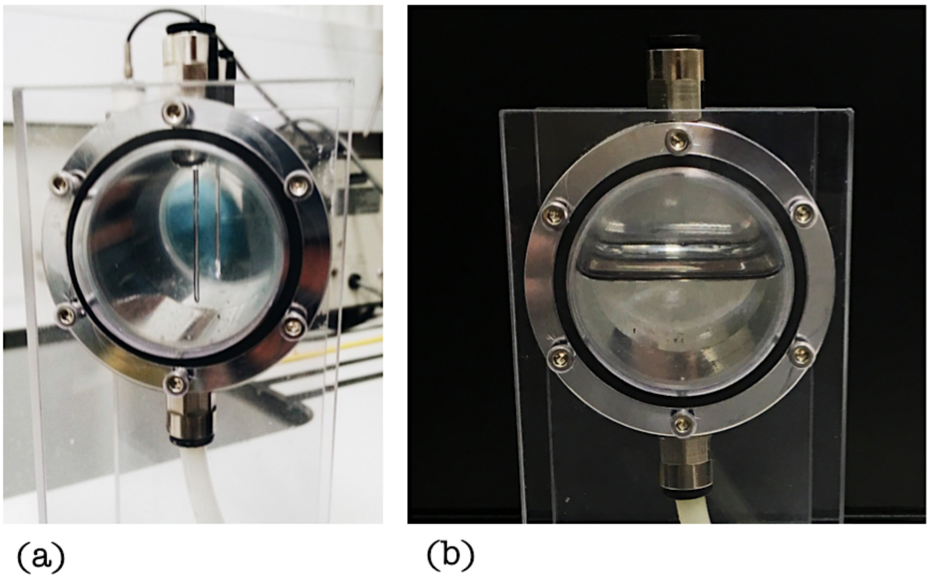

Figure 7.20:
(a) The original vessel filled with LAB PPO
(b) The vessel with added mirror wall. The picture was taken when we were refilling the vessel.

- The signals were obtained by Hamamatsu 38 mm R980 PMTs placed in front of the vessel.

Signals from the PMTs were read out via the oscilloscope and analysed by custom written programs using a LABVIEW interface and Python.

7.5.2 Measurements in Sussex University.

The main purpose of holding an initial test in the radioactive laboratory at Sussex University was to confirm that observing an ^{90}Y decay was plausible. Due to the small volume of the vessel and high decay rate of ^{90}Y the contribution from cosmic ray muons could be considered negligible. Prior to deploying the source, we measured the scintillator noise by taking the readout from pure scintillator inside the vessel.

Three days after the calibration source was manufactured, we started data taking that was performed periodically for some time. ^{90}Y spectra at each day can be seen in Figure 7.21. The scintillator noise was subtracted from all distributions.

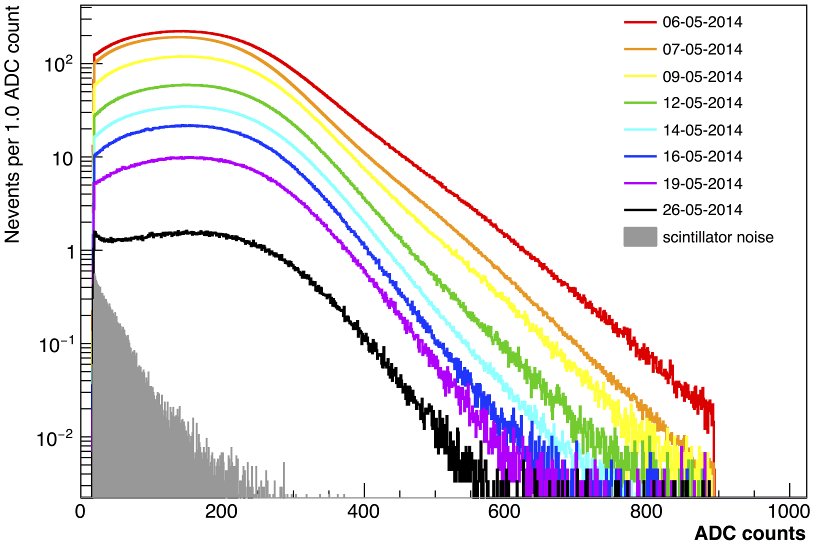

Figure 7.21: Spectra of ^{90}Y-decay over time.

Data obtained on the 6th of May, when the activity of the source was high, demonstrates pile up between multiple decays in the same readout window. The spectrum obtained in the last day, when the source cooled down considerably, can be seen in Figure 7.22.

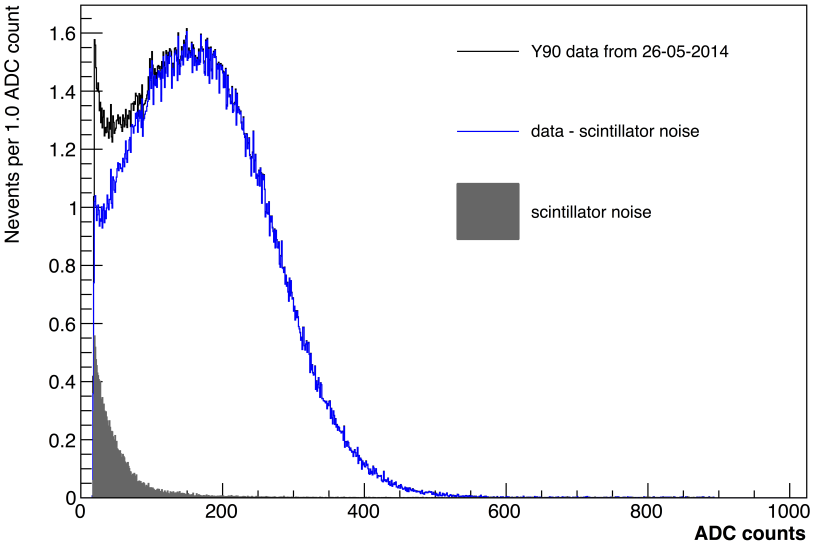

Figure 7.22: An ^{90}Y spectrum and the pure scintillator background.

Unfortunately, the setup was too small to see the full γ capture to perform an accurate calibration.

We estimated the half-life of the calibration source, based on the distribution of the counts on a day by day basis and compared it to the half-life of ^{90}Y. Every time the data was accumulated during a certain time period (usually about 900 s). We scaled the number of collected counts over time to get an activity of the calibration source. To build the distribution, we assigned the activity to the middle of the data taking time block, see Figure 7.23.

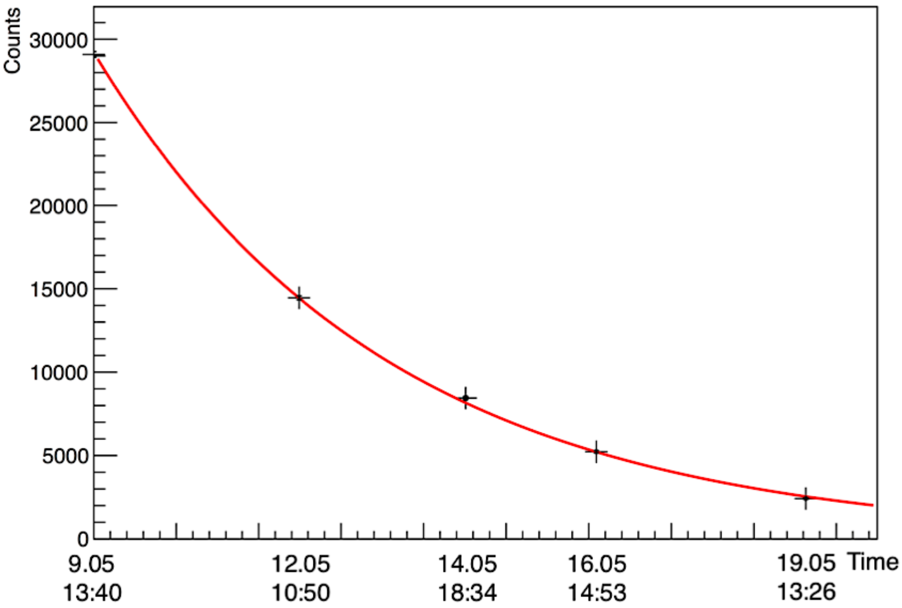

Figure 7.23: Count rate of calibration source over time. On x axis, we give the dates and times when the measurements took place.

Performing TMinuit fitting with A(t) $= e^{C} \cdot e^{S \cdot t}$ we get the parameters:

- Constant $C = 29208.8 \pm 156.634$,
- Slope $S = -2.82742 \cdot 10^{-6} \pm 1.64505 \cdot 10^{-8} \mathrm{s}^{-1}$.

Hence,

$$T_{1/2} = -\frac{\ln 2}{S} = \frac{\ln 2}{2.82742 \cdot 10^{-6}} = 68.1 \text{ hours.} \tag{7.5.8}$$

From the error of the slope we calculate the uncertainty in the calculations of the half-life

$$\delta T_{1/2} = \delta \left(-\frac{\ln 2}{S} \right) = 0.4 \text{ hours} \tag{7.5.9}$$

Therefore, the half-life of the calibration source from is

$$T_{1/2} = 68.1 \pm 0.4 \text{ hours} \tag{7.5.10}$$

This is not in a precise agreement with the actual half-life of ^{90}Y ($T_{1/2}^{real} = 64$ hours). Possible reasons for this can be contamination with long lived isotopes and pileup events presenting in ^{90}Y spectra.

The performed test confirmed that the observed spectrum is dominated by ^{90}Y-decay in the first order. Since we used the simple bench top experiment with the single uncalibrated PMT and no DAQ system, an accurate result was not expected. Nevertheless, we accomplished the goal of this test and concluded that it would be possible to observe ^{90}Y-decay in a larger scale setup.

7.6 Tests in the University of Pennsylvania.

We shipped two capillaries to the University of Pennsylvania to use it for testing three scintillator cocktails. At the time of writing, two wave-length shifters, bisMSB and Perylene, were considered. Hence to support either choice various groups were performing the comparison using the Monte Carlo simulations. The goal of making the laboratory ^{90}Y tests was to physically observe the difference and quantify the relative performances of the cocktails.

7.6.1 Experimental setup.

All components of the setup except for the data acquisition system were positioned inside a 2m x 2m x 0.9m dark box, see Figure 7.24. The dark box was made of wooden plates attached to the floor. The edges of the lid were lined with silicon to make a tight connection. The floor, the wires and the dark box itself were covered with felt. During the data taking the light in the laboratory was turned off in case the box wasn't completely isolated from light leaks.

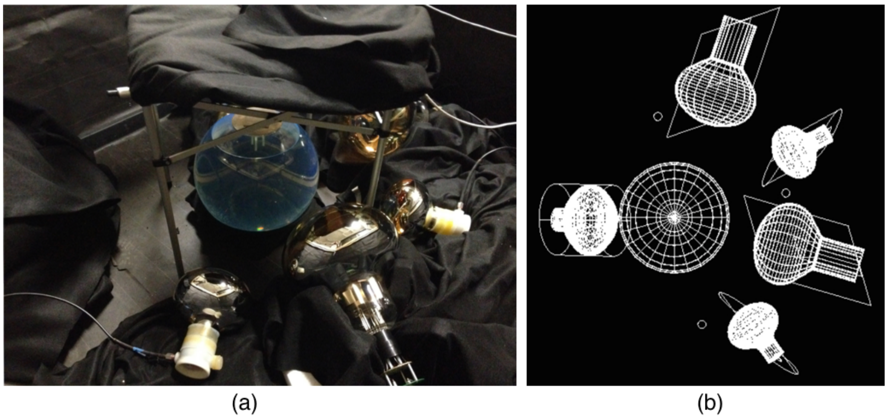
(a) (b)

Figure 7.24: Experimental setup in the University of Pennsylvania. The vessel with scintillator is in the middle, the two larger PMTs are R11780-HQE, the smaller PMTs are R1408.
(a): The photo of the setup (b): Visualization of the setup.

There were three available scintillator cocktails in the laboratory: LAB PPO, LAB PPO with a wavelength shifter Perylene and LAB PPO with a wavelength shifter bisMSB. To run the tests a liquid was filled into a large spherical acrylic vessel with the diameter of 40 cm, which can be seen in the middle in Figure 7.24. To study different scintillators, they were substituted using an additional vessel and the pump.

The capillary was loaded into the vessel by a custom made mount, see Figure 7.25. The dowels were made of plastic and the cup to hold the capillary was made of acrylic.

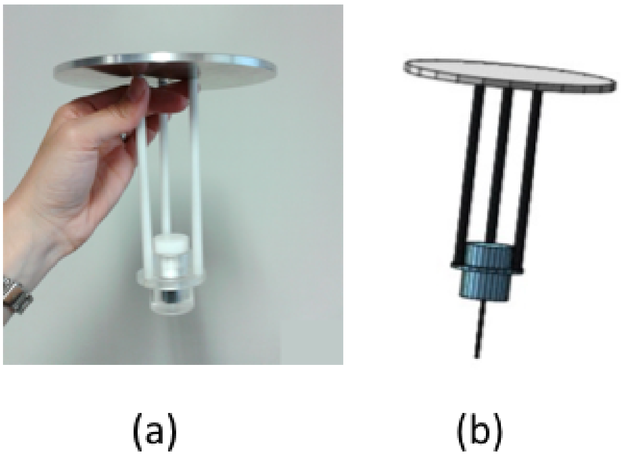

Figure 7.25: The mount to load the capillary. The capillary will be placed inside the acrylic cup in the middle and will be held by the stopper. (a): The photo of the mount. Here the cup is closed with the white lid for the transportation. (b): Visualization of the mount with the capillary inside it.

The signals from the capillary were obtained by five Hamamatsu PMTs positioned in a semicircle around the vessel. An ETL-9354KB PMT was used as the trigger PMT; other PMTs were recording the data: two R11780-HQE PMTs and two R1408 PMTs that were previously used in the SNO experiment.

7.6.2 Measurements in the University of Pennsylvania.

Performing measurements we encountered several technical difficulties. Due to the short half-life of ^{90}Y, we were taking the measurements whilst still commissioning the setup. A number of occurred problems were beyond control and complicated the analysis. These difficulties were introduced by the change of the oscilloscope during the study, mixed connections of the channels, and breakage of one of the capillaries inside the tank.

The source delivered to the University of Pennsylvania stopped being a point source. Due to pressure changes during the transportation (plane delivery) ^{90}Y distributed non-uniformly along the capillary volume. Therefore, the Monte-Carlo modelling of such a source could not accurately describe the geometry.

A further complication was because none of the PMTs were calibrated prior to running the test with ^{90}Y. Thus we were analysing data from each PMT separately.

In order to introduce a PMT response to the simulated data, we measured a single photoelectron spectrum (SPE) of each PMT with a laboratory ^{90}Sr source placed at a distance of about 1 m. The distributions of two R11780-HQE PMTs can be seen in Figure 7.26. We then convolved the corresponding SPE spectrum with the simulated events using the approach of random sampling and compared the new spectrum with the real data.

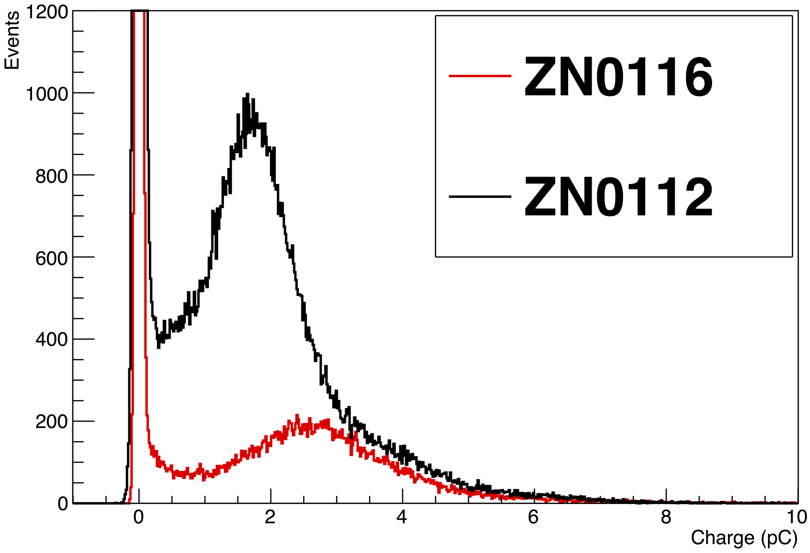

Figure 7.26: SPE distributions of two R11780-HQE PMTs: ZN0116 and ZN0112.

Another complication was introduced by the geometry of the setup which was just established and wasn't fully understood and tested prior to the measurements with ^{90}Y. As a result, the shapes of simulations and real data were fundamentally different.

We took measurements of ^{90}Y in all scintillator cocktails periodically and also took data with a laboratory ^{60}Co disk source that was placed outside of the tank. The ^{60}Co (for decay scheme see Figure 7.27) was used as a calibration source.

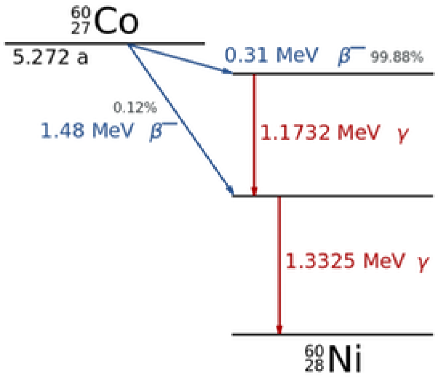

Figure 7.27: The decay scheme of ^{60}Co.

We simulated ^{60}Co and fitted the simulations to the data using scaling and shifting parameters. We then applied the same fitting parameters to the simulated ^{90}Y. The resultant histograms are shown in Figure 7.28. As was mentioned above, due to lack of experience working with the setup we weren't able to accurately describe its geometry, which together with other complications resulted in an inaccurate Monte Carlo model. Despite that, by comparing data from the different scintillator cocktails on the same PMT proves a change in light yield, see Figure 7.29.

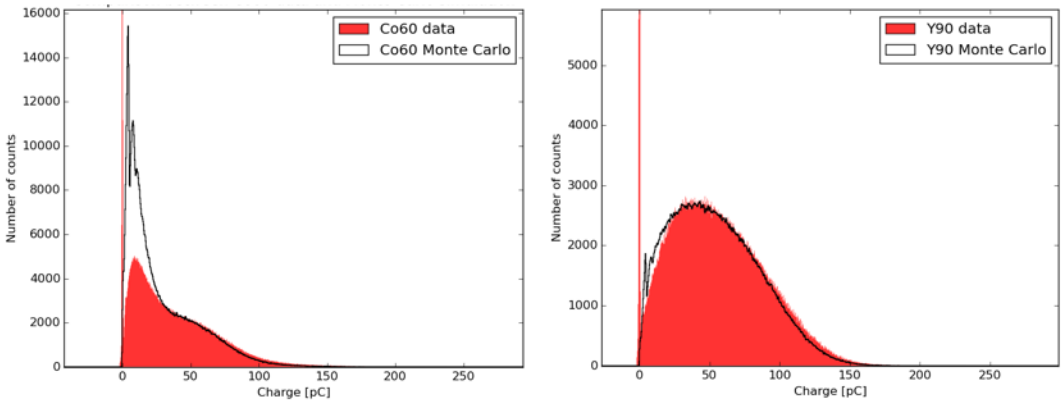

(a) (b)

Figure 7.28: Comparison of simulated ^{60}Co and ^{90}Y sources and real data. The simulated spectra were convolved with the SPE peak of the ZN0116 PMT.
(a): ^{60}Co spectra.
(b): ^{90}Y spectra.

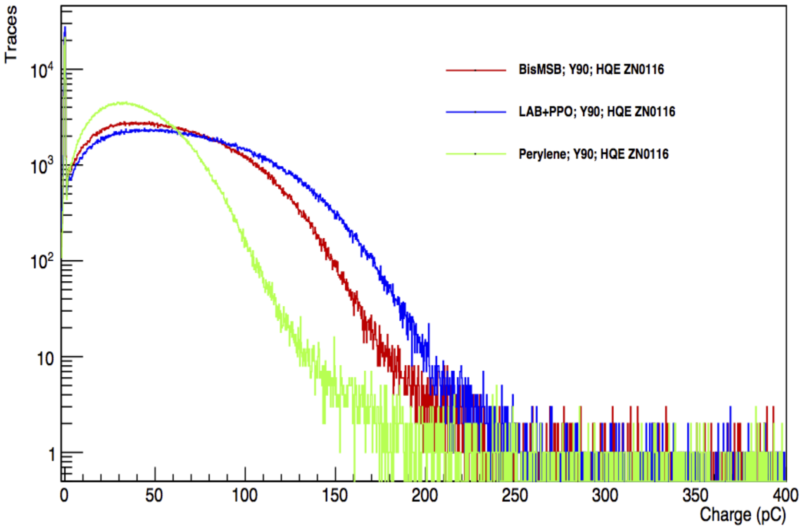

Figure 7.29: The ^{90}Y charge spectra in the three scintillator cocktails: LABPPO, LABPPO with BisMSB, LABPPO with Perylene. The data was obtained with a ZN0116 PMT.

At the time of performing the measurements we could not draw a conclusion about either the geometry of the source or the experimental setup, therefore the obtained data was not reliable enough to perform a full analysis. We operated with this setup for the first time and could not resolve encountered complications during the course of data taking. Another campaign is required to continue the study.

7.7 Discussion and Conclusion.

We have developed and documented a procedure to encapsulate ^{90}Y and manufacture a calibration source. We highlighted the risks related to the production and suggested approaches to avoid them. The procedure is straightforward and repeatable.

Due to the delicate nature of the capillary, deploying it as a calibration source into the detector is not possible because of the risk of contamination. However, the significant progress described in this chapter indicates that there is a promising potential to use ^{90}Y in a smaller scale setup, for example, to study the properties of scintillators and their responses to electrons. It is important to keep in mind that the calibration source must be manufactured in close proximity to the laboratory, in order to keep it in the original conditions. Pressure changes might cause movement of the source and even scatter it along the capillary.

Although the tests described in this thesis were not accomplished as expected, we were able to use this experience to identify the weakness of the procedure and update it. Taking into consideration the technical difficulties we encountered, it can be suggested to run other tests using the ^{90}Y calibration source.

Chapter 8

Conclusions

SNO+ is a liquid scintillator experiment whose main purpose is a search for the $0\nu2\beta$ decay of ^{130}Te. The data taking process will be divided into three phases: water phase, pure scintillator phase and tellurium loaded phase. The early phases of SNO+ will allow the experiment to investigate physics phenomena including reactor antineutrino oscillations, low energy solar neutrinos, geo-neutrinos, and supernova neutrinos, as well as searching for exotic physics such as invisible nucleon decays. These phases are also important in order to calibrate the detector and constrain backgrounds that are important for the $0\nu2\beta$ phase.

In preparation for data taking during all phases, the SNO+ collaboration has prepared and tested a processing chain that will help to ensure the delivery of quality physics data. The Channel Software Status (CSS) will be one of the parts aiming to monitor the performance of the channels against various criteria. Chapter 3 has developed the framework for CSS and validated it on the air-fill data. The framework is fully ready for future tuning using stable water data.

Sensitivity for the $0\nu2\beta$ decay search will be limited by the level of backgrounds in the ROI. It is, therefore, crucial to be able to reduce and/or constrain these background events as much as possible to maximise the experiment's capability. Chapter 5 of this thesis has investigated pileup backgrounds in the first year of the Te-loaded scintillator phase and estimated their contribution to the ROI. It was demonstrated that the expected number of pileup events in the ROI was 33.16, while the expected number of events of all other backgrounds combined together was 20.81. Chapter 5 described in detail distinguishing topologies of pileup events and a range of techniques for their rejection. Allowing a 1.02% signal sacrifice, the level of pileup backgrounds was reduced down to 0.32 events in the ROI in the first year of the Tellurium phase.

To demonstrate the vital importance of the pileup rejection analysis, Chapter 6 showed an improvement in the SNO+ sensitivity from 1.951×10^{25} years for the lower limit on the $0\nu2\beta$ half-life of ^{130}Te, without pileup rejection, to 2.586×10^{25} years.

In the next step of this study, we will include the external backgrounds and estimate levels of all possible pileup combinations. Since their levels are relatively high, see Table A.3 and Appendix A, it is possible that pileup between external backgrounds and pileup between external and internal backgrounds will contribute to the ROI. However, due to the radial dependence of externals, with the majority at high radius, spatial pileup rejection cuts are expected to be very effective.

Further studies will concentrate on the optimisation of the cuts designed for the rejection of each background independently. Applying the pileup rejection techniques will potentially reduce the number of unwanted events in the ROI caused by other internal backgrounds.

SNO+ has developed an extensive range of optical and radioactive sources in order to calibrate the detector response, including sources that are deployed into the detector. Chapter 7 proposed the use of a pure beta-emitter, ^{90}Y isotope, to test position and energy reconstruction of electron-like events. We described the design of the calibration source and its manufacturing procedure. Due to the high risk of contamination, ^{90}Y will unlikely be deployed into the detector. Nevertheless, the tests performed in the laboratories of Sussex University and the University of Pennsylvania proved it to be promising for future ex-situ measurements of scintillator properties. In SNO+, performing such measurements with ^{90}Y could be considered to study the higher Tellurium loadings.

Appendix A

Backgrounds table

The expected number of decays of radioactive backgrounds in the Te-loaded scintillator phase. The 0.3% ^{130}Te loading is assumed [169].

Table A.1: Expected levels of internal backgrounds in the first year of the Te-loading scintillator phase [169].

Source	Expected number of decays in the first year
URANIUM CHAIN:	
^{238}U	755258
^{234}U	755258
^{234m}Pa	755258
^{234}U	755258
^{230}Th	755258
^{226}Ra	755258
^{222}Rn	755258
^{218}Po	755258
^{214}Pb	755258
^{214}Bi	755099 (beta) + 159 (alpha)
^{214}Po	755099
^{210}Tl	159
^{210}Pb	790274
^{210}Bi	790274

Table A.1: (continued)

Source	Expected number of decays in the first year
^{210}Po	1.66×10^{7}
THORIUM CHAIN:	
^{232}Th	28099
^{228}Ra	28099
^{228}Ac	28099
^{228}Th	28099
^{224}Ra	28099
^{220}Rn	28099
^{216}Po	28099
^{212}Pb	28099
^{212}Bi	17983 (beta) + 10116 (alpha)
^{212}Po	17983
^{208}Tl	10116
CUORE:	
^{210}Po	2.13×10^{9}
OTHER:	
^{39}Ar	79243
^{14}C	6.4×10^{9}
^{85}Kr	79552
^{40}K	7860

Table A.2: Expected levels of leaching backgrounds in the first year of the Te-loading scintillator phase [169]. In order to estimate the leaching rates we assumed 9 months of water phase, 6 months of LAB phase before the Te-loaded scintillator phase. The assumed leaching rates are at 12° C.

Source	Expected number of decays in the first year
INTERNAL:	
^{210}Po	9.54×10^{9}
^{210}Bi	7.94×10^{9}

Table A.2: (continued)

Source	Expected number of decays in the first year
^{210}Pb	7.93×10^{9}
INNER AV:	
^{210}Po	2.25×10^{10}
^{210}Bi	2.14×10^{10}
^{210}Pb	2.14×10^{10}
OUTER AV:	
^{210}Po	2.69×10^{10}
^{210}Bi	2.60×10^{10}
^{210}Pb	2.60×10^{10}

Table A.3: Expected levels of external backgrounds in one year of the Te-loading scintillator phase [169].

Source	Expected number of decays in one year
Internal Calibration Ropes:	
^{214}Bi	4966
^{210}Tl	1.04
^{208}Tl	418
^{212}Bi - ^{212}Po	743
^{40}K	2.81×10^{4}
Hold-up Ropes:	
^{214}Bi	8.34×10^{5}
^{210}Tl	175
^{208}Tl	4.78×10^{5}
^{212}Bi - ^{212}Po	8.5×10^{7}
^{40}K	3.9×10^{7}
Hold-down Ropes:	
^{214}Bi	4.06×10^{6}
^{210}Tl	853

Table A.3: (continued)

Source	Expected number of decays in one year
^{208}Tl	2.32×10^{6}
^{212}Bi - ^{212}Po	4.13×10^{6}
^{40}K	1.89×10^{8}
Water Shielding:	
^{214}Bi	1.26×10^{8}
^{210}Tl	2.65×10^{4}
^{208}Tl	3.73×10^{6}
^{212}Bi - ^{212}Po	6.63×10^{6}
Acrylic Vessel:	
^{214}Bi	1.28×10^{7}
^{210}Tl	2682
^{208}Tl	1.50×10^{6}
^{212}Bi - ^{212}Po	2.67×10^{6}
^{40}K	7.32×10^{7}
Acrylic Vessel External Dust:	
^{214}Bi	7.75×10^{5}
^{210}Tl	163
^{208}Tl	4.6×10^{5}
^{212}Bi - ^{212}Po	8.2×10^{5}
^{40}K	1.76×10^{7}
Acrylic Vessel Internal Dust:	
^{214}Bi	4.15×10^{4}
^{210}Tl	8.7
^{208}Tl	2.48×10^{5}
^{212}Bi - ^{212}Po	4.41×10^{4}
^{40}K	9.4×10^{5}
PMTs:	
^{214}Bi	3.7×10^{11}

Table A.3: (continued)

Source	Expected number of decays in one year
^{210}Tl	7.8×10^{10}
^{208}Tl	4.4×10^{10}
^{212}Bi - ^{212}Po	7.8×10^{10}

Appendix B

Statistical tools used in echidna software

A probability density function (p.d.f.) $f(x)$ gives the probability of observing a value of a random variable x within an infinitesimal interval $[x, x+dx]$:

$$P = f(x)dx. \tag{B.0.1}$$

The p.d.f. is normalized such that the total probability is equal to one:

$$P_{total} = \int f(x)\, dx = 1. \tag{B.0.2}$$

The result of any physical experiment is different each time the measurement is performed, hence it is fair to say that the result of a physical experiment x is a random variable with some p.d.f (one can generate this p.d.f. by performing a series of measurements and storing the results in a histogram).

One can use Monte-Carlo simulations of the physical process in consideration and generate the model for the unknown experimental p.d.f.. Usually, a simulated p.d.f. will not coincide with experimentally measured p.d.f., due to various factors such as attenuation, and electronic and other noise. Assuming that the simulated p.d.f. depends on some set of parameters $\boldsymbol{\alpha}$, i.e. has the form $f\left(x|\boldsymbol{\alpha}\right)$, one can ask the question of how to choose these parameters in such a way that the simulated p.d.f. will coincide with experimentally measured data as closely as possible.

In other words, how do we estimate the values of the parameters $\boldsymbol{\alpha}$ of the p.d.f. $f\left(x|\boldsymbol{\alpha}\right)$ using n_{tot} experimental values of the random variable x? There are several approaches to this problem. We will concentrate on the method of maximum likelihood in this chapter.

If x_i are outcomes of n_{tot} measurements, then the likelihood function can be constructed as follows:

$$L(\boldsymbol{\alpha}) = \prod_{i=1}^{n_{tot}} f(x_i|\boldsymbol{\alpha}). \tag{B.0.3}$$

The best-fit values for the parameters $\boldsymbol{\alpha}$ correspond to the maximum of the likelihood function. It is more convenient to maximise the logarithm of the likelihood function

$$\log L(\boldsymbol{\alpha}) = \sum_{i=1}^{n_{tot}} \log f(x_i|\boldsymbol{\alpha}). \tag{B.0.4}$$

B.0.1 Extended maximum likelihood

Often in experiments the number of measurements cannot be fixed precisely, but itself is an observable. Because the measurements are independent of each other one can assume that the number of measurements follows a Poisson distribution with mean value $\nu(\boldsymbol{\alpha})$, which is dependent on the parameters $\boldsymbol{\alpha}$. The likelihood function in this case is a product of the Poisson probability to find n and the usual likelihood function (B.0.3)

$$L(\nu(\boldsymbol{\alpha}),\boldsymbol{\alpha}) = L(\boldsymbol{\alpha}) = \frac{\nu(\boldsymbol{\alpha})^n}{n!} e^{-\nu(\boldsymbol{\alpha})} \prod_{i=1}^{n} f(x_i|\boldsymbol{\alpha}) = \frac{e^{-\nu}}{n!} \prod_{i=1}^{n} \nu(\boldsymbol{\alpha}) f(x_i|\boldsymbol{\alpha}). \tag{B.0.5}$$

Again, it is more convenient to consider the logarithm of this function

$$\log L(\boldsymbol{\alpha}) = -\nu(\boldsymbol{\alpha}) + \sum_{i=1}^{n} \log\left(\nu(\boldsymbol{\alpha}) f(x_i|\boldsymbol{\alpha})\right) - \log n!. \tag{B.0.6}$$

Since additive terms not depending on $\boldsymbol{\alpha}$ will not affect the maximisation procedure, the last term can be dropped, hence an actual expression for maximisation is

$$\log L(\boldsymbol{\alpha}) = -\nu(\boldsymbol{\alpha}) + \sum_{i=1}^{n} \log\left(\nu(\boldsymbol{\alpha}) f(x_i|\boldsymbol{\alpha})\right). \tag{B.0.7}$$

B.0.2 Parameter estimation with binned data

For a very large data sample the standard maximum likelihood approach becomes inefficient, because one must consider a very large product of $f(x_i|\boldsymbol{\alpha})$ for each measured value x_i (or sum of $\log f(x_i|\boldsymbol{\alpha})$ for log-likelihood maximisation). In this case it is useful to produce a histogram, where n_{tot} total measurements are distributed over N bins. This could be represented as an N-dimensional vector $\boldsymbol{n} = (n_1, \ldots, n_N)$, where

$$\sum_{i=1}^{N} n_i = n_{tot}. \tag{B.0.8}$$

The expectation values ν_i for the numbers of entries in each bin are given by

$$\nu_i\left(\boldsymbol{\alpha}\right) = n_{tot} \int_{x_i^{min}}^{x_i^{max}} f\left(x|\boldsymbol{\alpha}\right)\ dx. \tag{B.0.9}$$

Here x_i^{min} and x_i^{max} are i-th bin limits. From this it follows that the probability for the measurement to end up in the i-th bin is

$$p_i = \frac{\nu_i}{n_{tot}}. \tag{B.0.10}$$

Therefore, such a histogram approach can be treated as a single measurement of an N-dimensional random vector with a multinomial distribution, governed by probabilities p_i

$$f_{hist}\left(\boldsymbol{n}|\boldsymbol{\nu}\right) = \frac{n_{tot}!}{n_1!\ldots n_N!} p_1^{n_1}\ldots p_N^{n_N} = \frac{n_{tot}!}{n_1!\ldots n_N!}\left(\frac{\nu_1}{n_{tot}}\right)^{n_1} \ldots \left(\frac{\nu_N}{n_{tot}}\right)^{n_N}. \tag{B.0.11}$$

This p.d.f. is equivalent to the standard likelihood function (B.0.3). The logarithm of this expression is

$$\begin{aligned} \log L(\boldsymbol{\alpha}) &= \log f_{hist}\left(\boldsymbol{n}|\boldsymbol{\nu}(\boldsymbol{\alpha})\right) = \log\left(\frac{n_{tot}!}{n_1!\ldots n_N!}\right) + \sum_{i=1}^{N} n_i \left[\log \nu_i(\boldsymbol{\alpha}) - \log n_{tot}\right] = \\ &= \log\left(\frac{n_{tot}!}{n_1!\ldots n_N!}\right) - \sum_{i=1}^{N} n_i \log n_{tot} + \sum_{i=1}^{N} n_i \log \nu_i(\boldsymbol{\alpha}). \end{aligned} \tag{B.0.12}$$

Here the first two terms are independent of the parameters $\boldsymbol{\alpha}$ hence can be dropped, and the expression for maximisation will look as follows:

$$\log L(\boldsymbol{\alpha}) = \sum_{i=1}^{N} n_i \log \nu_i(\boldsymbol{\alpha}). \tag{B.0.13}$$

B.0.3 Extended maximum likelihood with binned data

In the case when the total number of measurements is treated as a random variable with a Poisson distribution with some mean $\nu_{tot}(\boldsymbol{\alpha})$ which is a function of parameters $\boldsymbol{\alpha}$ the likelihood function is a product of the Poisson probability to get n_{tot} measurements and the likelihood function for the binned data case (B.0.11)

$$f_{hist}\left(\boldsymbol{n}|\boldsymbol{\nu}\right) = \frac{\nu_{tot}^{n_{tot}}}{n_{tot}!} e^{-\nu_{tot}} \; \frac{n_{tot}!}{n_1! \ldots n_N!} \left(\frac{\nu_1}{\nu_{tot}}\right)^{n_1} \ldots \left(\frac{\nu_N}{\nu_{tot}}\right)^{n_N} \tag{B.0.14}$$

where the expected numbers of entries in each bin ν_i now also depend on ν_{tot} and are defined as follows

$$\nu_i\left(\boldsymbol{\alpha}\right) = \nu_{tot} \int_{x_i^{min}}^{x_i^{max}} f\left(x|\boldsymbol{\alpha}\right)\, dx. \tag{B.0.15}$$

From this definition it follows that $\sum_{i=1}^{N} \nu_i = \nu_{tot}$. Using this together with (B.0.8) the expression (B.0.14) can be simplified:

$$\begin{aligned} f_{hist}\left(\boldsymbol{n}|\boldsymbol{\nu}\right) &= \frac{\nu_{tot}^{n_{tot}}}{n_1! \ldots n_N!} e^{-\nu_{tot}} \; \frac{\nu_1^{n_1} \ldots \nu_N^{n_N}}{\nu_{tot}^{\sum n_i}} = \frac{\nu_{tot}^{n_{tot}}}{n_1! \ldots n_N!} e^{-\sum \nu_i} \; \frac{\nu_1^{n_1} \ldots \nu_N^{n_N}}{\nu_{tot}^{n_{tot}}} = \\ &= \frac{\nu_1^{n_1} \ldots \nu_N^{n_N}}{n_1! \ldots n_N!} e^{-\sum \nu_i} = \prod_{i=1}^{N} \frac{\nu_i^{n_i}}{n_i!} e^{\nu_i}. \end{aligned} \tag{B.0.16}$$

The logarithm of this likelihood function is

$$\begin{aligned} \log L(\nu_{tot}, \boldsymbol{\alpha}) &= \log f_{hist}\left(\boldsymbol{n}|\boldsymbol{\nu}\right) = \sum_{i=1}^{N} \left[n_i \log \nu_i - \nu_i - \log n_i!\right] = \\ &= \sum_{i=1}^{N} n_i \log \nu_i - \nu_{tot} - \sum_{i=1}^{N} \log n_i!. \end{aligned} \tag{B.0.17}$$

Dropping the last term we arrive at the following final expression of the maximisation function for the extended maximum likelihood method with binned data:

$$\log L(\nu_{tot}(\boldsymbol{\alpha}), \boldsymbol{\alpha}) = \sum_{i=1}^{N} n_i \log \nu_i(\boldsymbol{\alpha}) - \nu_{tot}(\boldsymbol{\alpha}). \tag{B.0.18}$$

B.0.4 Limit setting

A method for setting the limits used in echidna is outlined below.

The performance of a $0\nu\beta\beta$ beta decay experiment is quantified by the lower limit on the half-life and corresponding upper limit on the effective neutrino mass $m_{\beta\beta}$ that is excluded at a certain level of confidence if no signal is observed. In echidna software the profile likelihood method is used for establishing this limit.

In this method the Poisson likelihood χ^2 test statistic is constructed. One starts with the ratio of the likelihood functions (B.0.14) for the parameters $\boldsymbol{\nu}$, predicted by the chosen model, and unknown real values of the parameters $\boldsymbol{d}$, from an experiment with absolute precision,

$$\Lambda = \frac{L\left(\boldsymbol{n}|\boldsymbol{\nu}\right)}{L\left(\boldsymbol{n}|\boldsymbol{d}\right)}. \tag{B.0.19}$$

Then the χ^2 is defined as the logarithm of this ratio, multiplied by -2,

$$\chi^2_\Lambda = -2\log\Lambda = -2\log L\left(\boldsymbol{n}|\boldsymbol{\nu}\right) + 2\log L\left(\boldsymbol{n}|\boldsymbol{d}\right). \tag{B.0.20}$$

Using the Poisson nature of the distribution of the number of events in each bin, one can replace the unknown real values of the parameters $\boldsymbol{d}$ with their maximum likelihood estimators $\hat{\boldsymbol{\nu}} = \boldsymbol{n}$

$$\boldsymbol{d} = \hat{\boldsymbol{\nu}} = \boldsymbol{n}. \tag{B.0.21}$$

Then, using an explicit expression for the likelihood functions (B.0.14),

$$L\left(\boldsymbol{n}|\boldsymbol{\nu}\right) = \prod_{i=1}^{N} \frac{\nu_i^{n_i}}{n_i!} e^{-\nu_i}, \tag{B.0.22}$$

one can get the following expression for χ^2_Λ:

$$\chi^2_\Lambda = -2\log L(\boldsymbol{n}|\boldsymbol{\nu}) + 2\log L(\boldsymbol{n}|\boldsymbol{n}) = -2\log\left(\prod_{i=1}^{N}\frac{\nu_i^{n_i}}{n_i!}e^{-\nu_i}\right) + 2\log\left(\prod_{i=1}^{N}\frac{n_i^{n_i}}{n_i!}e^{-n_i}\right) =$$

$$-2\log\left(\prod_{i=1}^{N}\frac{\nu_i^{n_i}}{n_i!}e^{\nu_i}\frac{n_i!}{n_i^{n_i}}e^{n_i}\right) = -2\log\left(\prod_{i=1}^{N}e^{n_i-\nu_i}\left(\frac{\nu_i}{n_i}\right)^{n_i}\right). \tag{B.0.23}$$

Expanding the log of this product gives the final result,

$$\chi^2_\Lambda = 2\sum_{i=1}^{N}\left[\nu_i - n_i + n_i\log\left(\frac{n_i}{\nu_i}\right)\right]. \tag{B.0.24}$$

As follows from the definition of χ^2_Λ (B.0.20) its minimum corresponds to the maximum of the likelihood ratio (B.0.19), therefore by minimizing χ^2_Λ one is finding the best-fit values for the parameters of the model. In other words, the best fit value of the parameters correspond to the global minimum of χ^2_Λ.

If we want to set a limit on the rate of the $0\nu2\beta$ signal $\mathit{\Gamma}$ (the rate of the signal is equal to the inverse of the half-life, $\mathit{\Gamma} = T^{-1}_{1/2}$), then we need to include the rate as a parameter into the χ^2_Λ. And by singling out the dependence of χ^2_Λ only on the rate $\mathit{\Gamma}$ we get a one dimensional function $\chi^2_\Lambda(\mathit{\Gamma})$ with the minimum at $\mathit{\Gamma} = \mathit{\Gamma}_0$ corresponding to the best fit value of the rate of the signal.

In order to find the confidence interval for the best fit value one needs to find the points where $\chi^2_\Lambda(\mathit{\Gamma}) - \chi^2_\Lambda(\mathit{\Gamma}_0)$ has a specific value. It was shown in [25] that for the Poisson likelihood test statistic χ^2_Λ and 90% confidence interval this number is 2.71, hence

$$\chi^2_\Lambda(\mathit{\Gamma}) - \chi^2_\Lambda(\mathit{\Gamma}_0) = 2.71. \tag{B.0.25}$$

It is more appropriate to quote only an upper limit for the rate of $0\nu2\beta$ decay, hence the lower limit for the $T^{0\nu2\beta}_{1/2}$.

B.0.5 An output of echidna software

In this section we present detailed output of echidna software, which we have used in Chapter 6. We have performed a limit setting analysis for $0\nu2\beta$ half-life at 90% CL of ^{130}Te at 0.3% loading. The results of the analysis before and after pileup rejection are presented below. The Fiducial Volume cut is always applied.

Before pileup rejection

- $T_{1/2}^{0\nu2\beta} > 1.951 \cdot 10^{25}$ years at 90% CL.
- $m_{\beta\beta} < 0.1494$ eV.

Table B.1: Counts in the ROI of backgrounds after the first year of running the detector in the Te-loaded phase. The rejection techniques developed for single-decay events are applied. The pileup rejection cuts are not applied.

Source	Counts in the ROI
Internal backgrounds	
^{8}B	10.597978
^{130}Te	1.899678
^{212}Bi-Po	1.949520
^{214}Bi-Po	0.268819
^{219}Tl	1.539330
^{228}Ac	0.871664
^{208}Tl	0.090275
^{210}Bi	0.000000
^{234m}Pa	0.057673
^{234}Th	0.000000
^{232}Th	0.000000
^{230}Th	0.000000
^{39}Ar	0.000000
^{210}Bi	0.000000
^{14}C	0.000000

Table B.1: (continued)

Source	Counts in the ROI
^{216}Po	0.000000
^{210}Po	0.000000
^{85}Kr	0.000000
^{226}Ra (α)	0.000000
^{218}Po	0.000000
^{228}Th	0.000000
^{238}U	0.000000
^{220}Rn	0.000000
^{222}Rn	0.000000
^{234}U	0.000000
^{212}Pb	0.000000
^{40}K	0.000000
^{210}Pb	0.000000
^{224}Ra	0.000000
^{214}Pb	0.000000
^{228}Ra	0.000000
Pileup backgrounds	
Te130 + AVPo210	5.070054
AVPo210 + Te130	4.999250
Te130 + AVBi210	1.775899
AVBi210 + Te130	1.770567
Po210 + Te130	1.711970
Te130 + Po210	1.661875
Te130 + Bi210	0.884011
Bi210 + Te130	0.148233
AVPo210 + AVPo210 + AVBi210	3.271920
AVPo210 + AVBi210 + AVPo210	2.852124

Table B.1: (continued)

Source	Counts in the ROI
AVBi210 + AVBi210 + AVBi210	1.097254
AVBi210 + AVPo210 + Bi210	0.769626
AVBi210 + AVBi210 + Po210	0.697706
AVBi210 + Bi210 + AVPo210	0.691927
Bi210 + AVPo210 + AVBi210	0.676929
Bi210 + AVBi210 + AVPo210	0.606666
AVBi210 + Po210 + AVBi210	0.575089
AVBi210 + AVBi210 + Bi210	0.351919
AVBi210 + Bi210 + AVBi210	0.316714
Po210 + AVBi210 + AVBi210	0.310813
AVBi210 + Bi210 + Po210	0.300961
Bi210 + AVBi210 + Po210	0.293287
Bi210 + Bi210 + AVPo210	0.284163
Po210 + Bi210 + AVBi210	0.280936
Bi210 + AVPo210 + Bi210	0.252594
Po210 + AVBi210 + Bi210	0.251591
AVBi210 + Po210 + Bi210	0.247906
Bi210 + AVBi210 + AVBi210	0.170576
Bi210 + AVBi210 + Bi210	0.146121
Bi210 + Bi210 + AVBi210	0.142210
AVPo210 + Bi210 + Bi210	0.140070
Bi210 + Bi210 + Po210	0.080363
AVBi210 + Bi210 + Bi210	0.063294
External backgrounds	
Hold-up Ropes	
^{208}Tl	0.105032
^{214}Bi	0.000000

Table B.1: (continued)

Source	Counts in the ROI
Hold-down Ropes	
^{214}Bi	0.030005
^{208}Tl	1.194957
Water Shielding	
^{214}Bi	0.177737
^{208}Tl	0.375165
Acrylic Vessel	
^{208}Tl	1.047133
Acrylic Vessel Internal Dust	
^{208}Tl	0.005010
^{214}Bi	0.000000
^{210}Bi	0.000000
^{210}Po	0.000000
Acrylic Vessel Outer Dust	
^{208}Tl	0.459642
PMTs	
β, γs	0.407807

In the second case, we apply the pileup rejection cuts to the pileup backgrounds. We don't apply such cuts to other single-decay events. The counts of single-decay backgrounds stayed the same as before.

After pileup rejection

- $T_{1/2}^{0\nu 2\beta} > 2.586 \cdot 10^{25}$ years at 90% CL.
- $m_{\beta\beta} < 0.1298$ eV.

Appendix C

Capillary Filling Procedure

Here we describe the full approved step-by-step procedure of the manufacturing the ^{90}Y calibration source.

Pre-training:

1. Learn how to operate fume cupboard
2. Learn how to operate GM tubes
3. Learn how to operate Scalar
4. Learn how to operate blow torch
5. Practise capillary filling and handling in full PPE. Should make 5 good capillaries before working with radiation.

Procedure:

1. Put sign up saying no entrance under any circumstances, radiation work in progress.
2. Capillaries are prepared with the 'stopper' glued in place $2-3$ cm from the end of the capillary (use a marked stick for guidance) at least 24 hours in advance to allow glue to dry. Ensure that washer does not move and that the

glue is completely dry first in a radiation free environment. Capillaries should be handled as little as possible and only held by the stopper once it is in place.

3. Capillary is placed in the custom made stand supported by the stopper, with short end upwards. Stand is placed behind perspex radiation shield in the fume cabinet standing in the drip tray, which is lined with benchkote.

4. Extractor fan in fume cupboard is turned on. Learn to use. Also ensure fume cupboard is fully closed.

5. Ensure all equipment is to hand in fume cupboard: Drip tray lined with benchkote GM monitor, blow torch, P20 Gilson Pipette in pipette stand set at $2\mu L$, disposable pipette tips, wipes, cotton buds, tweezers, magnifying glass, arm rest, perspex shielding, perspex radiation disposal box with liner bag, squirty container of water and empty beaker, perspex capillary washing container (CWC) with both lids off ready, perspex capillary transport container (CTC), lid off ready, paper and pencil, hand-pump vacuum chamber, bottom lined with benchkote. Plus draw up a non-permeable chair, as this takes time. Spill kit should be ready beside the fume cupboard

6. Check that GM monitor has batteries and that there is sufficient fuel in the blow torch. Turn GM on.

7. Place appropriate signage on laboratory door and put on PPE (gloves, lab coat, goggles)

8. Check working area with radiation monitor prior to introducing source.

9. Get ^{90}Y source vial out of radiation storage cabinet and place vial behind perspex shield in fume cabinet. Check source paperwork in order. Wipe test the source vial with GM.

10. Attach new tip to pipette using the tweezers and set dial to $2\mu L$ (this is 0 on the bottom dial (red) and 2 on the central dial (black), 0 on the upper dial (black)). Place pipette back in holder.

11. Open the source vial and place back on bench. Unscrew pig lid, flip over and use to unscrew vial lid then remove vial lid with one's hand.
12. Steady arm on support, fully depress pipette and insert tip into solution to extract $2\mu L$ of solution by removing thumb from plunger. Place pipette in holder.
13. Replace lid on source vial, put vial lid on and use pig lid to screw tight, then screw on pig lid
14. Remove thumb from plunger. Move pipette so tip is now inserted in the top of the open capillary using arm rest for support. Depress plunger so that source transfers to capillary in one movement.
15. Withdraw pipette, discard the tip into the Perspex radioactive waste container using tweezers.
16. Dial pipette to $5\mu L$ and attach a new tip.
17. Reinsert pipette into top of capillary and depress plunger to inject air into capillary and push source droplet into position, withdraw pipette and repeat until the droplet is in the desired position, halfway between the bottom of the capillary and the washer.
18. Discard pipette tip into waste container using tweezers and return pipette to stand.
19. Use cotton buds to gently wipe the top of capillary in case any trace of source collected at entrance. Dispose of in radioactive bin, measure with GM first.
20. Turn the blow torch dial in the direction of the + and press the ignition button whilst facing the torch away from the apparatus.
21. Direct the central point of the flame at the top of the capillary for $10 - 20$ seconds until end appears to be sealed closed. Extinguish torch. Use tweezers to rotate capillary in the holder. (NOTE - may be better to seal horizontally

rotating capillary in flame - you can lift the stand and rotate it with left hand whilst blow-torching with right hand.)

22. Visually inspect the melted end with the magnifying glass (use upside down). If not completely sealed, reapply the torch.

23. Using tweezers, hold the capillary by the stopper and turn it over so that it is the other way up in the stand (start with hand upside down).

24. Follow steps $20-22$ and $17-19$ above to seal the other end of the capillary.

25. Use Scalar to measure capillary activity.

26. Bathe capillary in beaker of water and look for leaks - take care to work over drip tray for steps up to 35.

27. Remove capillary with tweezers and visually inspect for leaks/movement of droplet (if positively identified follow section E below).

28. Use Scalar to measure capillary activity.

29. Using tweezers transfer capillary to the CWC and seal the top (smaller) lid. Lay the CWC on its side on a piece of paper and make marks to indicate the exact location of the source.

30. Test the water in the beaker for activity with the GM. Record value - any reading above background indicates source got on the outside of the capillary or that capillary has leaked - pay particular attention to visual inspection (see section E below).

31. Turn the capillary washer over and fill $50-60\%$ with water using a larger pipette. Insert the bottom screw lid and shake gently for one minute.

32. Remove bottom lid. Drain water into empty large beaker, lay the CWC in the same position on the paper and check that droplet in capillary has not moved. Do not remove from the CWC unless it looks like movement has occurred and closer inspection is required under the magnifying glass (in which case use tweezers).

33. Repeat $30 - 31$ and $23 - 24$.
34. Test the waste water with the G-M tube. If there is any reading above background, repeat steps $23 - 26$ and $30 - 31$ using a fresh empty beaker until waste water shows no reading. Use scalar GM to measure capillary activity and compare again.
35. Transfer the capillary to the stand and gently wipe away remaining water with cotton bud.
36. Test the seal. Place capillary in the hand-pump vacuum chamber. Close chamber and pump (at least 40 pumps). Visually inspect capillary in chamber whilst still under vacuum.
37. Release vacuum and remove capillary. Return to CWC to check source position against original marks.
38. If there is any sign of source movement, or water entry into the capillary discard this capillary (Perspex storage), making note of the activity and start again.
39. If seal is good replace gloves, switch to new tweezers, place old ones aside and radioactive bin old gloves.
40. Transfer the capillary to the CTC or directly in the dark box experimental setup for measurements.
41. Return source vial and CTC to shielding in locked radiation cabinet, fill in paperwork for amount of source used and activity of capillary and CTC with the GM.
42. Dispose of beaker of waste water down sink, rinse thoroughly.
43. Rinse CWC thoroughly and monitor with GM tube.
44. Use GM tube to monitor working area for radioactivity. Wipe as required and dispose of wipes and any contaminated benchkote material in radioactive waste container.

45. Store radioactive waste container in locked source cabinet.
46. Use GM tube to monitor yourself. Remove PPE and wash hands. Bin gloves in normal bin.
47. Fill in waste record sheet and ^{90}Y sample log. Take down no access sign.
48. Wipe down all equipment, place waste in radioactive bin.
49. Take waster to radioactive decay store, estimate upper limit of activity.
50. Clean all equipment in the sink.

In the event that

A The capillary breaks: Any broken capillaries that have come into contact with the ^{90}Y must be discarded into the radioactive waste container use tweezers to move parts, and wipes/spill equipment to mop up. Check activity with GM before discarding and after. Repeat wipe and monitor steps until there is no reading above background. The amount of radioactivity in the waste should be estimated and recorded such that the waste can be stored for the requisite amount of time. The RPS should be informed. If there is any broken glass, replace glove as soon as it has been tidied up in case small shards puncture gloves.

B A spill on objects: Inform RPS. Use GM to monitor where activity is and wipe up using wipes from spill kit. If the volume of spill is large (This will only happen if you contaminate a solution - water or liquid scintillator), use absorbent tubing in spill kit to contain spill. For small spills, wipe up visible spill then monitor full working area for splashes etc. Dispose of all wipes in radioactive waste bin, monitor full area with GM and repeat until no activity detected. Use GM to monitor yourself (follow C if a positive reading) and gloves. Dispose of gloves in radioactive waste.

C A spill on humans: Remove clothing affected and place in radiation bag. Inform RPS. Wash affected area at radiation sink. If necessary, take a shower, monitor with GM and repeat as necessary. Assign person to clean up lab space following B.

D Droplet does not enter the capillary cleanly resulting in loss of ^{90}Y solution down the outside of the tube: Wipe with cotton buds until cotton buds indicate no activity with the GM. Dispose of cotton buds in radioactive waste.

E The capillary is not properly sealed (includes seals that are too large, such that capillary does not fit in the holder) and droplet moves: Discard capillary in the radiation waste bin (perspex box), monitor working area and start again, note outcome in documentation logs.

Appendix D

Table of theoretical activities of ^{90}Y at various times

Activity of $2\mu L$ drop of ^{90}Y from first batch at calibration time, $A_0 = 528571$ Bq.

Table D.1: Theoretical activities of $2\mu L$ drop of ^{90}Y from first batch at the times when experimental measurements were performed.

Date & time	Activity in Bq
May 6, 13:16 UK Time	12.95
May 9, 13:40 UK Time	5.91
May 12, 10:50 UK Time	2.8
May 14, 18:34 UK Time	1.53
May 16, 14:53 UK Time	0.95
May 19, 13:26 UK Time	0.44

Activity of $2\mu L$ drop of ^{90}Y from second batch at calibration time, $A_0 = 634286$ Bq.

Table D.2: Theoretical activities of $2\mu L$ drop of ^{90}Y from second batch at various times.

Date & time	Activity in Bq
February 17, 17:00 UK Time (Capillaries were produced)	172923
February 23, 17:00 UK Time (Capillaries arrived in Penn)	36352.7
February 28, 17:00 UK Time (5 days after arrival in Penn)	9910.71
March 5, 17:00 UK Time (10 days after arrival in Penn)	2701.93
March 10, 17:00 UK Time (15 days after arrival in Penn)	736.618
March 15, 17:00 UK Time (20 days after arrival in Penn)	200.822
March 25, 17:00 UK Time (30 days after arrival in Penn)	14.9262

Bibliography

[1] R. P. Feynman, M. Gell-Mann, *Theory of the Fermi Interaction*, Phys. Rev. 109.193 (1958).

[2] E. C. G. Sudarshan, R. E. Marshak, *Chirality Invariance and the Universal Fermi Interaction*, Phys. Rev. 109.1860 (1958).

[3] C. L. Cowan, F. Reines, F. B. Harrison, H. W. Kruse and A. D. McGuire, *Detection of the free neutrino: A Confirmation*, Science **124**, 103 (1956).

[4] W. Pauli, *Open letter to the group of radioactive people at the Gauverein meeting in Tubingen*, [`microboone-docdb.fnal.gov/cgi-bin/RetrieveFile?docid=953;filename=pauli%20letter1930.pdf`].

[5] E. Fermi, *Tentativo di una teoria dell'emissione dei raggi beta*, Ric. Sci. **4**, 491 (1933).

[6] C. L. Cowan, F. Reines, F. B. Harrison, H. W. Kruse and A. D. McGuire, *Detection of the free neutrino: A Confirmation*, Science **124**, 103 (1956).

[7] R. Davis, Jr., *Attempt to detect the antineutrinos from a nuclear reactor by the* $Cl^{37}(\bar{\nu}\ , e^-)\ A^{37}$ *reaction*, Phys. Rev. **97**, 766 (1955).

[8] E. J. Konopinski and H. M. Mahmoud, *The Universal Fermi interaction*, Phys. Rev. **92**, 1045 (1953).

[9] C. M. G. Lattes, G. P. S. Occhialini and C. F. Powell, *Observations on the Tracks of Slow Mesons in Photographic Emulsions*, Nature **160**, 453 (1947).

[10] G. Danby, J. M. Gaillard, K. A. Goulianos, L. M. Lederman, N. B. Mistry, M. Schwartz and J. Steinberger, *Observation of High-Energy Neutrino Reactions and the Existence of Two Kinds of Neutrinos*, Phys. Rev. Lett. **9**, 36 (1962).

[11] K. Kodama *et al.* [DONUT Collaboration], *Observation of tau neutrino interactions*, Phys. Lett. B **504**, 218 (2001), [`hep-ex/0012035`].

[12] J. N. Bahcall, *Solar models: An Historical overview*, AAPPS Bull. **12**, no. 4, 12 (2002) [Nucl. Phys. Proc. Suppl. **118**, 77 (2003)] [Int. J. Mod. Phys. A **18**, 3761 (2003)] doi:10.1016/S0920-5632(03)01306-9 [astro-ph/0209080].

[13] C. Giunti and C. W. Kim, *Fundamentals of Neutrino Physics and Astrophysics*, Oxford, UK: Univ. Pr. (2007).

[14] J. N. Bahcall, A. M. Serenelli and S. Basu, *New solar opacities, abundances, helioseismology, and neutrino fluxes*, Astrophys. J. **621**, L85 (2005) doi:10.1086/428929 [astro-ph/0412440].

[15] S. Turck-ChiÃĺze, *The Standard Solar Model and beyond*, J. Phys. Conf. Ser. **665**, no. 1, 012078 (2016). doi:10.1088/1742-6596/665/1/012078

[16] B. T. Cleveland, T. Daily, R. Davis, Jr., J. R. Distel, K. Lande, C. K. Lee, P. S. Wildenhain and J. Ullman, *Measurement of the solar electron neutrino flux with the Homestake chlorine detector*, Astrophys. J. **496**, 505 (1998). doi:10.1086/305343

[17] W. C. Haxton, *The solar neutrino problem*, Ann. Rev. Astron. Astrophys. **33**, 459 (1995) doi:10.1146/annurev.aa.33.090195.002331 [hep-ph/9503430].

[18] B. Pontecorvo, *Neutrino Experiments and the Problem of Conservation of Leptonic Charge*, Sov. Phys. JETP **26**, 984 (1968) [Zh. Eksp. Teor. Fiz. **53**, 1717 (1967)].

[19] Z. Maki, M. Nakagawa and S. Sakata, *Remarks on the unified model of elementary particles*, Prog. Theor. Phys. **28**, 870 (1962).

[20] A. Bellerive *et al.* [SNO Collaboration], *The Sudbury Neutrino Observatory*, Nucl. Phys. B **908**, 30 (2016) doi:10.1016/j.nuclphysb.2016.04.035 [arXiv:1602.02469 [nucl-ex]].

[21] S. Fukuda *et al.* [Super-Kamiokande Collaboration], *Determination of solar neutrino oscillation parameters using 1496 days of Super-Kamiokande I data*, Phys. Lett. B **539**, 179 (2002) doi:10.1016/S0370-2693(02)02090-7 [hep-ex/0205075].

[22] Q. R. Ahmad *et al.* [SNO Collaboration], *Measurement of the rate of $\nu_e + d \rightarrow p + p + e^-$ interactions produced by ^8B solar neutrinos at the Sudbury Neutrino Observatory*, Phys. Rev. Lett. **87**, 071301 (2001), [`nucl-ex/0106015`].

[23] Low energy neutrino physics, [`http://www.staff.uni-mainz.de/wurmm/juno.html`].

[24] M. Maltoni, T. Schwetz and J. W. F. Valle, *Combining first KamLAND results with solar neutrino data*, Phys. Rev. D **67**, 093003 (2003) doi:10.1103/PhysRevD.67.093003 [hep-ph/0212129].

[25] K. A. Olive *et al.* [Particle Data Group Collaboration], *Review of Particle Physics*, Chin. Phys. C **38**, 090001 (2014).

[26] K. Abe *et al.* [T2K Collaboration], *Evidence of Electron Neutrino Appearance in a Muon Neutrino Beam*, Phys. Rev. D **88**, no. 3, 032002 (2013) doi:10.1103/PhysRevD.88.032002 [arXiv:1304.0841 [hep-ex]].

[27] P. Adamson *et al.* [MINOS Collaboration], *Combined analysis of ν_μ disappearance and $\nu_\mu \rightarrow \nu_e$ appearance in MINOS using accelerator and atmospheric neutrinos*, Phys. Rev. Lett. **112**, 191801 (2014) doi:10.1103/PhysRevLett.112.191801 [arXiv:1403.0867 [hep-ex]].

[28] G. J. Feldman, J. Hartnell and T. Kobayashi, *Long-baseline neutrino oscillation experiments*, Adv. High Energy Phys. **2013**, 475749 (2013).

[29] P. A. R. Ade *et al.* [Planck Collaboration], *Planck 2015 results. XIII. Cosmological parameters*, [`arXiv:1502.01589 [astro-ph.CO]`].

[30] R. Barate *et al.* [ALEPH Collaboration], *An Upper limit on the tau-neutrino mass from three-prong and five-prong tau decays*, Eur. Phys. J. C **2**, 395 (1998). doi:10.1007/s100520050149

[31] J. Lesgourgues and S. Pastor, *Neutrino mass from Cosmology*, Adv. High Energy Phys. **2012**, 608515 (2012) doi:10.1155/2012/608515 [arXiv:1212.6154 [hep-ph]].

[32] M. Goldhaber, L. Grodzins and A. W. Sunyar, *Helicity of Neutrinos*, Phys. Rev. **109**, 1015 (1958).

[33] E. Majorana, *Theory of the Symmetry of Electrons and Positrons*, Nuovo Cim. **14**, 171 (1937).

[34] M. Goeppert-Mayer, *Double beta-disintegration*, Phys. Rev. **48**, 512 (1935).

[35] Erlangen centre for astroparticle physics, [`http://www.ecap.physik.uni-erlangen.de/nexo/research.shtml`].

[36] G. Racah, *On the symmetry of particle and antiparticle*, Nuovo Cim. **14**, 322 (1937).

[37] W. H. Furry, *On transition probabilities in double beta-disintegration*, Phys. Rev. **56**, 1184 (1939).

[38] Double beta decay, [`https://en.wikipedia.org/wiki/Double_beta_decay`].

[39] S. M. Bilenky and C. Giunti, *Neutrinoless Double-Beta Decay: a Probe of Physics Beyond the Standard Model*, Int. J. Mod. Phys. A **30**, no. 04n05, 1530001 (2015) doi:10.1142/S0217751X1530001X [arXiv:1411.4791 [hep-ph]].

[40] H. PÃď's and W. Rodejohann, *Neutrinoless Double Beta Decay*, New J. Phys. **17**, no. 11, 115010 (2015) doi:10.1088/1367-2630/17/11/115010 [arXiv:1507.00170 [hep-ph]].

[41] J. Schechter and J. W. F. Valle, *Neutrinoless Double beta Decay in SU(2) x U(1) Theories*, Phys. Rev. D **25**, 2951 (1982). doi:10.1103/PhysRevD.25.2951

[42] E. Takasugi, *Can the Neutrinoless Double Beta Decay Take Place in the Case of Dirac Neutrinos?*, Phys. Lett. **149B**, 372 (1984). doi:10.1016/0370-2693(84)90426-X

[43] S. R. Elliott and P. Vogel, *Double beta decay*, Ann. Rev. Nucl. Part. Sci. **52**, 115 (2002) doi:10.1146/annurev.nucl.52.050102.090641 [hep-ph/0202264].

[44] J. Engel and J. MenÃĺndez, *Status and Future of Nuclear Matrix Elements for Neutrinoless Double-Beta Decay: A Review*, Rept. Prog. Phys. **80**, no. 4, 046301 (2017) doi:10.1088/1361-6633/aa5bc5 [arXiv:1610.06548 [nucl-th]].

[45] J. Menendez, A. Poves, E. Caurier and F. Nowacki, *Disassembling the Nuclear Matrix Elements of the Neutrinoless beta beta Decay*, Nucl. Phys. A **818**, 139 (2009) doi:10.1016/j.nuclphysa.2008.12.005 [arXiv:0801.3760 [nucl-th]].

[46] T. R. Rodriguez and G. Martinez-Pinedo, *Energy density functional study of nuclear matrix elements for neutrinoless $\beta\beta$ decay*, Phys. Rev. Lett. **105**, 252503 (2010) doi:10.1103/PhysRevLett.105.252503 [arXiv:1008.5260 [nucl-th]].

[47] H. V. Klapdor-Kleingrothaus and I. V. Krivosheina, *The evidence for the observation of 0ν beta beta decay: The identification of 0ν beta beta events from the full spectra*, Mod. Phys. Lett. A **21**, 1547 (2006).

[48] B. Majorovits [GERDA Collaboration], *The search for 0Î¡ÎšÎš decay with the GERDA experiment: Status and prospects*, AIP Conf. Proc. **1672**, 110003 (2015), [`arXiv:1506.00415 [hep-ex]`].

[49] M. Agostini *et al.* [GERDA Collaboration], *Improved Limit on Neutrinoless Double-β Decay of ^{76}Ge from GERDA Phase II*, Phys. Rev. Lett. **120**, no. 13, 132503 (2018) doi:10.1103/PhysRevLett.120.132503 [arXiv:1803.11100 [nucl-ex]].

[50] M. Agostini *et al.* [GERDA Collaboration], *Searching for neutrinoless double beta decay with GERDA*, Int. J. Mod. Phys. Conf. Ser. **46**, 1860040 (2018) doi:10.1142/S2010194518600406 [arXiv:1710.07776 [nucl-ex]].

[51] C. E. Aalseth *et al.* [Majorana Collaboration], *Search for Neutrinoless Double-Îš Decay in ^{76}Ge with the Majorana Demonstrator*, Phys. Rev. Lett. **120**, no. 13, 132502 (2018) doi:10.1103/PhysRevLett.120.132502 [arXiv:1710.11608 [nucl-ex]].

[52] N. Abgrall *et al.* [LEGEND Collaboration], *The Large Enriched Germanium Experiment for Neutrinoless Double Beta Decay (LEGEND)*, AIP Conf. Proc. **1894**, no. 1, 020027 (2017) doi:10.1063/1.5007652 [arXiv:1709.01980 [physics.ins-det]].

[53] R. Arnold *et al.* [NEMO-3 Collaboration], *Measurement of the $2\nu\beta\beta$ decay half-life of ^{150}Nd and a search for $0\nu\beta\beta$ decay processes with the full exposure from the NEMO-3 detector*, [`arXiv:1606.08494 [hep-ex]`].

[54] R. Arnold *et al.* [NEMO-3 Collaboration], *Search for neutrinoless double-beta decay of ^{100}Mo with the NEMO-3 detector*, Phys. Rev. D **89**, no. 11, 111101 (2014), [`arXiv:1311.5695 [hep-ex]`].

[55] P. Guzowski, *Status of the SuperNEMO experiment*, Presentation at the IoP 2016 Conf. (2014).

[56] E. Andreotti *et al.*, *^{130}Te Neutrinoless Double-Beta Decay with CUORICINO*, Astropart. Phys. **34**, 822 (2011), [`arXiv:1012.3266 [nucl-ex]`].

[57] L. Canonica *et al.*, *Results from the CUORE-0 experiment*, J. Phys. Conf. Ser. **718**, no. 6, 062007 (2016). doi:10.1088/1742-6596/718/6/062007

[58] C. Alduino *et al.* [CUORE Collaboration], *First Results from CUORE: A Search for Lepton Number Violation via $0\nu\beta\beta$ Decay of ^{130}Te*, Phys. Rev. Lett. **120**, no. 13, 132501 (2018) doi:10.1103/PhysRevLett.120.132501 [arXiv:1710.07988 [nucl-ex]].

[59] A. Gando *et al.* [KamLAND-Zen Collaboration], *Search for Majorana Neutrinos near the Inverted Mass Hierarchy Region with KamLAND-Zen*, [`arXiv:1605.02889 [hep-ex]`].

[60] J. Shira, *Results and future plans for the KamLAND-Zen experiment*, Presentation at the Neutrino 2016 Conf. (2016).

[61] J. B. Albert *et al.* [EXO-200 Collaboration], *Search for Majorana neutrinos with the first two years of EXO-200 data*, Nature **510**, 229 (2014), [`arXiv:1402.6956 [nucl-ex]`].

[62] J. B. Albert *et al.* [EXO Collaboration], *Search for Neutrinoless Double-Beta Decay with the Upgraded EXO-200 Detector*, Phys. Rev. Lett. **120**, no. 7, 072701 (2018) doi:10.1103/PhysRevLett.120.072701 [arXiv:1707.08707 [hep-ex]].

[63] L. Yang, *Status and prospects for the EXO-200 and nEXO experiments*, Presentation at the Neutrino 2016 Conf. (2016).

[64] R. Arnold *et al.* [NEMO-3 Collaboration], *Measurement of the double-beta decay half-life and search for the neutrinoless double-beta decay of ^{48}Ca with the NEMO-3 detector*, Phys. Rev. D **93**, no. 11, 112008 (2016), [`arXiv:1604.01710 [hep-ex]`].

[65] A. S. Barabash *et al.* [NEMO Collaboration], *Investigation of double beta decay with the NEMO-3 detector*, Phys. Atom. Nucl. **74**, 312 (2011), [`arXiv:1002.2862 [nucl-ex]`].

[66] B. Schwingenheuer, *Neutrinoless double beta decay with ^{76}Ge*, CERN EP Seminar, Geneva, Switzerland (2017).

[67] S. Sch´onert, *Results from GERDA and prospects for LEGEND: background-free search for neutrinoless double beta decay of ^{76}Ge*, NeuTel 2017, Venice, Italy (2017).

[68] C. Arnaboldi *et al.* [CUORE Collaboration], *CUORE: A Cryogenic underground observatory for rare events*, Nucl. Instrum. Meth. A **518**, 775 (2004) doi:10.1016/j.nima.2003.07.067 [hep-ex/0212053].

[69] D. R. Artusa *et al.* [CUORE Collaboration], *Searching for neutrinoless double-beta decay of* ^{130}*Te with CUORE,*' Adv. High Energy Phys. **2015**, 879871 (2015) doi:10.1155/2015/879871 [arXiv:1402.6072 [physics.ins-det]].

[70] V. Lozza, in Proceedings of Magellan Workshop, Hamburg, Germany, March 2016 (2016).

[71] K. Singh, *Neutrinoless Double Beta Decay Search with SNO+*, DBD16, Osaka, Japan (2016).

[72] J. Klein, NSAC NLDBD Review, Washington, DC, USA (2016).

[73] J. Shirai, *Results and future plans for the KamLAND-Zen*, Neutrino 2016, London, UK (2016).

[74] B. Mong, *nEXO Double Beta Decay*, HQL2016, Blacksburg, VA, USA (2016).

[75] P. P. Povinec [SuperNEMO Collaboration], *Background constrains of the SuperNEMO experiment for neutrinoless double beta-decay searches*, Nucl. Instrum. Meth. A **845**, 398 (2017). doi:10.1016/j.nima.2016.06.104

[76] R. Arnold *et al.* [SuperNEMO Collaboration], *Probing New Physics Models of Neutrinoless Double Beta Decay with SuperNEMO*, Eur. Phys. J. C **70**, 927 (2010) doi:10.1140/epjc/s10052-010-1481-5 [arXiv:1005.1241 [hep-ex]].

[77] S. Andringa *et al.* [SNO+ Collaboration], *Current Status and Future Prospects of the SNO+ Experiment*, Adv. High Energy Phys. **2016**, 6194250, [`arXiv:1508.05759 [physics.ins-det]`].

[78] R. Arnold *et al.* [NEMO-3 Collaboration], *Measurement of the Double Beta Decay Half-life of* ^{130}*Te with the NEMO-3 Detector*, Phys. Rev. Lett. **107**, 062504 (2011), [`arXiv:1104.3716 [nucl-ex]`].

[79] M. Redshaw, B. J. Mount, E. G. Myers and F. T. Avignone, III, *Masses of Te-130 and Xe-130 and Double-beta-Decay Q Value of Te-130*, Phys. Rev. Lett. **102**, 212502 (2009), [`arXiv:0902.2139 [nucl-ex]`].

[80] G. Orebi Gann, *SNO+*, Talk at the Neutrino 2018 Conf. SNO+ Document 5095-v4, June 2018.

[81] M. Chen, SNO+ report, circulated via emails, August 2018.

[82] S. N. Ahmed *et al.* [SNO Collaboration], *Constraints on nucleon decay via 'invisible' modes from the Sudbury Neutrino Observatory*, Phys. Rev. Lett. **92**, 102004 (2004) doi:10.1103/PhysRevLett.92.102004 [`hep-ex/0310030`].

[83] W. C. Haxton and A. M. Serenelli, *CN-Cycle Solar Neutrinos and Sun's Primordial Core Metalicity*, Astrophys. J. **687**, 678 (2008), [`arXiv:0805.2013 [astro-ph]`].

[84] J. Wilson, *Solar neutrinos review and future prospects*, Presentation at the NuPhys 2015 Conf. (2015).

[85] B. Aharmim *et al.* [SNO Collaboration], *Measurement of the Cosmic Ray and Neutrino-Induced Muon Flux at the Sudbury Neutrino Observatory*, Phys. Rev. D **80**, 012001 (2009) doi:10.1103/PhysRevD.80.012001 [arXiv:0902.2776 [hep-ex]].

[86] J. Boger *et al.* [SNO Collaboration], *The Sudbury neutrino observatory*, Nucl. Instrum. Meth. A **449**, 172 (2000), [`nucl-ex/9910016`].

[87] N. Fatemi-Ghomi, *Cover gas commisioning report, operational Manual*, SNO+ collaboration report, SNO+ Document 2918-v1, February 2015.

[88] K. Singh, *The Expected Performance and Motion of the Upward and Downward Ropes in the SNO+ Rope Net*, SNO+ collaboration report, SNO+ Document 1872-v1, April 2013.

[89] R. Ford, *Scintillator Operating Modes and Liquid Handling System Specifications and Process Descriptions*, SNO+ internal document, SLDO-SNP-TR-5003-v1, March 2013.

[90] M. Yeh, *Radiopure Metal-doped Liquid Scintillator*, Presentation at the Low Radioactivity Techniques Conference, (2015).

[91] J. B. Birks et all., *The theory and practice of scintillation counting 1st Edition*, Pergamon Press, January 1964.

[92] S. Grullon [SNO+ Collaboration], *Te-LAB Light Yield and Scintillation Decay Time Constants*, SNO+ collaboration report, SNO+ Document 2410-v1, March 2014.

[93] R. J. Ford [SNO+ Collaboration], *A Scintillator Purification Plant and Fluid Handling System for SNO+*, AIP Conf. Proc. **1672**, 080003 (2015), [`arXiv:1506.08746 [physics.ins-det]`].

[94] A. Bialek, *He-leak Check Documentation Package*, SNO+ collaboration report, SNO+ Document 2799-v1, October 2015.

[95] A. Bialek, *Leak Checking of the Scintillator Plant*, SNO+ collaboration report, SNO+ Document 3046-v1, March 2015.

[96] *The Advantages of Swagelok VCR and VCO Fittings*, [`https://edmontonvalve.swagelok.com/`].

[97] *Edwards nXDS 6i Scroll vacuum pump Instruction Manual*, July 2013.

[98] [`https://www.edwardsvacuum.com/`].

[99] [`http://www.inficon.com/`].

[100] Leybold Inficon. Technical Handbook. UL 200 Helium Leak Detector, December 1997.

[101] P. Skensved, *PMT Repairs / Replacements*, SNO+ collaboration report, SNO+ Document 1617-v1, August 2015.

[102] D. Braid, *PMT Repairs March 12, 2016*, SNO+ collaboration report, SNO+ Document 3568-v1, March 2016.

[103] J. Klein, R. Van Berg, *The SNO Trigger System*, SNO+ collaboration report, SNO+ Document 827-v1, February 2011.

[104] S. Brice, *Monte Carlo and Analysis Techniques for the Sudbury Neutrino Observatory*, PhD thesis, University of Oxford, (1996).

[105] G. Orebi Gann, *Dealing With Time in RAT*, SNO+ collaboration report, SNO+ Document 481-v2, February 2011.

[106] J. Caravaca, *ECA Calibration*, SNO+ collaboration report, SNO+ Document 3698-v1, April 2016.

[107] J. Caravaca, *PCA Calibration*, SNO+ collaboration report, SNO+ Document 1987-v1, May 2016.

[108] S. Peeters, *ELLIE*, SNO+ collaboration report, SNO+ Document 349-v1, August 2010.

[109] G. Orebi Gann et al., *Calibration plan for SNO+*, SNO+ collaboration report, SNO+ Document 1698-v6, August 2013.

[110] K. Clark et al., *The SMELLIE Hardware Manual*, SNO+ collaboration report, SNO+ Document 3511-v2, January 2016.

[111] R. Alves et al., *The calibration system for the photomultiplier array of the SNO+ experiment*, SNO+ collaboration report, SNO+ Document 2821-v2, Octobet 2014.

[112] J. R Sinclair, *Positioning and timing calibration of SNO+*, SNO+ collaboration report, SNO+ Document 4309-v1, March 2017.

[113] E. Leming et al., *TELLIE hardware manual*, SNO+ collaboration report, SNO+ Document 4486-v1, July 2017.

[114] J. Maneira et al., *Optics Overview Aug16*, SNO+ collaboration report, SNO+ Document 3826-v2, August 2016.

[115] S. Langrock et al., *Scattering Length Monitoring at the SNO+ Detector*, SNO+ collaboration report, SNO+ Document 3748-v7, June 2016.

[116] J. R Sinclair, *Scintillator Phase Laserball HW Status*, SNO+ collaboration report, SNO+ Document 2901-v1, January 2015.

[117] J. Hu, *N16 Calibration Source WNPPC2017*, SNO+ collaboration report, SNO+ Document 4159-v3, February 2017.

[118] L. Lebanowski, *(technical note) SNO+ calibration with the N16 source*, SNO+ collaboration report, SNO+ Document 5003-v1, March 2018.

[119] E. Mony, *Na-24 Source*, SNO+ collaboration report, SNO+ Document 2447-v1, March 2014.

[120] L. Sibley, *CAP 2015 - 60Co calibration source for SNO+*, SNO+ collaboration report, SNO+ Document 3171-v2, June 2015.

[121] V. Lozza, *Scandium-48 source review*, SNO+ collaboration report, SNO+ Document 3719-v3, May 2016.

[122] Y. Liu, *AmBe source calibration in SNO+ water phase*, SNO+ collaboration report, SNO+ Document 4837-v2, February 2018.

[123] I. Semenec, *AmBe Design for Scintillator*, SNO+ collaboration report, SNO+ Document 4488-v2, July 2017.

[124] S. Steibert et al., *RAT: Reactor Analysis Tools*, 2014, [`http://rat.readthedocs.org/en/latest/index.html`].

[125] S. Agostinelli et al., *GEANT4 âĂŤ a simulation toolkit*, Nuclear Instruments and Methods in Physics Research A, 506:250âĂŞ303, (2003).

[126] G. Horton-Smith et al., *GLG4Sim - An adaptation of KamLANDâĂŹs KGL4Sim*, 2005, [`http://neutrino.phys.ksu.edu/ GLG4sim/`].

[127] R. Brun et al., *ROOT - An Object Orientated Data Analysis Framework*, Nuclear Instruments and Methods in Physics Research A, 389:81âĂŞ86, (1997).

[128] HepRep: a Generic Interface Definition for HEP Event Display Representables, [`http://www.slac.stanford.edu/ perl/heprep/`].

[129] Echidna software github page, [`https://github.com/snoplusuk/echidna`].

[130] E. Arushanova et al., *echidna status and analyses*, SNO+ collaboration report, SNO+ Document 3601-v1, March 2013.

[131] NumPy package, [`http://www.numpy.org/`].

[132] Private communication with collaborators during the collaboration meetings

[133] N. Fatemi-Ghomi, *CSS current status*, SNO+ collaboration report, SNO+ Document 2642-v6, August 2014.

[134] K. Majumdar, *On the Measurement of Optical Scattering and Studies of Background Rejection in the SNO+ Detector*, SNO+ collaboration report, SNO+ Document 3460-v2, October 2015.

[135] Private communications with collaborators during the collaboration meetings, group meetings and Skype calls

[136] B. Aharmim *et al.* [SNO Collaboration], *Combined Analysis of all Three Phases of Solar Neutrino Data from the Sudbury Neutrino Observatory*, Phys. Rev. C **88**, 025501 (2013) doi:10.1103/PhysRevC.88.025501 [arXiv:1109.0763 [nucl-ex]].

[137] O. Chkvoret, *Leaching studies, March,2014*, SNO+ collaboration report, SNO+ Document 2384-v1, March 2014.

[138] O. Chkvoret, *Results on leaching Pb-210 and daughters from acrylic vessel and spiked acrylic samples, Draft*, SNO+ collaboration report, SNO+ Document 1811-v1, March 2013.

[139] O. Chkvoret, *Leaching rate TeBD*, SNO+ collaboration report, SNO+ Document 3599-v1, May 2016.

[140] B. Liggins, *Channel Software Status*, SNO+ collaboration report, SNO+ Document 4977-v1, March 2018.

[141] B. Liggins, *Channel Software Status*, SNO+ collaboration report, SNO+ Document 5270-v2, Aug 2018.

[142] G. Orebi Gann, *Dynamic PMT status in RAT*, SNO+ collaboration report, SNO+ Document 458-v4, May 2016.

[143] E. Arushanova et al., *Water Analysis Review - PMT calibration*, SNO+ collaboration report, SNO+ Document 3734-v1, June 2016.

[144] J. Walker, *Study of Invisible Mode Nucleon Decay in the SNO+ Detector*, SNO+ collaboration report, SNO+ Document 3856-v1, August 2016.

[145] F. Alessandria *et al.*, *CUORE crystal validation runs: results on radioactive contamination and extrapolation to CUORE background*, Astropart. Phys. **35**, 839 (2012), [`arXiv:1108.4757 [nucl-ex]`].

[146] R. Ford, *A Scintillator Purification Plant and Fluid Handling System for SNO+*, Proceedings for the LRT-2015 conference, SNO+ Document 3186-v1, March 2015.

[147] Muon Tagging in SNO+ RAT 6.16.3 software github page, [`https://github.com/snoplus/rat/blob/6.16.3/src/calib/cleaning/MuonTag.hh`], [`https://github.com/snoplus/rat/blob/6.16.3/src/calib/cleaning/MuonTag.cc`].

[148] A. Soerensen, *An analytical muon-track fitter for SNO+*, SNO+ collaboration report, SNO+ Document 2175-v2, October 2013.

[149] M. Chen et al., *Expected radioactive backgrounds in SNO+*, SNO+ collaboration report, SNO+ Document 507-v34, July 2016.

[150] C. Arpesella *et al.* [Borexino Collaboration], *Direct Measurement of the Be-7 Solar Neutrino Flux with 192 Days of Borexino Data*, Phys. Rev. Lett. **101**, 091302 (2008), [`arXiv:0805.3843 [astro-ph]`].

[151] M. Jones, *Background rejection for the neutrinoless double-beta decay experiment SNO+*, PhD thesis. Oxford University, 2011.

[152] J. Wilson, *A Coincidence Event Generator for RAT*, SNO+ collaboration report, SNO+ Document 178-v1, August 2008.

[153] P. Jones, *Fitter classifier structure*, SNO+ collaboration report, SNO+ Document 1430-v2, February 2013.

[154] I. Coulter, *Modelling and reconstruction of events in SNO+ related to future searches for lepton and baryon number violation*, SNO+ collaboration report, SNO+ Document 2269-v1, January 2014.

[155] M. Mottram, *Updated functional form energy reconstruction: EnergyRThetaFunctional*, SNO+ collaboration report, SNO+ Document 3488-v1, December 2015.

[156] J. Dunger, *Segmentor*, SNO+ collaboration report, SNO+ Document 2783-v4, September 2014.

[157] K. Majumdar, *Seeded Alpha Classifier*, SNO+ collaboration report, SNO+ Document 1522-v1, August 2012.

[158] E. Marzec, *BiPo Event Reduction using Likelihood Ratio Cut*, SNO+ collaboration report, SNO+ Document 1994-v1, July 2013.

[159] K. Majumdar, *BiPo Pileup Rejection*, SNO+ collaboration report, SNO+ Document 2309-v1, March 2014.

[160] M. Mottram, *Reconstruction summary*, SNO+ collaboration report, SNO+ Document 3423-v1, August 2015.

[161] J. Wilson, *Mistagging and Efficiency Studies for the 214Bi and 212Tags*, SNO+ collaboration report, SNO+ Document 2836-v2, December 2014.

[162] K. Goebel, W. Yan, W. Cheetham, *A Method to Calculate Classifier Correlation for Decision Fusion*, 2002 Information, Decision and Control, (2002).

[163] S. Baker and R. D. Cousins, *Clarification of the Use of Chi Square and Likelihood Functions in Fits to Histograms*, Nucl. Instrum. Meth. **221**, 437 (1984). doi:10.1016/0167-5087(84)90016-4

[164] C. Patrignani *et al.* [Particle Data Group], *Review of Particle Physics*, Chin. Phys. C **40**, no. 10, 100001 (2016). doi:10.1088/1674-1137/40/10/100001

[165] J. Wilson, *Proposal for an Y90 source*, SNO+ collaboration report, SNO+ Document 689-v1, November 2010.

[166] CMS Scientific, [`http://www.cmscientific.com/`].

[167] Perkinelmer Inc., [`http://www.perkinelmer.com/`].

[168] G. L. Weissler, *Vacuum Physics and Technology (2 ed.)*, Academic Press. p. 315. ISBN 978-0-12-475914-5, (1979).

[169] V. Lozza et al., *Expected radioactive backgrounds in SNO+*, SNO+ collaboration report, SNO+ Document 507-v27, August 2015.

[170] J. Klein, *Draft Report of the New Nd Verification Task Force*, SNO+ collaboration report, SNO+ Document 1728-v2, March 2013.

[171] J. Kotila and F. Iachello, *Phase space factors for double-β decay*, Phys. Rev. C **85**, 034316 (2012), [`arXiv:1209.5722 [nucl-th]`].

[172] J. Barea, J. Kotila and F. Iachello, *Nuclear matrix elements for double-β decay*, Phys. Rev. C **87**, no. 1, 014315 (2013), [`arXiv:1301.4203 [nucl-th]`].